The assessment of biomechanical modelling and PET/MR imaging in coronary atherosclerosis

Chang Sun

Department of Radiology

University of Cambridge

This dissertation is submitted for the degree of

Doctor of Philosophy

Christ's College

Sep 2021

Declaration

I, Chang Sun, hereby declare that I am the sole author of this thesis. Except where specific reference is made to the work of others, the contents of this dissertation are original and have not been submitted in whole or in part for consideration for any other degree or qualification in this, or any other university. The work presented is my own and where additional help, either technical or other, was sought, it has been appropriately acknowledged.

The work was conducted in the Department of Radiology, University of Cambridge, under the supervision of Professor Martin J Graves, and Dr Zhongzhao Teng. This dissertation contains less than 65,000 words including appendices, bibliography, footnotes, tables and equations and has less than 150 figures.

Abstract

Chang Sun: The assessment of biomechanical modelling and PET/MR imaging in coronary atherosclerosis

Supervised by Prof Martin J Graves

The life-threatening acute coronary syndromes (ACSs) are caused mainly by the rupture of the coronary atherosclerotic plaques. Angiography-defined luminal stenosis is the only validated criterion for clinical decision making. However, post-mortem studies showed that only 14% of myocardial infarctions (MIs) were caused by plaques with >70% stenosis. Plaque vulnerability, characterised by morphological and compositional features, is more important than the luminal stenosis measurements. Mini-invasive virtual-histology intravascular ultrasound (VH-IVUS), optical coherence tomography (OCT), computed tomography angiography (CTA), magnetic resonance imaging (MRI) and positron emission tomography (PET) have been developed to characterise lesion morphology, composition, function and metabolism. However, the overall predictive power of an imaging-defined high risk feature for future ischaemic events is insufficient for clinical decision making. New biomarkers are therefore needed. Coronary atherosclerosis is a chronic inflammatory disease, and the plaque is subject to mechanical loading due to dynamic blood pressure and flow, as well as bending due to heart motion. The mechanical loading estimation and the inflammation quantification have the potential in generating new biomarkers for vulnerability assessment. An accurate mechanical analysis depends on many factors, such as material properties, loading conditions and modelling strategies. The influence of material properties and loading conditions has been widely studied, whilst modelling strategies are currently less investigated. A PET/MR system provides simultaneous anatomical and metabolic imaging. However, accurate attenuation correction is essential for quantitative PET reconstruction in the thorax, and the application of PET/MR in coronary imaging is limited due to the challenges of obtaining good quality images of the coronary vessels.

The work presented in this thesis first investigates the influence of computation strategies and bending on the calculation of mechanical parameters, in particular, plaque structure stress (PSS). The hypothesis is that the 3D structure only finite element analysis (FEA) can accurately predict the PSS with good time efficiency, and bending is an important factor in coronary biomechanical analysis. Mechanical parameters calculated from the 3D fully coupled fluid-

structure interaction (FSI) model with the patient-specific bending were used as references. 3D structure-only FEA showed a good agreement with the gold standard model and a shorter solution time (Chapter 3). The comparison of mechanical features with and without patient-specific coronary bending showed an increase in PSS due to the bending and revealed the importance of bending in coronary FEA (Chapter 4).

For the imaging part, a hybrid bias correction method was proposed for the thoracic region using zero echo time (ZTE) images, which were converted to pseudo-CT images of the lung region. These images were integrated with the standard MR attenuation map to improve the accuracy of attenuation correction (AC) in PET reconstruction (Chapter 5). We hypothesise that non-Cartesian MR sequences could improve the coronary image quality in a PET/MR system, and the incorporation of ZTE based pseudo-CT in the lung can improve the PET attenuation correction. The imaging part of this work involved the development of 3D non-Cartesian (spiral and radial) trajectory MR sequences for the PET/MR system (Chapter 6).

Overall, the 3D structure only FEA with patient-specific bending can accurately estimate the coronary PSS with a reasonable computation time. The ZTE based pseudo-CT attenuation correction in the lung region can improve the accuracy of thoracic PET reconstruction. The application of non-Cartesian sequences for coronary imaging requires further development in the PET/MR system.

Acknowledgements

I would like to express my gratitude and appreciation to my academic supervisors, Prof Martin J Graves and Dr Zhongzhao Teng, who have provided unconditional support and guidance throughout the study, research and preparation of this thesis. Prof Graves has provided me with patience and continuous guidance with his tremendous experience and knowledge in MR physics. He has been very supportive in light of restrictions due to the COVID-19 pandemic, and I enjoy the out-of-hour scanning sessions with him. Dr Teng has led me into the biomechanical field and inspired me in various mechanical, image processing and vascular modelling topics. He gave me enormous freedom and support to explore my research interest in the biomedical imaging field. I feel privileged to have them as my supervisors.

This project would not have been possible without the support of many people and I wish to thank the people who contributed to this project. I would like to thank Prof Fiona J Gilbert for her supervision and tremendous support as the Head of the Department of Radiology. I am thankful to Prof Jonathan H Gillard for bringing me to this motivated research group and for his supervision in my first year. I feel grateful to Dr Roido Manavaki for her expertise and collaboration in the PET imaging field. I must thank Dr Jason Tarkin for kindly sharing the patient data from his research project and offering clinical advice from his perspective. I wish to thank Prof Martin Bennett, Prof James HF Rudd, Dr Adam Wolf, and Ms Sophie Gu for their valuable clinical insights; Prof Michael Sutcliffe, Dr Yuan Huang, and Dr Shuo Wang for their contribution to mechanical and statistical analysis; Dr Joshua D Kaggie, Dr Mary A McLean for their suggestion and insights in MR physics and sequence development. I also want to thank Dr Chao Li, Dr Hao Li, Dr Aziz Tokgoz, Mr Tao Luo, and Mr Jin Zheng for their help as collaborators, friends, and colleagues.

I want to express my deepest gratitude to my parents for their love, trust and support in my life and study. I wish to thank my grandparents Tian and Sun, who unfortunately passed away during my research in Cambridge.

Contents

Contents ……..i
List of Figures..... iii
List of Tables.....vii
List of Symbols..... viii
List of publications.....xv
Glossary ……xvii
Chapter 1 Introduction.....1
1.1 Pathophysiology of Atherosclerosis.....1
1.2 Medical Imaging of Coronary Atherosclerosis.....5
1.2.1 Computed Tomography (CT).....5
1.2.2 Magnetic Resonance (MR) Imaging.....7
1.2.3 Conventional X-ray Angiography.....9
1.2.4 Intravascular Ultrasound (IVUS).....11
1.2.5 Optical Coherence Tomography.....12
1.2.6 Positron Emission Tomography (PET) and Other Imaging Modalities.....14
1.2.7 Multimodal Integration.....15
1.3 Vulnerability Assessment and Biomechanical Analysis of Coronary Atherosclerosis 16
1.3.1 Mechanisms of Plaque Rupture.....16
1.3.2 Morphology and Calcification in Plaque Vulnerability Assessment.....17
1.3.3 Fractional Flow Reserve (FFR) and Computational Fractional Flow Reserve (CFFR) in Plaque Vulnerability Assessment.....18
1.3.4 Mechanical Analysis in Plaque Vulnerability Assessment.....19
Chapter 2 Coronary Biomechanics and Modelling.....23
2.1 Concepts in Coronary Finite Element Analysis.....23
2.1.1 Description of Internal Deformation and Forces.....23
2.1.2 Constitutive Law.....27
2.1.3 Finite element analysis.....28
2.2 Finite Element Modelling of Coronary Artery.....31
2.2.1 2D Structure Mesh of VH-IVUS.....31
2.2.2 3D Central Line Reconstruction of DSA.....36

2.2.3 VH-IVUS and 3D central line integration 40
2.2.4 3D Mesh Generation 45
2.2.5 Physiological boundary conditions 47
2.3 Coronary bending quantification with multi-phase CCTA 49
Chapter 3 The influence of modelling strategy on the hemodynamic analysis of coronary atherosclerotic plaques 53
3.1 Introduction 53
3.2 Materials and Methods 54
3.3 Results 59
3.4 Discussion 64
Chapter 4 The influence of patient-specific bending in finite element analysis and vulnerability assessment of coronary atherosclerotic plaques 68
4.1 Introduction 68
4.2 Materials and Methods 69
4.3 Results 70
4.4 Discussion 82
Chapter 5 Hybrid bias correction of thoracic ZTE images and PET attenuation correction for lung region 87
5.1 Attenuation correction in PET 87
5.2 Hybrid bias correction of thoracic ZTE images 92
5.3 Lung pseudo-CT generation using ZTE images 103
Chapter 6 Magnetic Resonance Imaging 115
6.1 MR Theory 115
6.2 Coronary MR 121
6.3 Stack-of-spirals MR sequence 125
6.4 Stack-of-stars Sequence 136
Chapter 7 Conclusion 149
7.1 Conclusion 149
7.2 Limitations 151
7.3 Future directions 153
Reference 156

List of Figures

Figure 1.1 An atherosclerotic plaque.. 3

Figure 1.2 AHA classification of atherosclerotic lesion types. 4

Figure 1.3 Coronary CT images.....6

Figure 1.4 MR and histology image of a left internal carotid artery[4]. 8

Figure 1.5 Comparison of MRA and conventional X-ray angiography 9

Figure 1.6 Comparison of conventional X-ray angiography and DSA 10

Figure 1.7 Illustration and histological comparison of OCT 13

Figure 1.8. Illustration of computational fractional flow reserve (CFFR).....19

Figure 2.1 Image processing of VH-IVUS 33

Figure 2.2 Iterative structure mesh of VH-IVUS.....35

Figure 2.3 Conventional X-ray angiography segmentation and central line extraction 36

Figure 2.4 Illustration of angiographic projection 38

Figure 2.5 3D central line reconstruction. 39

Figure 2.6 Rotation initialization of VH-IVUS image.....41

Figure 2.7 Selection of branching landmarks in a VH-IVUS stack.....42

Figure 2.8 VH-IVUS and 3D central line integration.....43

Figure 2.9 Local reference system of the 3D central line. 44

Figure 2.10 Illustration of frame intersection.. 45

Figure 2.11 Illustration of 3D structure meshes connectivity.....46

Figure 2.12 Solid and fluid mesh of the coronary vessel.....47

Figure 2.13 Bending displacement and pressure boundary conditions.....49

Figure 2.14 CCTA coronary segmentation and central line (LAD) extraction 50

Figure 2.15 Coronary curvatures and bending (curvature difference) from CCTA central line extraction.....51
Figure 3.1 Reconstructed 3D geometry of each coronary vessel.....59
Figure 3.2 Solution time of different FEA strategies.....60
Figure 3.3 Luminal WSS, TAWSS, OSI, RRT of Patient 1.....61
Figure 3.4 Comparison of mesh and PSS (unit: kPa) of different computational strategies ...62
Figure 3.5 Bland-Altman plot of PSS and haemodynamic parameters in different computational strategies.....63
Figure 3.6 Bland-Altman plot of MSS and MPS in different computational strategies.....63
Figure 3.7 Comparison of pressure difference and average pressure gradients across plaques 64
Figure 4.1 Mean vessel central line curvature and standard deviation of central line curvature 71
Figure 4.2 Logarithmic ratio of mechanical features (Bending v Non-bending) 73
Figure 4.3 Logarithmic ratio of mechanical features (Bending vs Average bending).....75
Figure 4.4 Comparison of biomechanical features with different bending models.....77
Figure 4.5 Percentage PSS difference (logarithmic) and plaque morphology.....79
Figure 4.6 Comparison of PSS with morphological risk factors 81
Figure 4.7 Longitudinal location of morphological risk factors and high PSS region 82
Figure 5.1 Time sequence diagram of RUFIS ZTE sequence 91
Figure 5.2 Bias field corrupted original ZTE image, surface fitting (N4ITK) corrected image, and histogram-based corrected image.....93
Figure 5.3 Image processing flow chart for N4ITK and histogram-based bias correction, mask generation and hybrid bias correction 97

Figure 5.4 Illustration of the hybrid bias correction method. 98

Figure 5.5 Intensity normalization of ***ZTEN4*** images 99

Figure 5.6 Probability density function (PDF) of the tissue and lung regions. 100

Figure 5.7 Boxplot showing the coefficient of variation for the body, tissue and lung regions (n = 9 patients). 100

Figure 5.8 Lung and bone segmentation mask (above) and ZTE images (bellow) 101

Figure 5.9 Joint histogram of ZTE and CT intensity in lung.....105

Figure 5.10 CT, ZTE, pseudo-CT images and their difference 107

Figure 5.11 Integrated MR-based attenuation maps 108

Figure 5.12 PET intensity and difference of different MRAC methods in the lung.....109

Figure 5.13PET intensity and difference of different MRAC methods in the thorax.....110

Figure 5.14 Comparison of PET intensity in different regions of interest among all patients 111

Figure 6.1 A slice selection gradient and SINC RF pulse are shown, which causes a rectangular spatial region, Δz, to be excited 119

Figure 6.2 Pulse sequence diagram of 3D spoiled gradient recalled echo sequence 120

Figure 6.3 Cartesian k-space trajectory and image 121

Figure 6.4 Cardiac MR images acquired with 3T PET/MR using 3D HEART sequence.....124

Figure 6.5 k-space trajectory, image and gradient waveform of spiral sequence.....126

Figure 6.6 Spiral Trajectories and the Voronoi boundaries of the central k-space. The images were reconstructed with and without density compensation of Voronoi areas. 128

Figure 6.7 Spiral images with and without off-resonance correction (acquired using a 1.5 T GE 450w), and a spiral image acquired using a PET/MR (3.0 T GE Signa, without off-resonance correction) 130

Figure 6.8 Frequency segmented off-resonance correction 131

Figure 6.9 Time segmented off-resonance correction 132
Figure 6.10 Spiral image and an off-resonance frequency map were acquired. The off-resonance map was segmented by frequency and frequency segmented off-resonance correction was applied to the image.....133
Figure 6.11 Focusing criteria at different frequencies and off-resonance frequency map 134
Figure 6.12 Spiral images with no off-resonance correction, with auto-focusing off-resonance correction and with additional medial filtering of off-resonance frequency map. 135
Figure 6.13 Radial trajectories, k-space, image, gradient waveform and 3D trajectories of a 3D stack-of-stars sequence. 136
Figure 6.14 A sinogram was created by inverse Fourier transforming the signal of each spoke. The same data were gridded to a k-space. The phantom images were reconstructed with the filtered back-projection method and 2D IFFT. 138
Figure 6.15 Evenly rotated and golden angle rotated radial trajectories, and their images ..140
Figure 6.16 Gradient delay estimation uses a pair of antiparallel spokes for each orientation. 142
Figure 6.17 The ideal radial trajectory is shifted according to the estimated gradient delay in each direction, and the images reconstructed with the two trajectories are shown. 143
Figure 6.18 Stack-of-stars images of a healthy volunteer.....144
Figure 6.19 Self-gating signals were extracted from the peak spoke signals and from the sum of spoke magnitudes 147

List of Tables

Table 2.1 Correlation coefficients of coronary curvatures and bending.....51

Table 4.1 Patient index and physiological information 70

Table 4.2 Percentage (%) difference of mechanical features with different bending models .78

Table 5-1 Comparison of machine learning models with cross-validation 106

List of Symbols

Symbol	Annotation	Associate Equation/ Chapter
$\boldsymbol{X}$	Undeformed coordinate	2.1
$\boldsymbol{x}$	Deformed coordinate	2.1
u	Field function of displacement	2.1
t	Time	
$\boldsymbol{F}$	Deformation gradient tensor	2.3
$\boldsymbol{I}$	Identity matrix	2.4
δ_{iK}	Kronecker delta function	2.4
$\boldsymbol{H}$	Displacement gradient tensor	2.4
l_X^2	Length of displacement $d\boldsymbol{X}$	2.5
$\boldsymbol{C}$	Right Cauchy-Green deformation tensor	2.6
λ_i	Principal stretches of $\boldsymbol{C}$	2.7

$\boldsymbol{N}_i$	Principal stretches direction of $\boldsymbol{C}$	2.7
I_i^C	Invariants of $\boldsymbol{C}$	2.7
$\boldsymbol{E}$	Lagrangian finite strain tensor	2.9
F	Force	2.10
A	Cross sectional area	2.10
σ	Stress in uniaxial tension	2.10
$\boldsymbol{\sigma}$	Cauchy stress tensor	2.11
$\boldsymbol{T}^{(\boldsymbol{n})}$	Stress vector on a plane with normal vector **n**	2.12
σ_e	Effective stress	2.13
$\widehat{W}(I_1, I_2, I_3)$	Strain energy density function (SEDF) defined with strain invariants	2.14
$\widetilde{W}(\lambda_1, \lambda_2, \lambda_3)$	SEDF defined with stress invariants	2.14
c_1, C_1, D_1, D_2	Material constants of modified Mooney-Rivlin SEDF	2.16, 3.1
κ	Lagrangian multiplier	2.16
σ_i	Principal stress	2.17

$\boldsymbol{b}$	Body force per unit mass	2.18
ρ	Solid density	2.18
a	Acceleration	2.18
S_u	Boundary surface of displacement	2.18
$\bar{\boldsymbol{u}}$	Displacement on the boundary surface S_u	2.18
S_t	Boundary surface of traction force	2.18
$\boldsymbol{T}$	Traction force on the boundary surface S_t	2.18
$\boldsymbol{v}$	Velocity vector	2.19
μ	Dynamic viscosity constant	2.19
$\boldsymbol{e}$	Strain rate tensor	2.19
$\vec{r}$	Position of 2D VH-IVUS nodes	2.20
N	Total number of 2D VH-IVUS nodes	2.20
$r_{i,j}$	Euclidean distance between node $\vec{r}_i$ and $\vec{r}_j$	2.20
$r_{i,edge}$	Euclidean distance between node $\vec{r}_i$ and the nearest component edge	2.20

α	Empirical coefficient of forces	2.20
$f(s)$	Curve parametric function of variable *s*	2.21
a_0, a_1, b_n, c_n	Constants of curve parametric function	2.21
p_i	2D projection of the central line on angiographic plane i	2.22
RT_i	Rotational matrix	2.24
θ_i, φ_i	Rotational angles with respect to x, y axes in angiographic plane i	2.24
p	Pressure	3.4
σ_{VM}	Von Mises stress, effective stress	3.8
$\sigma_{ii}\ (i = x, y, z)$	Principal tensile stress	3.8
τ	Shear stress	3.8
I_o	Initial photon intensity	5.1
μ	Linear attenuation coefficient	5.1
$B(x, y)$	Bias field	5.2
$\epsilon(x, y)$	Noise field	5.2

$\sigma(I_i)$	Standard deviation of image intensity I_i	5.4
$\mu(I_i)$	Mean of image intensity I_i	5.4
γ	Gyromagnetic ratio	6.1
B_0	External magnetic field	6.1
N_{up}, N_{down}	Number of spins in the up/down state with respect to the direction of B_0	6.2
$\Delta\epsilon$	Energy difference (J)	6.2
κ_B	Boltzmann constant	6.2
T	Absolute temperature (K)	6.2
$\boldsymbol{M}$	Bulk magnetization vector	6.2
B_1	Magnetic field induced by radiofrequency	Ch 6.1
$M_{x,y,z}$	Magnetization in x, y, z plane	6.3
$B_{x,y,z}$	Magnetic field strength in x, y, z plane	6.3
$G_{x,y,z}$	Magnetic gradient in x, y, z plane	6.4
ω	Precessional frequency	6.7

$S(x)$	MR signal function	6.8
$\rho(x)$	Spin density function	6.8
$\phi(x), \Delta\phi(x)$	Phase function, phase offset function	6.11
Δz	Slice thickness	6.12
$\Delta\omega_{RF}$	RF bandwidth	6.12
$I(x,y)$	Image intensity function	6.13
$S(u,v)$	MR signal function (k-space)	6.13
$\vec{k}(t), [k_x, k_y, k_z]$	k-space trajectory vector	6.14
$\vec{G}$	Gradient vector	6.14
$r(t)$	Spiral radius	6.16
λ	Spiral constant	6.16
$\theta(t)$	Azimuthal angle	6.16
S_R,	Slew rate	6.20
G_{max}	Maximum gradient amplitude	Ch 6.3
$\Delta\omega(\vec{r})$	Spatial function of off-resonance frequency	6.21

$f_{max}, f_{min}, f_{bin}$	Maximum, minimum off-resonance frequency and mean off resonance frequency of correction bin	Ch 6.3
T_{acq}	Acquisition time	Ch 6.3
[H]	Proton density	6.23
α_E	Ernst Angle	6.24
S_f, S_b	Forward and backward radial MR signal	6.25
$FT(s)$	Fourier Transformation of s	6.25
$g(x)$	Gradient delay function	6.25
k_{shift}	Shift in k-space due to gradient delay	6.26

List of publications

Manuscripts under review/revision/in preparation:

1. **Chang Sun**, Yuan Huang, Martin Bennett, Zhongzhao Teng. The influence of patient specific bending in finite element analysis and vulnerability assessment of coronary atherosclerotic plaques (manuscript)
2. **Chang Sun**, Yuan Huang, Martin Bennett, Zhongzhao Teng. The influence of modelling strategy on the structural and hemodynamic simulation of coronary atherosclerotic plaques. (in preparation)
3. **Chang Sun**, Roido Manavaki, Jason Tarkin, Christopher Wall, James HF Rudd, Fiona J Gilbert, Martin J Graves. Lung pseudo CT generation with Zero echo time (ZTE) images and MR attenuation for lung in PET/MR (in preparation)

Conference presentations:

1. **Chang Sun**, Yuan Huang, Martin Bennett, Zhongzhao Teng. The influence of computational strategy on prediction of mechanical stress in coronary atherosclerotic plaques with bending. BioMedEng21, Online, Sep 2021.
2. **Chang Sun**, Mary A McLean, Titus Lanz, Frank Riemer, Rolf F Schulte, Fiona J Gilbert, Martin J Graves, and Joshua D Kaggie. Hybrid bias correction of thoracic ZTE images. ISMRM annual meeting, Online, May 2021.
3. **Chang Sun**, Mary A McLean, Titus Lanz, Frank Riemer, Rolf F Schulte, Fiona J Gilbert, Martin J Graves, and Joshua D Kaggie. Quantitative sodium imaging in the carotid and aorta. ISMRM annual meeting, Online, May 2020.
4. Zhongzhao Teng, Shuo Wang, **Chang Sun**, Aziz Tokgoz, Valentina Taviani, Joseph Bird, Umar Sadat, Yuan Huang, Andrew J Patterson, Nichola Figg, Martin J Graves, Jonathan H Gillard. Identification of vulnerable atherosclerotic plaques: from In vivo imaging, material and biomechanical analysis. European Society of Biomechanics 25th Congress, Vienna, Aug 2019.
5. Chao Li, **Chang Sun**, Shuo Wang Carola-Bibiane Schönlieb, Stephen J Price. Intra-

tumoural perfusion habitats showed prognostic value in glioblastoma patients. British Neuro-Oncology Society annual meeting, London, Apr 2019.

Other publications produced during the period of this thesis:

1. Shuo Wang, Aziz Tokgoz, Yuan Huang, Yongxue Zhang , Jiaxuan Feng, Priya Sastry, **Chang Sun**, Nichola Figg, Qingsheng Lu, Michael PF Sutcliffe, Zhongzhao Teng, Jonathan H Gillard. Bayesian inference-based estimation of normal aortic, aneurysmal and atherosclerotic tissue mechanical properties: from material testing, modelling and histology. *IEEE Trans. Biomed. Eng*., 2019 Aug;66(8):2269-2278.
2. Joshua Kaggie, Titus Lanz, Mary A McLean, Frank Riemer, Rolf F Schulte, Arnold Benjamin, Dimitri A Kessler, **Chang Sun**, Fiona J Gilbert, Martin J Graves, and Ferdia A Gallagher. Combined 23Na and 13C imaging at 3.0 T using a single-tuned large field of view birdcage coil. *Magnetic Resonance in Medicine*, 86(3): 1734-1745.

Other manuscripts produced during the period of this thesis:

1. Aziz Tokgoz, Shuo Wang, Priya Sastry, **Chang Sun**, Nichola L. Figg, Yuan Huang, Martin R. Bennett, Sanjay Sinha, Jonathan H. Gillard, Michael P. F. Sutcliffe, Zhongzhao Teng. Association of collagen, elastin, glycosaminoglycans and macrophages with tissue ultimate material strength and extreme extensibility in human thoracic aortic aneurysms: a uniaxial tension study.
2. Sophie Z. Gu, Charis Costopoulos, Yuan Huang, Christos Bourantas,Adam Woolf, **Chang Sun**, Zhongzhao Teng, Sylvain Losdat, Lorenz Räber Habib Samady, and Martin R. Bennett. High-intensity Statins Reduce Plaque Structural Stress through Remodeling Artery Geometry and Plaque Architecture.
3. Chao Li, **Chang Sun**, Shuo Wang, Carola-Bibiane Schönlieb, Stephen J Price. Intratumoral perfusion habitats in glioblastoma reveals different prognostic value of tumoral vascularity.

Glossary

AC	Attenuation correction
AHA	American Heart Association
ALE	Arbitrary Lagrangian-Eulerian formulation
BHF	British Heart Foundation
CABG	Coronary artery bypass grafting
CAC	Coronary arterial calcification
CAD	Coronary artery disease
CBVD	Cerebrovascular disease
CCTA	Coronary Computed Tomography angiography
CFD	Computational fluid dynamics
CFFR	Computed fractional flow reserve
CHD	Coronary heart disease
CJV	Coefficient of joint variation
CNN	Convolutional neural network
CS	Compress sensing
CSA	Cross-sectional area
CT	Computed tomography
CTAC	Computed Tomography based attenuation correction
CTP	Computed tomography perfusion
CV	Coefficient of variation
CVD	Cardiovascular disease
DSA	Digital subtraction angiography
EEM	External elastic membrane
EM	Expectation Maximization
FA	Flip angle
FDG	Fluorodeoxyglucose
FEA	Finite element analysis
FEM	Finite element method
FFR	Fractional flow reserve
FFT	Fast Fourier transformation
FOV	Field of view
FSI	Fluid structure interaction
FWHM	Full width at half maximum
GMM	Gaussian mixture model
HU	Hounsfield unit
ICA	Invasive coronary angiography
IFFT	Inverse fast Fourier transformation
IQR	Interquartile range
IVUS	Intravascular ultrasound
LAD	Left anterior descending (artery)
LCA	Left coronary artery

LDL	Low-density lipoprotein
MACE	Major adverse cardiac events
MBF	Myocardial blood flow
MI	Myocardial infarction
ML	Maximum Likelihood
MLA	Minimum luminal area
MPS	Maximum principal strain
MR	Magnetic resonance
MRA	Magnetic resonance angiography
MRAC	Magnetic resonance attenuation correction
MRI	Magnetic resonance imaging
MSS	Maximum shear stress
NEX	Number of excitation
NIFR	Near-infrared fluorescence
NIRS	Near-infrared spectroscopy
NUFFT	Non-uniform fast Fourier transformation
OCT	Optical coherence tomography
OSI	Oscillatory shear index
PB	Plaque burden
PCA	Principal component analysis
PCI	Percutaneous coronary intervention
pCT	Pseudo-CT
PDF	Probability density function
PET	Positron emission tomography
PSS	Plaque structural stress
QCA	Quantitative coronary angiography
RBW	Receiver bandwidth
RCA	Right coronary artery
RF	Radiofrequency
ROI	Region of interest
RRT	Relative residence time
SEDF	Strain energy density function
SMC	Smooth muscel cell
SNR	Signal noise ratio
SPECT	Single photon emission computed tomography
SPGR	Spoiled gradient echo
SUV	Standardized uptake value
TAWSS	Time averaged wall shear stress
TCFA	Thin-cap fibroatheroma
TE	Time of echo
TOF	Time-of-flight
TR	Time of recall
UTE	Ultrashort time of echo
VH-IVUS	Virtual-histology intravascular ultrasound
VH-TCFA	Virtual-histology defined thin-cap fibroatheroma
VOI	Volume of interest
WSS	Wall shear stress
ZTE	Zero time of echo

Chapter 1 Introduction

Atherosclerosis is a chronic inflammatory disease characterised by the deposition of lipid materials and the formation of atheromatous plaque under the endothelium in arterial walls[1,2]. Atherosclerosis leads to lumen narrowing and subsequent cardiovascular diseases (CVDs), including coronary heart disease (CHD) and cerebrovascular disease (CBVD), primarily due to plaque rupture. According to the World Health Organization, CVD is the most common cause of death globally. In 2019, an estimated 17.9 million deaths were attributed to CVD, accounting for 32% of all-cause deaths[3]. CHD and CBVD are two significant manifestations of atherosclerosis and claim 47.1% and 37.3% of CVD deaths worldwide, respectively[4].

Among atherosclerotic complications, CHD is the most prevalent form of atherosclerosis in the UK. An estimated 2.3 million UK citizens are diagnosed with CHD, representing 33% of CVD patients[5,6]. Because of the wide prevalence and severity of CHD, the economic burden caused by CHD is higher than any other disease in the UK, costing £ 7.1 billion annually[6]. With the growth of the ageing population, CHD's impact on health and the economy is expected to increase[7].

1.1 Pathophysiology of Atherosclerosis

The exact pathogenesis and mechanisms of atherosclerosis progression are complex and are partially understood. According to the contemporary model, initiation of atherosclerosis is thought to be the dysfunction of vascular endothelial cells due to irritating stimuli (such as dyslipidaemia, hypertension or pro-inflammatory mediators), causing the expression of adhesive molecules and changing of endothelial permeability[8]. Previous studies have identified risk factors such as an elevated low-density lipoprotein (LDL) level, cigarette smoking, and hypertension[9,10]. High LDL levels play a significant role in atherosclerosis, and its mechanism has been extensively studied in the literature.

High LDL concentrations in the blood increase the transportation rate and accumulation of

LDL in arterial walls[11,12]. Penetration of LDL into the vessel intima is likely to happen in the region with low and oscillatory endothelial shear stress, where pro-atherogenic genes are overexpressed through a mechanosensitive gene pathway[11–13]. Penetrated LDLs undergo multiple stages of modification, including oxidation, lipolysis, and aggregation. Oxidised LDLs (oxLDLs) demonstrate pro-inflammatory properties by promoting adhesion molecules' expression and increasing the adhesion of leukocytes (monocytes) at the site of atherosclerosis[9,14,15]. Oxidized LDLs then stimulate the production of macrophage colony-stimulating factors from the endothelial cell, facilitating the differentiation of monocyte to macrophage[14]. Recruited macrophages and smooth muscle cells (SMCs) uptake oxLDLs and perform cholesterol esterification. Macrophages' lipid uptake is uncontrolled and is imbalanced with their lipid efflux, resulting in the accumulation of cholesterol esters stored as cytoplasmic lipid droplets[16]. Macrophages with large lipid deposits are termed "foam cells", and are the hallmark of early stage atherosclerotic lesion[2,16]. The accumulation of lipid droplets within foam cells and the formation of fibrous tissues increases the thickness of intima, resulting in pathological intimal thickening[9].

During atherosclerotic progression, the massive lipid deposition causes apoptosis of foam cells, forming a necrotic lipid core. As the necrotic lipid core deforms the arterial wall, the loose intimal connective tissue is gradually replaced by the collagen-rich fibrous tissue produced mainly by smooth muscle cells (SMCs)[9]. Within the lesion, microvessels grow from the vasa vasorum. New microvessels are leaky and lack structural integrity, resulting in haemorrhage and amplifying inflammation[17]. The necrotic lipid core, together with intraplaque haemorrhage, fibrous tissue and calcification, form the basic structure of an atherosclerotic plaque (Figure 1.1).

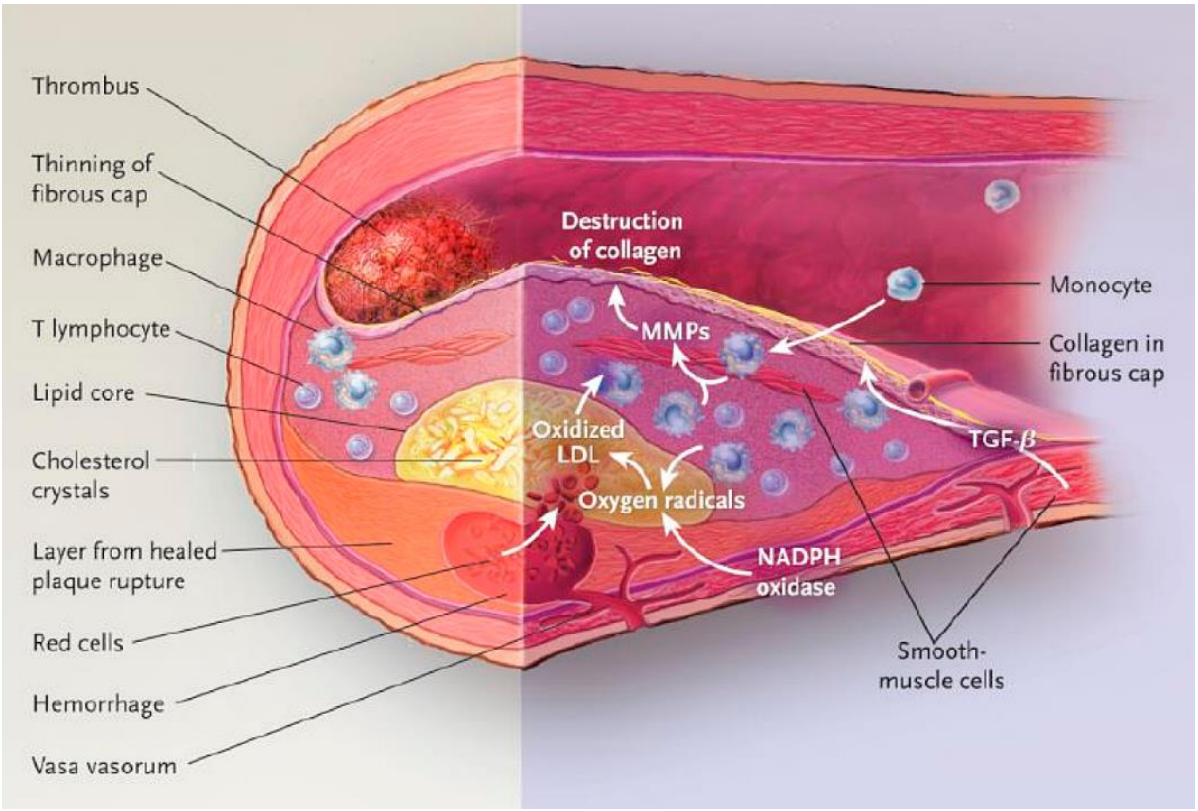

Figure 1.1 An atherosclerotic plaque[18]. An atherosclerotic plaque, including a large lipid core, a thin fibrous cap and a thrombus at the plaque shoulder, a haemorrhage near the vasa vasorum, and the infiltrated inflammatory cells. The mechanism of fibrous cap thinning and production of oxLDLs is shown schematically. Inflammation in the plaque triggers the release of matrix metalloproteinases (MMPs), which destroy collagen and cause fibrous cap thinning. Oxygen radicals produced by NADPH oxidases and inflammatory cells oxidise LDLs, resulting in oxLDLs and the formation of a necrotic lipid core.

The presence of atherosclerotic plaque may cause ischaemia and stable angina but is rarely lethal in the absence of scarring of the myocardium[9]. According to post-mortem studies, life-threatening acute coronary syndromes (ACSs) are most often caused by thrombosis associated with plaque rupture or plaque erosion[19–21]. Plaque rupture is defined as the disruption in the fibrous cap that separates the necrotic lipid core from the lumen[19]. Exposure to highly thrombogenic necrotic lipid core initiates platelet aggregation and blood coagulation and sometimes causes life-threatening thrombosis[22]. For a thrombosed arterial segment without plaque rupture, smooth muscle cells, proteoglycans, and an absence of endothelium are usually found. This condition is termed plaque erosion[23]. The lack of macrophage infiltration and thickening of intact media in plaque erosion segments suggest vasospasm as the potential cause of this endothelial damage[24]. However, the mechanism of plaque erosion and the association between missing endothelium and thrombosis are unclear.

Not all thromboses are lethal. Depending on the thrombogenicity of the exposed materials, local flow disturbances, and systemic thrombotic propensity, the magnitude of thromboses is different[9]. A relatively minor thrombosis caused by plaque rupture or erosion can heal, resulting in a multilayer structure comprised of multiple necrotic lipid cores and fibrous layers[20,25]. The healed thrombosis is a significant factor in causing chronic high-grade coronary stenosis and explains the phasic progression of coronary diseases[25].

Atherosclerotic lesions are classified into different types based on their histological morphologies and pathological stages. The classification scheme introduced by the American Heart Association (AHA) is a commonly accepted scheme[26,27]. Figure 1.2 illustrates the lesion types in the AHA classification.

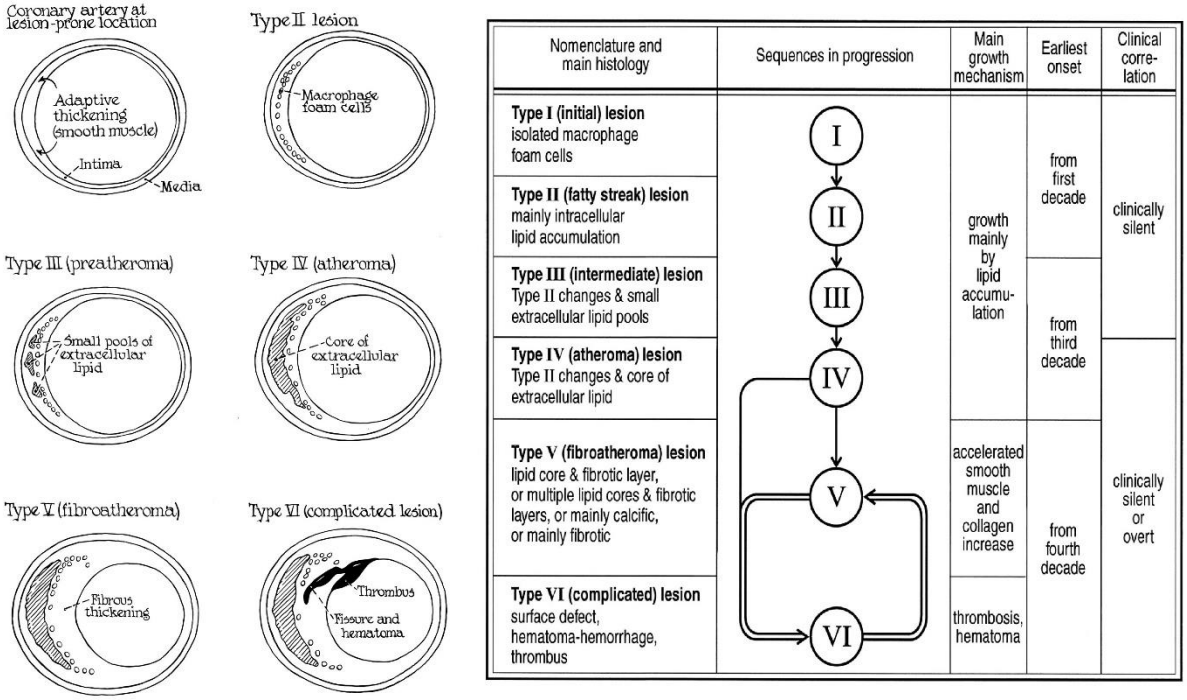

Figure 1.2 AHA classification of atherosclerotic lesion types[26]. The drawings of vascular cross-sections on the left illustrate typical structures of lesion types. The table on the right indicates the characteristics of lesion types, and their progression (arrows indicate the possible change of lesion types), growth mechanisms, clinical onsets and clinical correlations.

Lesions are classified into six types and are arranged in a generally linear pattern of atherosclerotic progression. The AHA scheme defines type IV, or atheroma, as a dense accumulation of extracellular lipids contained by a smooth muscle-rich fibrous cap[22,26]. If a

type IV lesion forms new fibrous connective tissue, the lesion progresses to a type V lesion. The shoulder area of a type IV lesion is particularly vulnerable to plaque rupture and results in a type VI lesion with thrombotic events. Thus, a type IV lesion has good potential for clinical significance according to the AHA classification scheme[26].

In microscopic examinations, plaque rupture sites usually have a thin fibrous cap, few or no SMCs, and are infiltrated by macrophages[9]. Quantitative microscopy indicates the average ruptured cap thickness is 23 μm, and the majority (95%) of plaque rupture occurs where fibrous cap thickness <65 μm [19]. Based on the AHA classification scheme and post-mortem observations, the concept of thin-cap fibroatheroma (TCFA) is proposed to characterised vulnerable plaques[22,28]. TCFA is defined as a fibroatheroma with a thin fibrous cap (<65 μm in thickness), a large necrotic core and increased macrophage infiltration[29]. TCFA has been found to be responsible for 60% of acute thrombi with plaque rupture[22], and is regarded as the characteristic vulnerable plaque subtype [22,24,28,30–32].

1.2 Medical Imaging of Coronary Atherosclerosis

The rapid development in medical imaging techniques enables the *in vivo* imaging of coronary arteries with high spatial and temporal resolution in clinical practice and research. The techniques can be generally classified as non-invasive and mini-invasive techniques. While non-invasive imaging techniques (such as computed tomography, and magnetic resonance imaging) are recommended for asymptomatic patients in diagnosis, invasive imaging techniques (such as X-ray angiography, and intravascular ultrasound) can provide images with higher resolution and are usually used for patients with more extensive conditions[33].

1.2.1 Computed Tomography (CT)

Electron-beam computed tomography (EBCT) and multi-detector computed tomography (MDCT) are commonly used in coronary imaging because of their high spatial and temporal resolution. EBCT utilises a stationary multisource detector with electronic beam rotation, which gives EBCT good temporal resolution[34]. Since the acquisition rate no longer depends on the rotational speed of the mechanical gantry, EBCT can produce images with high spatial resolution in 50-100 ms, at 3 mm slice width[35,36]. MDCT differs from traditional single

detector–row CT in its multi-row detector array and can produce CT images in <500 ms, at 0.5-0.75 mm slice width[36]. The multiple row detector in MDCT also increases the imaging field's coverage, enabling accurate 3D volumetric reconstruction for coronary imaging.

Coronary arterial calcification (CAC) is a common feature of atherosclerotic plaques (Figure 1.3 A). Calcium has a high X-ray attenuation coefficient and can be detected in EBCT and MDCT with high contrast. CT based CAC measurements (usually in the form of an Agatston calcium score) have been proven to have predictive value in future CAD events[33,34,37]. Intermediate-risk patients with high CAC scores have a 2.8% annual rate of cardiac death or myocardial infarction (MI)[33]. However, CT is less accurate for detecting and characterising non-calcified plaques, and the partial volume problem impairs CT's ability to quantify plaque burden[38]. The study also indicates the calcification related risk in plaque rupture is inversely associated with the calcium density[39]. Large calcification detected in CT potentially stabilises the plaque, and the micro-calcification beyond the CT resolution plays a major role in the stress concentration and rupture of vulnerable plaque.

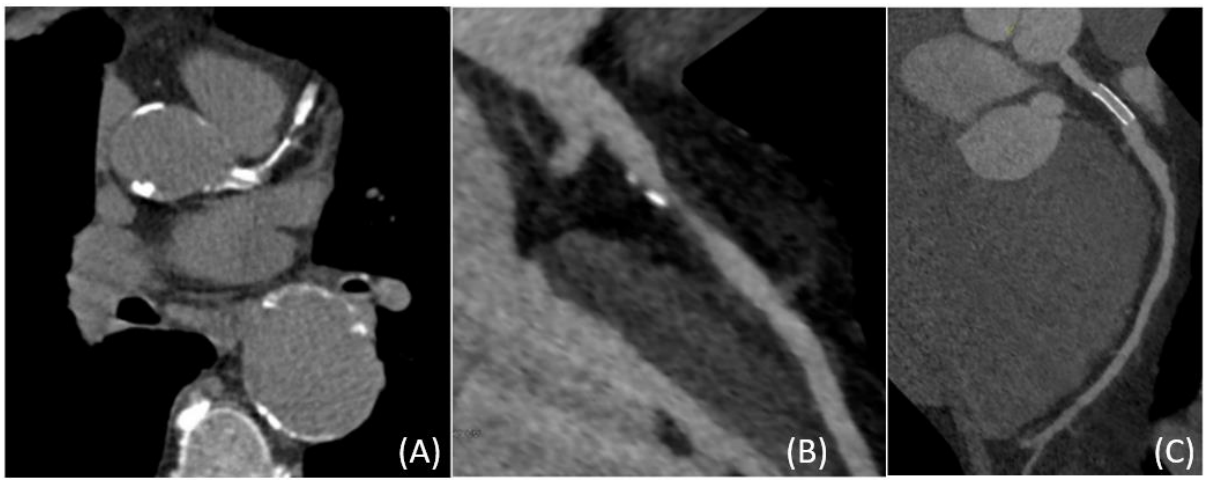

Figure 1.3 Coronary CT images. Calcification in the left main artery, LAD and aorta is visualised in a native calcium CT scan (A). The CCTA image (B) shows a less calcified lesion with severe stenosis, and a stented vessel after revascularisation is shown in the CCTA image (C).

Coronary CT angiography (CCTA) after an intravenous contrast infusion can identify local stenosis and plaque morphology. CCTA has been proposed as the alternative to traditional invasive coronary angiography (ICA) in assessing arterial stenosis, surrounding calcification,

and revascularisation after stent implantation (Figure 1.3 B, C). However, the spatial and temporal resolutions of CCTA are lower than ICA (spatial resolution: 400 μm versus 200 μm; temporal resolution: 80-190 ms versus 10 ms)[33]. The strong attenuation of calcium may obscure the luminal area in specific directions, causing artefacts in image reconstruction. Despite the relatively low resolution and possible image artefact, CCTA has been used in the functional analysis of ischemic coronary diseases. CCTA provide a non-invasive visualisation of the luminal geometry, facilitating the computational analysis of fluid mechanics in the coronary arteries. The computed fractional flow reserve (CFFR) derived from the estimated distal and proximal blood pressures reflects the functional impact of coronary stenosis and has been shown to have clinical benefits in risk stratification[40].

X-ray attenuates linearly with the concentration of the iodine contrast agent, and signal attenuation due to contrast agent perfusion can reflect the local perfusion of arteries[40]. The static CT perfusion (CTP) technique scans a single phase during the contrast agent injection, and detection of the hypo-attenuated or non-enhanced region in the CTP image reflects the myocardium perfusion. However, perfusion difference and bolus arrival time can only be estimated in practice, and the peak attenuation might not be imaged in static CTP. The dynamic CTP technique captures the dynamic attenuation curve during contrast agent injection with multiple scans, and the myocardial blood flow (MBF) is calculated to assess the coronary perfusion quantitatively. Despite the concerns over radiation dosage, dynamic CTP shows a higher prognostic value in major adverse cardiac event (MACE) prediction compared to CCTA[40].

Because of its wide accessibility, short acquisition time and sensitivity to plaque calcification, CT remains the primary imaging modality for asymptomatic patients with low to intermediate risk (usually >40 years old)[33]. The significant disadvantages of CT are its limited resolution and contrast in coronary plaque characterisation, ionising radiation exposure, and the unclear role of CAC in atherosclerosis prognosis[36].

1.2.2 Magnetic Resonance (MR) Imaging

Magnetic resonance imaging is a non-invasive imaging technique free of ionising radiation. MR differentiates biological tissues based on their biophysical and biochemical properties[41,42]. When a patient is placed inside an external magnetic field, the spins of protons either align or

oppose the external magnetic field, creating a longitudinal magnetisation in the patient's body. An electromagnetic radiofrequency (RF) pulse at resonant frequency excites the protons in selective regions. These selected protons absorb energy from the RF pulse and produce a local transverse magnetisation perpendicular to the external magnetic field. The precessing transverse magnetisation generates a measurable current in the receiver coil, which decays as excited protons realign to the external magnetic field. The time of decay, or relaxation time, is used to characterise different tissues.

The abundance of protons and the heterogeneity of relaxation times give MR imaging better soft-tissue contrast than CT and enable the plaque component characterisation. With multiple sequences of different T_1 and T_2 weighting, plaque components such as lipid core, intraplaque haemorrhage, fibrous tissue, and calcium deposits can be identified in MR images[43]. Figure 1.4 illustrates a T_2 weighted MR image with the corresponding histology. The characterisation is based on the T_2 weighted, intermediate weighted and T_1 weighted MR images.

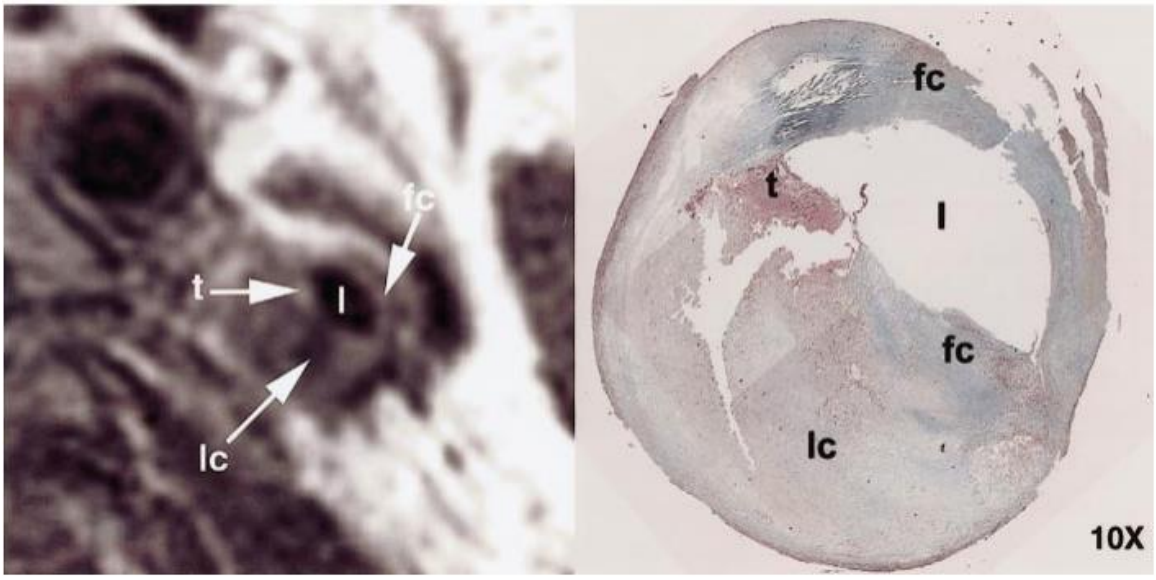

Figure 1.4 MR and histology image of a left internal carotid artery[43]. Left: a transverse T2-weighted fast spin echo MR image. Right: corresponding histopathologic image with Mason-eosin stain). l = lumen; fc = fibrous cap; t = thrombus; lc = lipid core.

MR plaque characterisation is primarily applied to carotid atherosclerosis. The application in coronary atherosclerosis is limited because of the insufficient resolution and motion artefacts[41]. Although improvement in MR has pushed the resolution down to 0.5-0.7 mm[41,44], this is still

beyond the thickness of plaque components in the coronary artery. Motion artefact from cardiac motion and breathing further degrades the resolution of coronary MR. With cardiac and respiratory gating, the bright blood imaging sequence (e.g. balanced steady-state free precession (bSSFP)) can characterize the coronary lumen, enabling MR angiography (MRA) for coronary arteries. Similar to traditional angiography and CCTA, MRA provides the morphology of the arterial lumen and can identify stenosis in the coronary artery, as shown in Figure 1.5 A. The same stenosis is confirmed by conventional X-ray angiography (Figure 1.5 C). In addition to the arterial lumen, MRA also has good soft-tissue contrast in the myocardium, allowing 3D reconstruction of the whole heart (Figure 1.5 B).

Unlike CT, MR is a non-invasive imaging modality without ionising radiation. MR is suitable for repeated scans to monitor plaque progression and acquire dynamic images with a prolonged acquisition time. Additional MR sequences and dynamic contrast injection provide information on diffusion, perfusion, blood flow quantification, strain, and motion of the tissue, allowing the functional and mechanical analysis of the vessel in a single imaging modality.

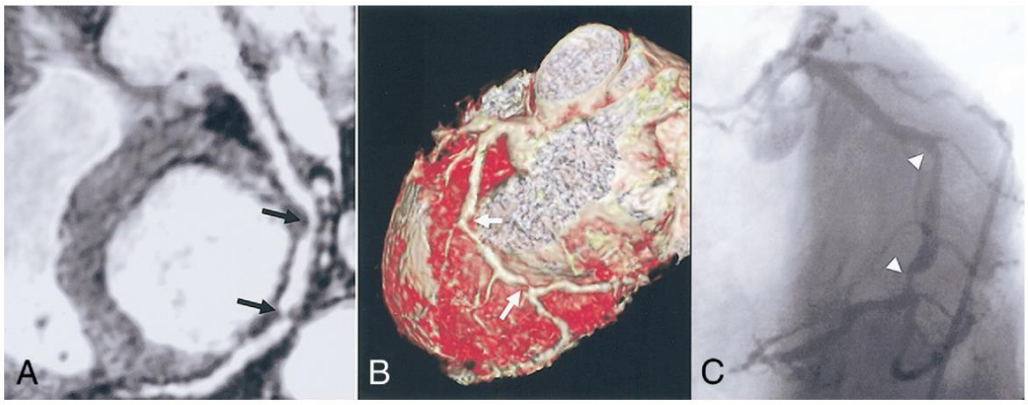

Figure 1.5 Comparison of MRA and conventional X-ray angiography[45]. (A) MRA identified stenosis in a left anterior descending artery (LAD, black arrow) (B) Volume rendered view from MRA (white arrow indicating stenosis) (C) Image of the same stenosis in conventional X-ray angiographic (white arrowhead)

1.2.3 Conventional X-ray Angiography

Conventional X-ray angiography is the gold standard for identifying arterial stenosis related to atherosclerosis and provides reliable anatomical information in determining medical therapies such as percutaneous coronary intervention (PCI) or coronary artery bypass grafting (CABG)[42].

During conventional angiography, catheterisation to the artery of interest is the first step. For coronary angiography, the cannula is placed at the entrance of the right coronary artery (RCA) or the left coronary artery (LCA, connecting the left anterior descending artery (LAD), left circumflex artery (LCx), and other sub-branch arteries). An iodinated radiographic contrast medium is injected through the catheter upstream of interested arteries. Because conventional X-ray angiography only captures the 2D projection of the arterial lumen, multi-angle rotational angiography is necessary to depict the 3D morphology of the arterial lumen.

Advancements in digital imaging systems make digital X-ray angiography widely available, allowing digital processing to improve image quality[46]. Digital subtraction angiography (DSA) can enhance the contrast resolution and reduce contrast injection using temporal subtraction, in which the stationary surrounding soft tissues and bones are removed from the images[46–48]. Figure 1.6 illustrates the effect of DSA in identifying small vessel branches. Because of motion artefacts, most conventional cardiac X-ray angiographies are unsubtracted, but other digital image processing methods, such as frame rate correction, can be applied in cardiac angiography[46].

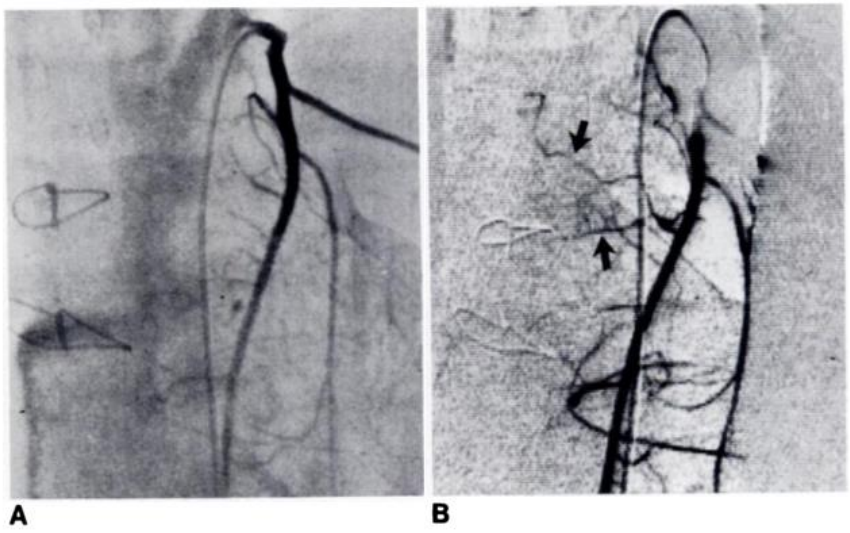

Figure 1.6 Comparison of conventional X-ray angiography and DSA[48]. (A) Conventional X-ray angiography image (B) DSA image of the same vessel (black arrow indicates small vessel branches found in DSA)

Conventional X-ray angiography can accurately acquire the arterial lumen's silhouette, identify the location and degree of arterial stenosis, and demonstrate perfusion[42]. The degree of stenosis,

occlusion, lesion length, and perfusion calculated in quantitative coronary angiography (QCA) have been used to guide intervention operations and to evaluate the end-point of clinical therapies[49]. However, conventional coronary X-ray angiography has pitfalls in branch superimposition, inadequate vessel opacification, and ionising radiation exposure. The pathological connection and prognostic value of conventional X-ray angiography derived morphological measurements are challenged. Little *et al.* evaluated the conventional X-ray angiography of 42 patients and found no significant correlation between angiographic severity and subsequent MI[50].

1.2.4 Intravascular Ultrasound (IVUS)

Intravascular ultrasound is a mini-invasive imaging technique designed for imaging coronary arteries. A limitation of non-invasive imaging and X-ray conventional angiography is the lack of information about the composition of the coronary arterial wall[36]. IVUS addresses this problem by providing a cross-sectional view of the lumen and arterial wall of coronary arteries. IVUS is a catheter-based imaging technique that places a mechanically rotating or electronically stationary transducer at the tip of the imaging cable[51]. The catheter is directed into the coronary artery using a guidewire. The rotational transducer sends and receives ultrasound in one direction and then rotates and repeats signal acquisition. A cross-sectional grey scale image of the artery is captured after a 360-degree scan. A stationary transducer utilises an electronically programmed annular transducer array to perform image acquisition. The imaging cable is pulled back using a motorised puller at a constant speed (0.5-1.0 mm/s) to provide axial movement of the imaging field[51].

Limited by ultrasonic frequency, attenuation, and aperture size, the axial and lateral resolution of IVUS (20-40 MHz) are 80 μm and 200-250 μm respectively[51], and image depth is 5-10 mm[52]. The high resolution and specificity of IVUS provide an accurate description of plaque and lumen morphology. Intima-lumen boundary and external elastic membrane (EEM, media-adventitia boundary) are reflective to ultrasound and can be segmented from IVUS images. Adventitial and periadventital tissues show no clear boundary in IVUS; therefore, the EEM boundary is often used as the reference vessel boundary. Morphological measurements such as luminal area, minimum and maximum atheroma thickness can be directly measured. The atheroma cross-sectional area (CSA) can be measured by subtracting luminal CSA from EEM CSA[36]. Other morphological measurements such as atheroma burden, lesion eccentricity and

lumen stenosis can be derived from direct measurements.

In addition, IVUS also identifies the compositional architecture of plaques using radiofrequency backscatter analysis. Through spectral analysis of the raw radiofrequency signals of IVUS after normalisation, different materials can be identified[51,53–57]. Different materials have different spectra in ultrasound backscatter[51,54]. Normalised spectra of the region of interest are calculated and summarised into spectral parameters to compare with standard material spectrum[54,55]. This technique is named virtual histology IVUS (VH-IVUS) and can identify plaque components, including the arterial wall, fibrous tissue, fibrofatty tissue, necrotic lipid core, and dense calcium[54,56]. Histological comparison with VH-IVUS classification has proven VH-IVUS is a reliable imaging modality for plaque composition[54,56]. Although the resolution of IVUS is not enough to capture the thin fibrous cap (<65 μm in thickness) of TCFA, VH-IVUS can identify plaque with morphology or composition close to TCFA. The virtual histology defined TCFA (VHTCFA) is characterised by plaque burden >40%, confluent necrotic core >10% of plaque cross-sectional area, and necrotic lipid core in contact with vessel lumen for three consecutive IVUS slices[32]. VHTCFA had been proven to associate with MACEs in various clinical trials[31,32].

1.2.5 Optical Coherence Tomography

Similar to IVUS, optical coherence tomography (OCT) utilises backscatter of light (wavelength ~1300 nm) to characterised different tissues[42,58]. Low coherence light is separated and directed into two interferometer arms. The light of the reference arm is reflected with a mirror, and the light of the sample arm is reflected from tissue with delay and amplitude change. Tissues with different reflective properties are characterised by the interferometric signal of combined light from the two arms[59]. The setup of OCT is illustrated in Figure 1.7 A.

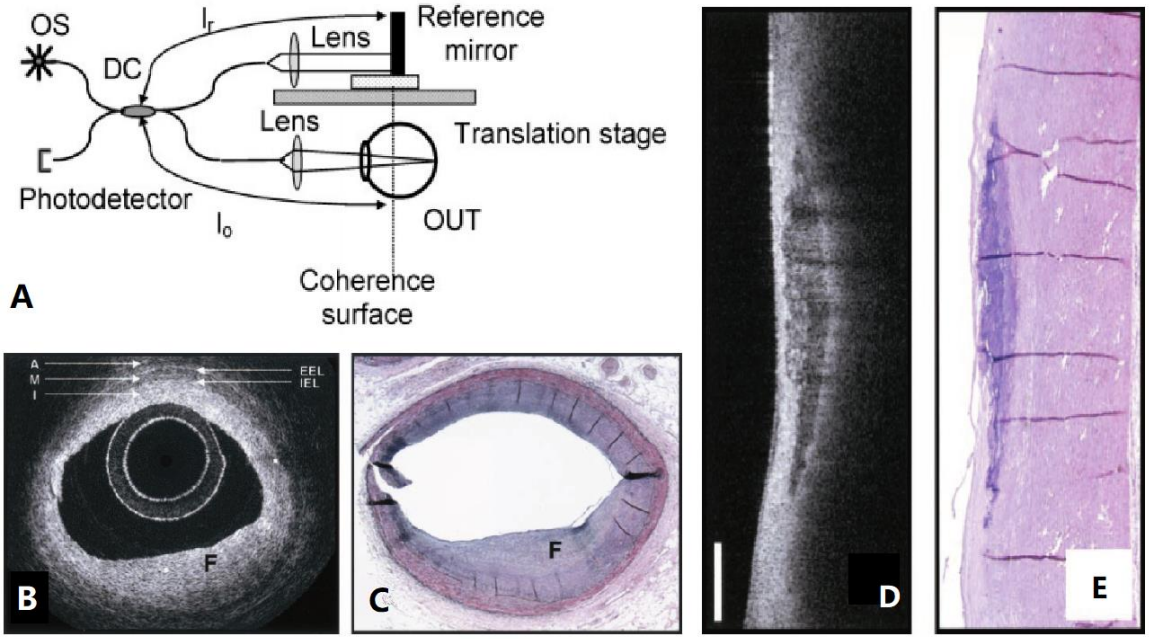

Figure 1.7 Illustration and histological comparison of OCT[59]. (A) Illustration of OCT setup (OS: optical source, DC: directional coupler, OUT: object under test) (B) Intravascular OCT image of a fibrous vessel (A: adventitia, M: media, I: intima, EEL: external elastic lamina, IEL: internal elastic lamina, F: fibrous tissue) (C) Histology comparison of OCT in B (D) Intravascular OCT image of calcified vessel (E) Histology comparison of OCT in D

In cardiovascular imaging, catheter-based intravascular OCT is usually performed. Because the wavelength of light is much smaller than the wavelength of ultrasound, the resolution of OCT (axial 10 μm, lateral 30-40 μm) is higher compared to IVUS[60]. In the extravascular setting, the spatial resolution of OCT can reach micron levels or even submicron levels[60]. The high resolution makes OCT suitable for identifying fine components near the luminal surface, especially for TCFA with thin fibrous cap thickness <65 μm. Figure 1.7 B demonstrates an example image of a fibrous vessel using OCT[61]. Compared with the histology in Figure 1.7 C, the OCT image clearly outlines the lumen and vessel boundary and identifies the fibrous tissue. OCT can also identify plaque material, including lipid, thrombus, and calcification[61–63]. Moreover, unlike ultrasound which is strongly reflected by calcification and causes shadowing artefact, OCT is less affected by calcification, and can better characterise calcified vessels, as illustrated in Figure 1.7 D and E[61,62].

The major limitation of OCT is its penetration depth, which ranges between 1.0-2.5 mm[42,59,64], compared to the 5-10 mm penetration depth of IVUS[52]. This limited penetration depth decreases OCT's ability in identifying lipid pools, which are usually embedded in plaques. In

addition, a significant scattering source in OCT is blood[59,62]. An injection of saline is necessary to displace blood and reduce the scattering, shortening OCT's screening window to approximately two seconds after each injection[62]. In addition, the acquisition rate of OCT is 4-8 frames per second, and cardiac movement can cause motion artefacts in coronary OCT imaging[61].

1.2.6 Positron Emission Tomography (PET) and Other Imaging Modalities

Positron emission tomography (PET) and single photon emission computed tomography (SPECT) are non-invasive molecular imaging techniques using radiolabeled tracers to characterise molecular processes in lesions[36]. PET utilises tracers with positron emitting isotopes, and SPECT utilises tracers with gamma-emitting isotopes. One of the most popular radiopharmaceutical tracers used in PET is ^{18}F-fluorodeoxyclucose (^{18}F-FDG), which is a radioactively labelled glucose molecule[36,65]. ^{18}F- FDG is readily consumed by cells at the same rate as glucose consumption but cannot be metabolised further in the glycolysis pathway[36]. Accumulation of FDG in cells increases the signal intensity of positron emission, and therefore high FDG-PET signal corresponds to a high metabolic rate[36,65].

In atherosclerotic imaging, FDG-PET signal in atherosclerotic plaque represents macrophage activity and quantifies inflammatory status[36,65]. Because PET and SPECT have poor anatomical resolutions (4–5 mm and 10–15 mm respectively) in practice, they are commonly co-registered with CT or MRI[36]. Previous studies using PET/CT indicate FDG-PET can detect early-stage atherosclerotic foam cells, and the signal is correlated with increasing gene expression of inflammatory and atherosclerotic markers[65]. However, a significant limitation of FDG-PET in coronary imaging is that myocardial uptake reduces contrast and specificity in inflammatory imaging[65]. To overcome myocardial spillover, a ^{68}Ga-DOTATATE PET tracer was recently developed to identify pro-inflammatory macrophages in atherosclerosis with high specificity, and provide accurate inflammatory analysis in atherosclerosis[66].

Another intravascular imaging technique is the near-infrared spectroscopy (NIRS). NIRS generates near-infrared light (wavelength 800-2500 nm)[67,68]. Molecules in biological tissue selectively absorb light at different frequencies based on their molecular vibrational energy levels[67]. The light spectra produced after absorption is used to characterise different biological

tissues. The properties of near-infrared light give NIRS a relatively large penetration depth into tissues (2~3mm), and good sensitivity in lipid-rich plaque[68].

1.2.7 Multimodal Integration

Each imaging modality has its advantages and drawbacks, providing a different perspective in characterising atherosclerotic plaques. Multimodal integration has been developed to overcome the limitations and to create a comprehensive picture of atherosclerotic plaques. The integration can be classified as image integration and hardware integration.

Image integration fuses images from different modalities through co-registration. Requiring no hardware modification, the integration is widely applied between many imaging modalities[68]. The combination of conventional X-ray angiography and IVUS was developed for attaining geometric and compositional information of plaques simultaneously and has been used in many biomechanical studies[68–70]. Similarly, combinations of conventional X-ray angiography, CCTA, IVUS, and OCT were developed to reconstruct accurate models of atherosclerotic plaques[68].

A significant weakness of image integration is the error in co-registration[68]. Hardware integration aims to reduce such errors through hardware modifications. Hybrid, dual probe catheters can perform multimodal intravascular imaging with small co-registration errors. NIFR/IVUS catheter is the first approved dual-probe technology, which obtains plaque morphology from IVUS, and accurate lipid characterisation from NIFR[68]. OCT/IVUS probes are under extensive development, targeting at an accurate description of TCFA for plaque vulnerability assessment[68,69]. Another example of hardware integration is the PET/MR system, which provides the metabolic, structural and functional images in the same scan. The integration of PET and MR reduced total scan time and errors due to motion and image registration. Compared to the PET/CT system, the PET/MR system induces less ionizing radiation and is more suitable for follow-up studies or paediatric imaging[71]. The strength of PET/MR system lies in the co-registered and simultaneous acquisition of PET and MR signals, which facilitates the dynamic reconstruction and motion correction[72].

1.3 Vulnerability Assessment and Biomechanical Analysis of Coronary Atherosclerosis

1.3.1 Mechanisms of Plaque Rupture

Post-mortem studies indicate plaque rupture is the main cause of coronary thrombosis regardless of the clinical presentation, age or sex[19]. Plaque rupture is found to be associated with 73% of coronary thrombi in sudden coronary deaths[22], and usually occurs where the fibrous cap is the thinnest[9]. Macrophage infiltration causes fibrous cap thinning by degrading the collagen-rich matrix that provides mechanical stability[9]. The degradation of smooth muscle cells (SMCs) further impairs the stiffness of the fibrous cap, making it vulnerable to rupture. Under physiological conditions, plaque is subject to mechanical loadings due to dynamic blood pressure and flow. If these loadings exceed the material strength of fibrous cap, a rupture might occur. Mechanical loading is governed by many factors, including lesion geometry, location, material properties, blood pressure and heart rate. For a specific patient, when spontaneous or emotional stimulus increases his or her heart rate and blood pressure, vulnerable plaque fails to sustain the elevated stress. As a result, a gap occurs on the fibrous cap due to rupture, exposing the thrombogenic core that activates blood coagulation and thrombus formation[9]. The fibrous cap thinning mechanism is supported by autopsy studies[9]. The rupture sites usually have a thin fibrous cap, few or an absence of SMCs, infiltrated by macrophages, and often locate at the shoulder regions where the local luminal curvature is large[73].

Moreover, these post-mortem studies also indicate other features of ruptured plaques, including a large necrotic core, expansive remodelling, neovascularisation, intraplaque haemorrhage, adventitial inflammation and spotty calcification[9,19,22]. Both inflammatory features and compositional features change the mechanical properties of atherosclerotic plaque and contribute to plaque rupture by affecting the balance between local biomechanical forces and the plaque's material strength[74]. Biomechanical analyses based on physiological environment and plaque composition, therefore, improve the pathological understanding and the prediction of plaque rupture and subsequent MACE[75–78].

1.3.2 Morphology and Calcification in Plaque Vulnerability Assessment

From intimal thickening to plaque rupture or erosion, the progression of atherosclerosis is accompanied by morphological changes. Many studies have compared the morphological features in ruptured plaques and non-ruptured plaques, and proposed morphological features for risk prediction[79–81]. For example, plaques that cause stenosis are more likely to precipitate clinical events than plaques that do not[31]. However, quantified angiographic measurements such as the maximum degree of stenosis show no significant difference between the high-risk lesions and low-risk lesions[82]. Angiographic studies before and after MI indicate that most ACSs are caused by plaques with mild angiographic stenosis[9,22,31]. The angiographic mildness is explained by the expansive remodelling of the arterial wall, which is poorly captured in conventional X-ray angiography[79]. CCTA can describe the extent of luminal stenosis with reasonable accuracy and is used to quantify positive vessel remodelling in atherosclerosis. In a CCTA clinical trial with 1059 patients, voluminous plaques with high degrees of positive vessel remodelling were associated with a higher risk of subsequent ACSs[80].

Moreover, CT's sensitivity to calcification facilitates the invention of calcium scoring. Although macroscopic calcification usually stabilises plaque, discrete and spotty calcification in fibrous plaque is likely to associate with plaque rupture[83]. The Agatston calcium score is used to measure coronary arterial calcification (CAC) based on the stratified CT intensity and the size of calcium[84]. Because CT is non-invasive and widely available in diagnosis, large scale CAC clinical studies have been carried out[85,86]. These studies show that the Agatston calcium score significantly improves the risk classification of patients at low or intermediate risk of acute coronary events[85,86]. However, the relationship between vascular calcification and subsequent ACSs is unknown, and calcium scoring does not help identify high-risk plaques[83]. Intravascular imaging techniques with better resolution may further analyse the presence and role of spotty calcification in plaque rupture.

IVUS can identify vessel intima, media, lumen and plaque components, providing an accurate measurement of plaque morphology and calcification. In IVUS, plaque burden is defined as the plaque and media cross-sectional area divided by the external elastic membrane (EEM) cross-sectional area[31]. Spotty or macroscopic calcification is measured as a dense calcium area. In the PROSPECT (Providing Regional Observations to Study Predictors of Events in the Coronary Tree) study[82], 697 patients underwent angiography and IVUS. Comparison of lesions

from the high-risk and low-risk patients reveals significant differences in plaque burden, minimum luminal area, and dense calcium area identified in IVUS or VH-IVUS[82]. No significant difference was found in the QCA measurements, including maximum stenosis diameter. In addition, the PROSPECT study and other studies indicate that non-culprit lesions associated with recurrent MACE could be characterised by a plaque with plaque burden >70%, minimum luminal area <4 mm^2 and virtual histology thin-cap fibroatheroma (VHTCFA) in VH-IVUS[31,32,87].

1.3.3 Fractional Flow Reserve (FFR) and Computational Fractional Flow Reserve (CFFR) in Plaque Vulnerability Assessment

Besides plaque morphology and calcification, the functional severity of coronary stenosis can be helpful in assessing myocardial ischaemia. Fractional flow reserve (FFR) is an invasively measured, pressure-based index of functional severity[88]. FFR is calculated by the ratio of distal coronary pressure to aortic pressure measured simultaneously at maximal hyperaemia[89,90]. In a normal coronary artery without stenosis, there is very little drop in pressure, and FFR is approximately 1.0. In stenotic coronary arteries, an FFR value <0.8 corresponds to ischaemic-causing stenosis with 90% accuracy[90]. FFR quantifies the perfusion of specific stenosis and provides lesion-specific guidance in appropriate PCI operations[88]. A clinical trial compared the performance of standard angiography-guided PCI with angiography and FFR-guided PCI, and concluded that the FFR guided PCI uses fewer stents (2.7 ± 1.2 vs 1.9 ± 1.3, $p<0.001$), and had lower event rates (events comprised of death, nonfatal myocardial infarction, and revascularisation) during one year follow up (18.3% vs13.2%, $p=0.02$)[90].

The computational fractional flow reserve (CFFR) is developed based on coronary CCTA and computational fluid dynamics (CFD) to assess the functional severity in a non-invasive measure. The CFFR method is illustrated in Figure 1.8.

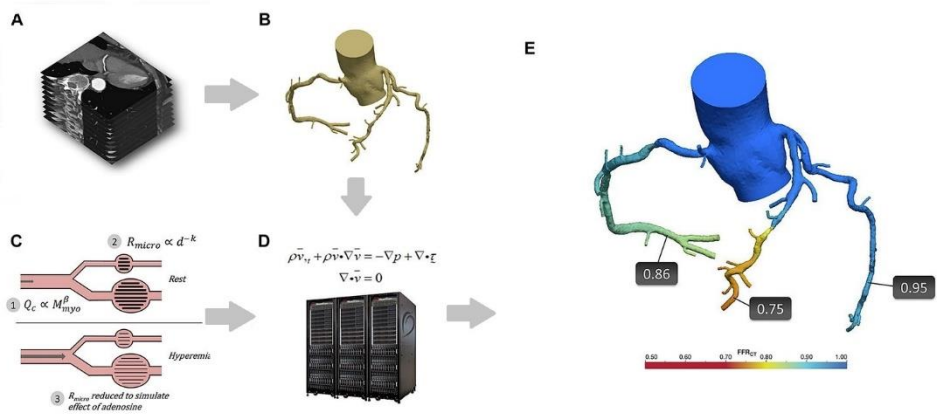

Figure 1.8. Illustration of computational fractional flow reserve (CFFR)[91]. (A) Routine CCTA data is acquired. (B) A 3D anatomic model is reconstructed from the CCTA data. (C) A physiological model is constructed from patient-specific data and assumptions of coronary blood flow. (D) Governing functions of fluid dynamics are numerically solved for the patient-specific models. (E) CFFR values are derived for each point in the coronary tree.

From routine CCTA imaging volumes (Figure 1.8 A), a 3D anatomic model of coronary and aortic arteries can be reconstructed[91] (Figure 1.8 B). The physiological model (Figure 1.8 C) of CFFR assumes[91]:

1. Resting coronary flow is proportional to myocardial mass.
2. Microvascular resistance is inversely proportional to vessel size.
3. Maximal hyperaemia can be simulated by reducing microvascular resistance.

The numerical solution to fluid dynamic governing functions is calculated for the model (Figure 1.8 D), and the calculated pressure is used to derive CFFR as plotted in Figure 1.8E. Previous studies using CFFR shows a good correlation between CFFR and FFR, with a Pearson's correlation coefficient of 0.72-0.82 ($p< 0.01$)[91,92]. Compared with CCTA, CFFR also has better performance in classifying ischaemic-causing coronary stenosis[91,92].

1.3.4 Mechanical Analysis in Plaque Vulnerability Assessment

Experimental and clinical data indicate biomechanical forces have an important role in atherosclerosis[74]. Plaque development and rupture are influenced by the interaction between biological and mechanical factors[93]. Biomechanical forces regulate the cellular activities and

plaque composition, which then determine the plaque's mechanical stability under loading. Two important biomechanical forces in the natural history of atherosclerosis are the wall shear stress (WSS) acting on the luminal surface and the plaque structural stress (PSS) acting on the vessel wall[74].

- **Wall Shear Stress (WSS)**

WSS is a frictional force exerted by the blood flow on the endoluminal surface in the direction parallel to blood flow[74]. WSS can be estimated using CFD or more advanced fluid-structure interaction (FSI) techniques[70,74,94]. FSI is a coupled method of CFD and 3D solid finite element analysis (FEA), in which the fluid model interacts with the solid model by iteratively exchanging pressure and displacement information. FSI can provide both WSS and PSS simultaneously, and better represents the mechanical environment in arteries[95]. However, FSI requires labour-intensive meshing processes and complex computations and is difficult to converge[95,96].

In CFD, the geometric model can be reconstructed from medical images such as conventional X-ray angiography, IVUS, or CCTA[70,94]. Boundary conditions such as inlet and outlet flow rates are measured *in vivo*, or derived from the images[70]. The intravascular flow characteristics are obtained by solving the governing transport equations, assuming blood being an incompressible Newtonian fluid[70,94]. The WSS is then calculated at the endoluminal surface.

Using CFD or FSI, many studies revealed WSS distributions in coronary arteries. The magnitude of WSS ranges around 1-10 Pa[74], and its distribution varies at different anatomical locations, with high WSS usually found in the distal vessel or arterial side branches[97]. The non-uniform distribution of WSS partly explains the multifocal nature of atherosclerosis[74]. Vessel geometry influences WSS such that WSS is high at the outer curvature of the artery and low at the inner curvature. Moreover, the magnitude of WSS is positively influenced by blood flow velocity. For a constant blood flow rate, the local blood flow velocity increases at stenosis, producing a high WSS at stenotic site[74,93].

The causal role of WSS in plaque initiation has been confirmed in many studies[70,74,94]. Low WSS induces local endothelial cell dysfunction, leading to a more proatherogenic endothelial cell phenotype that alters the microstructure of vessel walls[70]. The low, oscillating WSS also

triggers the inflammatory signalling pathway in endothelial cells, releasing inflammatory adhesion molecules, and promoting the adhesion of monocytes[74,93]. In clinical studies, low local WSS is associated with progressive enlargement of the necrotic core and plaque, resulting in constrictive remodelling and formation of rupture-prone TCFAs[70,94]. Some studies indicated high WSS transforms plaque into high-risk phenotypes through calcification progression, regression of fibrous and fibrofatty tissue, and expansive remodelling[70]. However, this conflicts with findings in other studies[94]. Experimental data indicate that WSS can induce plaque erosion and increase thrombogenicity, making WSS a potential biomarker of plaque rupture[74].

- **Plaque Structural Stress (PSS)**

PSS is the stress within the plaque component or arterial wall, caused by vessel expansion and stretch due to blood pressure and bending caused by heartbeat[74]. Like WSS, PSS can be estimated with numerical methods, namely finite element analysis (FEA). FEA requires reconstruction of vessel geometry, and boundary conditions of blood pressure or flow rate. In addition, FEA takes the plaque components' architecture and material properties into account. Both plaque morphology and its component structure can be obtained from IVUS[30,74,76]. Despite patient specificity, the material properties of these plaque components are measured in *ex vivo* tensile tests of plaque samples[74,98]. After solving the governing equations, PSS is described as the maximum principal stress, the effective stress, or the variation of the two stresses[30,74].

FEA studies with idealised models indicate PSS ranges around 1-1,000 kPa[74], and varies with plaque geometry, composition, architecture and remodelling[99,100]. High PSS is associated with a decrease in the degree of stenosis[101] and fibrous cap thickness[95,99], and an increase of lipid necrotic core volume[74], lumen eccentricity[76], and positive vessel remodelling[101]. These findings are confirmed in FEA using patient-specific models, indicating fibrous cap thinning is the most influential factor in PSS calculations[95,100,101]. In addition, the effect of calcification on PSS depends on the size, extent and location of calcium deposits. While initial superficial calcification increases PSS, this increase reaches a plateau and may even reduce PSS as calcification becomes more extensive[30,101]. Spotted and microscopic calcifications in the plaque body itself can significantly increase local PSS by more than five-fold[74].

PSS has been calculated using clinical data in many studies, and it has been proven to be different between patients with different clinical syndromes and between different plaque subtypes[30,75,76,102]. Patients with ACSs tend to have higher PSS[30]. PSS is significantly increased in high-risk plaques, characterised by TCFA with plaque burden >70% and minimum lumen area <4 mm^2 [75]. Compared with non-ruptured plaque, the ruptured plaque has a higher PSS, and higher variation in PSS[76]. For ruptured plaques, PSS in the proximal segment to the rupture site is higher than the PSS in the distal segment. Fibroatheroma in the proximal segment is particularly at risk[76]. In addition, follow-up studies at one year indicate high PSS is associated with an increase in atheroma volume and the presence of virtual histology thin-cap fibroatheroma[103]. PSS has become a positive predictor in the identification of clinical presentations[30] and the prediction of MACE[75] and disease progression[103].

Most of the previous PSS studies were based on 2D models and used 2D FEA structure analysis to calculate 2D PSS[75,99–103]. Although FSI can accurately provide WSS and 3D PSS simultaneously, few studies use FSI because of difficulties in meshing, convergence and computational power[95,96] when multi-components and arterial bending due to heart beating are included in the simulation.

This study aims to reconstruct the coronary 3D geometry through the VH-IVUS and DSA images and study the influence of computational strategy and coronary bending in the biomechanical simulations. To non-invasively acquire the coronary morphology and inflammation, and to improve the image quality of the PET/MR system, this study improves the thoracic MR attenuation correction for the lungs, and attempts to develop a non-Cartesian MR sequence for the free-breathing continuous coronary MR acquisition.

Chapter 2 Coronary Biomechanics and Modelling

The constitutive law and governing equations in classical mechanics allow us to mathematically connect the stress (force) and strain (deformation). Introduced by *Hrennikoff et al.* in the 1940s, the finite element analysis (FEA) is a generic numerical method for solving the mechanical differential equations of a discretised model, and for calculating the structural and fluid parameters of the model with sufficient boundary conditions. This chapter describes the basic concepts in FEA (section 2.1) and demonstrates the process of coronary FEA modelling from the VH-IVUS and DSA images (section 2.2). The last section (section 2.3) also explores the coronary bending patterns, which is a unique and important mechanical factor in 3D coronary FEA simulations. The methods and results described in sections 2.2, and 2.3 were original work for this dissertation unless mentioned or referenced specifically.

2.1 Concepts in Coronary Finite Element Analysis

2.1.1 Description of Internal Deformation and Forces

The FEA method has been applied in different structural analyses. For coronary biomechanical analysis, the arterial wall and the blood flow are modelled as two continuum bodies (solid structure and fluid) and are solved independently or interactively. The primary goal is to solve the internal deformation and force of the whole model with the external physiological loadings.

- **Displacement**

For a particle of a body in the undeformed (reference) configuration, the coordinate is $\boldsymbol{X}$. The

body deforms to the deformed state, and the particle transfers into a new coordinate $\boldsymbol{x}$. The deformation of the body is defined by the deformation field

$$\boldsymbol{x} = \boldsymbol{x}(\boldsymbol{X}, t)$$
$$\boldsymbol{u}(\boldsymbol{X}, t) = \boldsymbol{x}(\boldsymbol{X}, t) - \boldsymbol{X} \qquad 2.1$$

where **u** is the field function of displacement of particle $\boldsymbol{X}$ at time t.

- **Deformation gradient**

For two particles P (with coordinate $\boldsymbol{X}$) and Q (with coordinate $\boldsymbol{X}+d\mathbf{X}$) of a body, the vector $d\mathbf{X}$ connects the coordinates of the P and Q. The body deforms at time t, and the two particles move to new coordinates $\boldsymbol{x}(\boldsymbol{X},t)$ and $\boldsymbol{x}(\boldsymbol{X}+d\mathbf{X},t)$, and $d\mathbf{x}$ is the vector that connects the new position of P and Q

$$d\boldsymbol{x} = \boldsymbol{x}(\boldsymbol{X} + d\boldsymbol{X}, t) - \boldsymbol{x}(\boldsymbol{X}, t) \qquad 2.2$$

For a continuous displacement, $d\mathbf{X}$ **is** infinitesimal, and

$$d\boldsymbol{x} = \nabla_{\boldsymbol{X}}\boldsymbol{x}(\boldsymbol{X}, t)d\boldsymbol{X} = \boldsymbol{F}d\boldsymbol{X}$$
$$F_{iK} = \frac{\partial x_i(\boldsymbol{X}, t)}{\partial X_K} \qquad 2.3$$

where $\boldsymbol{F}$ is the deformation gradient tensor that maps from the undeformed configuration $d\boldsymbol{X}$ to the deformed configuration $d\boldsymbol{x}$. The corresponding displacement gradient tensor $\boldsymbol{H}$ is defined as

$$d\boldsymbol{u} = d\boldsymbol{x} - d\boldsymbol{X} = (\boldsymbol{F} - \boldsymbol{I})d\boldsymbol{X} = \boldsymbol{H}d\boldsymbol{X} \qquad 2.4$$

$$\boldsymbol{H} = \boldsymbol{F} - \boldsymbol{I}$$

$$H_{iK} = \frac{\partial x_i(X,t)}{\partial X_K} - \delta_{iK}$$

$$\delta_{iK} = \begin{cases} 0 & i \neq K \\ 1 & i = K \end{cases}$$

where δ_{iK} is the Kronecker delta function.

- **Strain**

The strain is a normalised measure of deformation and represents the change of displacement after deformation. The length of a displacement $d\boldsymbol{X}$ in the undeformed state can be expressed as

$$l_X^2 = d\boldsymbol{X} \cdot d\boldsymbol{X} \tag{2.5}$$

Similarly, the length of the displacement after deformation $d\boldsymbol{x}$ is

$$l_x^2 = d\boldsymbol{x} \cdot d\boldsymbol{x} = \boldsymbol{F}d\boldsymbol{X} \cdot \boldsymbol{F}d\boldsymbol{X} = d\boldsymbol{X}\boldsymbol{F}^{\boldsymbol{T}}\boldsymbol{F}d\boldsymbol{X} = d\boldsymbol{X}\boldsymbol{C}d\boldsymbol{X} \tag{2.6}$$

where $\boldsymbol{C}$ is the right Cauchy-Green deformation tensor that describes the local deformation. An eigendecomposition to $\boldsymbol{C}$ gives

$$\boldsymbol{C} = \sum_{i=1}^{3} \lambda_i^2 \boldsymbol{N}_i \otimes \boldsymbol{N}_i$$

$$I_1^C = tr(C) = \sum_{i=1}^{3} \lambda_i^2 \tag{2.7}$$

$$I_2^C = \frac{1}{2}[tr(\boldsymbol{C})^2 - tr(\boldsymbol{C}^2)] = \lambda_1^2\,\lambda_2^2 + \lambda_2^2\,\lambda_3^2 + \lambda_3^2\,\lambda_1^2$$

$$I_3^C = \det(\boldsymbol{C}) = \lambda_1^2\lambda_2^2\lambda_3^2$$

where λ_i are the principal stretches (eigenvalues), $\boldsymbol{N}_i$ are the principal directions, and I_i^C are the invariants of $\boldsymbol{C}$. According to Equation 2.4, $\boldsymbol{C}$ can be expressed in $\boldsymbol{H}$

$$\boldsymbol{C} = \boldsymbol{H}^T + \boldsymbol{H} + \boldsymbol{H}^T\boldsymbol{H} + \boldsymbol{I} \tag{2.8}$$

There are different forms of strain tensors to describe local deformation for different purposes. For large deformation, the Lagrangian finite strain tensor is defined as

$$\boldsymbol{E} = \frac{1}{2}(\boldsymbol{C} - \boldsymbol{I}) = \frac{1}{2}\ (\boldsymbol{H}^T + \boldsymbol{H} + \boldsymbol{H}^T\boldsymbol{H}) \tag{2.9}$$

- **Stress**

Stress is a measure of the internal force in a deformed body. For a simple loading environment like the uniaxial tension, the stress can be defined as

$$\sigma = \frac{\boldsymbol{F}}{A} \tag{2.10}$$

where $\boldsymbol{F}$ is the force and A is the cross-sectional area, and the direction of one of the principal stresses is parallel to $\boldsymbol{F}$. However, in reality, force $\boldsymbol{F}$ is more complicated and distributes in all directions, and the stress $\boldsymbol{\sigma}$ varies at different orientations and locations**.** The Cauchy stress tensor is defined to describe the complicated stress using a matrix with an orthogonal basis:

$$\boldsymbol{\sigma} = \sigma_{ij} = \begin{bmatrix} \sigma_{11} & \sigma_{12} & \sigma_{13} \\ \sigma_{21} & \sigma_{22} & \sigma_{23} \\ \sigma_{31} & \sigma_{32} & \sigma_{33} \end{bmatrix} \tag{2.11}$$

where σ_{ij} is the stress component acting on a plane normal to the x_i direction, and acting along the x_j direction. By definition, the stress vector $\boldsymbol{T}^{(\boldsymbol{n})}$ on an arbitrary cutting plane with normal vector $\boldsymbol{n}$ can be calculated from the Cauchy stress tensor:

$$\boldsymbol{T^{(n)}} = \boldsymbol{n} \cdot \boldsymbol{\sigma} \qquad 2.12$$

The principal stress σ_i $(i = 1,2,3)$, and principal direction N_i $(i = 1,2,3)$ for the Cauchy stress tensor can be obtained from the eigendecomposition. To summarise the stress tensor with a scaler, the effective stress (also called the von Mises stress) is defined as

$$\sigma_e = \sqrt{\frac{1}{2}[(\sigma_1 - \sigma_2)^2 + (\sigma_2 - \sigma_3)^2 + (\sigma_3 - \sigma_1)^2]} \qquad 2.13$$

In this dissertation, effective stress is used as the plaque structural stress (PSS) to evaluate the stress state in all simulations.

2.1.2 Constitutive Law

The constitutive law describes the relationship between the force exerted on a substance and the deformation caused by the exerted force. Unlike typical engineering materials (such as aluminium) with linear and elastic properties, biological materials (such as vessel walls) usually exhibit non-linear stress-strain relationships and are usually modelled as hyperelastic materials. A typical hyperelastic material (such as rubber) can be subject to large deformation without any internal energy dissipation. The material has no motion memory and is dependent only on the current state variables. Once the external load is removed, the material will return to its initial state through a reversible process, and all work done during the loading is recovered during the unloading.

The characteristics of hyperelastic material facilitate the existence of a scalar value function that describes the energy stored within a unit volume due to deformation, which is the strain energy density function (SEDF):

$$W = W(\boldsymbol{C}) = \widehat{W}(I_1, I_2, I_3) = \widetilde{W}(\lambda_1, \lambda_2, \lambda_3) \qquad 2.14$$

where $\widehat{W}(I_1, I_2, I_3)$ and $\widetilde{W}(\lambda_1, \lambda_2, \lambda_3)$ are SEDF defined with the strain and stress invariants of isotropic material. The Cauchy stress tensor can be calculated from the SEDF as

$$\boldsymbol{\sigma} = 2\boldsymbol{F} \cdot \frac{\partial W}{\partial \boldsymbol{C}} \cdot \boldsymbol{F}^T$$
$$\sigma_i = \lambda_i \frac{\partial \widetilde{W}}{\partial \lambda_i} \qquad 2.15$$

Many types of SEDFs have been proposed to describe different hyperelastic materials. For biomechanical analysis, the modified Mooney-Rivlin model is commonly used to characterise arterial tissue because of its numerical stability and ability to capture linear deformation under small stretches and non-linear deformation under large stretches. The modified Mooney-Rivlin SEDF is defined as

$$\widehat{W} = C_1(\bar{I}_1 - 3) + D_1\left[e^{D_2(\bar{I}_1 - 3)} - 1\right] + \kappa(J - 1) \qquad 2.16$$

where $J = \det(\boldsymbol{F})$, $\bar{I}_1 = J^{-\frac{2}{3}}(\lambda_1^2 + \lambda_2^2 + \lambda_3^2)$, C_1, D_1 and D_2 are the material constants, κ is the hydrostatic pressure as a Lagrangian multiplier to enforce the incompressibility ($J = 1$). From Equations 2.15 and 2.16, the principal stress can be expressed as

$$\sigma_i = \lambda_i \left(\frac{\partial \widehat{W}}{\partial \bar{I}_1}\frac{\partial \bar{I}_1}{\partial \lambda_i} + \frac{\partial \widehat{W}}{\partial J}\frac{\partial J}{\partial \lambda_i}\right) = 2\lambda_i^2\left[C_1 + D_1 D_2 e^{D_2(\bar{I}_1 - 3)}\right] + \kappa \qquad 2.17$$

where κ is determined by the boundary conditions.

2.1.3 Finite element analysis

The primary goal of the biomechanical analysis is to calculate the response of a physical system to the imposed boundary conditions, which is achieved by solving the governing equations with constitutive laws and the morphology of the model. However, in arterial biomechanical analysis, the complexity of vessel morphology, the non-linearity of biological tissue, and the complex governing equations make the exact solution infeasible to be calculated analytically. The finite element method (FEM) is an engineering method to approximate the exact solution by discretising (meshing) the model into elements that can be described with simplified

mathematical models. The macroscopic response is then the accumulation of responses of the finite elements. Finite element theory has proved that the approximate solution converges to the exact solution as the physical dimension of the element decreases.

In arterial biomechanics, the vessel wall is modelled as a solid structure, and the blood flow is modelled as a fluid. The solid model can be described with a system of differential equations:

$$\begin{aligned} &\boldsymbol{\nabla}\cdot\boldsymbol{\sigma}+\rho\boldsymbol{b}=\rho\boldsymbol{a} \\ &\boldsymbol{\sigma}=2\boldsymbol{F}\cdot\frac{\partial W}{\partial \boldsymbol{C}}\cdot\boldsymbol{F}^{T} \\ &S_u: \quad \boldsymbol{u}=\overline{\boldsymbol{u}} \\ &S_t: \quad \boldsymbol{\sigma}\cdot\boldsymbol{n}=\boldsymbol{T} \end{aligned} \tag{2.18}$$

where $\boldsymbol{\sigma}$ is the Cauchy stress tensor; $\boldsymbol{b}$ is the body force per unit mass; ρ is the solid density; $\boldsymbol{a}$ is the acceleration; $\boldsymbol{F}$ is the deformation gradient; $\boldsymbol{C}$ is the right Cauchy-Green deformation tensor; $\boldsymbol{u}$ is the displacement; $\overline{\boldsymbol{u}}$ is the prescribed displacement on the boundary surface S_u; $\boldsymbol{T}$ is the prescribed traction force on the boundary surface S_t with $\boldsymbol{n}$ as the normal direction.

The motion of the fluid model is governed by the Navier-Stokes equations. Under the assumptions of an incompressible and Newtonian fluid, the governing equations of blood flow can be expressed in non-conservative forms for mass and momentum, respectively:

$$\begin{aligned} &\frac{\partial\rho}{\partial t}+\rho\boldsymbol{\nabla}\cdot\boldsymbol{v}=0 \\ &\rho\frac{\partial\boldsymbol{v}}{\partial t}+\rho\boldsymbol{v}\cdot\boldsymbol{\nabla}\boldsymbol{v}-\boldsymbol{\nabla}\cdot\boldsymbol{\tau}=0 \\ &\boldsymbol{e}=\frac{1}{2}(\boldsymbol{\nabla}\boldsymbol{v}+\boldsymbol{v}\boldsymbol{\nabla}) \\ &\boldsymbol{\sigma}=-p\boldsymbol{I}+2\mu\boldsymbol{e} \end{aligned} \tag{2.19}$$

where t is time, ρ is the fluid density. Under the incompressibility assumption, ρ is constant. $\boldsymbol{v}$ is the velocity vector, μ is the dynamic viscosity constant, $\boldsymbol{\tau}$ is the deviatoric stress tensor, $\boldsymbol{e}$ is the strain rate tensor, and $\boldsymbol{\sigma}$ is the stress tensor.

The solution processes for the solid and fluid models are similar. The geometry of each model is first discretised into the finite elements (a process called meshing). According to the defined material property (constitutive laws), a stiffness matrix is created for each element and is assembled to form the overall stiffness matrix for the whole model. The boundary conditions are transformed into the matrix form, which forms a large linear equation system with the stiffness matrix. The displacement of the element is calculated by solving the system of linear equations, and the strain is calculated by taking the derivative of displacements. Stress can also be evaluated using constitutive laws. In FEM, the finite elements are usually defined with connected nodes, and all mechanical parameters are calculated at the nodes. The mechanical parameters at a location that deviates from any nodes are calculated by interpolating the neighbouring nodes.

Although in arterial biomechanics, the solid and fluid models can be solved separately with idealised boundary conditions, they are not independent under physiological conditions. At the luminal surface where the solid and fluid model interacts, the blood flow exerts pressure and haemodynamic forces on the endothelial wall. The luminal surface deforms under the haemodynamic forces according to the material properties, altering the lumen morphology and the fluid mechanics of blood flow. Interaction between the solid and fluid domain is coupled at the luminal surface, and interactive modelling is necessary to accurately simulate the mechanical status.

The fully coupled fluid-structure interaction (FSI) method simulates the interaction mechanism by iteratively updating information at the fluid-structure interface between the two models. For each iteration, the fluid model is solved, and the stresses at the interface (luminal surface) are transferred to the solid model, which is used as the boundary condition for the solid solution. The solid model is then solved with the updated boundary conditions. The geometry at the interface is transferred back to the fluid model, which is used as the boundary condition in the fluid solution. Multiple iterations are performed until the system reaches a steady equilibrium state. This process then repeats for the next time step to simulate a dynamic process.

The iterative interaction of the fully coupled FSI method dramatically increases the computational complexity of the solution process and therefore decreases the simulation efficiency. In addition, the iterative process introduces numerical instability to the solution process. For example, a small numerical error in the fluid model creates a slightly larger force on the solid model. The solid model deforms accordingly, creating an abnormal local morphology and introducing an amplified instability to the fluid model in the next iteration. The numerical errors could be accumulated and amplified during the interactive iterations, and eventually, destabilise the model and cause convergence error. To partially overcome the drawbacks of fully coupled FSI, the one-way FSI is proposed by limiting the interaction to one direction only. Because the fluid model is more sensitive to geometry changes, the one-way FSI usually allows only the fluid-to-solid interaction. The solution process for the fluid model in one-way FSI is not different from a traditional CFD simulation with a rigid luminal surface as the boundary condition. For the solid model, the stresses at the luminal surface are defined by the information from the fluid model. The one-way interaction reduces the computational cost, improves the convergence rate and can serve as an approximate method to the fully coupled FSI under certain assumptions. To improve the numerical stability of the fully coupled FSI simulation in this study, we developed coronary structure mesh models with hexahedral elements and introduced damping of physiological loadings at the beginning of simulations.

2.2 Finite Element Modelling of Coronary Artery

For each patient, the 3D coronary geometry and plaque composition were reconstructed from the VH-IVUS and the digital subtraction angiography (DSA) images, using an in-house developed software (MATLAB R2020b, The MathWorks, Inc). The processing includes three steps: 2D VH-IVUS structure mesh, 3D central line reconstruction from DSA, and integration of VH-IVUS with the 3D central line.

2.2.1 2D Structure Mesh of VH-IVUS

The virtual histology process of grey-scale IVUS images identifies plaque components based on the backscattered radiofrequency signal and labels each plaque component with different colours on the grey-scale image. Preprocessing of VH-IVUS images with vessel and plaque component segmentation is necessary to facilitate more complicated image processing and

obtain basic morphology such as lumen and adventitial boundaries. The segmentation of non-grey-scale components (lipid, fibrous tissue, fibrofatty tissue) is straightforward, but the segmentation of grey-scale colour components (vessel wall and dense calcification) requires additional procedures. To determine the vessel region and EEM boundary, all pixels with the colour of the vessel wall (grey) were selected to construct a binary image (Figure 2.1 A, B). Then, all holes in the binary image were filled, and pixel areas of each isolated region were calculated subsequently (Figure 2.1C). The region with the largest area defined the segmented vessel region. The separation of the luminal area followed the same principle (Figure 2.1 D). This method was based on two assumptions:

1. The segmented vessel region was larger than individual background noise spots.

2. The segmented vessel region was closed and bounded by the vessel wall.

Given the sparsity of background noise and the arterial anatomy, these were reasonable assumptions for coronary VH-IVUS. Due to segmentation errors or image artefacts, the segmented vessel wall could be thin and discontinuous, which violated assumption 2. A convex hull algorithm was used to connect the gaps in the segmented vessel walls for these images. The final segmentation results were visually checked for validation.

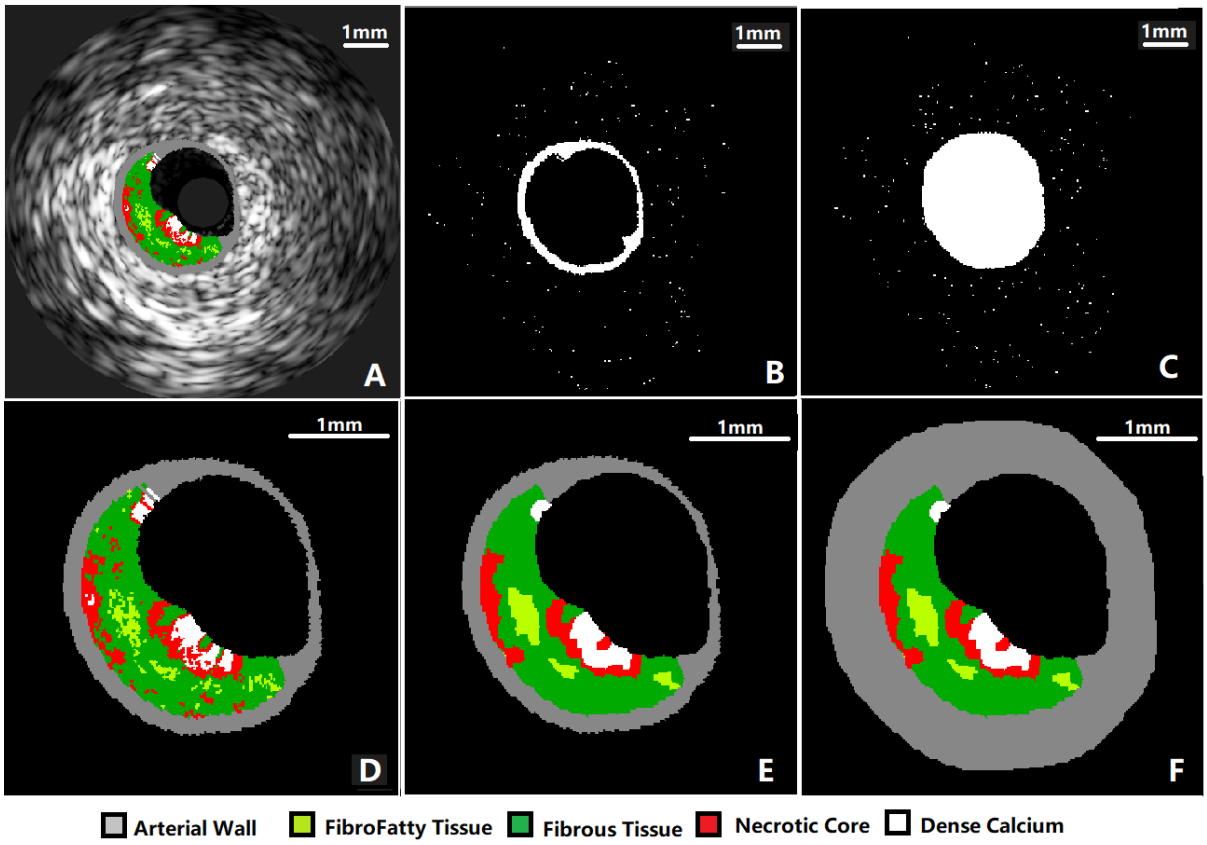

Figure 2.1 Image processing of VH-IVUS. From a VH-IVUS image (A), pixels with the colour of the arterial wall are selected as a binary image (B). After hole filling (C), the region with the largest area is used as a vascular mask to construct the background removed VH-IVUS (D). After regional smoothing for each plaque component (E), a layer of adventitia is attached to the arterial wall (F).

The virtual histology classification can result in small islands of components and rough component edges (Figure 2.1D). The islands with areas below the IVUS resolution often have irregular boundaries and create difficulties in image analysis tasks such as segmentation and resampling. To remove the component islands and smooth the boundary, individual components with an area <50 pixels were removed. The plaque component edges were smoothed by morphological operation, and the removed pixels were refilled through voting in the 3-by-3 Cartesian neighbourhood (Figure 2.1 E). Because of its low tissue density, the adventitial-perivascular tissue outside of the EEM is not visible in VH-IVUS, and only the intimal and medial layers were segmented as vessel walls. Despite its loose structure, the adventitia provided mechanical stability to the coronary artery, and it was necessary to include the adventitia in the vessel model[104]. To account for the mechanical support from the adventitial layer, a uniform layer of 350μm thickness was attached to the EEM boundary through image

dilation[105] (Figure 2.1 F).

To facilitate the finite element analysis, the preprocessed images were divided into quadrilateral elements through meshing. A radial grid mesh was created with nodes equally spaced between the lumen and the vessel wall, with the luminal centroid as the centre (Figure 2.2 B). While the radial mesh captures the lumen geometry and maintains a regular aspect ratio for each element, it also creates a large mismatch with the plaque component geometry. The mismatch results in a large component classification error after the component resampling. In order to represent component irregularity and maintain a suitable element aspect ratio at the same time, an iterative radial node adjustment was performed. In the adjustment, nodes were modelled as particles with repulsive force between each other (like the electrostatic force between two positively charged particles). The edges of plaque components were modelled as boundaries with attractive force to the nodes (like a negatively charged region). With slightly dominating attractive forces, the nodes conformed to the component edges and reduced morphological mismatch in meshing. The repulsive force avoided the collapse of nodes and maintained the element aspect ratio. An equilibrium state of the nodal system was found by minimizing the potential energy ($E(\vec{r})$) in the system.

$$\min_{\vec{r}} E(\vec{r}) = \sum_{i=1}^{N} \left(\sum_{j=1}^{N(j\neq i)} \frac{1}{r_{i,j}} - \frac{\alpha}{r_{i,edge}} \right) \qquad 2.20$$

where $\vec{r}$ is the position of nodes, N is the total number of nodes, $r_{i,j}$ is the Euclidean distance between node $\vec{r}_i$ and $\vec{r}_j$, $r_{i,edge}$ is the distance between the node $\vec{r}_i$ and the nearest component edge and α is an empirical coefficient that controls the balance between the nodal repulsive effect from $\sum_{j=1}^{N(j\neq i)} \frac{1}{r_{i,j}}$, and the edge attractive effect from $\frac{\alpha}{r_{i,edge}}$. The nodes tend to conform to the edge geometry under the attractive effect from the boundary. Figure 2.2 C illustrates the attractive field from component edges. The repulsive effect between nodes avoids the collapse of elements due to a cluster of nodes and maintains the element aspect ratio.

The movement of nodes was limited to the radial direction to enforce regular nodal connectivity. Although the radial only movement impaired the efficiency, flexibility and accuracy of the structure mesh, it improved the algorithm's robustness and reduced the solution time. A higher

nodal density in the radial or the circumferential direction could compensate for reduced accuracy due to radial movement limitation. However, a high nodal density leads to a significant increase in computational cost in the FEA analysis. A nodal (and element) density close to the VH-IVUS resolution could be a trade-off point between the computational cost and mesh reliability. Considering a typical coronary vessel radius of 1.5 mm, vessel thickness of 0.5 mm, the VH-IVUS resolution of 80 μm and 200-250 μm in the radial and circumferential direction, the node density was chosen to be five layers (six nodes) in the radial direction and 60 nodes (equally distributed for every six degrees) in the circumferential direction.

The nodes on the inner and outer edges were fixed as reference nodes to preserve lumen and adventitial surface geometry. A gradient descent algorithm was used to minimise Equation 2.19 and determine the adjusted nodal position (Figure 2.2 D). Quadrilateral elements were formed by connecting each node with its radial and circumferential neighbour. The component type of each element was determined through voting of the bounded pixel (Figure 2.2 E).

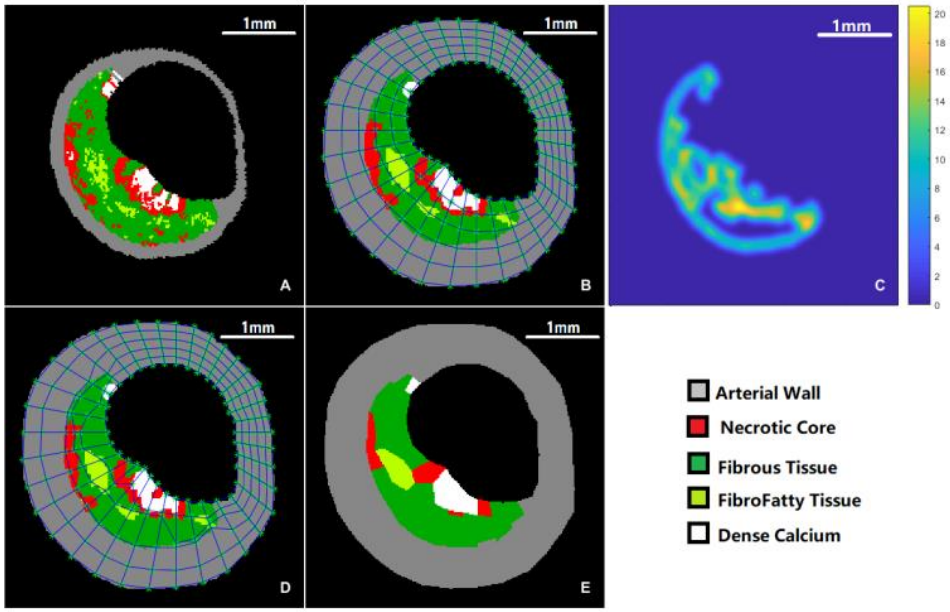

Figure 2.2 Iterative structure mesh of VH-IVUS. The vessel region of the VH-IVUS image was extracted (A), and a radial mesh with equally spaced nodes was created after component smoothing (B). An iterative nodal adjustment algorithm moved nodes towards edges (C: magnitude of the attractive force from component edges) whilst keeping distance between adjacent nodes. After the nodal adjustment (D), components of each quadrilateral element were resampled by voting of bounded pixels.

2.2.2 3D Central Line Reconstruction of DSA

While the VH-IVUS images provide 2D geometry and composition of the vessel, the information is limited to the perpendicular plane of the IVUS probe. Reconstruction of the 3D coronary vessel requires longitudinal information of the 3D vessel geometry, which can be obtained from the dual-plane DSA.

In a DSA video for the left coronary artery, a contrast medium was injected into the LCA through a coronary catheter and perfused into the lumen of the left circumflex artery (LCx) and the left anterior descending artery (LAD), forming a dark silhouette of the coronary lumen (Figure 2.3 A). Because IVUS was performed for each coronary artery separately, the 3D coronary model was also limited to the individual artery. To separate each artery (e.g. LAD in Figure 2.3) from the background and other vessels, a semi-automatic segmentation was performed on each angiographic frame.

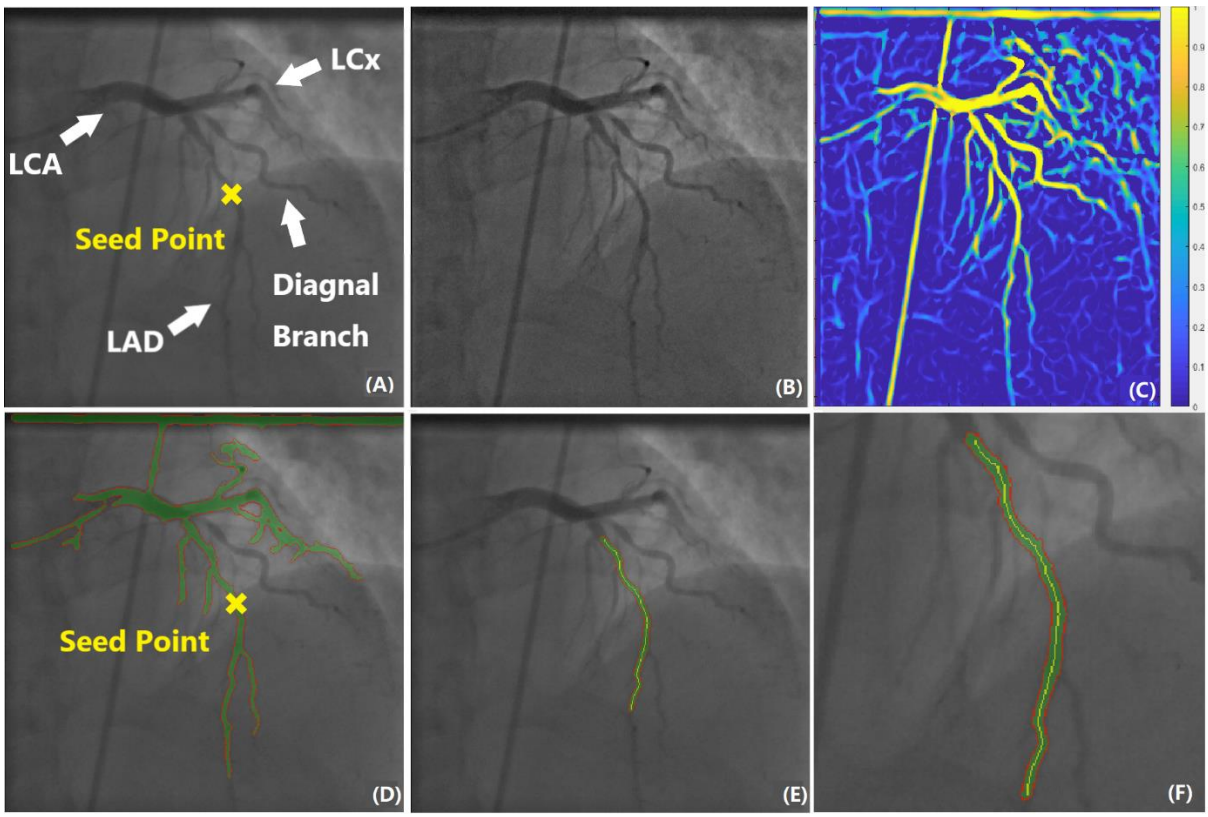

Figure 2.3 Conventional X-ray angiography segmentation and central line extraction. (A) Original angiographic frame. (B) Gaussian sharpened image. (C) Tubular feature map after Hessian filtering of image B. (D) Region growing segmentation result (lumen area is labelled

as green, the boundary is marked as red). (E) Manually corrected segmentation and central line (yellow line). (F) Enlargement of image E.

Firstly, the angiographic image underwent image enhancement. Gaussian sharpening was applied by subtracting the original image from the Gaussian blurred image. In Gaussian sharpening, the image intensity of the homogeneous regions was less affected, and that of the heterogeneous regions (e.g. edges) was enhanced (Figure 2.3 B). Next, Hessian-based filtering highlighted the tubular feature in the enhanced image. Hessian enhancement analysed the eigenvalues of a matrix comprised of second-order intensity derivatives, often called the Hessian matrix[106,107]. Hessian eigenvalues were sensitive to 2D tubular structures in an arbitrary direction, and a tubular feature map was extracted by comparing the local eigenvalues in a Hessian-filtered image[107] (Figure 2.3 C).

Although tubular structures were highlighted after Hessian enhancement, the vessel of interest could not be segmented easily because of the uneven illumination, feature noise and the overlaid structures (such as other vessels, catheters, bone and diaphragm). To identify the vessel of interest and refine auto segmentation, a manually selected seed point was placed on the original image (illustrated as a yellow cross in Figure 2.3 A, C). A regional growing algorithm with eight connectivity delineates the vessel of interest by starting from the seed point. The tolerance interval was determined using the Otsu automatic threshold of all feature intensities in the feature map[82]. The segmented area of the region growing algorithm is illustrated in Figure 2.3 D. After the region growing segmentation, most of the artefacts were removed. Manual correction of the segmentation further removed the vessel regions outside of the IVUS coverage (side branches, distal region and LCA) for precise vessel reconstruction. Finally, a skeletonisation algorithm was used to extract the central line from the manually corrected vessel segmentation[108], representing the path of the IVUS probe (Figure 2.3 E, F).

To capture the vessel movement during a cardiac cycle, two DSA videos taken from different directions were selected and were manually matched in temporal sequence based on their cardiac phase. The central line extraction processes were repeated for all frames in the matched DSA videos. Because the DSA videos were taken at a constant frame rate (15 frames per second), the number of frames in a cardiac cycle could provide the heart rate of the patient.

With paired 2D central lines extracted from the dual-angle DSA videos, 3D central lines were reconstructed based on the following assumptions:

1. The 2D projection of a central line to an angiographic plane could be decomposed into a rigid transformation and magnification.

2. Vessel movements were periodic across different cardiac cycles.

3. Registration between the 2D central lines could be approximated using the relative arc length as a reference.

Reconstruction of the 3D central line was performed in a forward modelling and curve-fitting approach, as illustrated in Figure 2.4. First, paired 2D central lines were downsampled to 50 sample points with equal 2D arc length between adjacent points (red triangle in Figure 2.5 A, B). Because distances from the X-ray source to the patient and to the intensifier were different, the two angiographic projections were scaled at different ratios. Scaling calibration was performed by rescaling distance with respect to the centre of each projection plane.

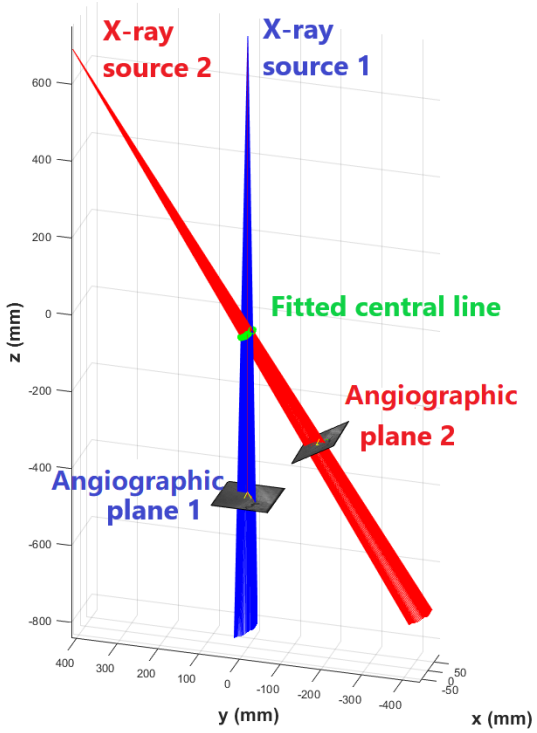

Figure 2.4 Illustration of angiographic projection. Light rays from two X-ray sources (red and blue lines) pass through the fitted central line (sample points), and project on the corresponding angiographic planes which are positioned according to their angiographic settings.

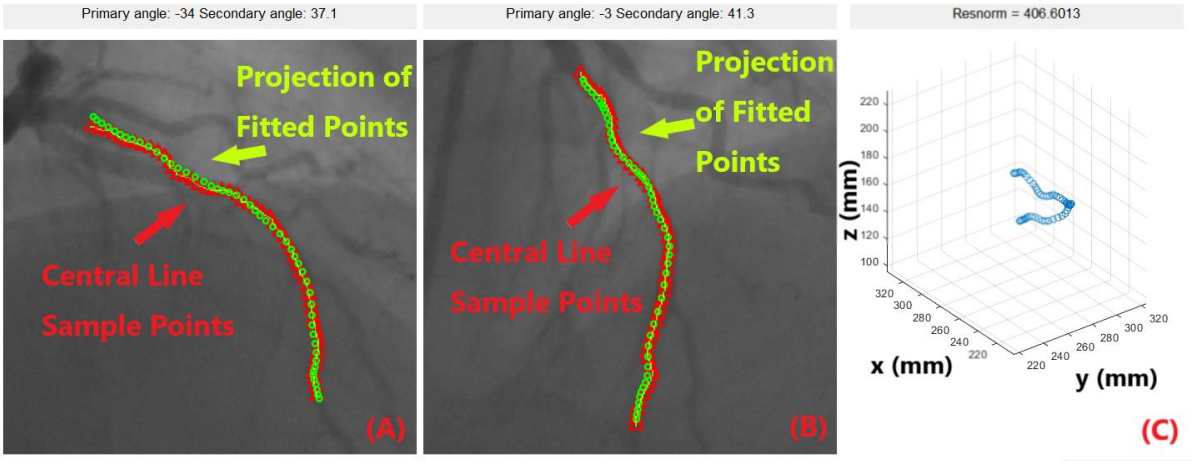

Figure 2.5 3D central line reconstruction. The central line sample points from the angiographic segmentation (red triangle) and from the fitted projection (green circle) are overlaid on conventional angiographic images (A: angiographic plane 1, B: angiographic plane 2). The 3D fitted central line is shown in image (C).

Then, a 3D Fourier series curve model was generated, with Equation 2.21:

$$f(s) = a_0 + a_1 \cdot s + \sum_{n=1}^{4} b_n \cos(2^n \pi \cdot s) + \sum_{n=1}^{4} c_n \sin 2^n \pi \cdot s \qquad 2.21$$

where $f(s)$ is the curve parametric function of variable s. a_0, a_1, b_n, c_n (n=1,…,4) are parameters to be fitted. The projection can be modelled as Equation 2.22:

$$p_i = \begin{bmatrix} 1 & 0 & 0 \\ 0 & 1 & 0 \\ 0 & 0 & 0 \end{bmatrix} \times \left(RT_i \times (f(s) + t) \right) \qquad 2.22$$

$$t = \begin{cases} t_0, & i = 2 \\ 0, & i = 1 \end{cases} \qquad 2.23$$

$$RT_i = \begin{bmatrix} 1 & 0 & 0 \\ 0 & \cos(\theta_i) & -\sin(\theta_i) \\ 0 & \sin(\theta_i) & \cos(\theta_i) \end{bmatrix} \times \begin{bmatrix} \cos(\varphi_i) & 0 & \sin(\varphi_i) \\ 0 & 1 & 0 \\ -\sin(\varphi_i) & 0 & \cos(\varphi_i) \end{bmatrix} \qquad 2.24$$

where p_i is the 2D projection of the central line on angiographic plane i ($i = 1,2$), RT_i is the

rotational matrix defined in Equation 2.19, and t is a relative shift between two angiographic planes (Equation 2.23). In Equation 2.19, θ_i, φ_i are rotational angles with respect to x, y axes in angiographic plane i, and are determined by the primary and secondary angles of the angiographic planes.

Fitted 3D central lines were initially simulated with 500 points, and were then projected and resampled to 50 points with equal arc length in between (green circles in Figure 2.D and Figure 2 E). Points on the 3D central line and the two 2D central lines were registered based on their relative arc lengths. The resampling allowed a comparison between the fitted central line and the extracted central line from the angiogram. The reconstruction then became a curve-fitting problem which minimised the Euclidian distances between sample points from the fitted curve projection and sample points from the DSA central line extraction. A least square curve fitting algorithm was used to determine the fitting coefficients and the 3D vessel geometry. The 3D central line reconstruction was repeated for all pairs of angiographic frames. The squared residual norm ("resnorm" in Figure 2.5 C) was calculated for each fit. The average squared residual norm was $1298.9\ pixel^2$, with pixel size $0.27\ mm$.

2.2.3 VH-IVUS and 3D central line integration

To combine the vessel's cross sectional morphology and longitudinal geometry, a multi-modality image integration process was performed for the VH-IVUS image and the 3D central line from DSA. The integration was based on the following assumptions:

1. Centroid of the VH-IVUS lumen was the vessel cross section's geometric centre and coincided with the 3D central line.
2. VH-IVUS slices were perpendicular to the 3D central line.
3. Axial rotation of adjacent VH-IVUS slices due to catheter curvature was small.

The integration process can be summarised into five steps:

1. Landmark VH-IVUS slices were identified based on the appearance of bifurcation or stenosis.

2. Considering the order, landmark feature, and the number of slices between landmark VH-IVUS slices, the corresponding DSA landmarks were identified in the diastole DSA frame and were back-projected to the 3D central line.

3. The landmark VH-IVUS slices were located in 3D by matching the 2D luminal centroid with the 3D landmark position. Slices between landmark slices were also located with an equal longitudinal distance between slices.

4. The slices were oriented such that the image plane is perpendicular to the local central line tangent vector, and the between slice rotation was determined with a parallel transportation method[109].

5. To initialise the circumferential orientation for the first slice, the position of the cardiac centre was estimated as the central line's curvature centre (Figure 2.6). Due to the stiffness of the ultrasound probe, a vector from the probe to the luminal centroid was assumed to point towards the cardiac centre.

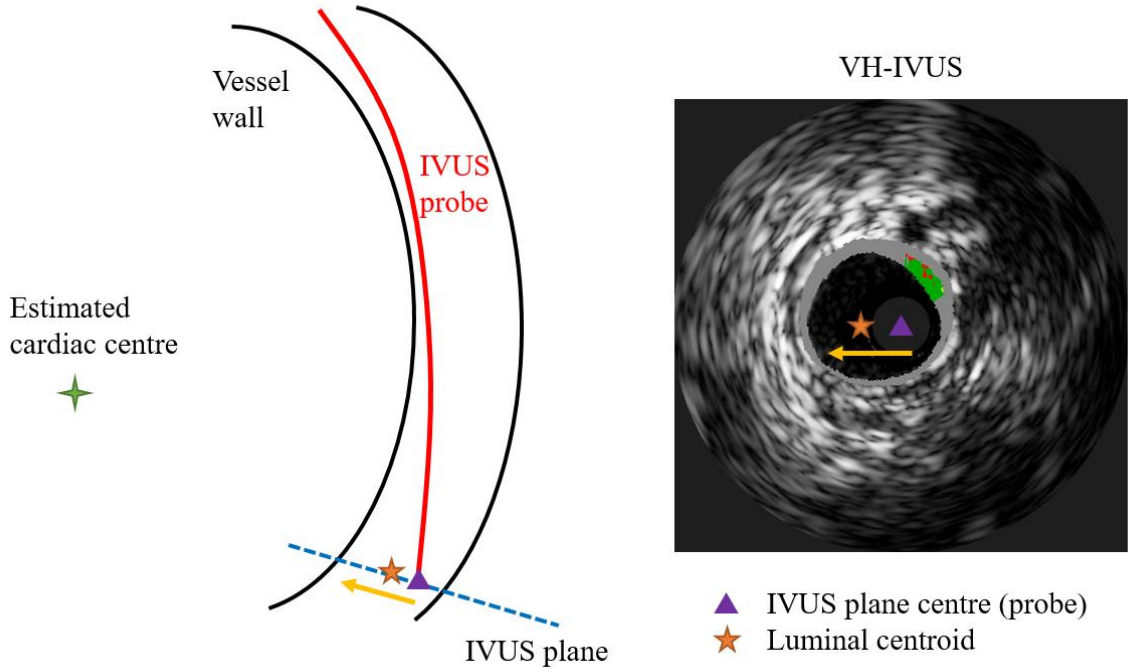

Figure 2.6 Rotation initialization of VH-IVUS image

It is challenging to locate VH-IVUS slices on a central line by comparing the VH-IVUS and

DSA images, because the signal penetration of VH-IVUS (penetration depth 3-4 mm) is much smaller than the field of view of X-ray angiography (130-150 mm). To observe morphological features on a large scale, a sequence of VH-IVUS slices was stacked into an image volume that represented a vessel segment. Because VH-IVUS slices were taken once per cardiac cycle, and the pullback speed was 5 mm/s, the longitudinal separation between adjacent VH-IVUS slices was 0.43 mm, given an average patient heart rate of 70 beats per minute. VH-IVUS slices were replicated to fill in the 0.43 mm gap between frames. The VH-IVUS images were converted to monochromatic images to visualise the image volume. A cutting plane along the longitudinal direction revealed the cross-section of the vessel, as shown in Figure 2.7.

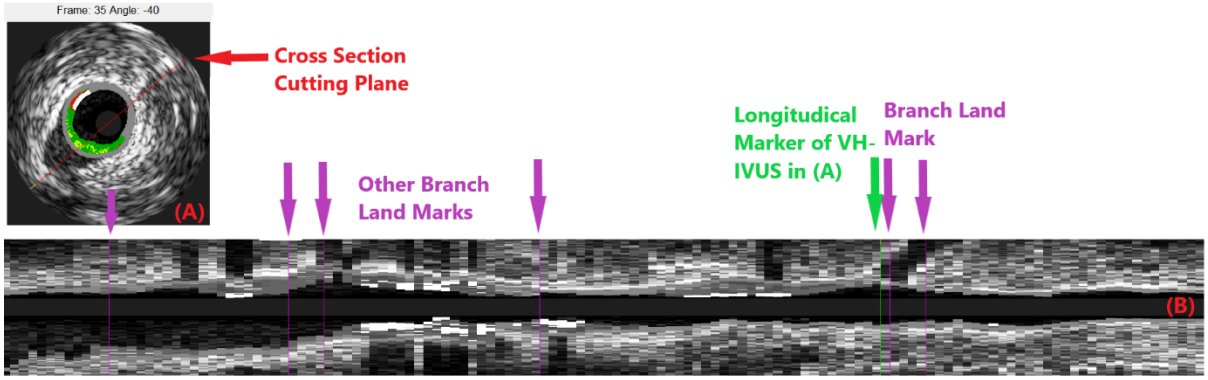

Figure 2.7 Selection of branching landmarks in a VH-IVUS stack. (A) Example VH-IVUS slice (the red line indicates cross-section cutting plane in B). (B) Cross-sectional view of VH-IVUS stack and branch landmarks.

For registration, the coronary artery branch points were the most apparent markers and could be identified in both VH-IVUS and angiography. Figure 2.7 A shows the VH-IVUS slice at the branch point labelled with a green arrow in Figure 2.7 B and illustrates the cutting plane direction with a red line. The “dark shadow” in Figure 2.7 A near the bottom left of the arterial wall is evidence of such branching. Comparing the VH-IVUS slice and cross-section of the image volume, branch point landmarks were identified (indicated as green or purple arrows) at different cutting plane angles.

Moreover, the gaps between VH-IVUS slices were non-uniform because of the curvature of the catheter path, and the variation in heart rate. Multiple image landmarks can reduce the inaccuracy in longitudinal registration. With these considerations, the stenosis and branches

were used as references to manually position the landmarks on the 3D central line. The landmarks were then projected onto the DSA plane (Figure 2.8 A). Between adjacent landmarks, VH-IVUS slices were equally distributed along the 3D central line (Figure 2.8 B).

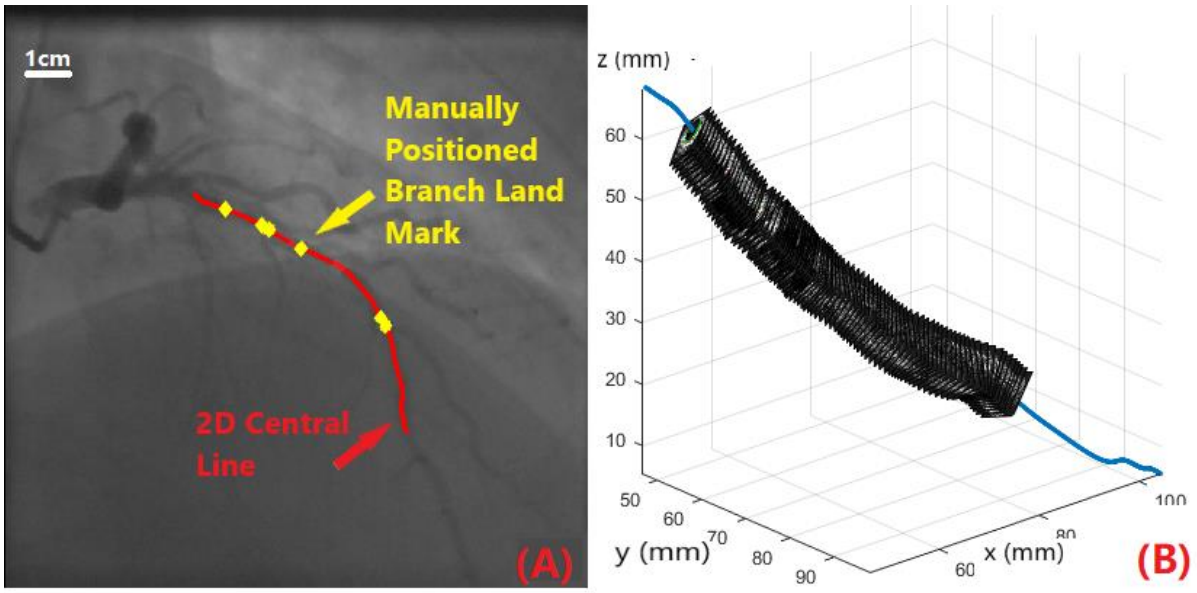

Figure 2.8 VH-IVUS and 3D central line integration. (A) Manual match of branch landmarks to an angiographic image, (B) Integration of VH-IVUS on the 3D central line,

After the translation of VH-IVUS to the 3D central line, the local orientation of each VH-IVUS slice was necessary for the 3D vessel reconstruction. Because the IVUS probe follows a curved path, the axial orientation of the VH-IVUS images changes between slices and the magnitude of change is related to the catheter path curvature. Although the axial rotation of adjacent VH-IVUS slices is small, the accumulation of axial rotation across multiple slices can produce a considerable change to the 3D coronary model. A local reference system accounting for the central line curvature is necessary to correct the axial rotation. A common local reference system used for a 3D curve is the Frenet-Serret coordinate system, which uses the normal tangent vector, and the normal unit vector (a unit vector pointing along the radius of curvature) to define a local reference system. The Frenet-Serret coordinate system is not applicable for a straight line because of the undefined curvature for the straight line. Although the 3D central lines of coronary arteries were not straight, the small magnitude of local curvature might create large distortions in the normal vector of the reference system, as shown in Figure 2.9 A.

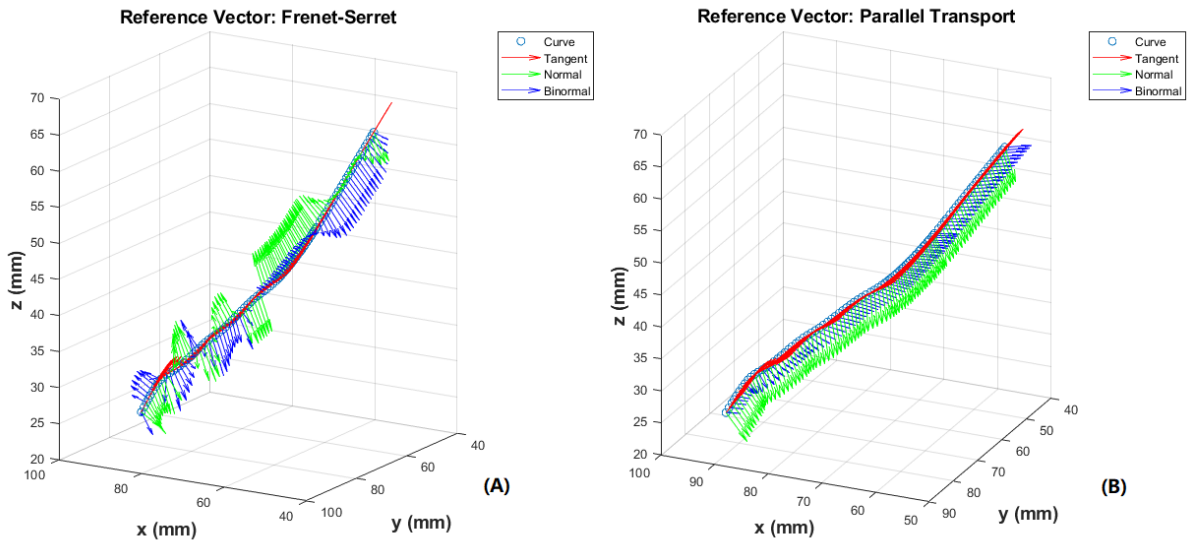

Figure 2.9 Local reference system of the 3D central line. (A) Frenet-Serret coordinate System. (B) Parallel Transport coordinate system.

The parallel transport theory was used to reduce the local distortion. Parallel transportation is the transportation of a vector along a differentiable curve (a smooth curve) such that the new vector is parallel to the previous one. Orientation of the first slice in parallel transportation was determined by aligning the probe, luminal centroid and the estimated cardiac centre, as illustrated in Figure 2.6. With the axial orientation of the first slice, the reference system was parallel transported along the central line. This method provided a smoother and more stable local reference system, as shown in Figure 2.9 B. Finally, VH-IVUS slices were translated by aligning luminal centroids to the corresponding location on the central line. Each VH-IVUS slice was rotated according to the local normal direction according to the parallel transported local reference system. The result of the integration is shown in Figure 2.9 B.

However, adjacent frames of VH-IVUS might intersect where the local curvature of the 3D central line was large. The intersection distorts the 3D connectivity of adjacent elements. Figure 2.10 A, B illustrates an example of frame intersection. Blue and red points represent the layer of nodes from adjacent frames 1 and frame 2. To address this problem, nodes of intersection were detected by projecting the nodal position vectors of frame 1 onto the normal vector of frame 2, where negative magnitude indicated nodes below frame 2, which were the intersected nodes. For the intersected nodes in frame 1, their nodal positions were switched with their

corresponding nodes at intersected frame (frame 2, in this case). Figure 2.10 C illustrates the result after the substitution of intersected nodes.

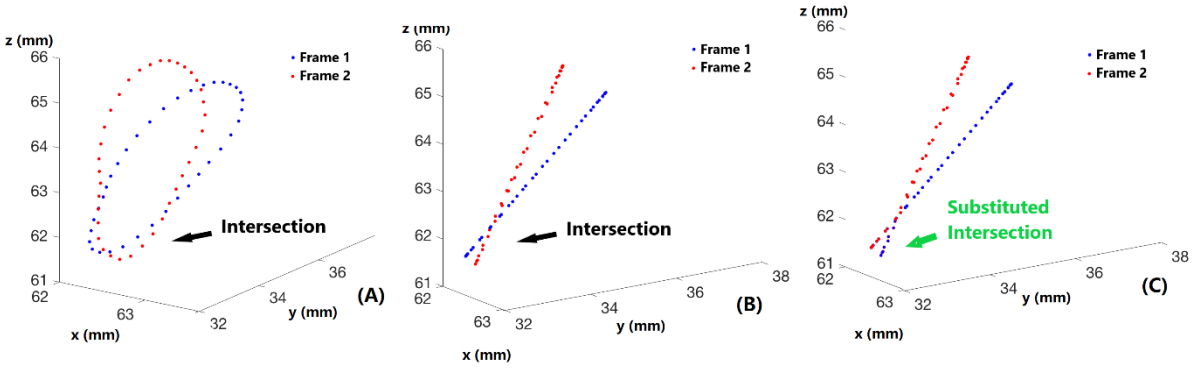

Figure 2.10 Illustration of frame intersection. The red and blue points are nodes from adjacent VH-IVUS slices which intersect (A, B). The intersection is corrected by switching nodes in the intersection region across the two frames (C).

2.2.4 3D Mesh Generation

With both the cross-sectional and longitudinal information of vessel geometry, we were able to position each node in 3D. Because of the nature of the structure mesh, the number of nodes in each slice was fixed, and the nodal connectivity was well defined. For longitudinal connectivity across slices, nodes in the 2D structure mesh were connected to the corresponding nodes in adjacent slices, forming a hexahedral 3D structure mesh of the vessel (Figure 2.11 A). The low axial rotation between adjacent slices and the controlled aspect ratio in 2D structure mesh both ensured a regular shape and connectivity for the 3D hexahedral elements and improved the convergence and stability in the following numerical simulations. The component category of the hexahedral elements was determined by the resampled component type in the 2D VH-IVUS structure mesh (Figure 2.2 E). For convention, the VH-IVUS slice at the proximal direction was used for component assignment. Figure 2.11 B illustrates a section of the 3D coronary vessel mesh using three adjacent VH-IVUS slices, and the colours of element edges represent the component categories.

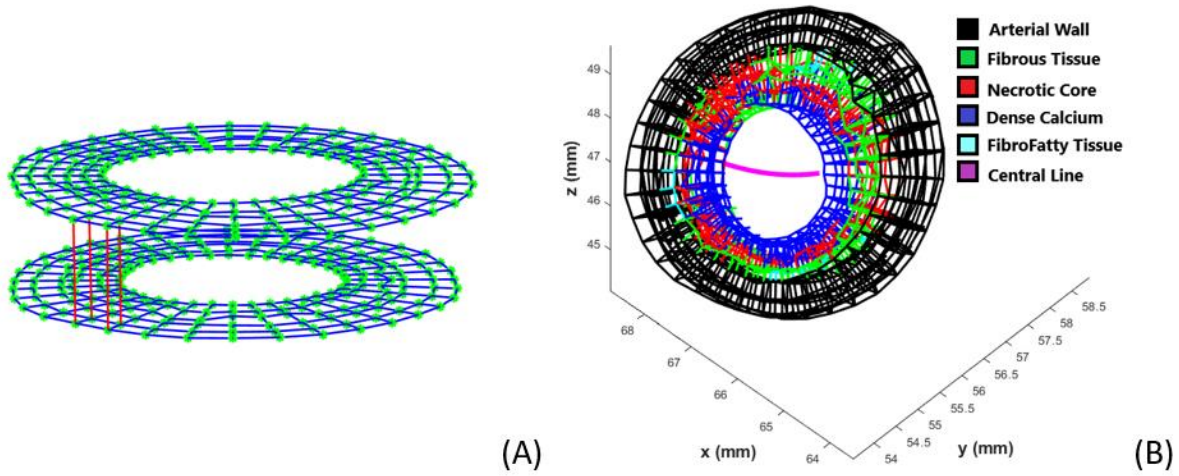

Figure 2.11 Illustration of 3D structure mesh connectivity. 3D structure mesh was generated by connecting the corresponding nodes of two adjacent 2D VH-IVUS mesh (A). Material category of the hexahedral elements was assigned according to the elements in the 2D VH-IVUS mesh (B).

An additional ten replicated slices were added to the proximal and distal ends to minimise the entry effect in the mechanical analysis (Figure 2.12 A). Under physiological conditions, the vessel is pressurised and longitudinally stretched. The in vivo VH-IVUS images were acquired under pressurised conditions. Shrinkage was needed to account for the residual stress in the vessel wall. A uniform in-slice shrinkage of 3% was applied in the radial direction (diameter) based on the experience in 2D coronary and carotid FEA studies[110,111].

Anatomical studies indicate that the coronary arteries were attached to the epicardial surface with a layer of loose connective tissue. To simulate the bending of coronary arteries due to heart motion, the epicardial surfaces were selected on the outer wall of the coronary. The epicardial surface for each slice was defined as the outer wall surface closest to the estimated cardiac centre. Because the coronary arteries wrap around the heart, the cardiac centre can be estimated by averaging the curvature vectors along the vessel central line (Figure 2.12 A). Under physiological conditions, the attachment of coronary arteries and connective tissue is non-rigid and certain shearing and shifting could happen. To avoid rigid bending, displacement loading was only applied to a few epicardial surfaces with distance in between (every ten VH-IVUS slices). A gasket layer made of the loose matrix was created on top of these epicardial loading surfaces to reduce stress concentration due to the displacement loading, and to allow a

certain shift between the loading and the vessel wall (Figure 2.12 C).

Having the solid structure mesh for the coronary artery, the fluid volume was defined as the volume enclosed by the solid model. A radial mesh centred on the central line was created for the fluid model, and the luminal surfaces were identified as the fluid-structure interfaces (Figure 2.12 B, D).

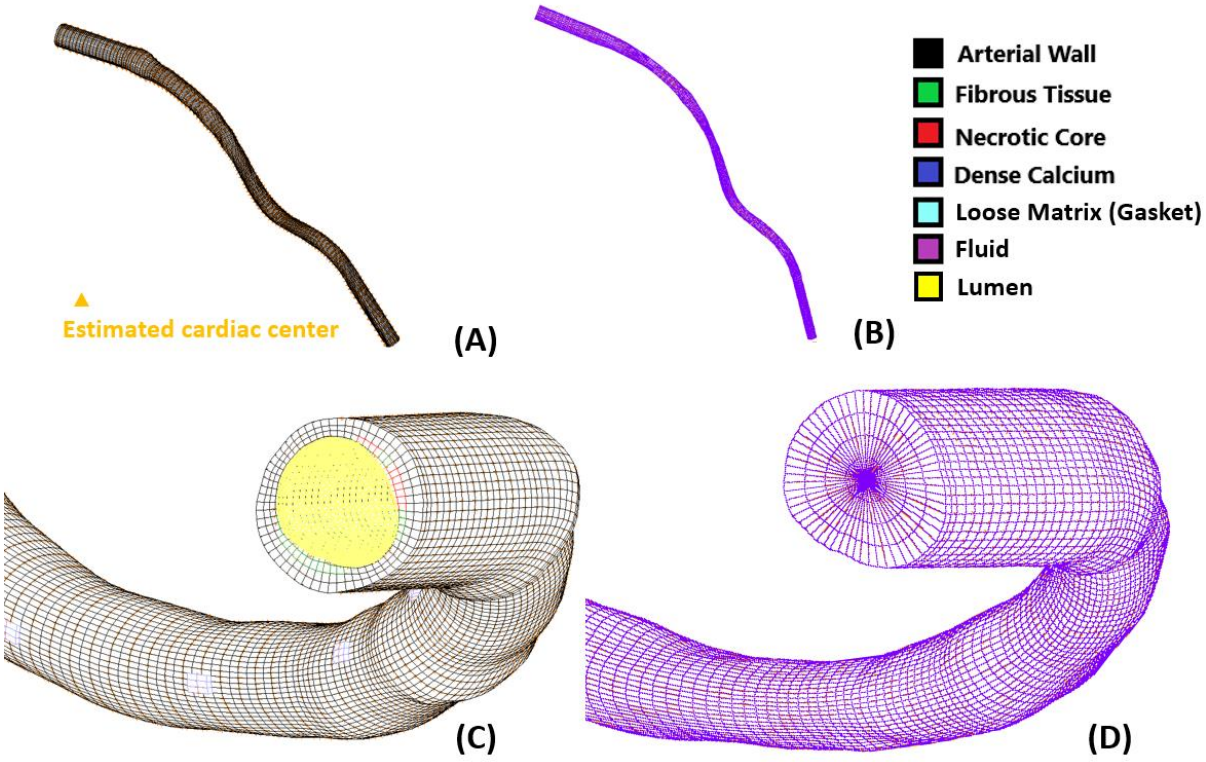

Figure 2.12 Solid (A) and fluid (B) mesh of the coronary vessel. Replicated slices were attached to the proximal (C, D) and distal ends. A gasket layer with loose matrix was created at the outer wall surface closest to the estimated cardiac centre.

2.2.5 Physiological boundary conditions

A series of displacement loadings were applied to the selected epicardial surfaces with gasket layers to simulate the bending of coronary arteries due to cardiac motion. Under physiological conditions, bending displacements were exerted on the epicardial surfaces, but the epicardial surfaces were not detectable in the current data. The epicardial surface displacement could not be quantified precisely. Since most displacement occurs at the distal coronary arteries, where the vessel radius is relatively small compared to the magnitude of displacement, we can approximate the displacement on epicardial surfaces with the displacement of the coronary

lumen.

The 3D central lines in the time series provided the geometrical change of the coronary lumen during each cardiac cycle. To quantify the displacement for the centroid of each slice, it was necessary to co-register the corresponding central line points across time. In the VH-IVUS central line integration process (Section 2.2.4), a parametric value (s, in Equation 2.21) was matched for each slice. Evaluating the time series of 3D central line models with the same parametric value s thus provided the trajectory of each centroid during the cardiac cycle. Due to the low sample rate (the sample rate of the DSA was 15 frames per second) and errors in the 3D central line reconstruction, the raw trajectories were smoothed and interpolated for the FEA simulations. Figure 2.13 A illustrates the smoothed trajectories for all VH-IVUS slices. The trajectories were first calibrated with respect to the proximal slice and were then calibrated with respect to the first (diastole) time point to determine the local displacements. The magnitude of displacement decreases from the distal to the proximal end. A fixation boundary condition was applied to the cross-sectional surfaces of the proximal slice. To improve the convergence and stability of the numerical simulations, all selected displacements were replicated for four cardiac cycles, and the magnitude of the first two cardiac cycles was damped by a linear ramping function. Two full displacement cycles followed the damped cycle stabilised the numerical result, and the mechanical analysis focused only on the last cardiac cycle. Figure 2.13 B, D illustrates the displacement trajectory and time function for the loading slices.

For fluid simulation, the inlet and outlet pressure profiles were generated by fitting the patients' diastole and systole blood pressure to a generic coronary pressure profile[112] (Figure 2.13 D). The duration of the pressure profile was fitted with the patient's heart rate measured from DSA frames. Similar to the displacement loading, the pressure profiles were replicated for four cardiac cycles, and the first two cycles were damped with a linear function (Figure 2.13 E). Pressure loadings were applied to the inlet and outlet surfaces of the fluid elements.

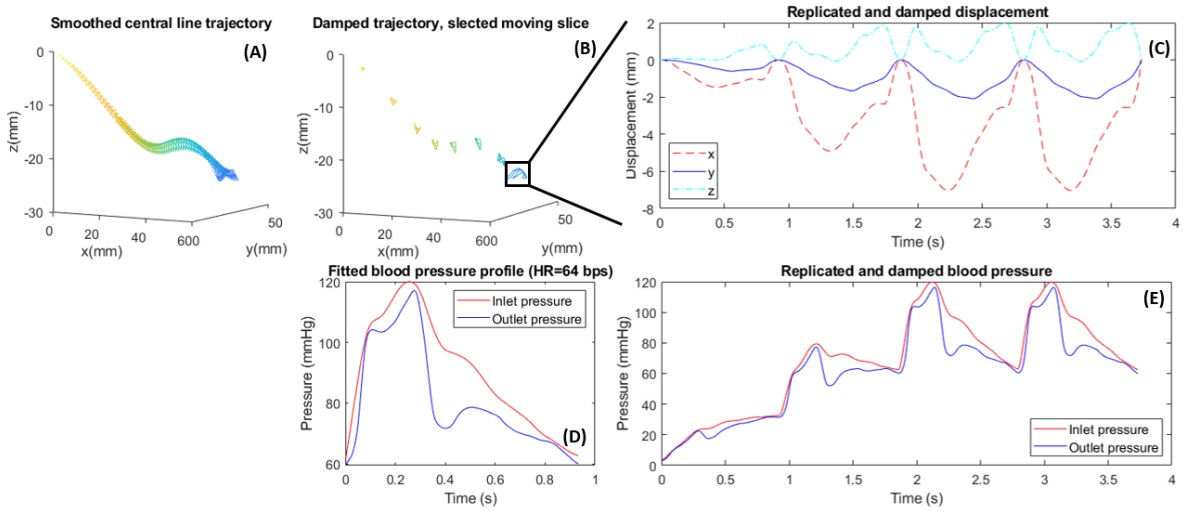

Figure 2.13 Bending displacement and pressure boundary conditions. Central line trajectories of each slice were extracted and smoothed from the reconstructed 3D central lines (A). Slice trajectories for loading slices with gasket layers were identified (B) and were replicated and damped for four cycles (C). Coronary blood pressure profiles were fitted for the patient's heart rate (D) and were also replicated and damped for four cycles (E)

2.3 Coronary bending quantification with multi-phase CCTA

Coronary artery movement has been shown to associate with coronary luminal stenosis and can influence the estimation of stresses and strains in coronary plaques[113–115]. As a common and persisting type of movement, coronary bending may associate with the patterns of coronary curvature and the coronary anatomy. The study of coronary bending can improve the modelling accuracy in biomechanical analysis and potentially reveal bending as a biomarker in understanding the pathophysiology of coronary diseases. In order to investigate the coronary bending and curvature, we performed coronary bending quantification in the major coronary arteries.

Multi-phase CCTA images were acquired by clinicians in 47 patients with anomalous origination of coronary arteries with voxel size 0.37×0.37×0.5 mm^3. The diastole and systole phases of the CCTA images were selected, and the coronary lumens were automatically segmented (Figure 2.14 A) using CT-VascularView (Nanjing Jingsan Science and Technology, Ltd., Jiangsu, China). In order to perform accurate volumetric operations, the CCTA images were resampled to an isotropic voxel size of 0.37×0.37×0.37 mm^3. A volumetric skeletonization algorithm extracted the central line for the lumen of LAD, LCx, and RCA.

Subbranches were removed from the central line analysis. The central line pixels were reordered according to their distance and connectivity to the left main artery. The central line extraction process was repeated for the CCTA images with different cardiac phases. An average smoothing with a span of five pixels smoothed the central lines, and the curvature was calculated along the smoothed central line. Figure 2.14 B demonstrates the extracted LAD central line and the red arrows are the curvature vectors representing the curvature magnitudes and normal directions. Coronary bending was defined as the change of curvature between the diastole and systole phases. Co-registration between the two coronary phases was based on the vessel sections (proximal, medial, distal) or the central line distance to the left main artery, assuming cardiac contraction will not significantly alter the coronary length.

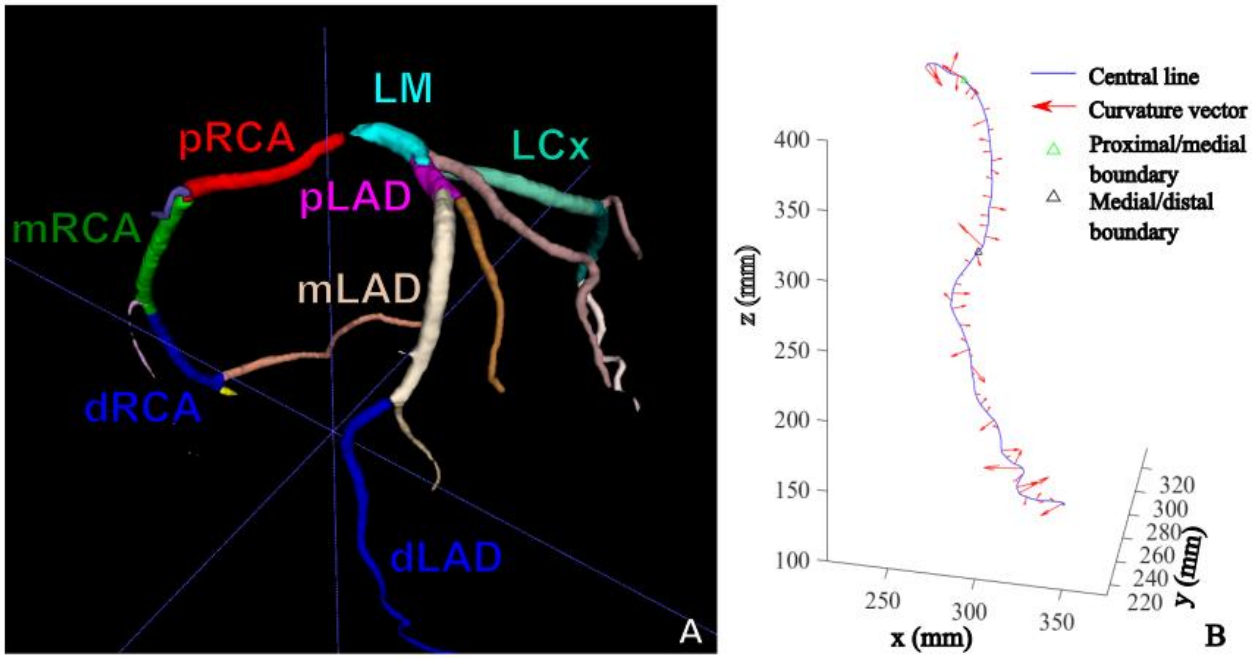

Figure 2.14 CCTA coronary segmentation and central line (LAD) extraction

Figure 2.15 illustrates the mean and standard error of bending and curvature (among 47 patients) at the diastole and systole phases. For statistical comparison, the central lines were aligned by their anatomical locations (proximal, medial and distal sections) or distance to the left main arteries. To avoid abnormal curvature due to segmentation or extraction errors, outlying curvature values ($\text{curvature} > Q3 + 2 \times IQR \; or \; \text{curvature} < Q1 - 2 \times IQR$) were excluded from statistical analyses.

(IQR: $interquaartile\ range$, $Q1$: $first\ quartile$, $Q3\ third\ quartile$)

The correlation coefficients were calculated between the diastole curvature with bending, and the systole curvature with bending for all vessels (Table 2.1).

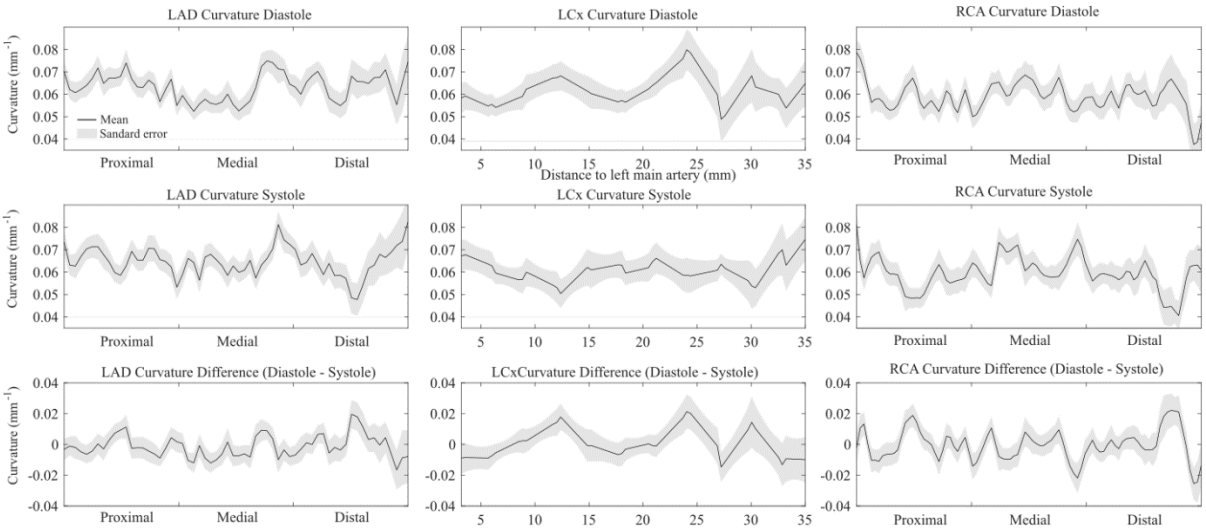

Figure 2.15 Coronary curvatures and bending (curvature difference) from CCTA central line extraction

Table 2.1 Correlation coefficients of coronary curvatures and bending

	LAD	LCx	RCA
Diastole vs Bending	0.61 ($p < 0.001$)	0.74 ($p < 0.001$)	0.67 ($p < 0.001$)
Systole vs Bending	-0.83 ($p < 0.001$)	-0.62 ($p < 0.001$)	-0.72 ($p < 0.001$)

The bending plots in Figure 2.15 show positive and negative curvature changes between the diastole and systole phases. For the LAD, although the overall curvature may increase as the heart contracts, the local curvature change is heterogenous along the artery. The uneven distribution of coronary bending may relate to the pathophysiology of focal coronary diseases such as atherosclerosis. The magnitude of bending in the LAD and LCx increased in the distal section, while the bending in the RCA showed no apparent difference between different

coronary sections.

In all three major coronary vessels, the bending is strongly correlated with the diastole or systole curvature. The correlation implicates the possibility of coronary bending estimation with either distal or systole coronary curvature. The widely available CCTA could potentially facilitate the bending and biomechanical analysis in a larger population. The curvature variation in the LAD and RCA correlates more strongly with the systole curvature, while the LCx correlates more strongly with the diastole curvature. The difference in correlation may relate to the orientation of coronary vessels. The LAD and RCA follow the longitudinal (atrium to ventricle) direction of the heart, and the LCx follows the circumferential (around the atrium) direction. During systole, the ventricular contraction deforms the epicardial surface and causes bending in the longitudinal direction. Therefore, the bending of the LAD and RCA is primarily dominated by the systole phase. During diastole, the atrium is refilled with blood, and the LCx near the atrium is extended. The bending of LCx is therefore dominated by the curvature in the diastole phase.

A limitation in the multi-phase CCTA curvature analysis is the lack of dynamic bending information. The epicardial and coronary movement due to heart motion is complex and varies across the cardiac cycle. Only the diastole and systole phases were analysed in this study, which may not fully reflect the bending movement during the entire cardiac cycle. Bending is one of the coronary movement categories. Other coronary movements such as contraction or displacement could also have implications on the modelling and physiology of coronary arteries. Because the patients had no significant atherosclerotic plaques, the association between atherosclerosis and patterns of coronary bending and curvature was not studied. Future studies with CCTA images of atherosclerotic patients could further assess the role of coronary bending and curvature in the development of atherosclerotic plaques.

In summary, the bending and curvature analysis with multi-phase CCTA indicates the bending of coronary arteries distributes unevenly along the arteries. We found a strong correlation between coronary curvature and bending, which could potentially be used to estimate coronary bending for biomechanical or clinical analysis. The bending patterns were related to the anatomical location of the coronary vessels. The association between coronary diseases and coronary bending requires further investigation.

Chapter 3 The influence of modelling strategy on the hemodynamic analysis of coronary atherosclerotic plaques

3.1 Introduction

Cardiovascular diseases (CVDs) are the leading cause of global death, responsible for 32% of global death, and 85 % of CVDs death are due to myocardial infarction and stroke[3]. Life-threatening acute coronary syndromes (ACSs) are most often caused by the rupture of a vulnerable plaque, which is characterized as a thin-cap fibroatheroma (TCFA) with a large necrotic lipid core and a thin fibrous cap[19,21]. Plaque rupture happens when the local stress exceeds the material strength of the overlying fibrous cap. Therefore the estimation of plaque structural stress (PSS) is important to the risk assessment of ischemic coronary diseases. PSS calculated by 2D finite element analysis (FEA) improves the accuracy in predicting major adverse cardiovascular events (MACEs) when combined with the morphological risk factors (plaque burden (PB) >70%, minimum luminal area (MLA) <4 mm^2, and virtual histology defined thin cap fibroatheroma (VH-TCFA))[75].

As an extension to the 2D FEA model, 3D FEA models include the modelling of axial stress and vessel movements and better represent the physiological environment. The accuracy and efficiency of the 3D FEA models depend on the material property, geometry reconstruction and modelling assumptions. An important modelling assumption is the interaction between the fluid (blood) and structure (vessel, plaque and other biological tissues) models. The 3D FEA models can be classified based on the fluid-structure interaction (FSI). The fully coupled FSI simulate the interaction with an iterative algorithm that exchanges information between the two models.

The accuracy of the fully coupled FSI model has been validated in theory and experiments[116,117]. The fully coupled FSI has been applied to vascular biomechanics to estimate stresses in the structural and induced by blood flow[118–122]. However, the computation of a fully coupled FSI required labour intensive pre-processing and the solution is time-consuming. Simplification of the interaction has been proposed to accelerate the procedure. The one-way FSI model assumes small structural deformation when the blood flow is modelled and a unidirectional interaction is employed for the structural analysis, and has been applied to the biomechanical studies of carotid atherosclerosis[123,124]. The structure only 3D FEA model neglects the interaction from the fluid model and was used in many studies because of its high computational efficiency[125,126]. *Huang* et al. compared the 2D/3D FEA and different modelling strategies in the biomechanical simulation of carotid arteries[111]. *Wang* et al. compared the different modelling strategies with cyclic bending on coronary arteries[127]. In this study, we intend to perform coronary FEA simulations with patient-specific bending, and compare the mechanical features estimated from different modelling strategies, including the 2D structure-mesh FEA, 2D free-mesh FEA, 3D structure only FEA, 3D one-way FSI, 3D fully coupled FSI, and 3D computational fluid dynamics (CFD).

3.2 Materials and Methods

- **Data acquisition**

Virtual histology intravascular ultrasound (VH-IVUS) and digital subtraction angiography (DSA) images of eight patients with coronary stenosis were obtained from the VH-IVUS in Vulnerable Atherosclerosis (VIVA) study with approval by the Cambridge Research Ethics Committee[32]. The VH-IVUS data were acquired before stenting with 20 MHz Eagle-Eye Gold catheters (Volcano Corporation, Rancho Cordova) at a motorized pullback speed of 0.5 mm/s. The VH-IVUS image analysis was performed offline on S5 consul software version 3.1 (Volcano Corporation, USA).

- **Vascular geometry reconstruction and mesh generation**

The method of vascular geometry reconstruction is described in Chapter 2.2. The 2D iterative radial meshing generated a 2D structure mesh for each VH-IVUS slice, and the frame-by-frame 3D reconstruction of the DSA images provided 3D coronary geometry during the cardiac cycle. Because the VH-IVUS images were obtained during diastole, a uniform in-slice shrinkage of 3% was applied during the 2D structure meshing to compensate for residual stress in the vessel wall. Common coronary features in the two modalities (such as stenosis and bifurcation) facilitated the integration of 2D structure meshes with 3D central lines. The parallel transportation method and the assumption on the slice's normal direction determined the local orientation of each 2D structure mesh. The slice intersection correction and 3D smoothing then finalize the nodal position. The 3D vascular mesh was generated by connecting the corresponding nodes in each slice. Two extended sections with ten replicated slices were created at the proximal and distal ends to account for the stress concentration in structural FEA and the entrance length in CFD. The elements were subdivided into sub-elements until the simulated result differences of PSS and WSS were less than 1%. The boundary conditions and material properties in the mesh convergence tests were the same as that in the final simulations.

The structure mesh reduces the number of elements and complexity of nodal connectivity in 3D FEA simulations. However, the low mesh density and reduced accuracy make it less suitable in 2D FEA simulations. To compare the predicted mechanical features from 2D and 3D models, we generated a 2D mesh using the free mesh method[30,112]. The image processing algorithm first removed the noise and small islands in the virtual histology, attached an adventitial layer, and then smoothed the contours of plaque components in the VH-IVUS image. The free mesh method created quadrilateral elements for each plaque component. The shrinkage method then depressurized the mesh to a zero-pressure state.

Six FEA models were created with different modelling strategies, including the 2D structure mesh FEA, 2D free mesh FEA, 3D structure only FEA, 3D one-way FSI, 3D fully coupled FSI and the fluid only CFD.

- **Finite element simulation**

The material properties of each component in the plaque (including vessel wall, lipid, fibrous tissue, and calcium) were assumed to be incompressible, homogeneous, non-linear isotropic, and hyperelastic as described by the modified Mooney–Rivlin strain energy density function,

$$W = c_1(\bar{I}_1 - 3) + D_1\left[\exp\left(D_2(\bar{I}_1 - 3)\right) - 1\right] + \kappa(J - 1) \quad 3.1$$

where $\bar{I}_1 = J^{-2/3}I_1$, I_1 is the first principal invariant of the modified right Cauchy-Green deformation tensor, κ is the Lagrange multiplier, J is the Jacobian of the deformation gradient tensor, and c_1, D_1, and D_2 are mechanical parameters derived from previous experiments. The material parameters used in this thesis were: arterial wall, $c_1 = 0.138$ kPa, $D_1 = 3.833$ kPa, $D_2 = 18.803$; fibrous tissue: $c_1 = 0.186$ kPa, $D_1 = 5.769$ kPa, $D_2 = 18.219$; necrotic lipid core $c_1 = 0.046$ kPa, $D_1 = 4.885$ kPa, $D_2 = 5.426$; dense calcium $c_1 = 1.147 \times 10^5$ kPa, $D_1 = 7.673 \times 10^4$ kPa, $D_2 = 2.838 \times 10^{-8}$; loose matrix $c_1 = 0.93$ kPa, $D_1 = 28.845$ kPa, $D_2 = 9.11$.[75,98]

The deformation of the structure was governed by the Cauchy momentum equation,

$$\rho u_{i,tt} = \sigma_{ij,j}(i, j = 1,2) \quad 3.2$$

with the boundary condition,

$$\sigma_{ij,j} \cdot n_j|_{outter\ wall} = 0 \quad 3.3$$

in which, $[u_i]$ and $[\sigma_{ij}]$ are displacement vector and Cauchy stress tensor, n_j is the normal vector, ρ is density, and t stands for time.

In order to mimic the impact of the heart beating in 3D FEA, the vascular displacement extracted from DSAs was applied to the outer wall of the coronary model. The bending displacement was applied at the outer wall surface closest to the cardiac centre. An additional gasket layer was created at the displacement surfaces to attenuate stress concentration. For 2D FEA, the displacement due to bending was not included, and fixation was applied on a few adventitial nodes as the boundary conditions.

In 3D FEA, the fluid simulation was governed by the Navier-Stokes equation with arbitrary Lagrangian-Eulerian (ALE) formulation, assuming the blood flow to be laminar, Newtonian, viscous, and incompressible,

$$\rho_b \frac{\partial \boldsymbol{v}}{\partial t} + \left[\left(\left(\boldsymbol{v} - \boldsymbol{v}_g\right) \cdot \nabla\right)\boldsymbol{v}\right] = -\nabla p + \mu \nabla^2 \boldsymbol{v}$$
$$\nabla \cdot \boldsymbol{v} = 0 \qquad 3.4$$

with boundary conditions,

$$p|_{inlet} = p_{in}(t), p|_{outlet} = p_{out}(t) \qquad 3.5$$

in which $\boldsymbol{v}$ is the blood velocity, $\boldsymbol{v}_g$ is grid velocity, p is pressure, and μ and ρ_b are the blood viscosity and density, respectively. On the fluid-structure inter surface, non-slipping condition,

$$\boldsymbol{v}|_\Gamma = \frac{\partial \boldsymbol{u}}{\partial t}|_\Gamma \qquad 3.6$$

and the loading interaction condition,

$$\boldsymbol{\sigma}_{ij}^f \cdot \boldsymbol{n}_j|_\Gamma = \boldsymbol{\sigma}_{ij}^s \cdot \boldsymbol{n}_j|_\Gamma \qquad 3.7$$

were applied. The inlet and outlet pressure profiles were generated by scaling a generic coronary pressure profile to patients' blood pressures.[128] Pressure loadings were applied to the surfaces of the inlet and outlet of the fluid model.

In the fully coupled FSI model, the fluid simulation and solid simulation interacted iteratively. For each time step, the fluid and solid results were mutually updated until convergence. In the one-way FSI model, the fluid model was simulated as in a typical fluid only CFD model. The fluid results were updated to the solid model, and the interaction happened only once before the solid simulation. For the structure only 3D model, the structure mesh 2D model and the free mesh 2D model, only the solid models were simulated. The blood pressure in the solid models was modelled as a spatially uniform pressure acting on the luminal surfaces or edges. All simulations with different modelling strategies were solved with a commercial finite element software ADINA 9.5.3 (ADINA R&D, Inc, Watertown, MA, USA), and on eight cores of an AMD Ryzen 3960X CPU and 16Gb RAM.

Plaque structural stress (PSS) was calculated as the peak Von Mises stress within the peri-

luminal area (10% vessel wall thickness) for each cross-sectional slice, using equation 2.19,

$$\sigma_{VM} = \sqrt{\frac{1}{2}\left[\left(\sigma_{xx}-\sigma_{yy}\right)^2+\left(\sigma_{yy}-\sigma_{zz}\right)^2+\left(\sigma_{zz}-\sigma_{xx}\right)^2\right]+3(\tau_{xy}^2+\tau_{yz}^2+\tau_{zx}^2)} \quad 3.8$$

where σ_{VM} is the effective stress, σ_{ii} $(i = x, y, z)$ is the principal tensile stress, and τ is the shear stress. Maximum shear stress (MSS) and maximum principal strain (MPS) were also calculated. To avoid stress concentration due to bending on calcification and lipid, luminal calcification and lipid nodes and slices with outlying PSS values ($\mathrm{PSS} > Q3 + 2 \times IQR$ *or* $\mathrm{PSS} < Q1 - 2 \times IQR$; *IQR*: interquartile range) were excluded from statistical analyses.

Pressure and time average wall shear stress (TAWSS) were calculated at the luminal surface. The oscillatory shear index (OSI) was calculated as:

$$OSI = 0.5 \times \left(1 - \frac{\left|\int_0^T \overrightarrow{WSS} dt\right|}{\int_0^T \left|\overrightarrow{WSS}\right| dt}\right) \quad 3.9$$

where $\overrightarrow{WSS}$ is the wall shear stress vector, *t* is the simulation time, *T* is the total simulation time. The relative residence time (*RRT*) is calculated as:

$$RRT = \left[(1 - 2 \times OSI) \times \frac{1}{T}\int_0^T \left|\overrightarrow{WSS}\right| dt\right] \quad 3.10$$

For statistical analysis, the fully coupled FSI model with bending was used as the gold standard. The Mann-Whitney was used for comparing unpaired variables with non-normal distribution, and the Wilcoxon sign-rank test was used for paired variables with non-normal distribution. Variables with normal distribution were reported as mean±standard deviation (SD), and variables with non-normal distribution were reported as median [1st and 3rd quantile]. A significant difference was assumed if $p < 0.05$.

3.3 Results

As described in section 2.2, the 3D meshes of coronary vessels were reconstructed from the VH-IVUS and DSA images. Figure 3.1 illustrates the geometry of each coronary mesh including the extended sections (10 slices) at the in-flow and out-flow ends.

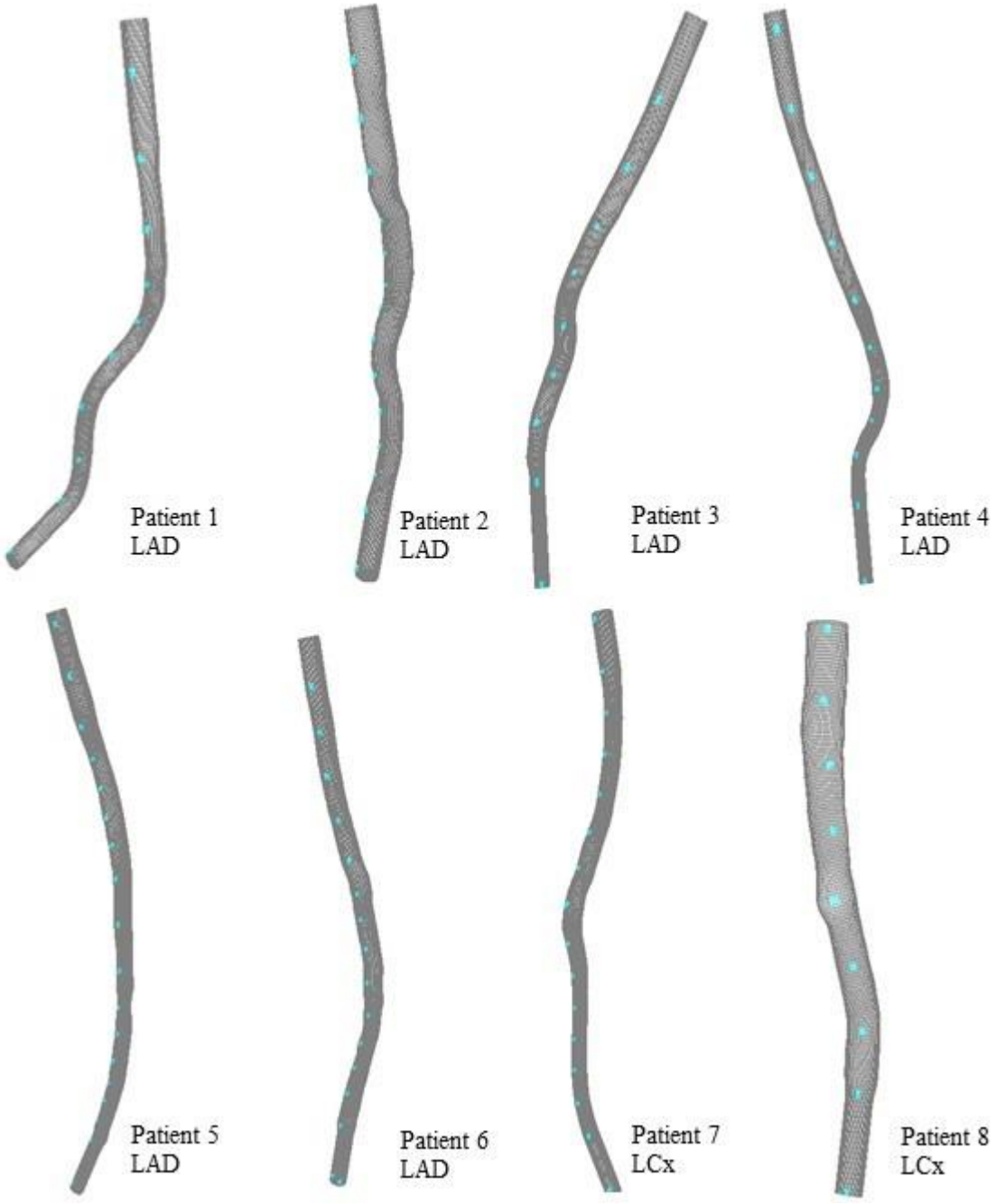

Figure 3.1 Reconstructed 3D geometry of each coronary vessel (blue colour indicates the location of bending displacement)

The blue colour in Figure 3.1 indicates the gasket layers on the outer surface, where dynamic displacement loading was applied to simulate the vascular bending.

Figure 3.2 illustrates the solution times for the six different modelling strategies. For each 2D or 3D model, a total number of 841 VH-IVUS slices were simulated for the eight patients, and each patient has a median of 101.5 [74.0, 131.5] VH-IVUS slices. Among all simulated slices, 554 slices were used in statistical analysis after removing slices with small plaque burden (PB<40%) and outlying PSS (PSS<$Q1$-2×IQR or PSS>$Q3$+2×IQR). The fully coupled FSI obtained solution in 1895 [1439, 2484] minutes, one-way FSI in 295 [237, 419] minutes, structure only 3D FEA in 126 [111, 191] minutes, 2D structure-mesh FEA in 1.53 [1.23, 1.90] minutes, 2D free-mesh FEA in 13.95 [9.05, 23.50] minutes and CFD in 121 [98, 162] minutes. The solution time for 3D FEA is significantly longer than for 2D FEA ($p < 0.001$).

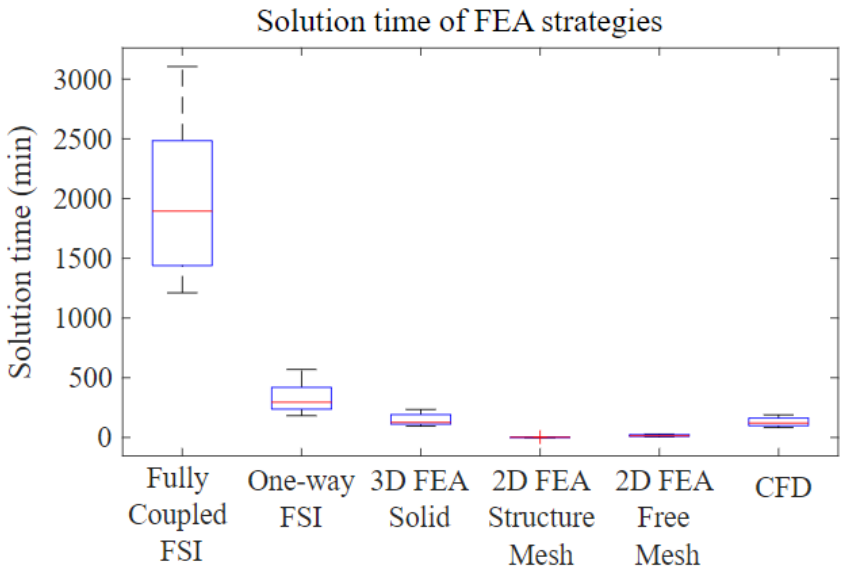

Figure 3.2 Solution time of different FEA strategies (n=8)

Figure 3.3 demonstrates the fluid parameters in a fully coupled FSI simulation. The luminal geometry and WSS were calculated at the time of maximum periluminal PSS, and the

TAWSS, OSI and RRT were calculated for the last cardiac cycle of the simulation.

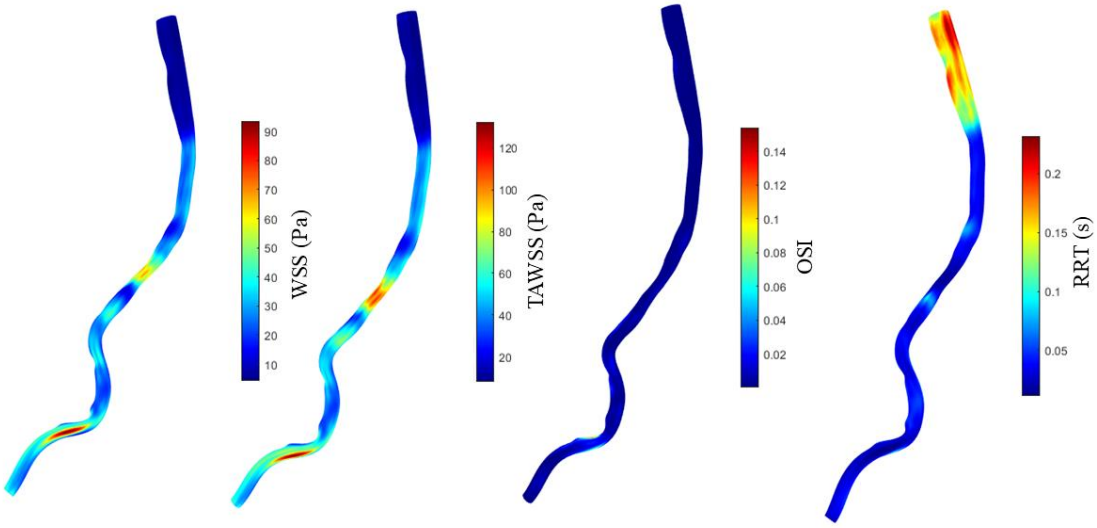

Figure 3.3 Luminal WSS, TAWSS, OSI, RRT of Patient 1

A cross-sectional plot (Figure 3.4) shows the VH-IVUS image, mesh and simulated PSS values for each model. The arrows illustrate the location and value of the maximum peri-luminal PSS. The peri-luminal lipid region in the structure mesh was removed from the

statistical analysis.

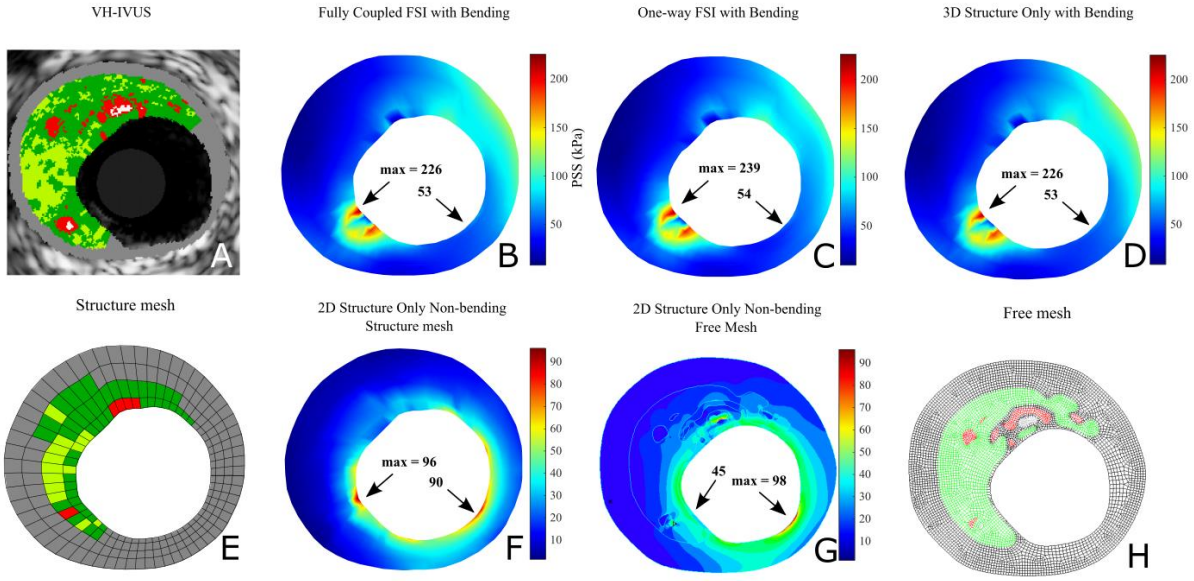

Figure 3.4 Comparison of mesh and PSS (unit: kPa) of different computational strategies

With the fully coupled FSI results as the gold standard, Bland-Altman analysis was used to assess the agreement between different models (Figure 3.5). The median percentage difference is shown as the solid line, and the 1.5 *IQR* ranges are shown as dash lines. The Wilcoxon sign rank test compared the distribution of the features from the two models, and the p-values are reported in the figure. For the solid analysis, the maximum peri-luminal PSS values of each model/slice were compared to those from the fully coupled FSI model. For fluid analysis, the fluid simulation of one-way FSI is equivalent to the fluid only CFD. Only the two FSI fluid results were independent, and the Bland-Altman analysis was applied between the fluid features (maximum peri-luminal pressure, TAWSS, RRT, OSI) from the fully coupled and one-way FSI models. Figure 3.6 illustrates the Bland-Altman plot for the maximum peri-luminal MSS and MPS.

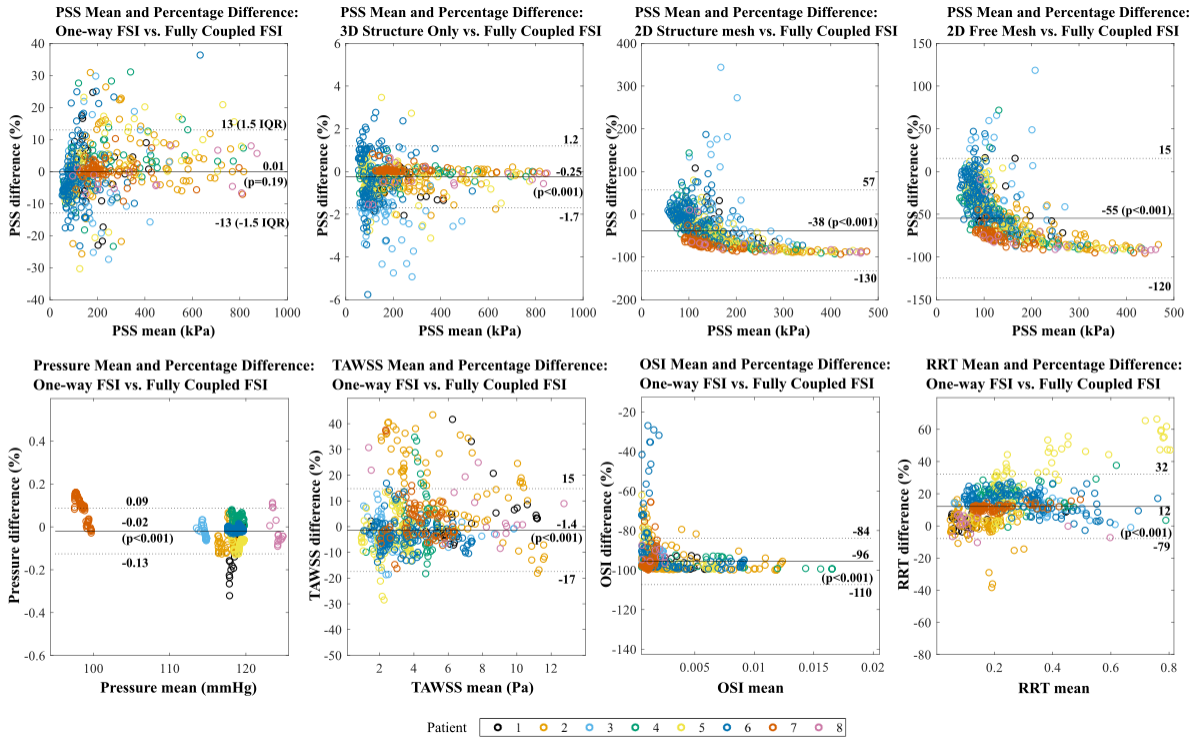

Figure 3.5 Bland-Altman plot of PSS and haemodynamic parameters in different computational strategies

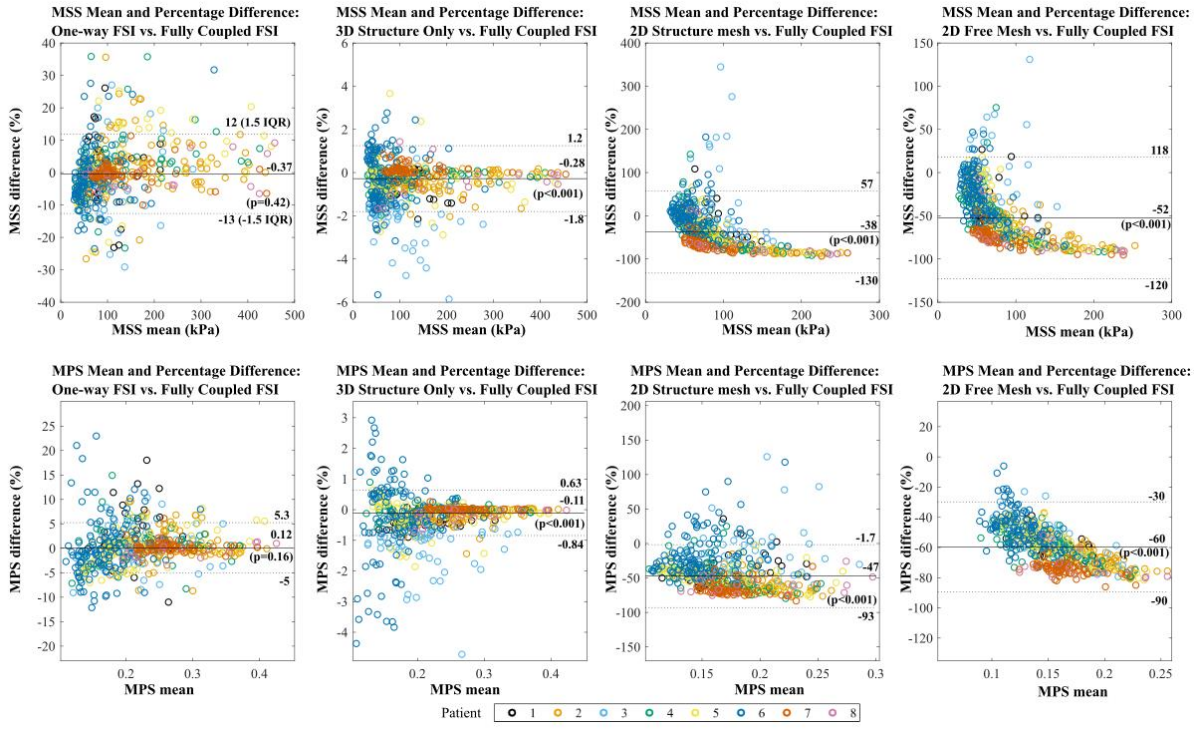

Figure 3.6 Bland-Altman plot of MSS and MPS in different computational strategies

In addition to the fluid feature agreement, the pressure difference and the average pressure gradient across the ten analyzed plaques were calculated (Figure 3.7). For the fully coupled FSI model, the pressure difference was -1.24% [-1.70%, -0.53%], and the pressure gradient was -0.06 [-0.12, -0.03] mmHg/mm. For the one-way FSI model, the pressure difference was --1.28% [-1.70%, -0.58%], and the pressure gradient was -0.06 [-0.12, -0.03] mmHg/mm. The Wilcoxon test report no significant difference between the pressure differences or the pressure gradients.

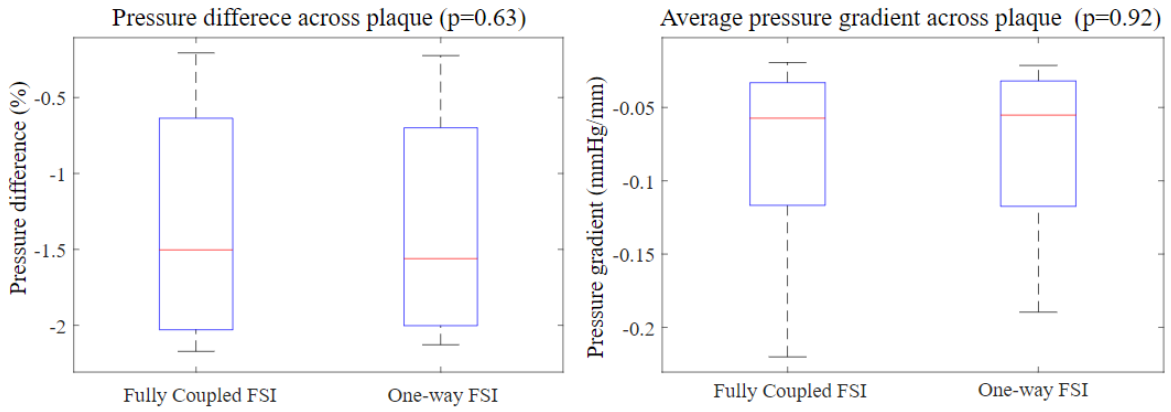

Figure 3.7 Comparison of pressure difference and average pressure gradients across plaques

3.4 Discussion

A major difficulty in the vascular biomechanical study is the lack of a gold standard to validate the simulation results. Direct measurement of vascular stress or strain with reasonable accuracy is infeasible with current technology. In the physiological environment, the fluid domain (blood) and the solid domain (vascular tissues) exert and respond to forces between each other simultaneously. The incorporation of mechanical behaviours in the fluid and solid domain is a typical interaction modelled by the FSI technique. The accuracy of the fully coupled FSI model has been experimentally validated in cardiac analysis[116] and is often regarded as the gold standard in vascular biomechanical studies[111,112,129]. The fully coupled FSI accurately simulates the interaction between the fluid and the solid model, at the cost of dramatically increased solution time (Figure 3.2). In addition, the iterative interaction introduced a convergence challenge because the numerical errors could accumulate and be amplified during the iterative

interaction. The manual diagnosis and solution of FSI convergence failure can be difficult and require a long feedback time due to computational complexity. The lengthy solution time (>24 hours) and convergence problem make the fully coupled FSI less suitable in clinical practice.

The one-way FSI model simplifies the interaction by allowing only one interaction from the fluid to the solid simulation. The fluid simulation in one-way FSI is no different from a CFD analysis with a rigid arterial wall. The accuracy of the one-way FSI relies on the assumption that the structural deformation is small and negligible. This assumption is violated in the coronary model, where biological tissue (such as plaque components and arterial walls) are highly deformable. The structural deformation is large due to cardiac motion and pulsatile blood pressure. Although the one-way FSI model reduced solution time by more than six-fold, it introduces an error of ±13% in the estimated PSS (-13%-12% in estimating MSS, -5%-5.3% in estimating MPS) when compared to the fully coupled FSI model (Figure 3.5, Figure 3.6). The percentage difference of the one-way FSI model was not biased and centred near zero in the Bland-Altman plot, which is consistent with the cross-sectional plot. The PSS distribution from the fully coupled FSI is similar to that from the one-way FSI (Figure 3.4 B, C). The location of maximum peri-luminal PSS (over slice) coincides in the two models, and the one-way FSI model overestimates the PSS value by 5.8%.

The structure only 3D FEA model ignored the fluid interaction and used a spatially uniform pressure to model the fluid behaviour. The solution time is further reduced to about two hours. We found a percentage difference of -1.7%-1.2% in the estimated maximum peri-luminal PSS values (-1.8%-1.2% in estimated MSS, -0.84%-0.63% in estimated MPS). The percentage differences are slightly biased, indicating a small underestimation in the structure only 3D FEA model. The Bland-Altman plots for the one-way FSI and the structure only 3D FEA models indicate a large variation of percentage difference at low stress/strain. Despite the influence from individual patients (e.g. patient 6), the variation could relate to the non-uniform distribution of stress/strains. Slices with low stress/strain were more common in the simulations and were oversampled in the Bland-Altman plots. The variation could also indicate a non-linear relationship in the agreements of mechanical features generated from each model. The current theory and studies[74,102] associate plaque rupture with high PSS, which is less affected by the errors due to different computational strategies.

Compared to the one-way FSI model, the structure only 3D FEA model had a better agreement with the fully coupled FSI model and achieved the solution in the shortest time among the 3D

models. The structure only 3D FEA model could serve as an alternative to the fully coupled FSI in estimating plaque structure stresses/strains within a reasonable solution time.

We found a large difference between the 3D fully coupled FSI model and the 2D models. Both 2D models show a significant underestimation of the estimated stresses and strains. PSS was underestimated by 38% in the 2D structural-mesh model and 55% in the 2D free-mesh model. The percentage differences were strongly biased, and the agreement with the 3D fully coupled FSI model was poor. The free-mesh model better represented the 2D plaque morphology, but the mesh difference compared to the 3D fully coupled FSI model increased the relative errors of mechanical results. The location and magnitude of maximum peri-luminal PSS were changed in simulation with the free mesh (Figure 3.4 G). Our finding is inconsistent with other studies that reported overestimated stresses and strains in the 2D FEA model[112,130]. The discrepancy is related to the modelling of coronary bending. The inclusion of patient-specific bending increased the magnitude of estimated stresses and strains in the 3D models. The magnitude of underestimation due to patient-specific bending is greater than the differences due to the modelling strategy (2D/3D), indicating the importance of patient-specific bending in coronary FEA simulations. Although efficient in modelling and computation, the 2D FEA produces large errors in coronary FEA due to the oversimplification of axial stress and coronary bending.

For fluid simulation, we compared the fluid features from the fully coupled FSI model and the one-way FSI model (equivalent to fluid only CFD). We found good agreement and very little difference in the estimated maximum peri-luminal pressure (-0.13%-0.19%) and a modest difference in the TAWSS (-17%-15%). The pressure and TAWSS were both slightly biased and underestimated in the one-way FSI model. The percentage differences in OSI were -96% (-110% - -84%), and were strongly biased. The difference in modelling strategies can explain the large underestimation of OSI. In the one-way FSI model, the fluid was bounded by a rigid and static fluid-solid boundary, and the boundary deformation was neglected. In the fully coupled FSI model, the fluid-solid boundary was deformed by the interaction at each time point. The deformation resulted from the hemodynamic forces and the cardiac motion (bending displacement) exerted on the solid model. Large and cyclic deformation of the boundary produced oscillation of the estimated WSS. The cyclic bending displacement introduced a strong oscillatory factor to the model and significantly increased the OSI magnitude in the

fully-coupled FSI model. Figure 3.3 also illustrates the influence of bending on OSI. The high OSI is concentrated in the region with large bending displacements. The RRT calculated from the OSI and the average WSS also had a large percentage difference of -79%-32%, although the difference was less biased.

The computed fractional flow reserve (CFFR) derived from the estimated distal and proximal blood pressure reflects the functional impact of coronary stenosis and has been shown to have clinical benefits in risk stratification[40]. To partially reflect the functional impact of the analyzed plaques, we calculated each plaque's pressure difference and pressure gradient. The magnitude for pressure differences (-1.2%) and gradients (-0.06 mmHg/mm) was small, and there was no significant difference between the results estimated from the two fluid models. However, a major difference between the models in this study and the models in CFFR analysis is the inclusion of sub-branches. Due to flow distribution between different branches, the pressure difference across stenosis would be larger and more accurate in the model with sub-branches[131]. Moreover, our results indicate that the fluid-solid interaction and bending have little impact on the pressure difference and pressure gradient estimation when sub-branches are ignored.

The comparison of fluid features suggests that for a coronary model with no sub-branch, the difference in modelling strategy has little impact on the pressure and pressure gradients, modest impact on TAWSS calculation, and strong influence on oscillatory features when bending displacement is included.

In Summary, we compared the accuracy and efficiency of different modelling strategies for coronary FEA models without sub-branch. The 3D one-way FSI showed modest agreement in the structural features and required a long solution time. The 3D structure only FEA had good agreement with the 3D fully coupled FSI in estimating the stresses and strains, and can be regarded as an alternative model with high computational efficiency. The 2D models failed to accurately model the stress and strains when patient-specific coronary bending is included. The modelling strategies and bending have little impact on the estimated pressure, modest impact on TAWSS and significant impact on the oscillatory fluid features.

Chapter 4The influence of patient-specific bending in finite element analysis and vulnerability assessment of coronary atherosclerotic plaques

4.1 Introduction

In FEA, the accuracy of the numerical simulation depends on the model's reliability, including the material property, model geometry, and loading environment (boundary condition). A more realistic model would improve the accuracy and predictive power of the estimated mechanical features in the plaque vulnerability assessment. Unlike most vessels in our body, coronary vessels are attached to the constantly moving epicardial surface, creating a unique bending environment that could significantly change the mechanical feature estimation. Due to anatomical and heart rate differences, the pattern and magnitude of coronary bending vary between and within patients. In this study, we performed 3D FEA (fully coupled and structure only) to the coronary vessels of eight patients to assess the influence of patient-specific bending in biomechanical simulations, and to explore the relationship between bending mechanical features and the morphological risk factors.

4.2 Materials and Methods

The image acquisition, vascular geometry reconstruction, mesh generation and the fully coupled FSI modelling processes were described in Chapter 3.2. The boundary conditions (e.g. bending displacements) were modified in this study.

In order to mimic the impact of myocardium contraction on the mechanical environment in plaque, the displacements extracted from the DSA images were used as one of the loading conditions and applied to the outer wall of the coronary artery, and were separated by every ten slices. Because the coronary vessels were attached to the epicardial surface, the bending displacement was applied to the epicardial surfaces. The epicardial surfaces were defined as the outer circumferential surfaces that were closest to the cardiac centre. To attenuate stress concentration near the location where the displacement loading was applied, the surfaces were extended by including two adjacent surfaces in the circumferential direction, and an additional layer of hexahedral elements was created as gaskets for loading.

The bending displacement of coronary vessels shares a common bending pattern because of anatomical similarities. For the LAD arteries, an average bending profile was generated to investigate the influence of the bending patterns and their commonality on the biomechanical analysis. The relative distance to the left main artery aligned the six LAD central lines, and the averaging of displacements for each section constituted the average bending profile. A linear interpolation of the average bending profile provided the average bending displacement for each artery. The fully coupled FSI models with the average bending displacement were simulated to obtain the mechanical features under the average bending.

In order to investigate the sensitivity of biomechanical features to the magnitude of bending displacement, we performed the fully coupled FSI simulation with 50% of patient-specific bending displacement. In total, four fully coupled FSI models were created with the same coronary mesh, and with no bending, 50% patient-specific bending, average bending, and full patient-specific bending.

A mixed effect model fitted by restricted maximum likelihood was used to evaluate the influence of bending on FEA simulation, and the fully coupled FSI model with bending was used as the gold standard. The unpaired Mann-Whitney test was used for comparing unpaired variables with non-normal distribution. The paired Wilcoxon signed-rank test was used for

comparing paired variables with non-normal distribution. Variables with normal distribution were reported as mean [95% confidence interval], and variables with non-normal distribution were reported as median [1st and 3rd quatile]. A significant difference was assumed if $p < 0.05$, and the p-value was corrected by the Bonferroni criteria for multiple comparisons.

4.3 Results

Among the analysed eight patients, six patients had LAD stenosis, and two patients had LCx stenosis. Two of the LAD patients had culprit lesions. The average diastole blood pressure of the patients is 67.4 [57.9, 76.9] mmHg, average systole blood pressure is 115.8 [104, 127.6] mmHg. In total, 841 VH-IVUS slices were simulated for the eight patients, and each patient has a median of 101.5 [74.0, 131.5] VH-IVUS slices. Among all simulated slices, 554 slices were used in statistical analysis after removing slices with a small plaque burden and outlying PSS.

Table 4.1 Patient index and physiological information

Patient index	1	2	3	4	5	6	7	8
Vessel category	LAD	LAD	LAD	LAD	LAD	LAD	LCx	LCx
Culprit	No	Yes	Yes	No	No	No	No	No
Blood pressure (mmHg)	61/120	76/119	65/115	80/120	80/120	80/120	60/100	75/125

The temporal mean and standard deviation of the central line curvature was calculated for each

analysed vessel (Figure 4.1). The curvatures were aligned according to the anatomical markers for comparison (diagonal branches for LAD, obtuse marginal branches for LCx). The coefficient of correlation was calculated for the mean and standard deviation of curvature.

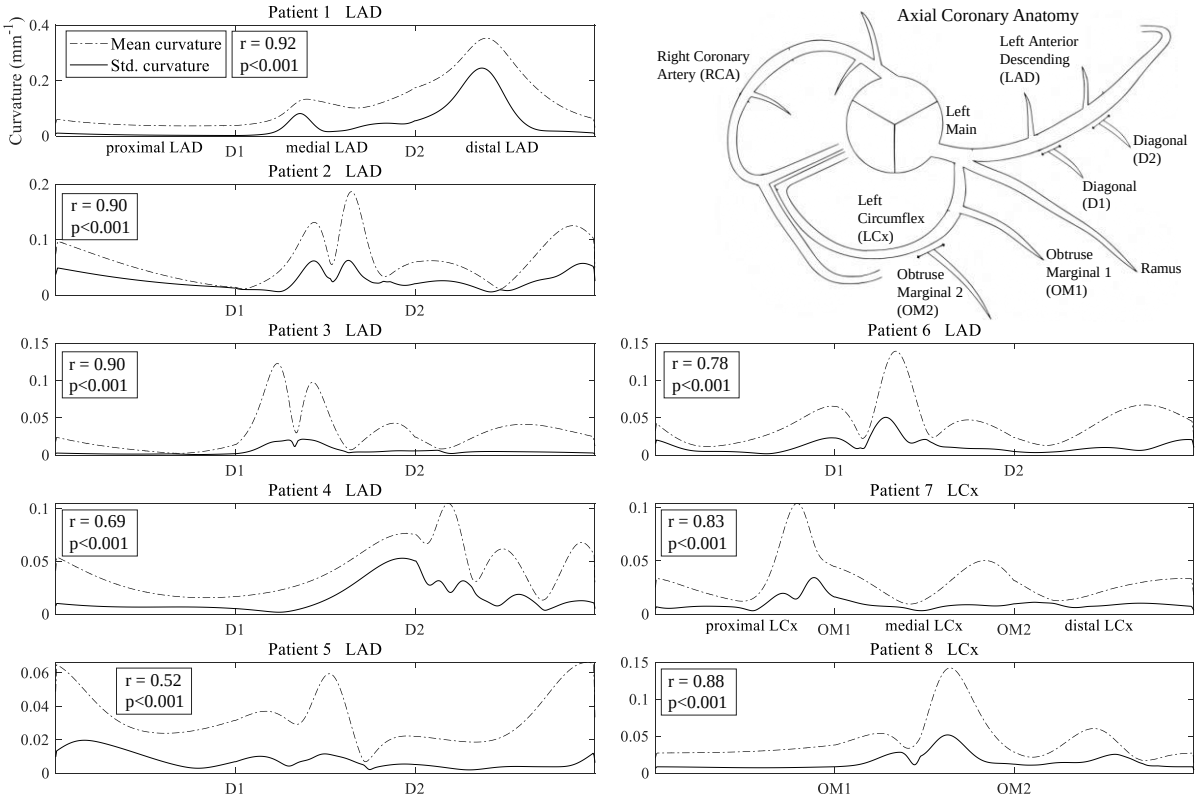

Figure 4.1 Mean vessel central line curvature and standard deviation of central line curvature (*r*: coefficient of correlation of curvature mean and standard deviation, *p*: *p*-value of *r*)

To assess the influence of bending on FEA simulation, the peri-luminal mechanical features were calculated for each slice, including the plaque structural stress (PSS), maximum shear stress (MSS), maximum principal strain (MPS), fluid pressure, time-averaged wall shear stress (TAWSS), oscillatory shear index (OSI), and relative residence time (RRT). For comparison, the logarithmic ratio of mechanical features was calculated as:

$$feature_{ratio} = log_{10}(\frac{feature_{FSI\ non-bending}}{feature_{FSI\ bending}}) \quad 4.1$$

A mixed effect model was fitted to each mechanical feature, with the patient and vessel category (LAD/LCx) as the random effect variable. The estimated fixed intercept and its *p*-

value were illustrated in Figure 4.2. A logarithmic feature ratio of 0 indicates no difference between the bending and non-bending model.

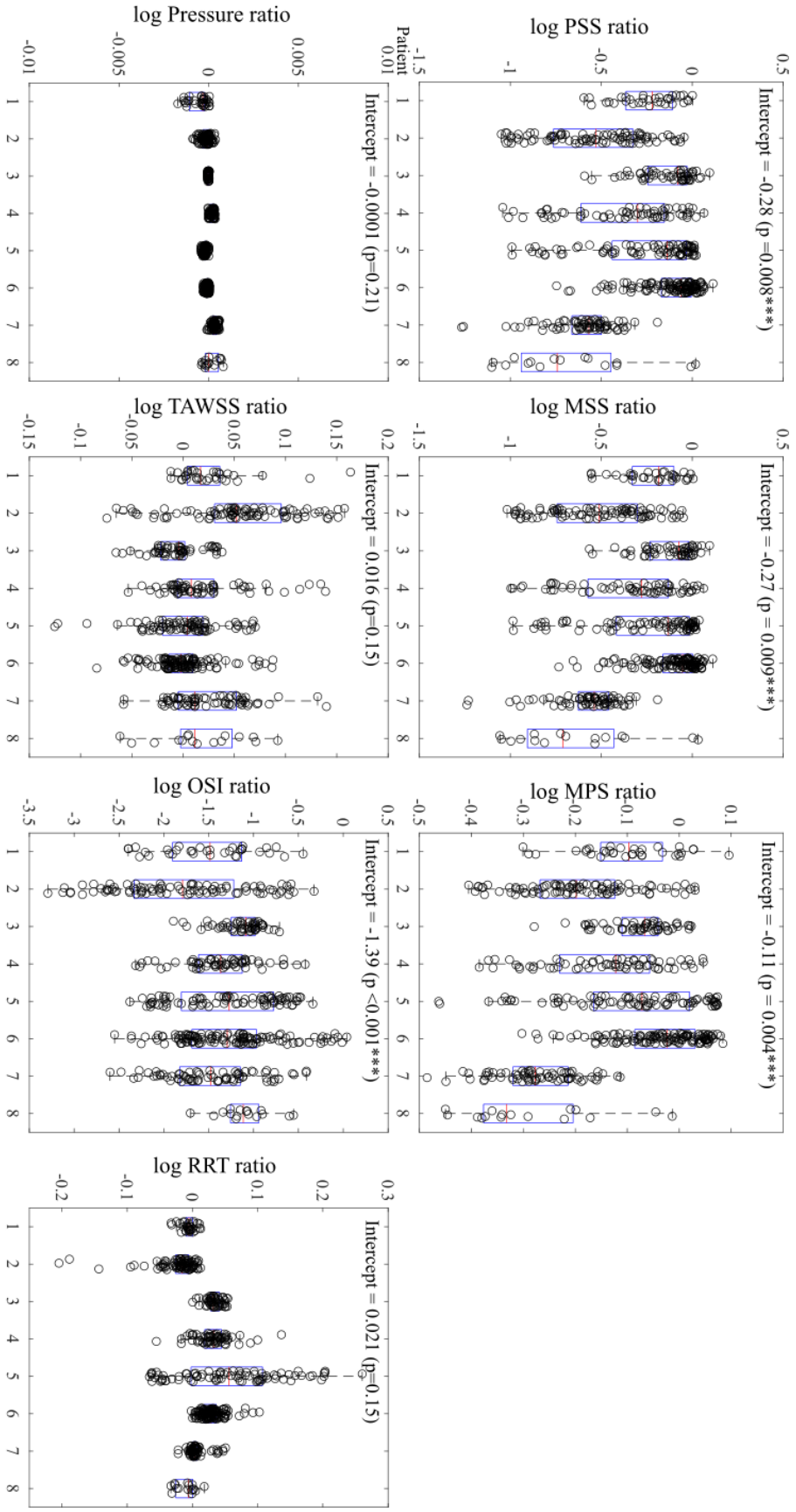

Figure 4.2 Logarithmic ratio of mechanical features (Bending v Non-bending)

Similarly, the mechanical feature ratio between FEA models with patient-specific bending and with average bending was defined as :

$$feature_{ratio} = log_{10}(\frac{feature_{FSI\ avg-bending}}{feature_{FSI\ bending}}) \quad 4.2$$

Figure 4.3 illustrates boxplots of the logarithmic ratios and the intercepts estimated by the

mixed effect model.

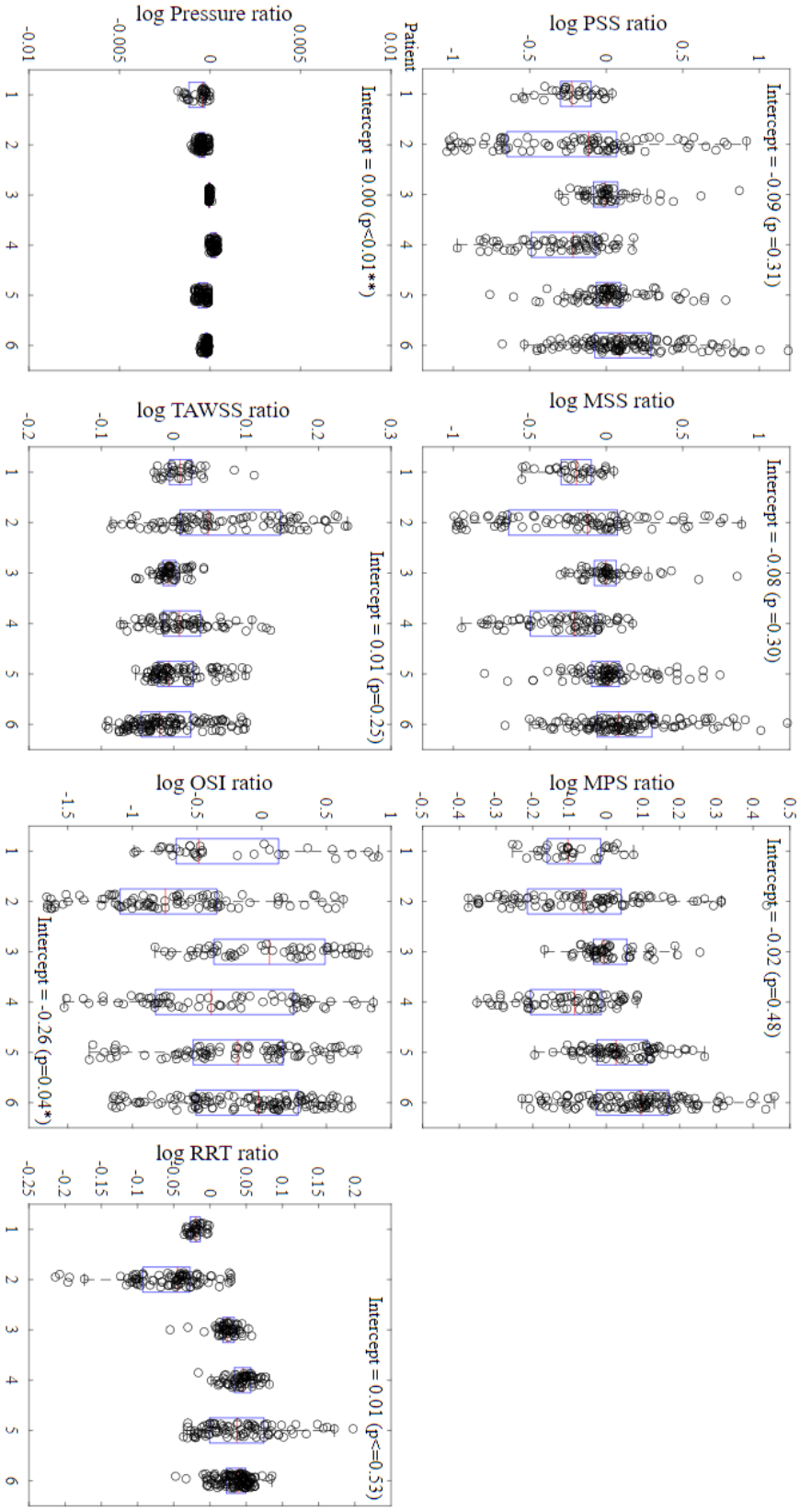

Figure 4.3 Logarithmic ratio of mechanical features (Bending vs Average bending)

Figure 4.4 compares the estimated biomechanical features in FEA models with full patient-specific bending, average bending, 50% patient-specific bending and no bending. Compared to the model with full bending, all other models show significant differences in the predicted mechanical features, except MPS in the average bending model. Table 4.2 reports the percentage difference of mechanical features under different bending conditions. The fully coupled FSI with a full patient-specific bending model was used as the reference.

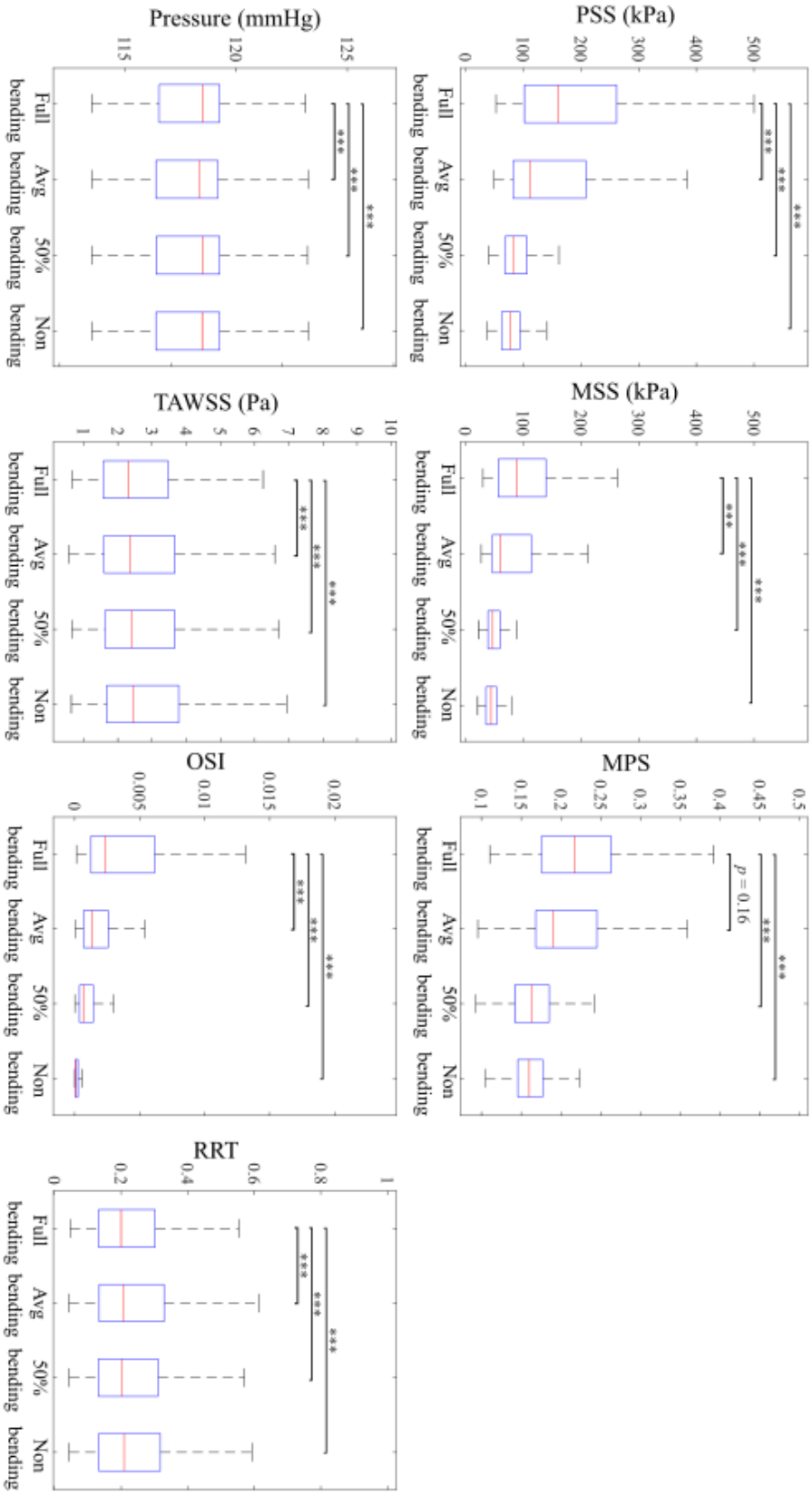

Figure 4.4 Comparison of biomechanical features with different bending models (p<0.001 ***, p<0.01 **, p<0.05 *)

Table 4.2 Percentage (%) difference of mechanical features with different bending models

	Average bending	50% bending	No bending
PSS	-45.0 [-8.6, 24.0]	-64.1 [-40.6, -12.1]	-72.0 [-46.3, -13.7]
MSS	-42.3 [-7.9, 22.1]	-63.3 [-39.1, -9.2]	-70.0 [-43.7, -11.4]
MPS	-21.7 [-2.6, 22.7]	-38.5 [-19.6, -5.6]	-40.7 [-23.2, -6.1]
Pressure	-0.08 [-0.03, 0.001]	-0.03 [-0.01, 0.01]	-0.04 [-0.01, 0.01]
TAWSS	-3.2 [1.4, 7.7]	0.8 [3.7, 7.6]	0.1 [4.4, 10.7]
OSI	-77.7 [-62.4, 38.0]	-76.1 [-71.7, -64.2]	-98.2 [-95.3, -90.0]
RRT	-2.5 [4.1, 10.5]	-1.3% [0.9, 4.3]	-0.8 [3.6, 8.8]

The logarithmic PSS percentage difference was calculated as:

$$PSS\ difference = log_{10}(\frac{PSS_{bending} - PSS_{non-bending}}{PSS_{non-bending}} \times 100\%)$$

A mixed linear effect model was fitted between the PSS difference and morphological factors, with the patient and vessel category as the random effect variables. The estimated fixed intercepts and slopes were illustrated in Figure 4.5, together with the *p*-values after Bonferroni correction for multiple testing.

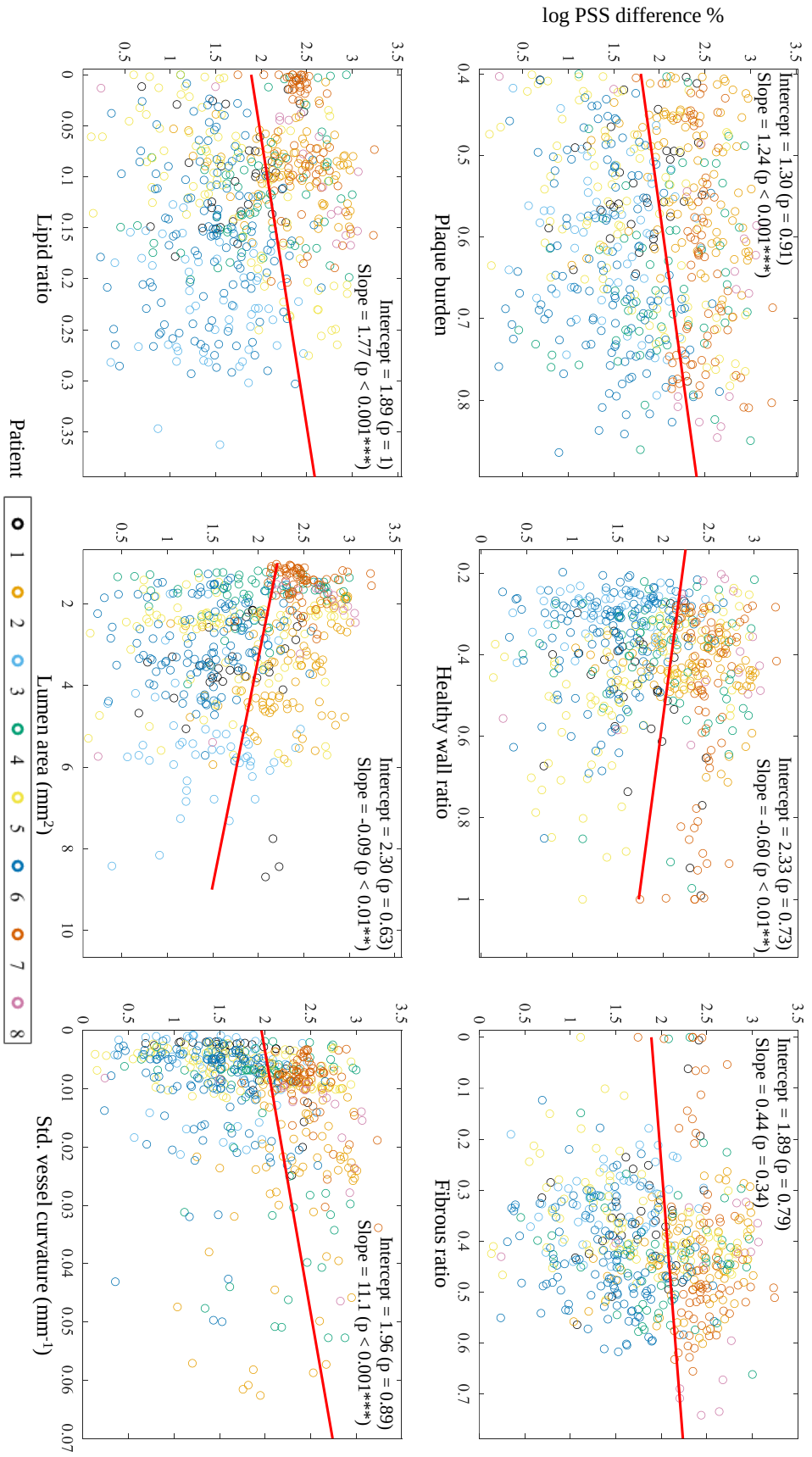

Figure 4.5 Percentage PSS difference (logarithmic) and plaque morphology

For each patient, the peri-luminal PSS values were separated into two groups according to the morphological risk factors (PB > 70%, MLA < 4 mm^2 , and VH-TCFA). The Mann-Whitney test was used to compare the difference between PSS in the low-risk group and the high-risk group (Figure 4.6).

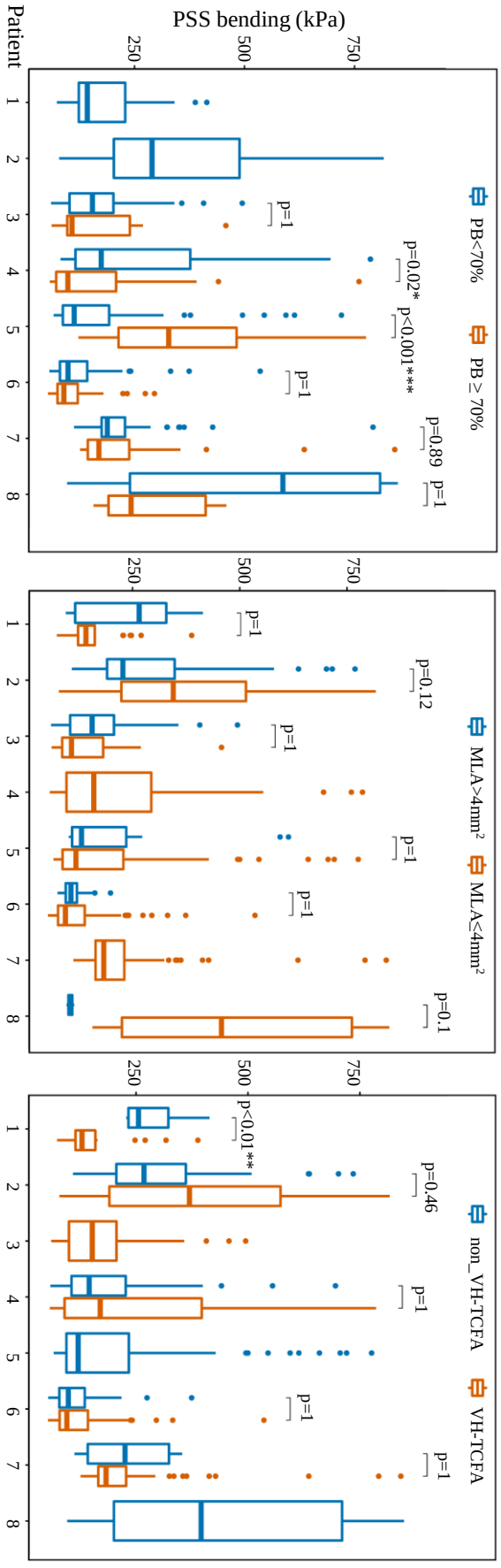

Figure 4.6 Comparison of PSS with morphological risk factors

To investigate the longitudinal distribution of risk factors along the vessel, a binary risk map was generated for each analysed vessel. Morphological risk factors (PB > 70%, MLA < 4 mm^2, VH-TCFA) and high PSS regions (PSS > 250 kPa) were identified in a longitudinal stack (Figure 4.7).

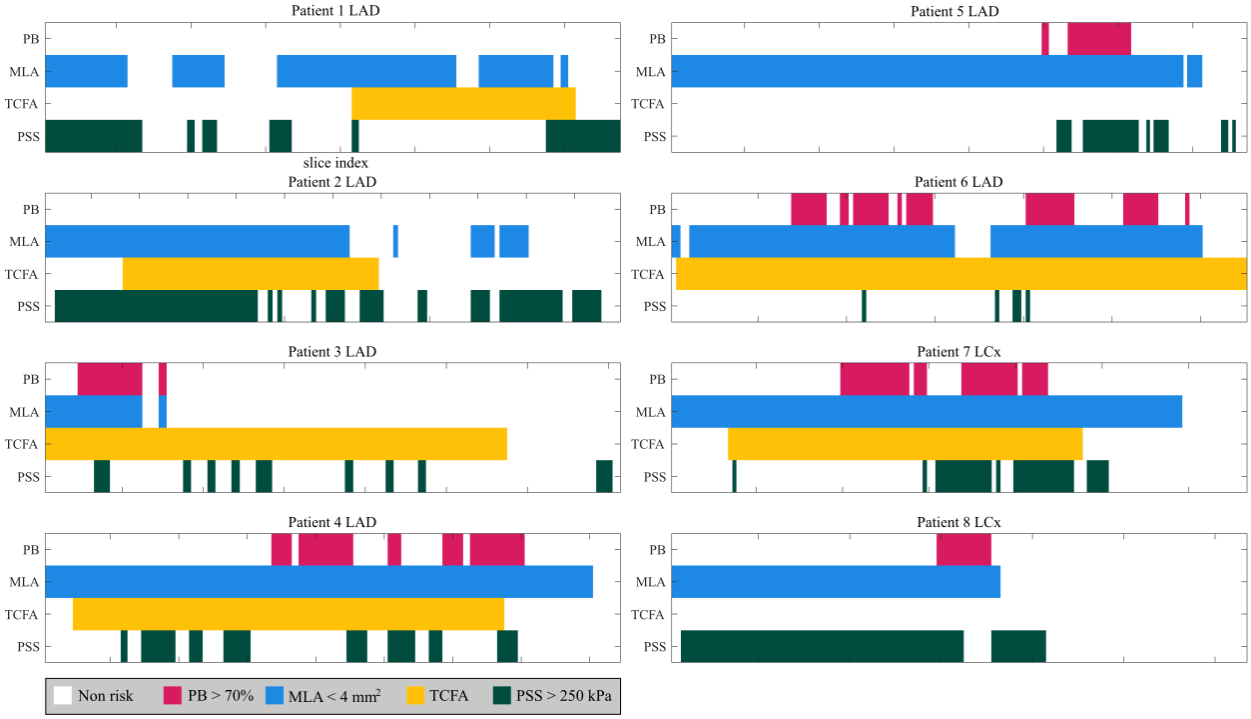

Figure 4.7 Longitudinal location of morphological risk factors and high PSS region

4.4 Discussion

The never-resting cardiac motion makes the coronary artery a unique vessel that experiences continuous and complex mechanical loading. The quantification of coronary geometry and bending movements may help us understand the role of bending in the pathophysiology and vulnerability assessment of coronary atherosclerosis. The measured coronary mean curvature and bending (defined as the standard deviation of curvature) varied between patients and between different coronary vessels (LAD vs LCx, Figure 4.1). For LAD, the proximal LAD

sections closed to the aortic root are less curving and experience less bending. The peak temporal mean curvature and bending are usually located at the medial or distal sections, where the artery is reaching the ventricle and apex with large movements and a large perfusion area. The LCx extends in the circumferential direction, where the radius of curvature is smaller than in the apex direction. The peak temporal mean curvature and bending for LCx locate closer to the proximal end. Despite variation in the peak location, the mean curvature and bending show a good correlation in all vessels (average $r = 0.80$ [0.69, 0.92]). The correlation between mean curvature and bending may implicate bending as a potential factor in the angiogenesis and remodelling of coronary arteries. The vessel curvature may help us estimate the cardiac and vessel movement in the absence of time-series images (e.g. for CT angiography).

The bending of coronary arteries also influenced the mechanical features predicted in the FEA. The logarithmic ratios of solid mechanical features (PSS, MSS, and MPS) in the bending and non-bending FSI models were significantly lower than zero (Figure 4.2). The negative ratios indicated the model without bending significantly underestimates the solid mechanical features. The absence of bending underestimates the PSS and MSS by about 48%, and MPS by about 23%. Compared to the LAD (patients 1-6), the solid mechanical features were further underestimated for LCx (patients 7, 8). Compare to the coronary PSS reported in other fully coupled FSI studies with bending (80-138 kPa)[69,81,127], the average PSS in this study is higher (165 kPa). In a comparative study of fully coupled FSI models with and without bending, Wang et al. reported a PSS difference of 11.5%[112], which is lower than the 72% difference in this study. The difference between PSS magnitude and PSS difference may relate to the application of patient-specific bending displacements. Wang's study uses a non-patient-specific bending that bends the vessel into a v-shape geometry. The patient-specific bending in this study was applied to gasket layers along the vessel's outer wall, and better represented the real loading environment. However, the patient-specific loading might also constrain the models and caused stress concentration and elevated PSS. To account for the residual stress in the vessel, Wang's study used a circumferential shrinkage method, instead of the radial shrinkage used in this study. Because of computational complexity in 3D FEA, the proper shrinkage method of the 3D coronary model is undeveloped. Both Wang's and this study indicate a significant PSS difference and a necessity of shrinkage in the 3D FEA of coronary simulations.

Unlike in the solid mechanical features, the influence of bending in the fluid mechanical features was limited for most of the features. Because no sub-branch bifurcation was

considered in the vascular model, pressure in the fluid model was dominant by the inlet and outlet pressure profile. The pressures for the two models were derived from the same coronary blood pressure profile, and therefore the pressure features from the two models showed little differences. With similar pressure and fluid properties, TAWSS was dominant by the geometry of luminal surfaces. The patients with lower underestimated deformation (lower MPS ratio, patients 2, 7, 8) experienced higher overestimation of TAWSS. Unlike the temporal averaged features, OSI reflects the oscillatory property of the wall shear stress. The cyclic bending introduced a strong oscillatory factor to the model and dramatically increased the OSI value. The OSI value was significantly underestimated in the non-bending model (95%). The RRT was calculated from the OSI and averaged WSS, and was less affected by bending since the magnitude of OSI was small compared to the averaged WSS.

The 4D vessel bending may not always be available in clinical practice. Due to anatomical similarity, vessels from the same anatomical location share similar bending patterns. The common bending pattern may serve as a substituted bending when patient-specific bending is not available. We investigated the influence of an averaged bending on predicting mechanical features for the six LAD vessels. The logarithmic feature ratios in Figure 4.3 indicates that the solid mechanical features were underestimated (PSS: 19%, MSS 17%, MPS: 5%). Compared to the model without bending, the inclusion of an averaged bending reduced the underestimation of solid mechanical features by 60%-80%. For the fluid mechanical features, the pressure and TAWSS ratios were less affected and had little difference compared to the model with patient-specific bending. The OSI was sensitive to oscillatory bending and was underestimated by 45% with the average bending. Compare to the model without bending, the inclusion of an averaged bending reduced the underestimation of OSI by 53%. However, because the sample size for the average bending models was relatively small (n=6), there was no statistical significance for the estimated ratio intercepts of PSS, MSS, MPS, TAWSS and RRT. A larger sample size is necessary to validate the performance of average bending in the prediction of mechanical features with FSI.

The relationship between displacement loading and estimated mechanical features is non-linear. The mechanical features' sensitivity to bending varied with different bending magnitudes (Figure 4.4). Despite a significant difference, the non-oscillatory fluid features were insensitive to the change of bending magnitudes, and have a small percentage difference compared to the

reference values (Table 4.2). The solid features and OSI showed large and non-linear variations with different bending magnitudes. Less variation between the non-bending and 50% bending indicates the solid features were less sensitive to bending at low magnitude. The increment of bending beyond 50% significantly increased the estimated stress and strains in the solid model. The average bending model showed the least feature differences among the three partially bent models. This indicated that the magnitude of bending could be more important than the bending profile in accurately estimating the mechanical features. The magnitude of bending can be estimated through non-invasive imaging techniques such as multi-phase CCTA. On the other hand, the estimation of the bending profile requires continuous imaging of coronary geometry and is difficult to achieve in practice. The sensitivity of mechanical features to bending magnitude implicates that a generic bending profile adjusted to a patient-specific bending magnitude could serve as a substitute bending source in coronary simulations. Due to the computational complexity of the fully coupled FSI models, the bending sensitivity comparison was performed only between models with 0%, 50% and 100% bending. The further assessment of bending sensitivity and the quantification of errors due to bending would require simulations with smaller intervals of bending magnitude.

In summary, the inclusion of bending in the single tube models significantly increased the solid mechanical features and the oscillatory fluid features. In contrast, the non-oscillatory mechanical features were less affected. The inclusion of an average bending profile reduced the magnitude of underestimation caused by the lack of bending and can serve as a substitute in the absence of patient-specific bending.

Although the inclusion of bending increased the PSS, the amount of PSS difference due to bending varied at locations with different plaque morphology. To investigate the influence of morphology on PSS difference, Figure 4.5 illustrates the linear correlation between morphological features and the PSS difference due to bending. We found no significant intercept, indicating the magnitude of PSS differences varies between patients. We found significant fixed effect slopes for plaque burden, healthy wall ratio, lipid ratio, luminal area and standard deviation of curvature (bending). Inclusion of bending created a larger PSS difference at a location with a high plaque burden, low healthy wall ratio, high lipid ratio, smaller luminal area and strong bending. These morphological features coincide with features of a diseased plaque, highlighting the importance of bending inclusion for PSS calculation at a diseased plaque.

2D PSS has shown to have additional predictive value for the plaque vulnerability assessment when combined with the morphological risk factors (PB > 70%, MLA < 4 mm^2, VH-TCFA)[75]. PSS calculated from the 3D FSI with bending was compared with the morphological risk factors in all patients (Figure 4.6). We found two patients (patients 4, 5) with significant yet contradicting PSS differences between the plaque burden risk groups, and one patient (patient 1) with significantly lower PSS in the TCFA group. No significant PSS difference was found in the other risk factor groups of each patient. There was no consistent group correlation between PSS and the morphological risk factors, making 3D PSS a distinct risk factor from the morphological risk factors.

Although we found no group correlation, the PSS may associate with the morphological risk factors in longitudinal locations. Figure 4.7 illustrates a binary risk factor map for the morphological risk factors and the high PSS risk factor (defined as regions with PSS > 250 kPa). The high PSS risk factor often appears where the morphological risk factor is changing. Among the 40 identified morphological risk factor changes (shoulder of the risk factor blocks), 25 (62.5%) changes are accompanied by the high PSS risk factor. The high PSS risk factor may indicate a potentially vulnerable site where the morphological risk factor is changing, and may improve the predicting accuracy by focusing on the morphologically risked lesion with high PSS.

In conclusion, the inclusion of bending in coronary FEA simulations significantly increased the value of solid mechanical features, and is more significant at a diseased plaque or strong bending. The PSS shows no consistent group correlation with the morphological risk factors, and the high PSS risk factor may associate with the shoulder region of morphological risk factors in the longitudinal direction. Further survival analysis with a larger population is necessary to assess the predictive power of the PSS risk factor in plaque vulnerability assessment.

Chapter 5 Hybrid bias correction of thoracic ZTE images and PET attenuation correction for lung region

The hybrid positron emission tomography (PET) and magnetic resonance (MR) system can provide functional and anatomical information simultaneously, reducing the scan time and minimising ionizing radiation exposure. Using different tracers, PET can quantitatively reflect the metabolism in patients with high sensitivity. Cardiac PET/MR with ^{18}F-fluorodeoxyglucose (^{18}F-FDG) tracer has shown incremental value in the evaluation of myocarditis[132]. The uptake of ^{18}F-FDG can quantitatively reflect the inflammation in carotid atherosclerosis plaques through its role in macrophage infiltration, which is a marker for vulnerable plaques[133]. ^{68}Ga-DOTATATE, a more specific tracer targeted at the somatostatin receptor 2 (SSTR-2), has shown an even stronger association with the cardiovascular risk factor[134] and potential in plaque vulnerability assessment. However, a major difficulty in the application of body PET/MRI is the accurate attenuation correction, which is critical for accurate PET quantification. A particular area of interest for PET/MRI attenuation estimation is the lung region, where current methods usually assign a population-based uniform attenuation coefficient. With the better characterisation of lung tissue in the ZTE images, we hypothesise that the ZTE images can be used to generate an attenuation map for the lung, and improve the performance of current MR attenuation correction algorithms in this area.

5.1 Attenuation correction in PET

Before each PET scan, a radiotracer is prepared by incorporating radioactive nuclides into biologically relevant molecules (such as glucose for ^{18}F-FDG). After administration to a patient, the radioactively labelled molecule participates in physiological processes within the human body and can be tracked through the detection of emitted radiation from the radionuclide by an external array of detectors. Therefore, PET can allow imaging of both the distribution and

concentration of the radiotracer inside the human body.

PET relies on the principle of radioactive decay and the emission of positrons (positive electrons) from the radiotracer. Following emission, the positron will travel a short distance in tissue before interacting with a nearby electron, resulting in the annihilation of both particles and the emission of a pair of 511-keV photons in almost opposite directions, which can be detected outside the body by the PET scanner. Given that the near-collinearity of the annihilation-photon pair provides a means for localising the position where the annihilation event occurred (i.e. the origin of the photons), the inherent relationship between the of number photons detected by the scanner and the activity of the radiotracer administered to the patient, one can process the data to reconstruct the distribution of the radiotracer inside the body.

As PET imaging involves the coincident detection of annihilation photons, physical effects causing these photons to deviate from their path must be estimated and compensated for an accurate estimate of the radioactivity distribution. Scattering and absorption lead to the attenuation of annihilation photons in tissue. As such, attenuation occurs when one or both photons interact with the material on their path and get absorbed or deflected off their original line of detection. Nevertheless, at 511 keV, the effect of photoelectric absorption is small, and the dominant interaction of photons in matter is Compton scattering, whereby a photon collides with an orbital electron causing the photon to deviate from its original path.

The probability that a photon will undergo interaction within an absorber material when travelling a unit distance through the medium is governed by the linear attenuation coefficient, μ, which is a characteristic of the medium. Assuming a narrow beam of photons with initial intensity I_o, the intensity at some distance x through the attenuating medium is given by:

$$I = I_o e^{-\mu x} \qquad 5.1$$

The attenuation coefficient is dependent on the electron density of the tissue and the energy of the photon. Since photons in PET have a characteristic energy, attenuation coefficients are only considered at 511 keV.

The attenuation of photons in the body varies strongly due to the presence of air, lung tissue, soft tissue and bone. Without attenuation correction, the reconstructed PET images contain

several image artefacts such as increased intensity near the body surface because of the short distance between the radiotracer and the detector, and prominent signal in a region with a low attenuation coefficient (e.g. the lung)[135]. Furthermore, small errors in estimating the attenuation correction factors may lead to significant qualitative and quantitative errors in PET images, and as such, attenuation is the most important correction required in PET imaging.

In PET/CT scanners, a CT scan is used to provide attenuation correction information. CT image intensity is related to the magnitude of X-ray attenuation within the body, and in turn also related to electron density. Since the annihilated photons with high energy in PET (511 keV) have a lower probability of being attenuated than the low energy X-ray photons (80–140 keV) in CT, a piecewise linear transformation (typically bilinear) is required to transform the CT Hounsfield units (HU) to the PET linear attenuation coefficient values. With the absence of a CT image in the PET/MR system, an attenuation map needs to be generated from the MR images. The MR based attenuation correction (MRAC) is challenging because there is no direct correlation between MR signals and electron density[136].

In general, the conversion of MR images to an attenuation map usually requires an atlas or tissue classification. In addition, the air, lung and bone have very short decay times and are therefore hypo-intense in most MR sequences. The lack of contrast creates additional difficulties in the registration and classification of MR images. Constant attenuation coefficients for these regions lead to significant errors in PET reconstruction due to their inhomogeneous attenuation effects.

Hofmann et al. proposed an atlas-based method in a brain PET/MR study to correlate MR image and attenuation map through a priori anatomical information between the patient's MR and an MR-CT dataset (atlas)[137]. For each patient, the MR dataset was co-registered to the T1-weighted images of the patient, and the same transformation was applied to the corresponding CT images in the atlas. To improve the performance of image co-registration, prior anatomical information was included as a reference in the co-registration process. A weighted average of the co-registered CT created the pseudo-CT images, which were then used for attenuation correction. The proposed atlas-based MRAC method results in a mean error of 3.2% compared to the CT-based MRAC method.

In segmentation-based MRAC methods, the attenuation correction map was generated by segmenting the MR images into tissue classes, and assigning corresponding attenuation

coefficients to each class for attenuation correction. Various MR sequences (e.g. spoiled gradient echo, Dixon, ultrashort TE (UTE), zero TE (ZTE)) can provide anatomical information for segmentation. Adipose tissue has a different attenuation coefficient compared with soft tissue. Because of the differentiation of water and fat, the two-point Dixon sequence is particularly suitable for MRAC. It is the most common sequence for MRAC in many PET/MR systems. The Dixon sequence exploits the difference in Larmor frequency of water and fat and creates the water, fat, in-phase and out-phase images from a multiple echo acquisition. Threshold and segmentation of the Dixon images generate multiple tissue classes, including air, lung, fat and soft tissue, and different attenuation coefficients are assigned to these regions to construct an attenuation map. Because air, lung, and cortical bone are all hypo-intense in the Dixon images, misclassification of bone with air/lung can happen and morphological operation is necessary to correct such misclassification[138,139]. Additional bone segmentation may be inserted with an atlas approach to account for the missing cortical bone. In a study with 35 patients, *Eiber* et al. compared the lesion standardized uptake value (SUV) in PET images with CTAC and Dixon segmented MRAC, and no significant difference in lesion diagnosis was found between the two attenuation correction methods[139].

As mentioned previously, the short decay times of bone and air reduce their contrast and become a major limitation in the Dixon segmentation MRAC. The rotating ultra-fast imaging sequence (RUFIS) is a commonly used ZTE sequence that can capture MR signals with very short decay times[140,141]. As shown in Figure 5.1, the RF excitation is performed after gradients have reached the target magnitudes, and the free induction decay (FID) signal effectively starts at TE = 0. The constant spoke gradients form a projection trajectory in k-space whose direction is determined by the ratio of gradient magnitudes. The finite switching time between the RF transmit and receiver mode (also known as the dead time) makes the acquisition of the first few FID signal sample points difficult. The absence of the first few sample points constitutes a hole at the centre of k-space and can be refilled with linear algebra assuming the imaging object is of finite support, and the imaging spokes are symmetric. Alternatively, additional data acquisition near the k-space centre with a lower gradient magnitude can also refill the missing samples[142]. The change of gradient magnitude between adjacent RUFIS spokes is small, reducing the ramp-up time, the influence of ramp sampling, the acoustic noise due to the rapid gradient switch and decreasing the eddy current.

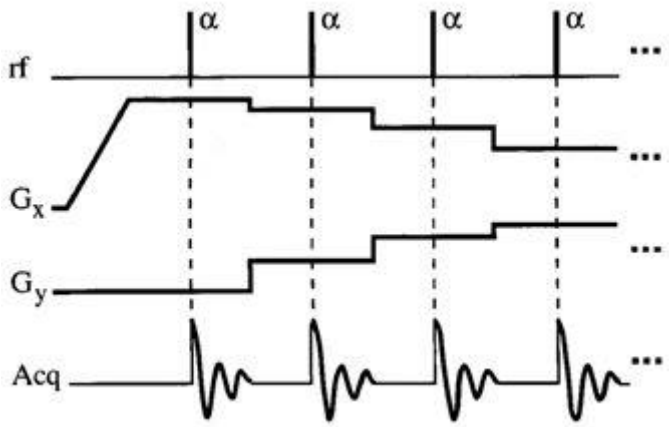

Figure 5.1 Time sequence diagram of RUFIS ZTE sequence[140]

The ZTE sequences can capture MR signals with a quick decay and very short TE and characterize cortical bones much better than the Dixon sequence. In a preliminary study, *Wiesinger* et al. found a good correlation between the ZTE intensity with the CT intensity in brain images[143]. *Yang* et al. performed segmentation with the brain ZTE, and generated an attenuation map with bone, soft tissue and air. A linear transformation generated the ZTE based attenuation map, and the PET image with ZTE based MRAC showed close quantification accuracy compared to the CTAC.

Hofmann et al. compared the atlas-based method with the segmentation based method in a whole-body PET/MR study[144]. Both methods were applied to the PET/MR data of eleven patients. Using a leave-one-out strategy, the atlas-based method outperformed the segmentation method and was more robust with image artefact due to metal implant. However, the mean error in the lung region (14%) was relatively large compared to other regions. For cardiac PET/MR, Lau *et al*. compared the PET images with CTAC and MR based attenuation correction (segmentation-based MRAC with two-point Dixon sequence) and found an excellent correlation in the myocardial SUV between the two attenuation correction methods[145].

Although the atlas-based method performs well in the brain region, its application to the body region is limited because of the complexity of image registration. The body region has more heterogeneity in patient size, anatomy, and pathology. It is challenging to construct an adequate atlas that is suitable for a large population, and the computational cost increases with the expansion of atlas datasets. In addition, the body PET/MR usually covers a larger field of view, and the accurate and efficient image co-registration becomes more challenging and

computationally expensive for the body regions. For the segmentation-based method, the major limitation is the lack of cortical bone as a significant attenuator. The adaptation of UTE and ZTE sequences provides a new opportunity to improve the segmentation-based MRAC, but also imposes challenges in accurate bone segmentation algorithms.

As an alternative to the atlas-based and segmentation-based methods, the deep learning methods generate pseudo-CT for MRAC through a highly non-linear model after training. *Leynes* et al. trained a deep convolutional neural network (CNN) model with U-net architecture and with pelvic Dixon and ZTE images from 10 datasets[146]. In the 16 validation datasets, the pseudo-CT generated with the trained CNN showed a good correlation with the CT intensity and was used for the subsequent MRAC. Compared to the segmentation-based Dixon MRAC, the CNN MRAC reduced mean errors in the reconstructed PET images. The preliminary results of deep learning MRAC have shown promising accuracy after validation. However, the performance of deep learning models depends on the size and quality of the training dataset. Without sufficient training, the CNN cannot adapt to the heterogeneity of anatomy and image intensity. Unpredictable artefacts such as misclassification of air and bone could degrade the accuracy. The normalization of the input MR images is crucial to its performance. Careful bias correction, data normalization and multi-centre, multi-vendor validation would be necessary to evaluate the performance of CNN MRAC.

5.2 Hybrid bias correction of thoracic ZTE images

It is intuitive that in medical images, the intensity of the same tissue should be similar regardless of location. However, in MRI or CT images, bias artefacts often impair the assumption and appear as inhomogeneous illumination across the images (Figure 5.2 A). The bias artefact can be defined as a low-frequency variation of intensity across the field of view caused by hardware limitations[147]. In addition to the bias field, noises (mainly due to thermal fluctuation) can influence the image intensity and are characterised by white noises distributed evenly across the spectrum. Because the bias field only dominates at low frequencies, noises become more prominent at high frequencies. Therefore, a mathematical model of the image can be expressed as:

$$S(x,y) = I(x,y)B(x,y) + \epsilon(x,y) \quad 5.2$$

where x, y are the coordinates in a 2D image, S is the corrupted image, I is the uncorrupted image, B is the bias field, and ϵ is the additive noises. Assuming the magnitude of ϵ is relatively small, the corrected image can be estimated by:

$$I(x,y) \approx S(x,y)/B(x,y) \quad 5.3$$

The bias artefacts do not always impede clinical diagnosis because human interpreters do not only rely on image intensity alone. However, bias artefacts can significantly influence the quantitative analysis and computer vision tasks such as image segmentation.

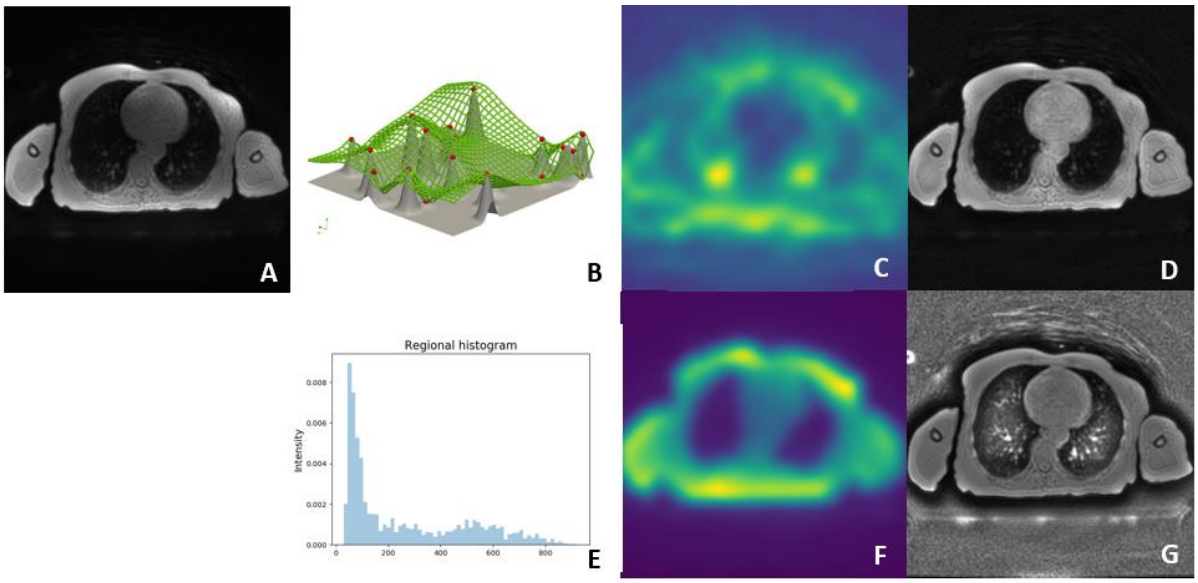

Figure 5.2 Bias field of the corrupted original ZTE image (A) was estimated with the surface fitting (N4ITK, B, C) and the histogram-based method (E, F). The corrupted ZTE image (A) was divided by the estimated fields (C, F) to generate the bias corrected images (D, G)

Prospective measures such as phantom calibration, special sequence design, and body coil calibration can suppress the bias artefact at the cost of extended scanning and processing time. In practice, retrospective correction methods are more commonly used to estimate and correct the bias field without the need for additional scans. Retrospective correction methods take advantage of the *a priori* properties of the image. For example, filtering-based methods attempt to remove the low-frequency variation from the high-frequency features in the image. Filtering-

based methods are efficient for some biased images, but are less effective for complex anatomy. A more flexible multi-parametric B-spline model (N4ITK, Figure 5.2 B) has been proposed to model and correct the bias field[148]. The bias field model is fitted to image features such as intensity or gradient (Figure 5.2 C). The modelling density (i.e. the number of control nodes in the B-spline model) and fitting tolerance control the degree of fitness. Once a bias field is estimated, the corrected image is calculated using equation 5.3 (Figure 5.2 D). The N4ITK method has been widely used in many neuroimaging applications.

An alternative bias correction method is the histogram-based method, which relies on the regional histogram properties. *Wiesinger* et al. proposed a bias correction method based on the regional intensity histogram distribution. Small image patches were extracted, and a negative logarithmic transformation was applied before the histogram analysis (Figure 5.2 E). The normalization factor, or the estimated bias field, was updated for the patch if the histogram peak exceeded a threshold. This process was repeated with different patch sizes (resolutions), and a low-pass filter smoothed the estimated bias field (Figure 5.2 F) before the final image correction (Figure 5.2 G). Because the bias field was estimated locally, the histogram-based method can adapt to large intensity differences, preserving regional image structures and edges.

Although the N4ITK surface fitting method is more robust and can suppress noises[149], the algorithm can fall into local minima when applied to the lung region (Figure 5.2 B), where the proton density is low. In addition, surface fitting often over suppresses the signal intensity in the lung, creating difficulties for subsequent quantitative analysis. The histogram-based method preserves the lung signal intensity, but the regional bias correction also amplifies noises and decreases contrasts in soft tissues (Figure 5.2 C). The histogram-based method brings challenges to the segmentation in soft tissues. To address this problem, we present a hybrid bias correction method that improves thoracic signal intensity uniformity by combining the surface fitting with the histogram-based method.

- Image acquisition

Nine patients (four male, five female, average age: 65) with diagnosed large-vessel vasculitis were recruited in the PITA study (PET Imaging of Giant Cell and Takayasu's Arteritis, NCT04071691), with the approval of the local research ethics committee (REC 19/EE/0043; 14/EE/0019). All patients underwent ^{68}Ga-DOTATATE PET/MR imaging, and six patients

underwent thoracic CT before the PET/MR scan. MR images were acquired on a 3T PET/MR scanner (SIGNA, GE Healthcare, Waukesha, WI) using the product ZTE (radial) pulse sequence and a 48-channel neck and chest coil in nine subjects: TE: 16 μs, TR: 228 ms, flip angle (FA): 1°, voxel size 1.9×1.9×2.6 mm^3, RBW: ± 244kHz, NEX: 4, field-of-view (FOV): 50 cm, 120 slices, acquisition time: 1:40 min. In- and out-of-phase images were acquired using a dual echo 3D Dixon sequence and the system body coil with TE1: 1.11 ms, TE2: 1.67 ms, TR: 4.05 ms, FA: 5°, voxel size 1.9 x 1.9 x 2.6 mm^3, RBW: ±166 kHz, NEX: 0.7, FOV: 50 cm, 120 slices, acquisition time: 2:52 min. Water and fat separated images were subsequently calculated. In addition, spiral thoracic CT images were acquired on a CT scanner (SOMATOM, Siemens, Munich, Germany) with X-ray tube current 594 mA, voxel size 0.98 x 0,98 x 2 mm^3, FOV: 50 cm, 174 slices, acquisition time: 30 s.

- Image processing

The ZTE image (Figure 5.3 A, Figure 5.4 A) was manually co-registered with the Dixon images (in-phase, out-phase, water, fat; Figure 5.4 D-G) using a rigid transformation. B-spline surface fitting (N4ITK)[148] and histogram-based bias correction[143] were used to create separate bias-corrected ZTE images (ZTE_{N4}, ZTE_{hist}; Figure 5.4 B,C), together with their estimated bias fields (Figure 5.4 J,K). To account for intensity differences, all bias-corrected images and bias fields were normalised by the mean tissue intensity of each image or bias field volume. Prior to intensity normalisation, two-class fuzzy c-means clustering was applied to ZTE_{N4} images to generate a body mask. Within each body mask, the mean tissue intensity was estimated with a two-class Gaussian mixture model (GMM). Figure 5.5 illustrates the histograms and the estimated Gaussian models for the ZTE_{N4} images. The mean soft tissue intensity was determined by the mean intensity of the soft tissue Gaussian distribution. Following intensity normalisation, principal component analysis was applied to the normalised Dixon images to extract the first two principal components. Segmentation of the lung region utilised a five-cluster k-means algorithm with the two Dixon principal components and the normalised ZTE_{N4} image as inputs (Figure 5.4 H,I). The five clusters intended to represent air, lung, soft tissue, fat, and bone. Morphological operation was applied to the lung segmentation to smooth the segmentation edge, and the eight-connected region with the largest 3D volume was used as the final lung segmentation. A tissue region was derived by subtracting the lung segmentation from the body mask. A hybrid bias field was generated by replacing the N4ITK bias field in the lung region with values from the histogram-based bias field. A 2D Gaussian

filter (FWHM: 7.1) was used to smooth the bias field at the edges of the lung segmentation (Figure 5.3 B, Figure 5.4 L). The original ZTE image (Figure 5.4 A) was divided by this hybrid bias field to produce a bias-corrected ZTE image (ZTE_{hybrid}; Figure 5.4 M).

To evaluate the performance of the bias correction methods, the coefficient of variation (CV) and coefficient of joint variation (CJV) for each bias correction method were calculated:

$$CV(I_i) = \frac{\sigma(I_i)}{\mu(I_i)} \tag{5.4}$$

$$CJV(I_i, I_j) = \frac{\sigma(I_i) + \sigma(I_j)}{|\mu(I_i) - \mu(I_j)|} \tag{5.5}$$

where i, j are indices of classes, I_i is the image intensity for class i, σ is the standard deviation and μ is the mean. A Wilcoxon signed-rank test with Bonferroni correction was used for statistical comparison. p-values <0.05 were considered statistically significant.

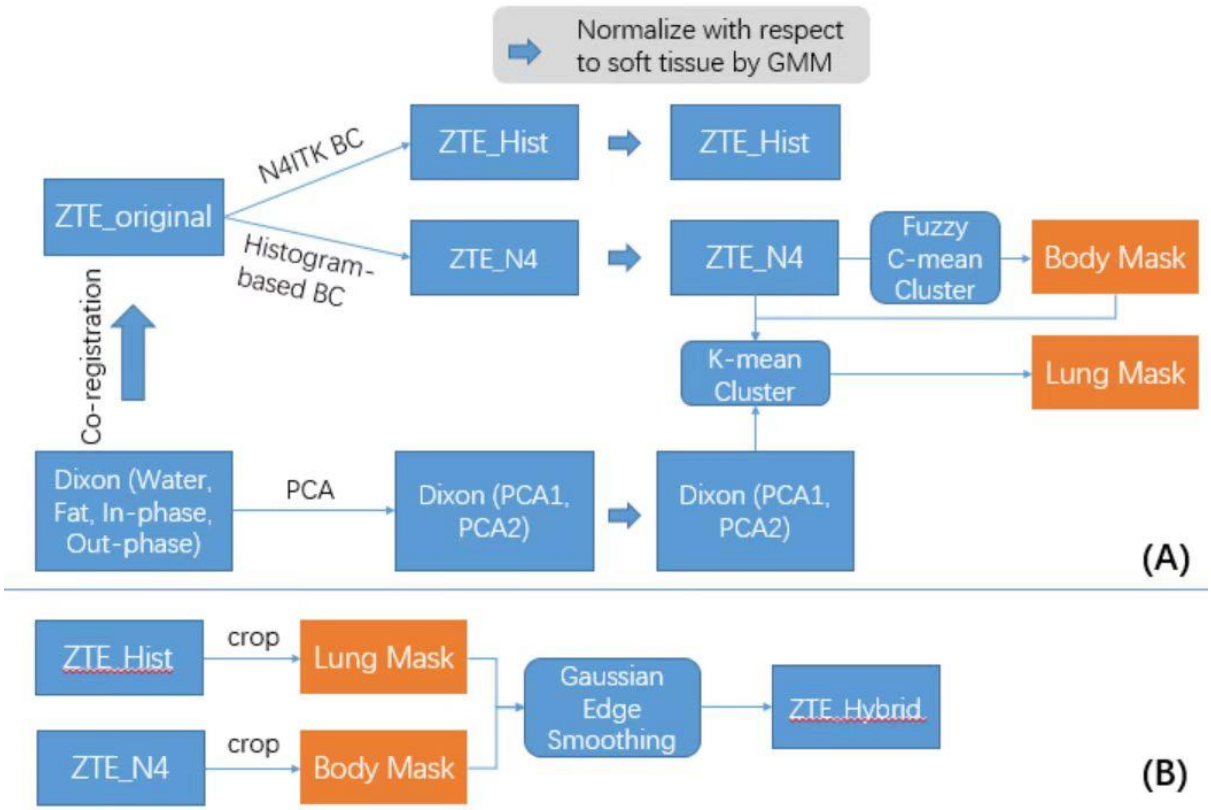

Figure 5.3 Image processing flow chart for N4ITK and histogram-based bias correction, mask generation (A) and hybrid bias correction (B) (BC: bias correction, GMM: Gaussian mixture model, PCA: principal component analysis)

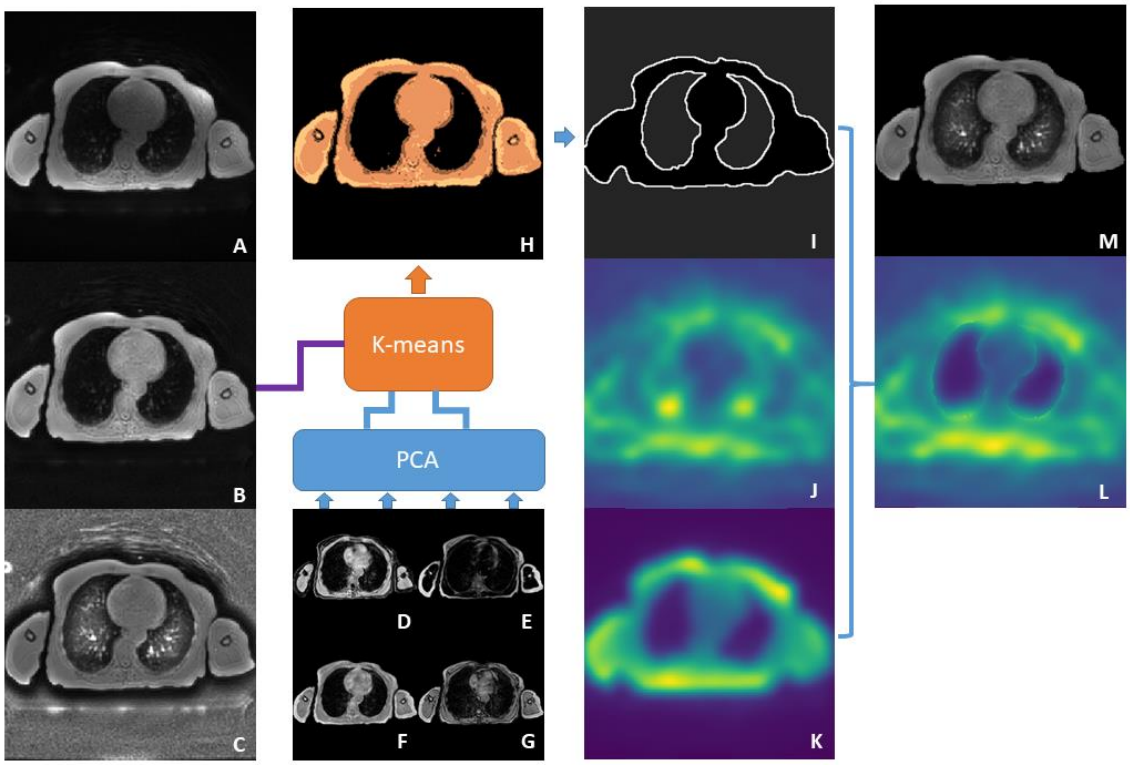

Figure 5.4 The original ZTE image (A) is bias-corrected with N4ITK (B, $\boldsymbol{ZTE_{N4}}$) and histogram-based methods ($\boldsymbol{ZTE_{hist}}$; C). PCA is applied to the Dixon images (D-G) to extract the first two principal components. These are input into a five-class k-means cluster (H) together with the normalised $\boldsymbol{ZTE_{N4}}$ image to obtain a lung segmentation (I). A hybrid bias field (L) is created by replacing the lung region values in the $\boldsymbol{ZTE_{N4}}$ bias field (J) with those from the $\boldsymbol{ZTE_{hist}}$ bias field (K). After smoothing the lung edges, a bias-corrected ZTE image (M) is calculated by dividing (A) by the hybrid bias field (L).

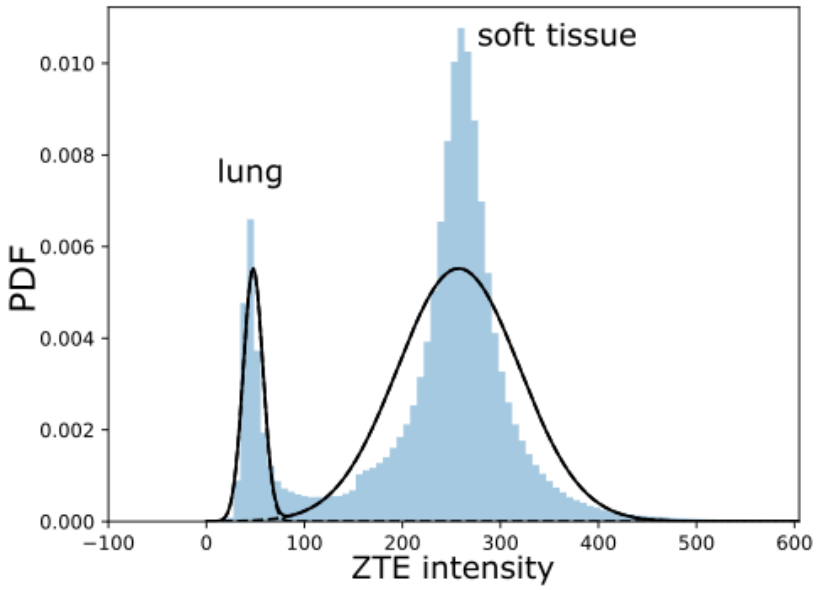

Figure 5.5 Intensity normalization of $\boldsymbol{ZTE_{N4}}$ images

- Results

Figure 5.6 illustrates the probability density function (PDF) of the signal intensity in the lung and tissue regions (n = 9). Compared to the original ZTE PDF (Figure 2A), the N4ITK method (Figure 5.6 B) normalised the signal intensity in tissue but not in the lung. The histogram-based method (Figure 5.6 C) broadened lung signal intensities, but the tissue signal intensity was less uniform than N4ITK. The hybrid method (Figure 5.6 D) combines the lung PDF from the histogram method and the tissue PDF from N4ITK. The hybrid method demonstrated a lower coefficient of variation in the body (Figure 5.7 A). Consistent with the results shown in Figure 5.6, tissue regions showed less variability for the hybrid algorithm than for the histogram-based method (Figure 5.7 B). No significant difference between algorithms was found for the lung (Figure 5.7 C). Additionally, the hybrid method showed higher inter-class joint variation between the lung and tissue regions than N4ITK (Figure 5.7 D). Figure 5.8 illustrates the lung and bone segmentations and the bias corrected ZTE images. The spinal and rib bones were distinguishable in the segmentations, but bone segmentation errors concentrated at the edge of the lung and soft tissue.

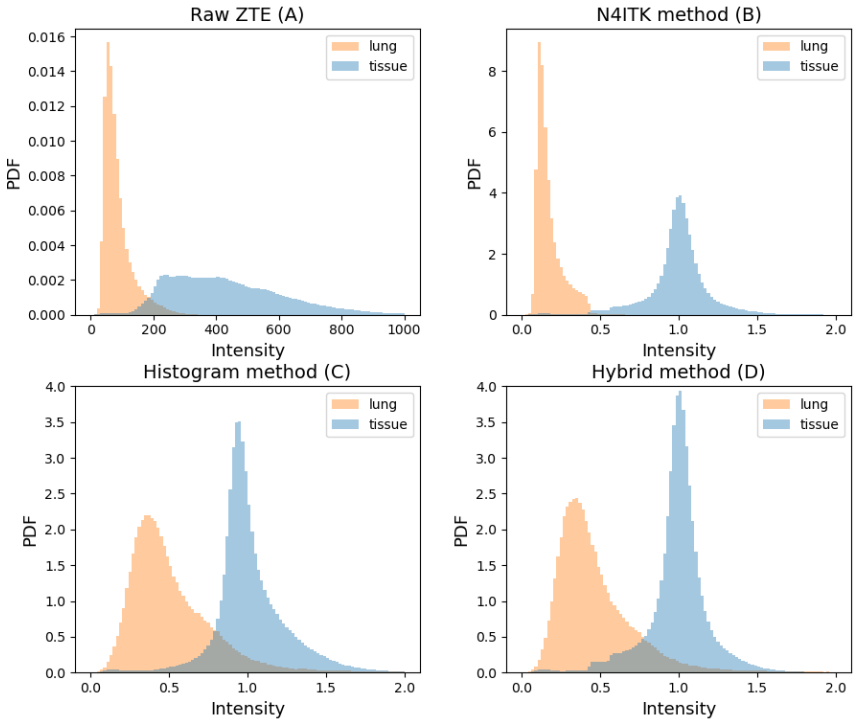

Figure 5.6 Probability density function (PDF) of the tissue and lung regions.

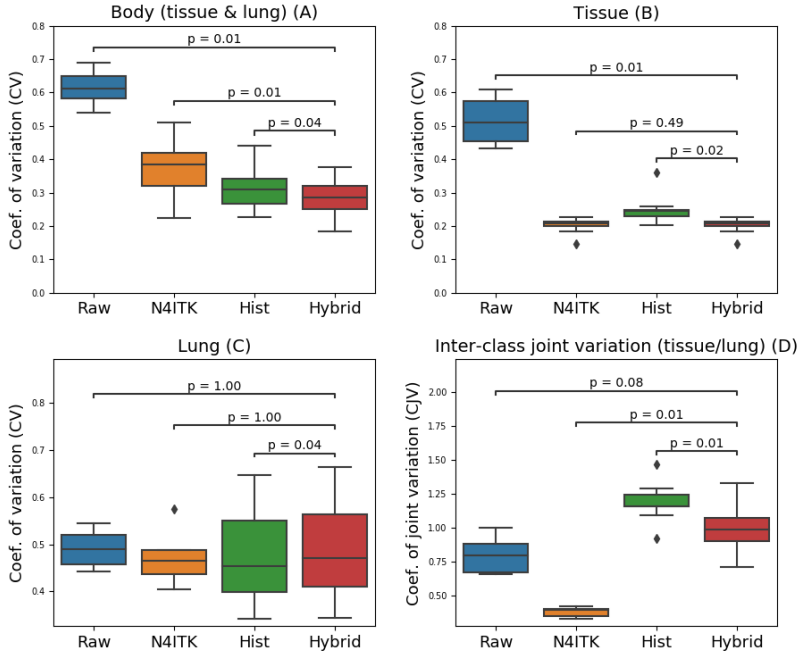

Figure 5.7 Boxplot showing the coefficient of variation for the body, tissue and lung regions (n = 9 patients). Subplot D illustrates the corresponding coefficient of joint variation for tissue and lung.

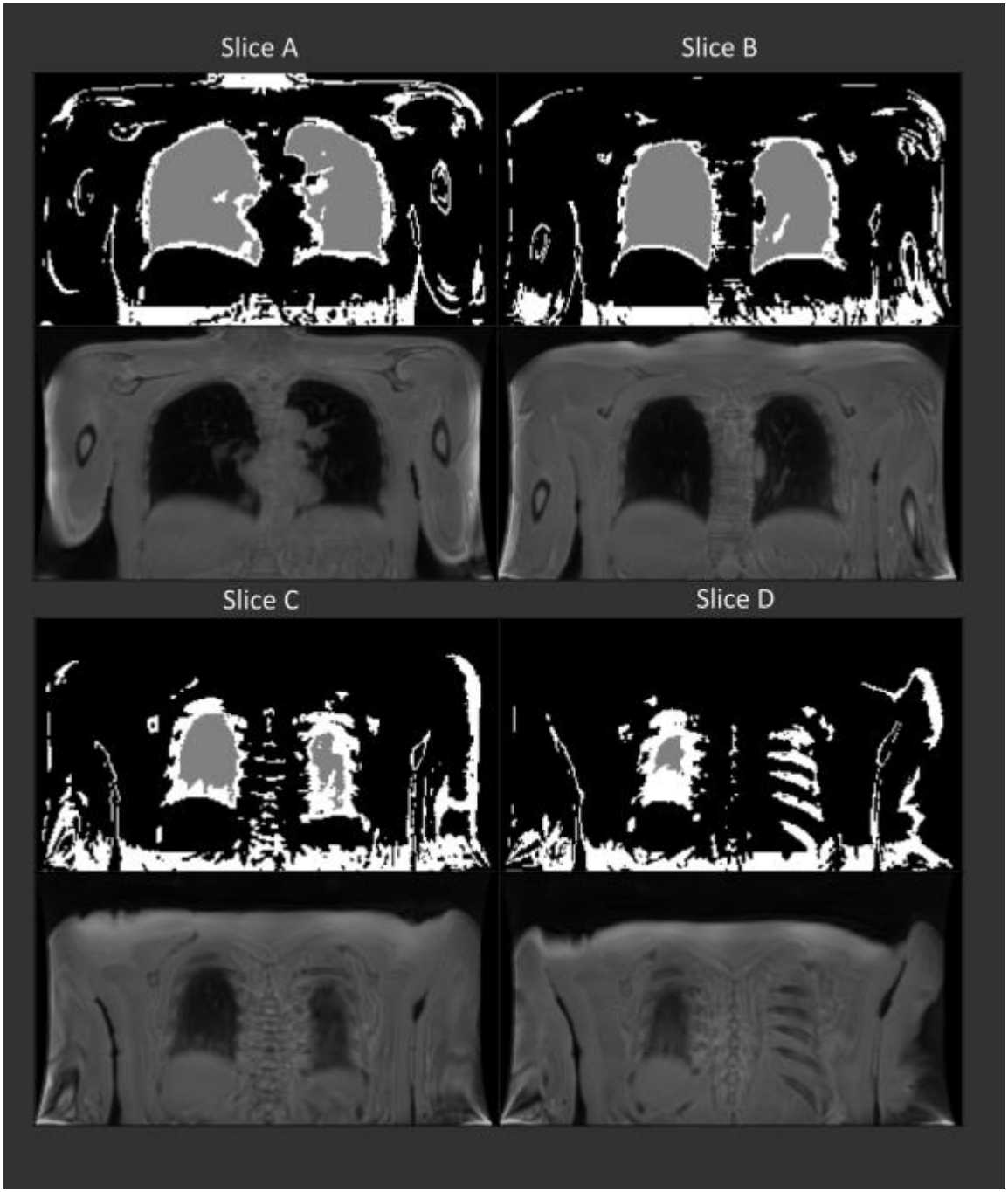

Figure 5.8 Lung and bone segmentation mask (above) and ZTE images (below). (Lung mask: grey, Bone mask: white)

- Discussion

N4ITK assumes that the bias field varies at a low frequency, and hence the image intensity variation is locally uniform. This does not hold in the lung, where the proton density varies, and signal intensity is low and non-uniform. The density of the bias field B-spline model is

limited to avoid overfitting to noise and to reduce computation complexity. The algorithm failed to normalise the sparse signals in lung. In addition, the N4ITK algorithm was originally optimised for neuroimaging, where the signal intensity is more uniform. When applied to thoracic images, the N4ITK algorithm regarded the lung region as a sparse noisy signal, and tended to suppress the signal in lung (Figure 5.4 J).

Histogram-based methods rely on local histogram analysis and are more suited to images with a range of intensity values at the local level. In the lung region, the low and sparse lung signals reduced the histogram intensity and the estimated bias field magnitude. The histogram-based algorithm tends to normalise the image by restoring the low intensity, and suppresses the high intensity within a 2D patch. The low intensity of the histogram-estimated bias field (Figure 5.4 K) in the lung region illustrates the enhancement of lung signal. In addition, the accuracy of the histogram requires a reasonable patch size. A small patch size will improve the accuracy of bias field estimation, at the cost of increased computational complexity and a decreased number of samples in the histogram analysis. In Figure 5.4 C, high intensities were observed near the back and the arm of the patient, indicating that the accuracy of bias correction degrades at continuous edges with sharp intensity changes.

The hybrid method combines the advantages of the N4ITK and histogram-based methods (Figure 5.6 D). It provided a normalized soft tissue intensity while maintaining a relatively normal signal distribution in lung. It provided the lowest tissue signal variation among all three methods, and a lung signal distribution more consistent with the known variation of signal intensity in the lung. The coefficient of variation reflected the variation among a dataset. The hybrid method provided the lowest body signal variation among all three methods (Figure 5.7 A), improved the signal uniformity and reduced the bias artefact. The hybrid method provided lower soft tissue variation than the histogram-based method and the original ZTE image(Figure 5.7 B). In lung regions, the three methods and the original image all showed similar coefficients of variation (Figure 5.7 C). Similar coefficients of variation in lung may result from the signal sparsity of lung regions. The change of intensities in the sparse lung structures could not largely influence the coefficients of variation. The inter-class joint variation reflected the signal consistency between the soft tissue and the lung regions. The hybrid method showed higher joint variation than the surface-fitting method and corrected the lung signal suppression in the surface-fitting method (Figure 5.7 D). However, considering the natural signal difference

between soft tissue and lung, the joint variation was not expected to be very large. Because the true bias fields were not measured in these experiments, the comparison with the coefficient of variation and coefficient of joint variation may not fully assess the performance of each bias correction method. To accurately compare the bias correction performance, bias field mapping and simulation will be necessary for future improvement.

The K-means segmentation process (Figure 5.4 K) provides five different clusters based on the image intensity in the bias-corrected ZTE images and two principal components of the Dixon images. The lung regions containing few protons were hypointense in all three images, and corresponded to the cluster with the lowest image intensity. The skeleton, including the cortical and spongy bones, had short TE and was hypointense in the Dixon images. In the ZTE images with very short TE (16 μs), MR signal intensities in bones were slightly higher than in the Dixon images. The difference in bone intensity in different images made bone a distinguishable cluster in the k-means segmentation. Figure 5.8 illustrates the lung segmentation (grey) and the bone segmentation (white) and the ZTE images. The lung segmentation matches well with the ZTE images. The bone segmentation contains more misclassification at the abdomen and diaphragm, but the rib, the clavicle, and the humerus bone are visually identifiable. For the vertebrae, the complex geometry and the mixture of cortical and cancellous bone made the segmentation less accurate. Only part of the vertebrae is visible in Figure 5.8 C. The rib bone is the bone closest to the heart and can contribute to attenuation errors in cardiac PET/MR imaging. However, rib bone segmentation is difficult because of its proximity to the lung region and the lack of significant contrast between the rib bone and the lung. The low intensity region surrounding the lung was often classified as a bone shell over the lung. Because the bone has a higher attenuation coefficient compared to the lung, the misclassification of bone will introduce errors in PET attenuation maps and subsequently quantification errors in PET images. Therefore, further differentiation of bone vs lung and the cleaning of bone segmentation would be necessary before the inclusion of bony structures in the ZTE-based MRAC.

5.3 Lung pseudo-CT generation using ZTE images

The hybrid bias correction of the thoracic ZTE images normalised the signal intensity of the ZTE images, and laid the foundation for quantitative transformation from the ZTE intensity to

the CT in Hounsfield units (HU). Previous studies indicated a negative linear relationship between the ZTE and CT intensity for bones[143,150]. Bones and air both have low proton density but have very different attenuation coefficients. In the lung, an inverse relationship between the ZTE and CT intensity was expected.

The thoracic CT images were co-registered to the ZTE images through a deformable registration algorithm on the basis of symmetric normalisation (SyN) with mutual information as the similarity metric within the Advanced Normalisation Tools package (ANTs). Within the segmented lung mask, The CT intensities in the Hounsfield unit and the ZTE intensities after bias correction and tissue normalization were extracted. Before the extraction, a 2D image erosion algorithm eroded the lung mask by three pixels. The erosion operation removes the edge of the lung mask where the rib bones may be wrongly included. The bone inclusion would cause significant errors in the intensity mapping between ZTE and CT. The first two principal components of the normalised Dixon images were also extracted within the eroded lung mask. Multiple regression with machine learning models and transformations were fitted to the data, with the normalised ZTE and the two Dixon principal intensities as inputs and the CT intensity as the output. The models included ordinary least square, histogram matching (200 bins), Lasso regression (alpha = 1, 1000 iteration), Ridge regression (alpha = 1, singular value decomposition solver, 1000 iteration), decision tree (maximum depth 5), and multilayer perceptron (100 hidden layers, relu activation, alpha = 0.0001, batch size 200, stochastic gradient optimizer). A cross-validation with a leave-one-out strategy was used to avoid overfitting and to assess the performance of each model. The mean absolute error and the mean absolute percentage error were calculated for each validation test and were reported as mean values (95% confidence interval).

The CT and pseudo-CT images created for the lung region were converted to the attenuation map with linear attenuation coefficients. A segmentation-based algorithm provided by the manufacturer generated the Dixon MR attenuation map. Two hybrid MR attenuation maps were created by substituting the lung region of the Dixon attenuation map with values from the CT and pseudo-CT attenuation maps. Before the integration, Gaussian smoothing with a 5mm full width at half maximum (FWHM) kernel was applied to the CT and pseudo-CT attenuation maps, followed by resampling from the ZTE space to the attenuation space (matrix size 128×128×154, pixel size 4.69×4.69×2.78 mm^3). For PET image reconstruction, emission data

from 50-80 min post injection of ^{68}Ga-DOTATATE were reconstructed into a 256×256×89 matrix with 2.34×2.34×2.78-mm voxels, using time-of-flight ordered-subsets expectation-maximization (TOF-OSEM) with 2 iterations and 28 subsets. Corrections for normalisation, dead-time, randoms, scatter, sensitivity and isotope decay were applied as implemented on the scanner, together with an isotropic 4-mm FWHM Gaussian filter post reconstruction. Attenuation correction was performed using the CT and pseudo-CT-based attenuation maps as well as the one produced by the scanner so as to evaluate the performance of each attenuation method. The Wilcoxon sign rank test was used to statistically compare data with non-normal distribution.

- Results

Figure 5.9 shows the joint histogram of the normalised ZTE intensity and the CT intensity in all patients; a least-square linear regression indicates a weak linear relationship ($r^2 = 0.02$).

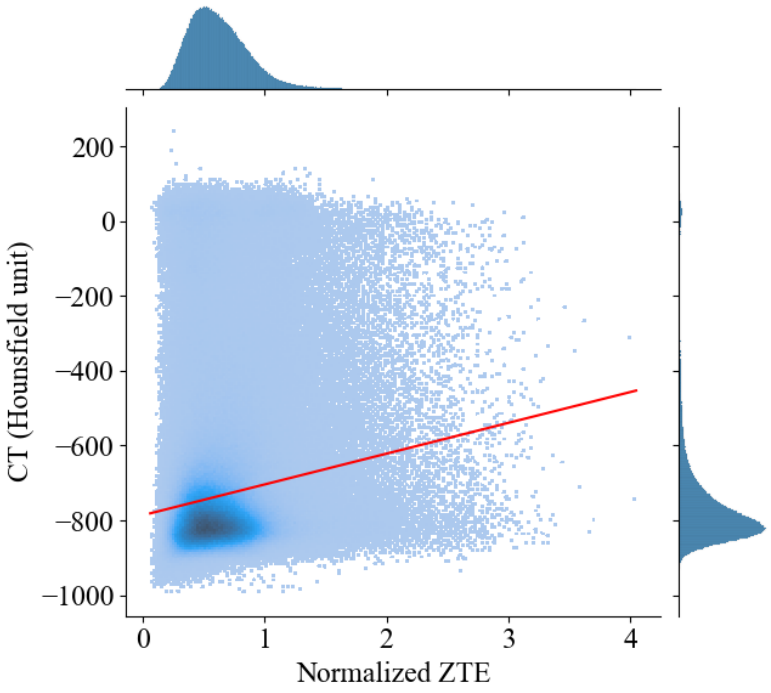

Figure 5.9 Joint histogram of ZTE and CT intensity in lung

Various machine learning models were used to predict the CT intensity from the ZTE and Dixon principal intensities. Table 5-1 summarises the accuracy of each regression model. The ordinary least square, Lasso, and Ridge models show similar errors and outperformed other

models. The ordinary least square model was used in the following pseudo-CT generation.

Table 5-1 Comparison of machine learning models with cross-validation

Machine learning model	Mean absolute error	Mean squared error	Mean absolute percentage error
Ordinary least square	112.3 [81.6,143.0]	32434.6 [7137.1,57732.0]	9.7% [7.4%,12.0%]
Histogram matching	139.3 [105.6,172.9]	51986.5 [23170.9,80802.0]	9.7% [7.6%,11.7%]
Lasso	112.3 [81.6,143.0]	32442.5 [7173.0,57671.9]	9.7% [7.4%,12.0%]
Ridge	112.3 [81.6,143.0]	32434.3 [7138.1,57730.5]	9.7% [7.4%,12.0%]
Decision tree	188.9 [155.2,222.6]	89056.4 [57186.3,120926.4]	12.1% [10.6%,13.6%]
Multilayer perceptron	182.1 [104.2,259.9]	71584.1 [14663.0,128505.2]	16.2% [8.1%,24.2%]

The pseudo-CT intensities predicted with the ordinary least square model were mapped to the lung region (intercept -767.2 [-788.6, -745.8], slope for ZTE 80.1 [55.3, 104.9], slope for the first Dixon principal component 11.0 [3.5, 18.5], slope for the second Dixon principal 8.8 [-3.0, 20.6]). Figure 5.10 demonstrates the CT images, normalised ZTE images, pseudo-CT images, and the difference between the CT and pseudo-CT images in the lung region. The mean absolute differences were calculated within the lung region and were consistent with the mean absolute error in cross-validation tests.

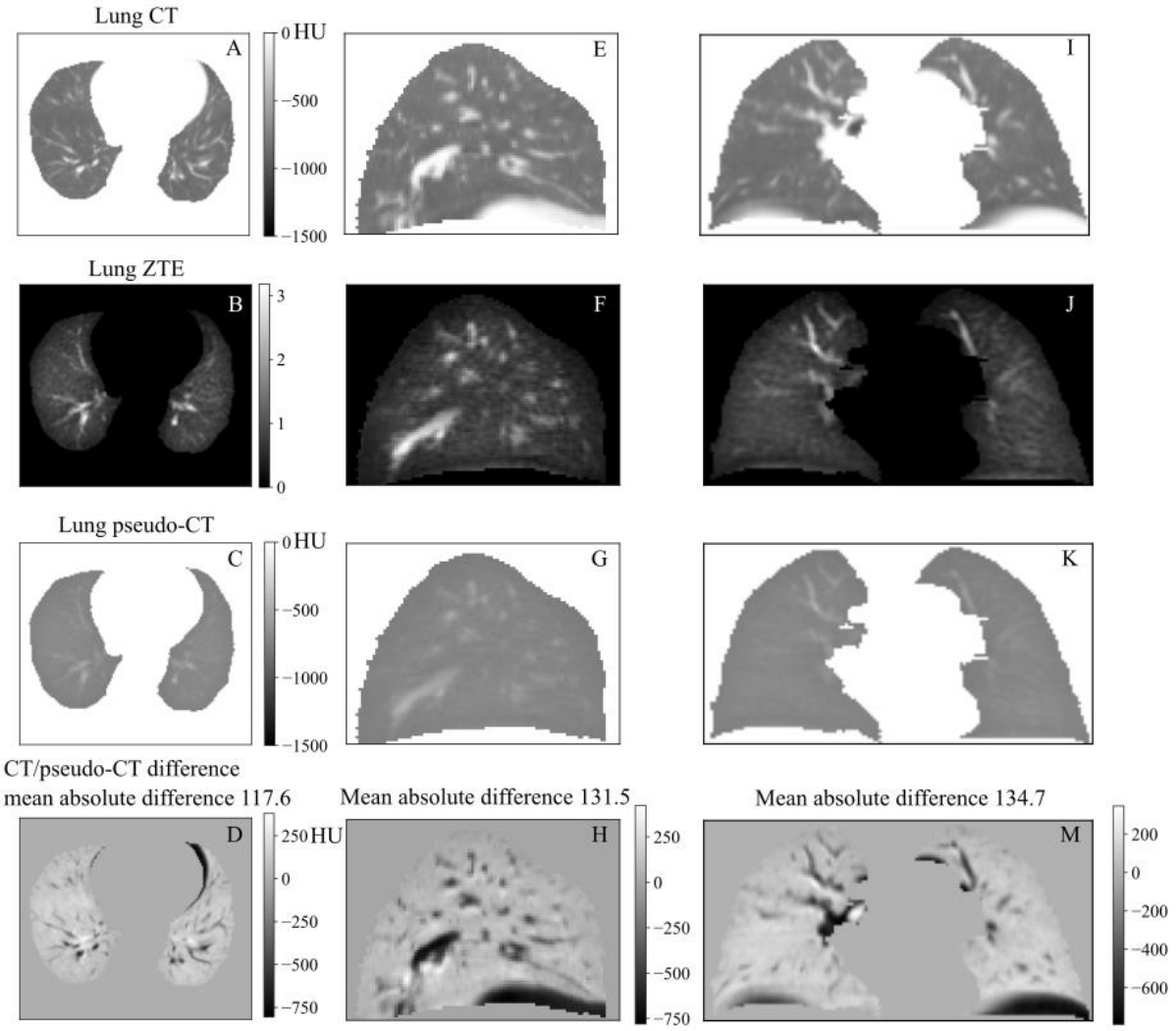

Figure 5.10 CT, ZTE, pseudo-CT images and their difference

Figure 5.11 (A-C) illustrates the attenuation correction map generated from the Dixon image. The hybrid attenuation maps were created by integrating the Dixon map with the CT and pseudo-CT generated attenuation maps in the lung region (Figure 5.11 D-F, G-I).

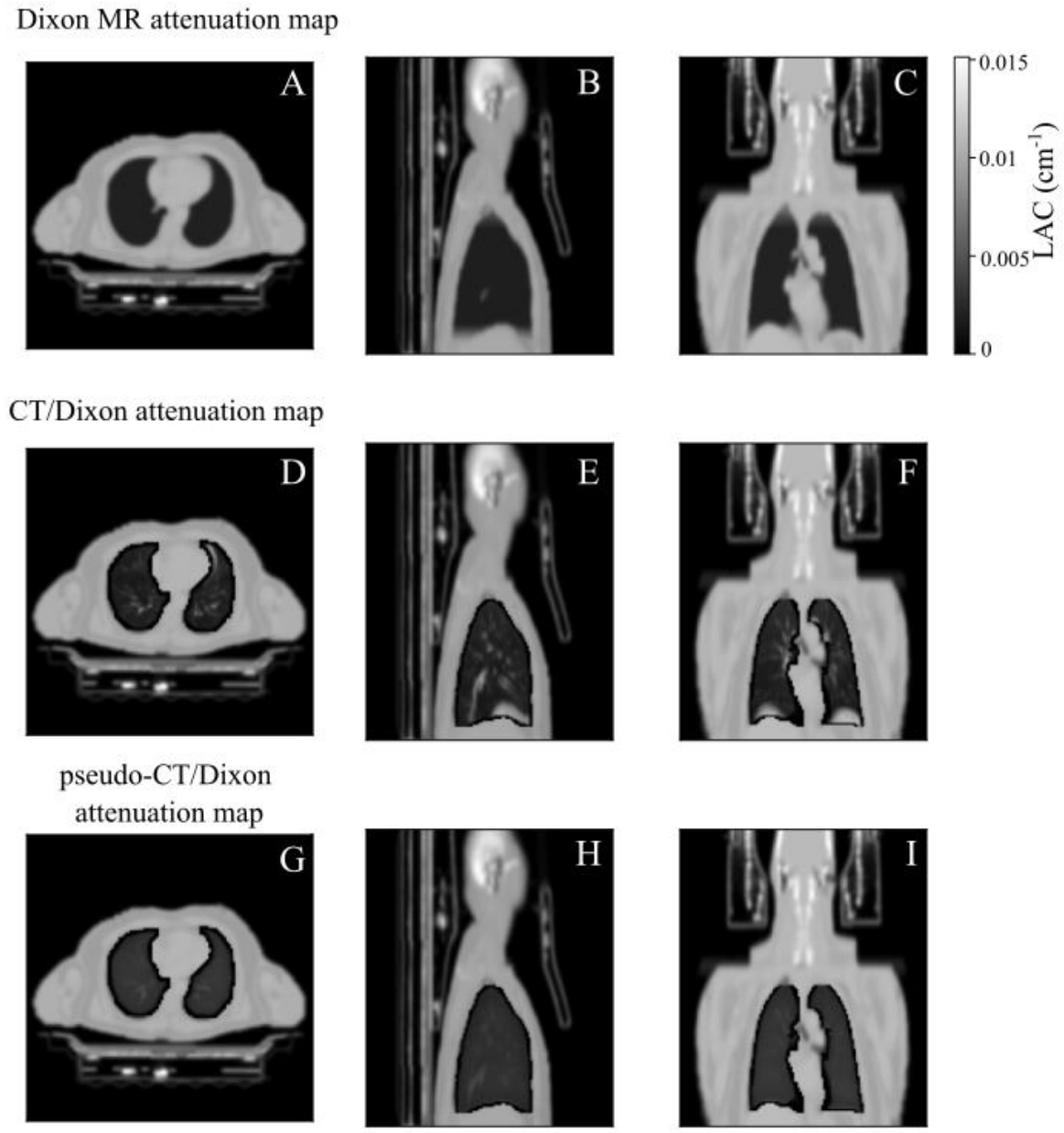

Figure 5.11 Integrated MR-based attenuation maps

The PET images were reconstructed for the Dixon/CT, Dixon/pseudo-CT, and Dixon based MR attenuation maps. Figure 5.12 illustrates the PET intensities within the lung region, and Figure 5.13 illustrates the PET intensities in the body. Percentage difference maps of the Dixon/pseudo-CT and Dixon corrected PET were calculated with the Dixon/CT corrected PET as the reference. The ZTE images were overlaid with the Dixon/CT corrected PET to show the anatomical and metabolic information.

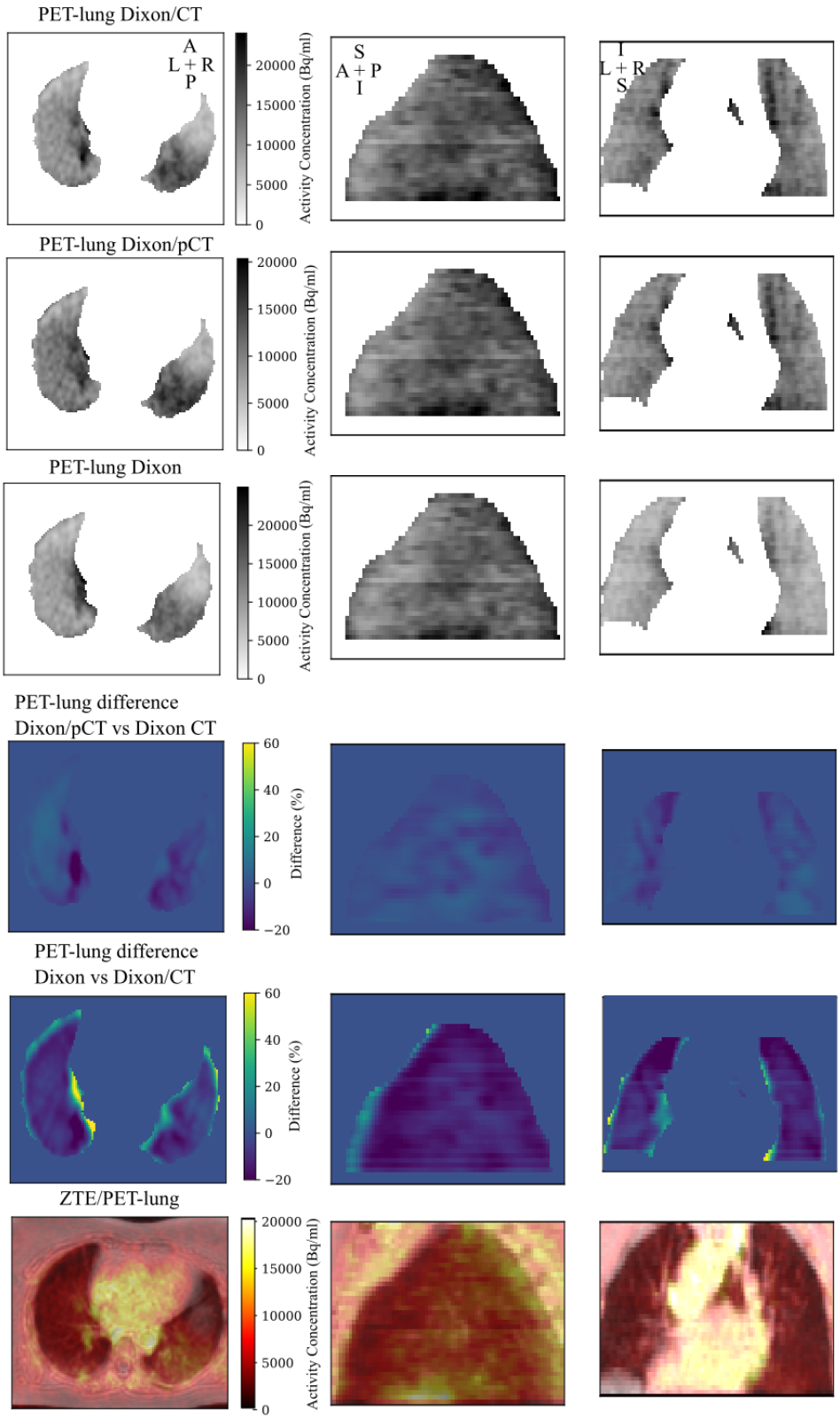

Figure 5.12 PET intensity and difference of different MRAC methods in the lung

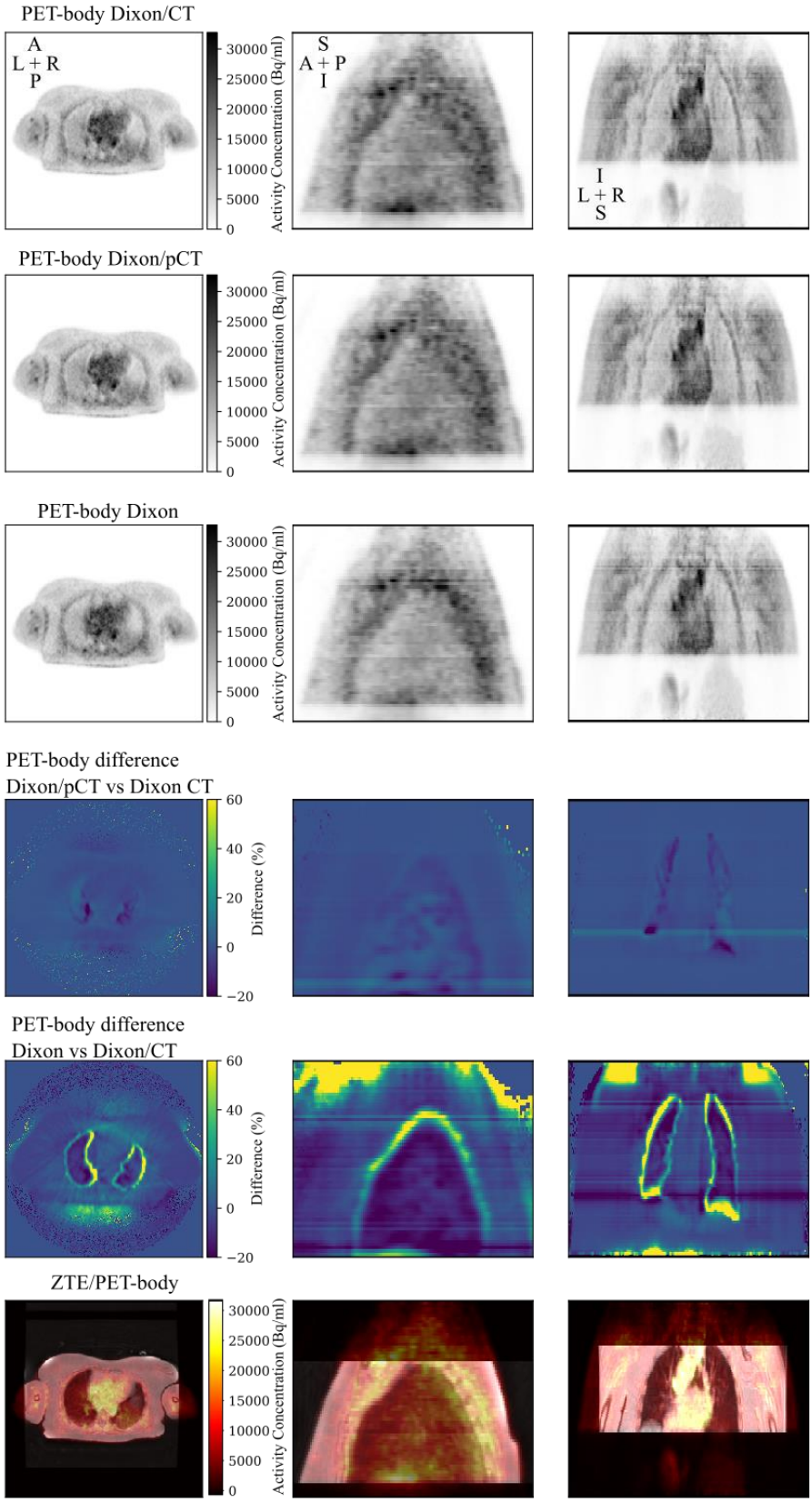

Figure 5.13PET intensity and difference of different MRAC methods in the thorax

Volumes of interest (VOIs) were selected for each lung lobe in the posterior/anterior and superior/inferior direction. VOIs were also selected in the descending aorta and near the coronary root. The VOI is a cylindrical volume with a circular area of 5 mm^2 and a height of three consecutive PET slices (slice thickness 2.78 mm). The mean SUV_{bw} of VOIs in different directions and of all lung VOIs were calculated and presented in Figure 5.14, in which each boxplot represents the SUV_{bw} of all patients. In all lung VOIs, the Dixon/pseudo-CT method has an error of 1.25% [0%, 6.46%], and the Dixon correction has an error of -4.26% [-9.17%, 0%]. The percentage differences of mean SUV_{bw} corrected with the Dixon/pseudo-CT and Dixon attenuation map were calculated with the Dixon/CT corrected PET as a reference.

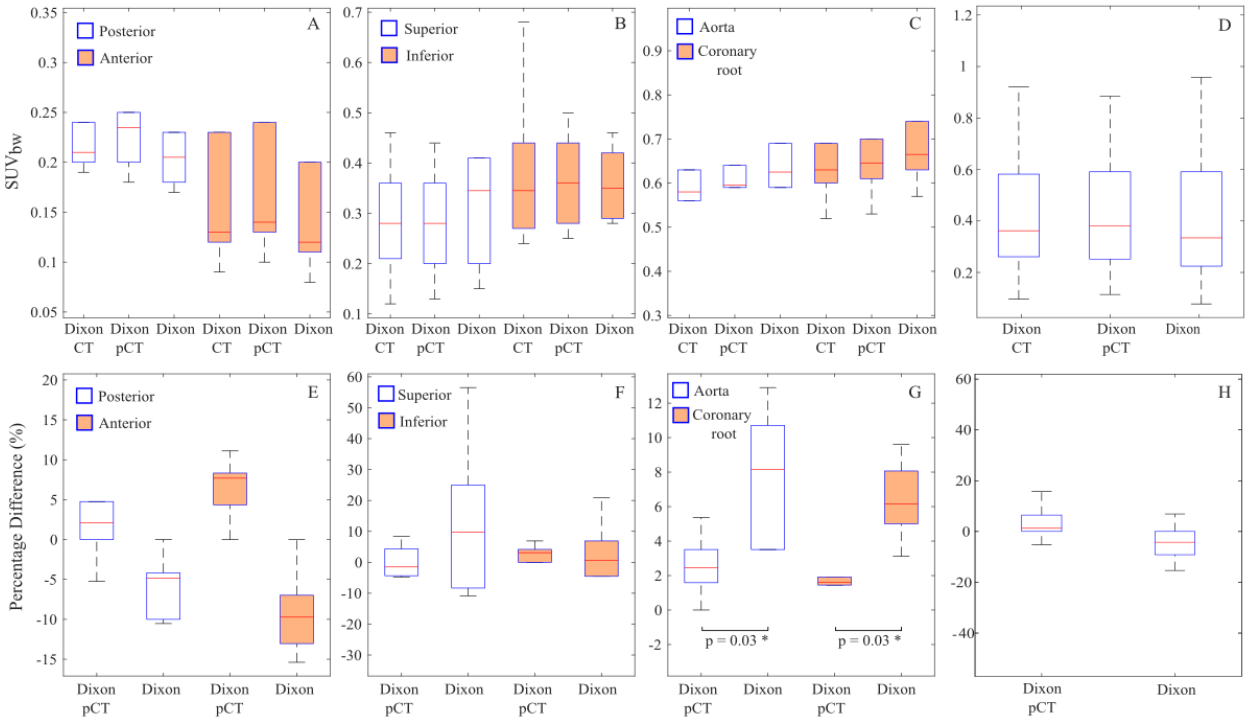

Figure 5.14 Comparison of PET intensity in different regions of interest among all patients

- Discussion

Histograms of CT intensity and normalised ZTE intensity showed similar distribution with a skewed tail towards the high intensity end. The joint histogram shows a hotspot at the low intensity region, where CT intensity is close to the intensity of air (-800 HU, air: -1000 HU). The elliptical hotspot indicates a weak linear relationship between the CT and ZTE intensity at low intensities. The linear fitting model (r^2=0.02) confirms the weak linear correlation. Because of the large number of low intensity pixels, the linear relationship between ZTE and CT was

dominant by the low attenuation regions. At the low ZTE intensity region, the spread of CT intensity is relatively large, leading to an increase in the linear intercept. The spread may be the result of misregistration of CT and ZTE images, segmentation error for the lung region, motion artefacts (especially near the diaphragm) and differences in anatomy due to lung remodelling. Because the patients' gestures were different in CT and PET/MR acquisition (arms up in CT, arms down in PET/MR), the shape of the lungs could be stretched differently in the two images, adding more difficulty to image registration between ZTE and CT. The misregistration mostly concentrated near the diaphragms where the lungs were largely stretched due to gestures.

Among the different machine learning models, the parametric multiple regression models such as the ordinary least square, Lasso, and Ridge models showed similar performance and a percentage error of 9.7%. The non-parametric regression models such as the histogram matching, decision tree, and multi-layer perceptron model showed worse performance than parametric modelling methods. The performance of the non-parametric model relies on a large number of independent samples. Although the number of pixels for training was large, the pixels were sampled from only six patients. The between patients differences could increase errors in model training. In addition, the quality of pixel intensity correlation was influenced by image registration, segmentation, motion and anatomical difference, which further degraded the modelling accuracy. A better registration process, larger sample size and inclusion of spatial features (such as texture or convolutional neural network) could potentially improve the intensity mapping accuracy between ZTE and CT.

Figure 5.10 compares the CT, ZTE and pseudo-CT images in the lung region. The major pulmonary arteries and lung structures were visible in both the CT and ZTE images. The anatomy of arteries and lung tissues was similar in both modalities. After a linear transformation, the contrast in the pseudo-CT image was decreased compared to the normalised ZTE image. Because the linear transformation was dominated by low intensity regions, smaller regions with higher intensity on the ZTE were usually underestimated. The dark region in the difference image illustrates the underestimation of the high intensity regions such as the pulmonary arteries. The underestimation indicates that the transformation from ZTE to CT intensity is not uniform for different regions. A non-linear or a piecewise linear model for the low and high intensity pixels could better characterize the transformation. Regional regressions of specific ROIs (e.g. vessel, lung tissue, air) may further reveal the correlation of ZTE and CT

in different tissues and improve the accuracy of pseudo-CT generation, but would also require additional segmentation within lungs. The high contrast (dark near light) region in the difference image indicates misregistration between the two image modalities. The dark region in the superior direction of the right lung in Figure 5.10 D resulted from the mismatch of the lung segmentation mask. The lung mask included part of the soft tissue in the CT images, causing a large error near the segmentation edge. The error near the diaphragm (Figure 5.10 H, M) is a typical error of the motion artefacts and could potentially be improved by motion-resolved reconstruction or correction in the image registration.

A comparison of the standard Dixon attenuation map and the hybrid attenuation map was illustrated in Figure 5.11. Segmented lung regions closely matched the lung regions in the standard Dixon attenuation map. The CT based hybrid attenuation map shows a large variation of attenuation coefficients in the lung. The high attenuation coefficient for the pulmonary arteries and lung tissues is close to the coefficient in the soft tissue. The high intensity near the diaphragm was caused by respiratory motion. The diaphragm artefact was not observed in the pseudo-CT based attenuation map, because both the Dixon and ZTE image were acquired during the same scanning session. This made the registration between ZTE and Dixon images more accurate than between ZTE and CT images due to fewer motion artefacts. Therefore, the MR-based attenuation maps were less sensitive to the motion and registration artefacts than the CT attenuation map.

The attenuation coefficient variation in the lung of the pseudo-CT attenuation map was decreased after the pseudo-CT transformation. The arteries and lung structures were underestimated in attenuation correction. The large volume of low attenuation region had less attenuation difference when compared with the CT based hybrid attenuation map. Compared to the Dixon attenuation map whose lung attenuation was nearly uniform, the pseudo-CT based MR attenuation map better characterized the attenuation variation in the low attenuation region, and preserved certain attenuation for the highly attenuating structures.

From the PET images, the Dixon/pseudo-CT attenuation correction tends to overestimate the PET intensity in the lung, while the Dixon correction tends to underestimate the intensity in the lung (Figure 5.12). A strong overestimation of intensity appears at the lung edges for the Dixon corrected images (Figure 5.13). The overestimation may result from the attenuation coefficient change in the Dixon/CT method because the Dixon/CT attenuation map was generated by substituting the lung attenuation in the Dixon map with CT based linear

attenuation coefficients. The transition between Dixon to CT attenuation coefficients could create attenuation artefacts at the segmented lung edges. Because the Dixon/pseudo-CT attenuation map was also generated through substitution, the lung edges have a lower percentage difference than the Dixon corrected images.

The VOI comparison indicates a bias of PET intensity in the posterior/anterior direction (Figure 5.14. A). The bias may relate to the absence of bone attenuation (particularly the spinal bones) in all three attenuation maps. The Dixon/pseudo-CT correction overestimated the intensity in these VOIs and has a less difference magnitude than the Dixon correction (Figure 5.14. E). In the superior/inferior direction, a PET intensity bias also appears (Figure 5.14. B). This could relate to the high intensity of the liver, causing an increase in PET intensity in the inferior lung region. The percentage difference in this direction mostly centred on zero. The Dixon/pseudo-CT correction shows less variation of differences than the Dixon correction, indicating the higher accuracy of the Dixon/pseudo-CT correction (Figure 5.14. F). In the descending aorta and coronary root region, the Dixon method shows a significant overestimation of PET intensities ((Figure 5.14. G). However, the overestimation may relate to the attenuation artefacts due to the lung attenuation substitution. The accurate comparison of the two correction methods near the lung edges would require the CT attenuated PET images as the gold standard. Overall, the Dixon/pseudo-CT correction reduced the absolute intensity error by 3.01% in the lung when compared to the Dixon attenuation correction (Figure 5.14. H).

Chapter 6 Magnetic Resonance Imaging

The significance of inflammation in the initiation, progression and vulnerability assessment of atherosclerosis plaques makes the hybrid PET/MR imaging system suitable for revealing the correlations between coronary inflammation and plaque morphology. In addition, MR's ability to depict coronary motion provides a non-invasive tool to quantify coronary bending, whose significance in the coronary vulnerability assessment has been revealed in Chapters 3 and 4. Despite the ability of coronary MR imaging in conventional MR scanners (usually with 1.5 T field strength), the successful acquisition of coronary images in PET/MR systems (usually with 3 T field strength) can be challenging due to different field strengths and the efficiency of acquisition. The original aim of this study is to develop an efficient non-Cartesian free breathing MR sequence for the PET/MR system to reveal the coronary morphology and motion, and their correlation with coronary inflammation reflected by the ^{68}Ga-DOTATATE PET signal.

6.1 MR Theory

Atomic nuclei have an intrinsic quantum mechanical property of spin in the form of angular momentum[151,152]. For specific nuclei such as ^{1}H (proton), ^{13}C, or ^{23}Na, the spin is non-zero, and a magnetic dipole moment exists. Because of the abundance in biological tissue, ^{1}H (proton) is the most common nuclei for MR imaging. When placed in an external magnetic field (B_0), the magnetic dipole will precess at the Larmor frequency ω_0:

$$\omega_0 = \gamma B_0 \qquad 6.1$$

where γ is the nuclei's gyromagnetic ratio. The precession direction can be either parallel (a lower energy state) or antiparallel (a higher energy state) to the direction of B_0. At thermal equilibrium, the distribution of nuclei in the two energy states is given by the Boltzmann distribution

$$\frac{N_{up}}{N_{down}} = e^{-\left(\frac{\Delta\epsilon}{\kappa_B T}\right)} \qquad 6.2$$

where, $\Delta\epsilon$ = energy difference (J), κ_B = Boltzmann constant 1.38x10^{-23}, and T = absolute temperature (K). Therefore, at 23° C (296.15K) and 1.5T (ω_0=63.86x10^6 Hz), the excess number of magnetic dipoles in the low energy state is approximately five ppm. The magnetic dipoles will produce an overall net effect, which is summarized as the bulk magnetisation vector $\boldsymbol{M}$.

In order to detect $\boldsymbol{M}$ in the presence of a strong static magnetic field B_0, $\boldsymbol{M}$ needs to be reoriented perpendicular to the static field (i.e. the transverse x-y plane)[153]. This reorientation can be achieved by applying an alternating magnetic field B_1, at the Larmor frequency, orthogonally, e.g. in the x-direction, to the direction of the static magnetic field B_0 (z-direction). The B_1 field is usually created within a resonant radiofrequency (RF) transmit 'coil' or 'antenna' that surrounds the object of interest, and the pulse to generate B_1 is termed the RF pulse. For example, an ideal 90° RF pulse will tip the magnetic moment $\boldsymbol{M_0}$ from its equilibrium direction (e.g. longitudinal, or z-direction) to the transverse plane (e.g. x-y plane). After the RF pulse, the longitudinal magnetization will return to equilibrium via T_1 relaxation. In the transverse plane, the spin phase coherence is gradually reduced through T_2^* relaxation due to spin-spin interactions (T_2) and magnetic field non-uniformities (T_2'), causing decay of transverse magnetization. The precessing transverse magnetic moment induces an electric current in the receiver coil, forming the MR signal. Although magnetic resonance is a quantum behaviour, due to a large number of spins, a classical model known as the Bloch Equation 6.3 is usually sufficient to describe the macroscopic behaviour of magnetic resonance.

$$\frac{d}{dx}\begin{pmatrix} M_x \\ M_y \\ M_z \end{pmatrix} = \begin{pmatrix} -1/T_2 & \gamma B_z & -\gamma B_y \\ -\gamma B_z & -1/T_2 & \gamma B_x \\ \gamma B_y & -\gamma B_x & -1/T_1 \end{pmatrix}\begin{pmatrix} M_x \\ M_y \\ M_z \end{pmatrix} + \begin{pmatrix} 0 \\ 0 \\ M_0/T_1 \end{pmatrix} \qquad 6.3$$

where γ is the gyromagnetic ratio, $M_{x,y,z}, B_{x,y,z}$ are the magnetization and magnetic field strength respectively in the longitudinal (z) and transverse (x, y) plane, and T_1, T_2 are the

longitudinal and transverse relaxation times, respectively.

To use magnetic resonance for imaging, we spatially encode the MR signal using magnetic field gradients (G)[154]. Because the magnetic moment precesses at the Larmor frequency that is proportional to the magnetic field strength, a magnetic field gradient applied in addition to B_0 will create different resonant frequencies along the gradient direction. Consider a magnetic field gradient along the x-direction and a static magnetic field B_0 in the z-direction, we have

$$\frac{\partial B_z}{\partial x} = G_x \tag{6.4}$$

Then this gradient is superimposed on the static magnetic field B_0, the magnetic field at a location x given by B(x), which can be expressed by

$$B(x) = B_0 + G_x x \tag{6.5}$$

According to the Larmor equation 6.1, the spins at position x will resonate at a frequency

$$\omega(x) = \gamma[B_0 + G_x x] \tag{6.6}$$

or in a reference frame rotating at a frequency ω_0, the precessional frequency at location x becomes

$$\omega(x) = \gamma G_x x \tag{6.7}$$

Let the spin density at location x be $\rho(x)$, in which case the signal for spins between location x to $x + \delta x$ can be written in a complex form as

$$dS(x) = \rho(x)e^{-i\omega(x)t}dx = \rho(x)e^{-i\gamma G_x x t}dx \tag{6.8}$$

or for the entire object from x to $x + \delta x$

$$S(x) = \int_{x}^{x+\delta x} \rho(x) e^{-i\gamma G_x x t} dx \qquad 6.9$$

These equations show that $S(x)$ is the Fourier Transform of $\rho(x)$. In the general case of a continuous distribution of spin density, the signal with 2D orthogonal encoding becomes

$$S(x,y) = \iint \rho(x,y) e^{-i\gamma G_x x t} e^{-i\gamma G_y y t} dx dy \qquad 6.10$$

The spin density, $\rho(x)$, incorporates all effects within the spin density, such as T_1 and T_2 relaxation.

By applying the gradients over a period of time, a spatially dependent phase offset can be created, which is thus used to encode the spins in different locations of the sample.

$$\Delta\phi(\mathrm{x}) = \gamma \int_{t_1}^{t_2} G_x(t) \cdot x \, dt \qquad 6.11$$

This phase offset can be applied either immediately before or during an acquisition. As a convention, it is helpful to consider this phase offset in a domain called *k*-space.

Gradient induced resonance frequency differences also enable slice selective excitation. When an RF pulse with a particular frequency and bandwidth is applied together with a gradient G_z, only the nuclei at the locations with matched resonance frequency can be excited. The profile of excitation can be modulated by controlling the magnetic gradient and RF pulse. The RF centre frequency determines the excited slice location; the magnitude of G_z and the RF bandwidth together determines the slice thickness (Figure 6.1). For example, while applying a gradient G_z, a SINC RF pulse with bandwidth $\Delta\omega_{RF}$ will generate a rectangular slice excitation with a slice thickness

$$\Delta z = \frac{\Delta\omega_{RF}}{\gamma G} \qquad 6.12$$

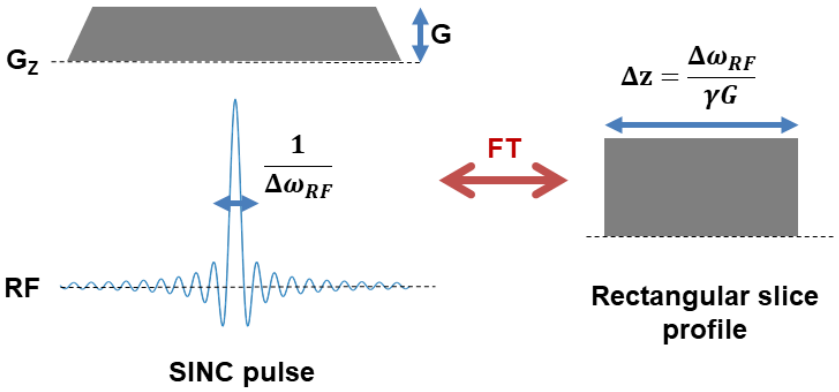

Figure 6.1 A slice selection gradient and SINC RF pulse are shown, which causes a rectangular spatial region, Δz, to be excited[153]

Besides frequency encoding, the phase of magnetic precession can also encode spatial information through the spin-warp imaging method[155]. When a phase encoding gradient G_y is applied, nuclei along this gradient direction start to precess at different frequencies. The relative phases start to accumulate at a rate proportional to the gradient amplitude and duration. The phase information will remain after G_y is switched off and will have prepared the spins for frequency encoding. For 3D imaging, a second phase encoding can be applied along the slice selection direction. The frequency encoding, phase encoding and slice selection together form the spatial encoding mechanism of MRI.

The pulse sequence diagram below (Figure 6.2) illustrates a typical spoiled gradient recalled echo sequence (SPGR), with the RF pulse, slice selective gradient (Gz), phase encoding gradient (Gy), and frequency encoding gradient (Gx). Additional rephasing gradients and spoiler gradients are applied to maintain a constant view-dependent phase but also dephase any remaining transverse magnetization.

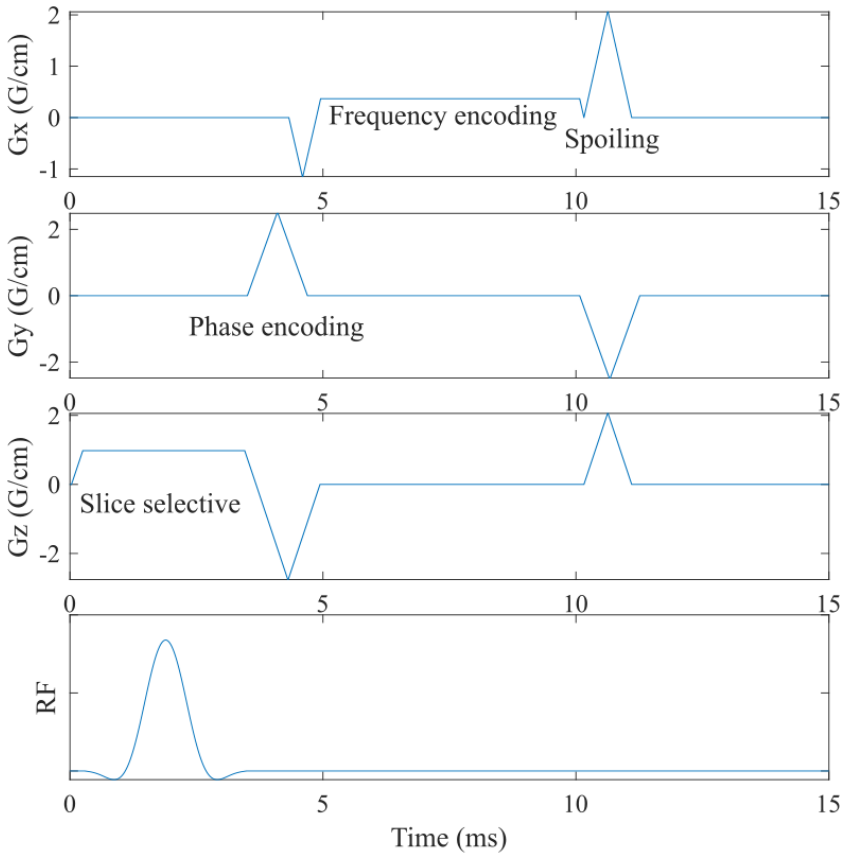

Figure 6.2 Pulse sequence diagram of 3D spoiled gradient recalled echo sequence

The MR signal acquired with the SPGR sequence can be arranged on a 2D grid according to the frequency and phase of each data point. Because the frequency and phase gradients are applied separately, the 2D grid represents the k-space, which is the 2D Fourier transformation of the image. The signal at each k-space location can be expressed as:

$$S(u,v) = \int_{-\infty}^{\infty} I(x,y) e^{-2\pi i \vec{k}(t)} dxdy \qquad 6.13$$

$$\vec{k}(t) = \frac{\gamma}{2\pi} \int_{0}^{t} \vec{G}(t') dt' \qquad 6.14$$

where $S(u,v)$ is the MR signal at a k-space location (u,v), $I(x,y)$ is the image intensity at the

image coordinate (x, y), and $\vec{k}(t)$ is the k-space trajectory that is proportional to the time integral of the gradient $\vec{G}$. A frequency or phase gradient application is equivalent to traversing the k-space along the frequency (horizontal) or phase (vertical) dimension, as shown in Figure 6.3. The image can be reconstructed with a simple 2D inverse fast Fourier transformation (IFFT). Because the sampling locations form a Cartesian grid, this trajectory is called the Cartesian trajectory.

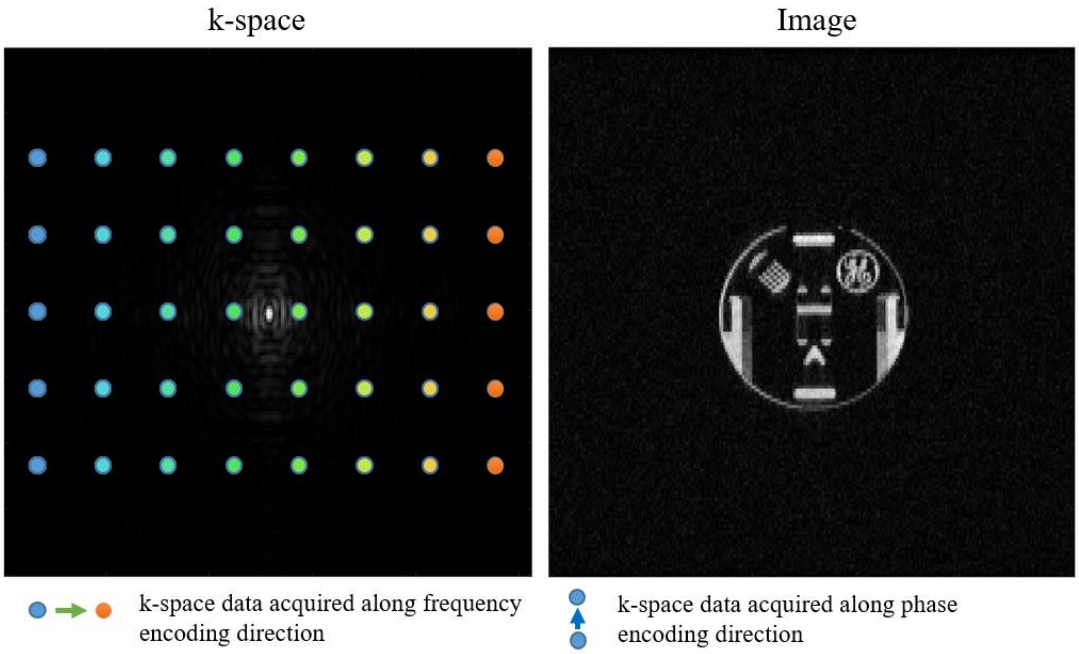

Figure 6.3 Cartesian k-space trajectory and image (acquired using a 1.5 T GE 450w)

In practice, most of the MR signal amplitude is at the centre of the k-space, representing the low-frequency components, and the high-frequency signals at the periphery are usually low in magnitude. To improve sampling efficiency, MR sequences with non-Cartesian trajectories, such as spiral and radial trajectories, were developed to increase the sampling density near the k-space centre.

6.2 Coronary MR

As mentioned in Chapter 1.2.2, the application of MR imaging in coronary diseases offers the characterization of plaque morphology and composition, and enables the evaluation of cardiac function without the risk of ionizing radiation. The major challenges in coronary MR

are the small calibre and complex motion of coronary arteries[156]. The improvement of spatial resolution requires more acquired data, and the motion suppression often requires gating of acquisition, both increasing the total scan time. An efficient data acquisition method is necessary for practical coronary MR imaging.

Sequences with non-Cartesian trajectories are known for their high sampling efficiency and resistance to motion and are often used in coronary MR. Spuentrup *et al.* compared the image quality of two steady-state free precession (SSFP) MR angiographies with Cartesian and radial trajectories, and showed that the radial sequence offers better image quality, vessel sharpness and less motion artefacts[157]. Bornert *et al.* compared the coronary MR angiography acquired with 3D Cartesian trajectory, 3D stack-of-spirals trajectories with single and double interleve[158]. The stack-of-spirals images showed a superior signal-to-noise ratio (SNR) and contrast-to-noise ratio (CNR) than the Cartesian images and a 50% reduction in scan time in the stack-of-spirals sequence with double interleaves. However, the non-Cartesian drawbacks such as susceptibility to off-resonance blurring and streaky artefacts were also reported in these comparisons.

The motion in coronary MR consists of cardiac and respiratory motions. Although the non-Cartesian sequences are less sensitive to motion artefacts, additional prospective or retrospective motion compensation is necessary for better image quality. Cardiac motion is often prospectively suppressed through ECG gating. Data are only acquired during the end-systolic or mid-diastolic phase of the cardiac cycle[156]. Since only one set of data is acquired for each cardiac interval, the scan time will increases for patients with reduced heart rate (e.g. with beta-blockade). Respiratory motion can also be suppressed through the gating of a respiratory signal. The combination of cardiac and respiratory gating may significantly extend the scan time. Alternatively, breath-holding acquisition entirely removes the respiratory motion but limits the acquisition window to <20 seconds.

On the other hand, retrospective motion compensation aims to reduce motion artefact by estimating and compensating the motion after data acquisition. During a free-breathing acquisition, the respiratory motion is recorded in the acquired data and can be estimated through an embedded 1D/2D navigator sequence. Wang *et al.* developed an adaptive motion correction sequence by placing two 1D navigator sequences (near the diaphragm) before and after the k-space acquisition train[159]. Data were collected with cardiac gating and free-

breathing. The respiratory displacement of each image echo was determined by interpolating the start and end navigator positions. During image reconstruction, the displacements were applied and multiplied by an adaptive factor that provides the sharpest image. The adaptive motion correction method showed an increase in image sharpness and improved scan efficiency.

For radial sequences, each radial spoke can function as a navigator, and the motion can be estimated through the principal component analysis (PCA) of each k-space centre[160]. With the motion information, the k-space data can be sorted and binned into different motion states. Because of data downsampling, iterative reconstruction with data acceleration is often used in combination, which provides motion resolved coronary images. Feng *et al.* developed a continuous free-breathing cardiac sequence with a golden angle stack-of-stars sequence. The acquired data were sorted by cardiac and respiratory states estimated from the partial Fourier transform of the centre of spokes. The sorted data were then reconstructed by an iterative algorithm that exploited the sparsity of radial trajectory data. Feng's method largely improved the acquisition efficiency of coronary MR and provide motion resolved images for future clinical analysis.

Besides motion correction, another challenge in coronary MR is generating adequate image contrast between the lumen, the vessel wall, the myocardium and the epicardial fat. Contrast enhancement is more important in 3D scans than in 2D scans because of the reduction of contrast between blood and myocardium due to the in-flow effects[161]. The lumen contrast can be achieved with or without a contrast agent. Late gadolinium enhancement technique can indicate inflammation in plaques through the non-specific uptake of contrast in patients with acute coronary syndroms[162]. When a contrast agent is unavailable, the non-contrast enhanced techniques offer a non-invasive alternative. For vessel wall imaging, a hyperintense lumen can overshadow the boundaries and components of plaques, and black blood is preferred to visualize. The double inversion recovery (DIR) and the motion-sensitized driven-equilibrium (MSDE) methods are two common preparation pulses to null the MR signal in blood. The DIR method uses a non-selective inversion pulse (180º) to invert the magnetization in the imaging volume, follow by another selective inversion pulse to restore the magnetization and allow in-flow of the inverted blood[163]. The MSDE method exploits the intravoxel dephasing of voxels with blood flow. A 90º pulse follows by a refocusing 90 º pulse, with motion-sensitized gradients before and after the refocusing pulse. Static tissue will experience net

zero moment, and moving tissue will experience the higher-order moment and dephasing[164,165]. Like MSDE, the Delay alternating with nutation for tailored excitation (DANTE) also induces the dephasing of moving spins[164]. In DANTE, a train of small flip angle RF pulses is interleaved with gradients. The moving spins cannot establish a steady state due to the spoiling effect of flow along the applied gradient, and the static spins preserve the phase coherence. In addition to the black blood preparation, the fat saturation preparation pulse is often used in cardiac MR to suppress signals from epicardial fat and separate the coronary lumen. The T2 preparation pulse is often used to suppress signals from the myocardial tissue.

The coronary MR in PET/MR scanners experiences more difficulties due to hardware constraints and system design. Volunteer images were acquired with a 3 T GE Signa PET/MR system using a product rapid gradient recall (3D HEART) sequence (FOV 42cm, flip angle 20^{o}, acquisition matrix 512×512×28, TE 2.0 ms, TR 7.98 ms, NEX=1, voxel 0.8×0.8×2 mm^3, RBW ±97.5kHz, acquisition time 4:45min, ECG gated).

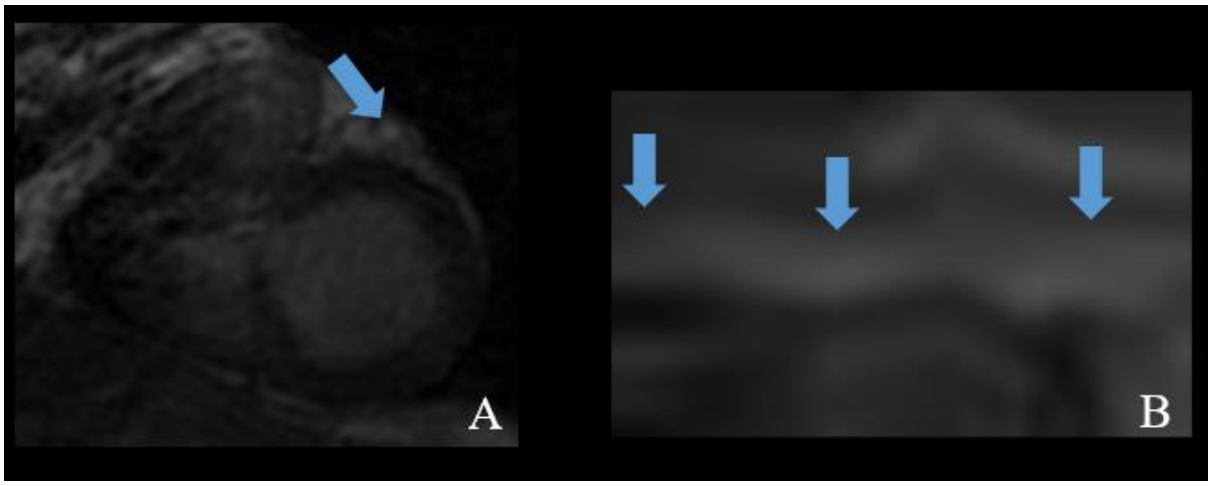

Figure 6.4 Cardiac MR images acquired with 3T PET/MR using 3D HEART sequence (A: short axial view, arrow indicates a coronary vessel, B: a curved plane view of the coronary vessel was reconstructed by tracking the centre of the vessel)

The integration of PET and MR systems requires compromises in hardware designs. For example, the gradient performance in the PET/MR system is degraded compared to a normal 3T MR scanner (maximum gradient strength GE 3T Signa PET/MR: 44 mT/m, GE 3T MR750: 50 mT/m). The lower gradient strength could limit the minimum TE/TR and influence the

image contrast in PET/MR images. Field homogeneity is another compromise in the PET/MR system, and could result in regional signal attenuation and off-resonance artefacts. In addition, the Cartesian trajectory acquisition and ECG trigger used in the 3D HEART sequence prolong the scan time. Although acquired with an ECG trigger, the image contained motion-blurring artefacts, especially near the right ventricular wall. In the PET/MR system, the more complex electromagnetic environment may interfere with the ECG signal, creating additional challenges in accurate ECG triggering. A non-ECG gated acquisition with retrospective motion correction or motion-resolved reconstruction may alleviate the motion blurring. To improve the limited image quality of the product sequence in the PET/MR system, an efficient non-Cartesian free breathing MR sequence will be desirable.

6.3 Stack-of-spirals MR sequence

The spiral sequence follows a spiral trajectory in k-space and can cover a large portion of k-space after each RF excitation, reducing the total scan time. Compared to the sequences with Cartesian trajectories, spiral sequences are more efficient in data collection because of their extensive coverage and not collecting data at the corners of k-space[166]. However, the non-Cartesian trajectories are more vulnerable to the off-resonance artefact. Resonance offset causes displacement of the off-resonant spins in the readout direction and appears as an image shift in the Cartesian trajectory images, For the non-Cartesian trajectories, the displacement rotates and accumulates as the trajectories' direction change and appears as blurring artefacts in the image. Unlike Cartesian trajectories, the sampling density in spiral trajectories is not uniform. Spiral trajectories sample at a higher density at the centre of k-space and sample more sparsely as the radius increases. The oversampled k-space centre makes spiral trajectories less sensitive to patient motion but requires density compensation during image reconstruction.

When designing the spiral trajectory, the trajectory curvature and k-space distance of adjacent data points are limited by the maximum slew rate and the maximum gradient amplitude of the MR system. Multiple spiral interleaves with different rotations can reduce the distance between k-space data points and achieve a desirable field of view (FOV) in the image domain (Figure 6.5 A). For 3D imaging, additional phase encoding is necessary. For example, separate phase encoding gradients G_z will create stack-of-spirals trajectories in the slice selection direction (Figure 6.5 D); a simultaneous G_z with the spiral gradients G_x , G_y will create a 3D cone shape trajectory.

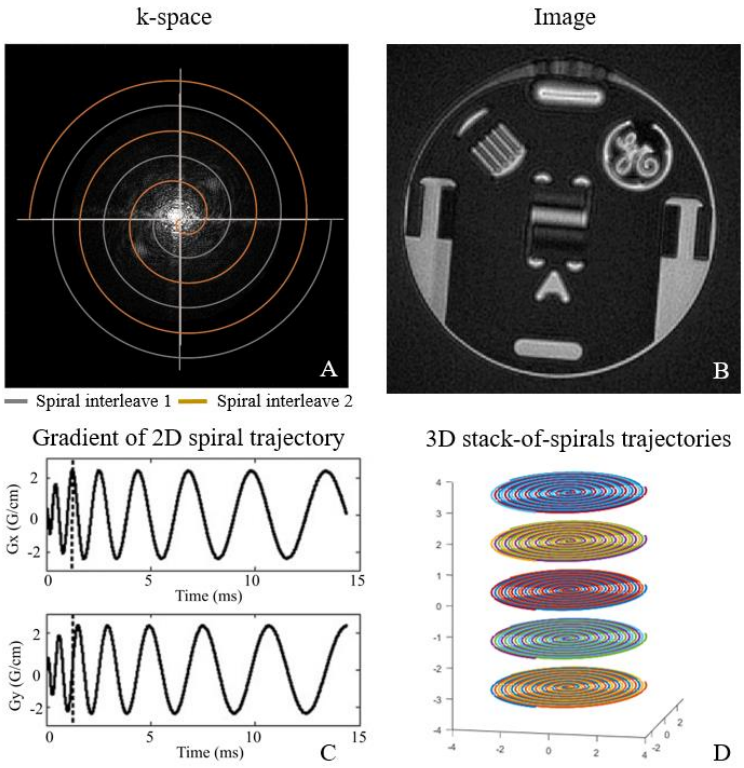

Figure 6.5 k-space trajectory (A, D), image (B) and gradient waveform (C, redrawn from literature[167]) of spiral sequence (acquired using a 1.5 T GE 450w)

Spiral sequences usually use the Archimedean spiral in which the radius r is proportional to the azimuthal angle θ. The Archimedean spiral trajectory can be modelled as:

$$r(t) = \lambda\theta(t) \qquad 6.15$$

$$k_x = rcos(\theta) = \lambda\theta cos(\theta);\ \ k_y = rsin(\theta) = \lambda\theta sin(\theta) \qquad 6.16$$

where λ is a spiral constant that controls the spiral density. Combining Equation 6.16 with Equation 6.15, the spiral gradient G_x, G_y and its magnitude $G(t)$ can be expressed as:

$$G_x = \frac{2\pi}{\gamma}\dot{k}_x = \frac{2\pi}{\gamma}\lambda\dot{\theta}(\cos(\theta) - \theta\sin(\theta)) \quad 6.17$$

$$G_y = \frac{2\pi}{\gamma}\dot{k}_y = \frac{2\pi}{\gamma}\lambda\dot{\theta}(\sin(\theta) + \theta\cos(\theta)) \quad 6.18$$

$$G(t) = \sqrt{G_x^2 + G_y^2} = \frac{2\pi}{\gamma}\lambda\dot{\theta}\sqrt{1+\theta^2} \quad 6.19$$

where $\dot{}$ and $\ddot{}$ represents the first and second order of derivative with respect to time. The slew rate S_R, which is the time derivative of the gradient, can be expressed as:

$$\begin{aligned} S_R(t) &= \sqrt{S_{Rx}^2 + S_{Ry}^2} = \sqrt{(\dot{G}_x)^2 + (\dot{G}_y)^2} \\ &= \frac{2\pi}{\gamma}\lambda[\left(\ddot{\theta} - \theta\dot{\theta}^2\right)^2 + (2\dot{\theta}^2 + \theta\ddot{\theta})^2]^{1/2} \end{aligned} \quad 6.20$$

Near the centre of the spiral, the trajectory is limited by the maximum slew rate (Figure 6.5 C before the vertical dotted line), where $S_R(t) = S_{R,max}$, $G(t) < G_{max}$. As the radius increases, the trajectory enters the gradient limited segment (Figure 6.5 C after the dotted line), where $G(t) = G_{max}$. Solving G_x, G_y under the slew rate and gradient constrain provides the gradient waveform for the Archimedean spiral trajectory. In practice, a closed form approximate solution is usually used to calculate spiral gradients[166] (Figure 6.5 C).

The image reconstruction for spiral images requires additional processing before Fourier transformation. Because of non-uniform sampling density, the data of low-frequency components are over-represented in the spiral data. Density compensation is necessary to suppress the low-frequency signals by inversely scaling the data according to the local sampling density. The k-space Voronoi areas can estimate the k-space area for each data point, which can be multiplied with k-space data intensity for density compensation in non-Cartesian trajectories. Figure 6.6 A illustrates the k-space trajectories of eight interleave spirals, and the corresponding Voronoi boundaries are shown in Figure 6.6 B. After density compensation, the low-frequency component in the reconstructed image (Figure 6.6 C) was suppressed, and the

image is less blurred than the image without density compensation (Figure 6.6 D).

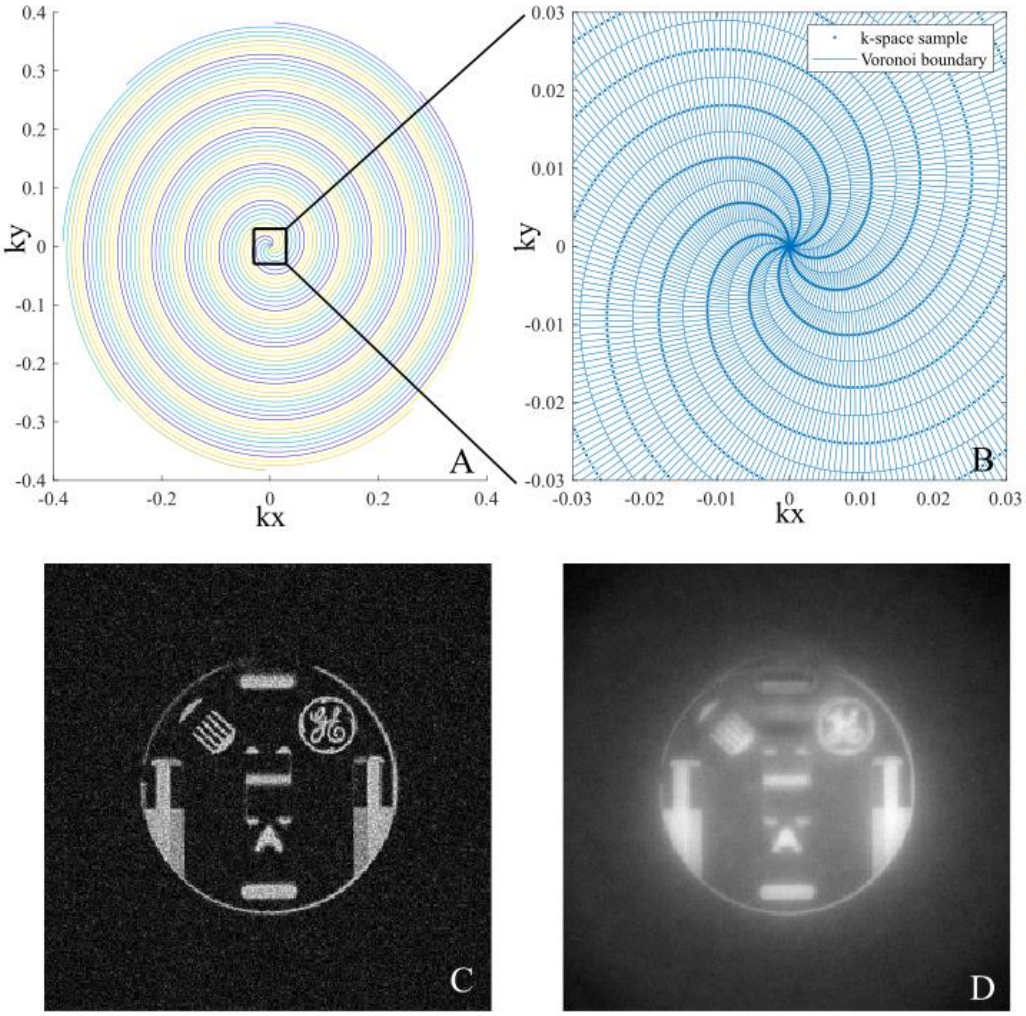

Figure 6.6 Spiral Trajectories (A) and the Voronoi boundaries of the central k-space. The images were reconstructed with (C) and without (D) density compensation of Voronoi areas. (Acquired using a 1.5 T GE 450w)

There are two standard methods to reconstruct images with density compensated k-space data: gridding and the non-uniform fast Fourier transformation (NUFFT)[168]. A Cartesian k-space grid is created in the gridding method, and data on the Cartesian grid is estimated by interpolating the surrounding non-Cartesian data. Each non-Cartesian data is convolved with a gridding kernel and is then mapped to the Cartesian grid[167]. The choice of convolution kernel can influence the aliasing in the gridding, and the Kaiser-Bessel filter is an optimized filter to reduce the aliasing and gridding error. Convolution with a finite extent kernel will cause

aliasing sidelobe artefacts. The replica sidelobes can be pushed away from the central FOV by increasing the grid density. The gridding accuracy has a trade-off between subsampling rate and computational complexity; a subsampling rate of two is usually sufficient to reduce the sidelobes. The interpolated Cartesian grid is transformed to the image through an inverse 2D FFT, and the FOV is cropped. The gridding kernel also results in signal apodization, appearing as signal attenuation towards the edge of FOV. The image is divided by the Fourier transformation of the gridding kernel to correct such attenuation.

The NUFFT approach implements the reconstruction by solving an optimization problem. An initial image is first multiplied by a diagonal scaling matrix and is then transformed to a Cartesian k-space via a forward FFT operation. The Cartesian data is interpolated to the non-Cartesian trajectory, and the data consistency is calculated by subtracting the acquired non-Cartesian data. The data consistency function is used as the cost function, whose gradient can be calculated from the adjoint of the forward operators (scaling, FFT, and interpolator[168]). Iterative solvers such as gradient descent can solve this inverse problem and produce the reconstructed image once the data consistency satisfies a predefined tolerance. Compared to the gridding method, NUFFT does not require the density compensation process and can be applied to data sampled under the Nyquist frequency.

While a non-Cartesian trajectory provides high sampling efficiency, it is also more vulnerable to aliasing signals from the off-resonance effect. With a Cartesian trajectory, the resonance offset appears as displacements of the image along the frequency encoding direction. For a spiral trajectory, the frequency encoding direction is effectively the tangent of the spiral trajectory and rotates along the trajectory. The off-resonance spins in the spiral trajectory appear as a circular blurring of the true image (Figure 6.7 B, C). The blurring depends on the magnitude of resonance offset and the cumulated phase error. A large resonance offset and long readout time will lead to more blurring artefacts. Higher field strengths will accelerate phase accumulation and therefore increase the blurring in spiral images (Figure 6.7 C).

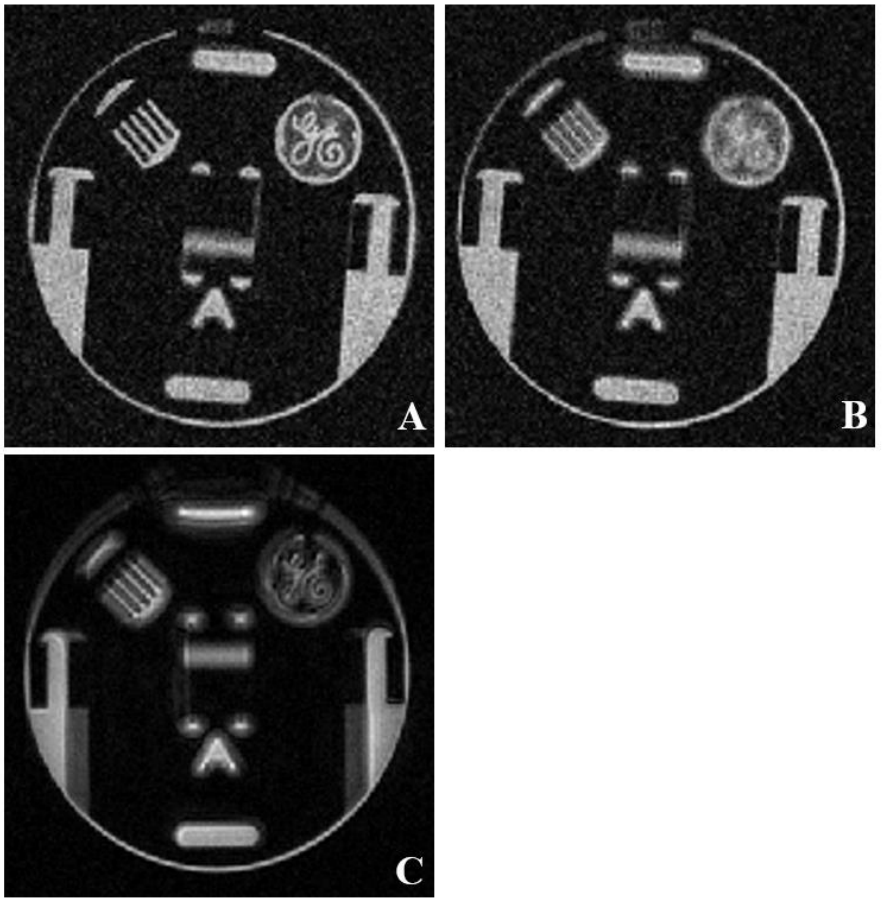

Figure 6.7 Spiral images with (A) and without (B) off-resonance correction (acquired using a 1.5 T GE 450w), image (C) is a spiral image acquired using a 3.0 T GE PET/MR, without off-resonance correction

The off-resonance correction for the spiral trajectory is complex because the phase error is a function of both space and time. The signal with an off-resonance effect can be modelled as:

$$s(t) = \int \rho(\vec{r}) exp\{-i[2\pi \vec{k}(t) \cdot \vec{r} + \Delta\omega(\vec{r})t]\}\, d\vec{r} \qquad 6.21$$

where $s(t)$ is the signal acquired at time t, $\vec{r} = r(x, y)$ is the spatial position, $\rho(\vec{r})$ is the proton density, $\vec{k}(t)$ is the k-space trajectory, and $\Delta\omega(\vec{r})$ is the spatial distribution of off-resonance frequency. Segmentation-based retrospective off-resonance corrections use binning to isolate either the spatial/frequency or the temporal component, apply phase correction and then assemble the binned component[169]. For example, the frequency segmented method

separates the off-resonance frequency into multiple bins (Figure 6.8). Phases of the k-space data are modulated by the mean frequency of each bin through a temporal conjugate multiplication ($e^{i2\pi f_{bin}t}$, where f_{bin} is the mean off-resonance frequency of each bin). FFT is applied to reconstruct images modulated by different off-resonance frequencies. The corrected image is created by assembling pixel values from each modulated image according to the spatial off-resonance frequency map. The number of segmentation bins is a trade-off in correction performance and computational complexity. In practice, the number of bins is usually approximated by $4(f_{max} - f_{min})T_{acq}$, where f_{max}, f_{min} are the maximum and minimum off-resonance frequency, and T_{acq} is the acquisition time[169].

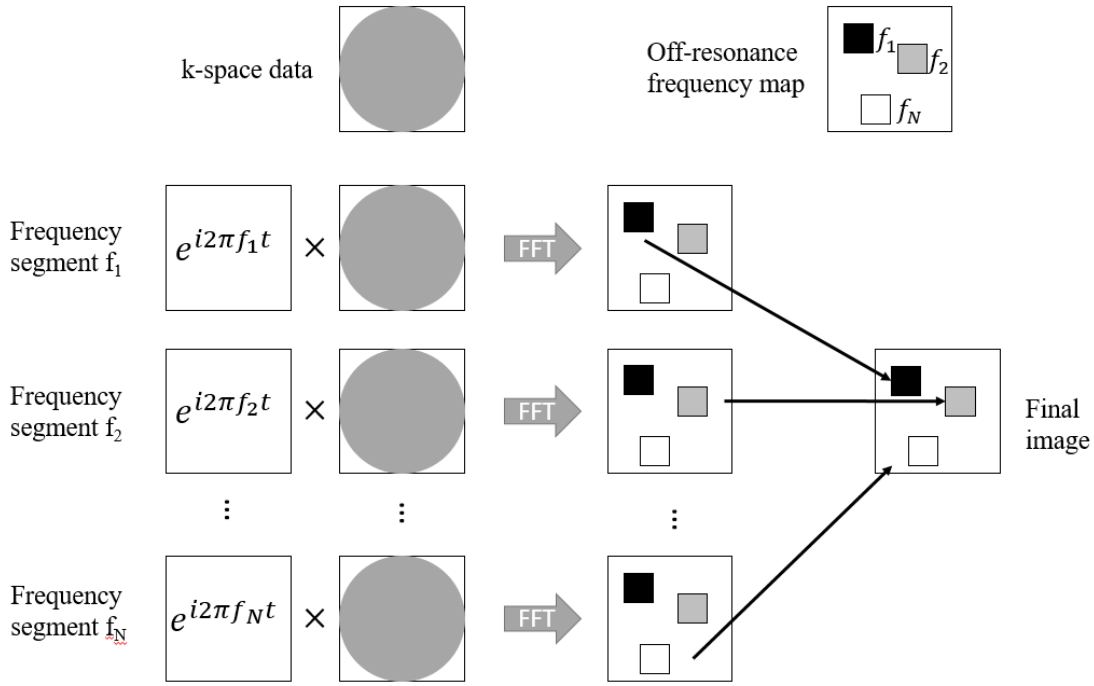

Figure 6.8 Frequency segmented off-resonance correction (redrawn from [166])

Similarly, the time-segmented method separates data into different temporal bins (Figure 6.9). For an Archimedean spiral trajectory, the k-space radius is proportional to time. The temporal bins corresponded to various k-space areas with circular or ring shapes. Phases of each temporal bin are modulated through a frequency conjugate multiplication ($e^{i2\pi\Delta\omega t_{bin}}$, where t_{bin} is the mean time of each bin). The final image is reconstructed by summing the Fourier transformation of each binned data.

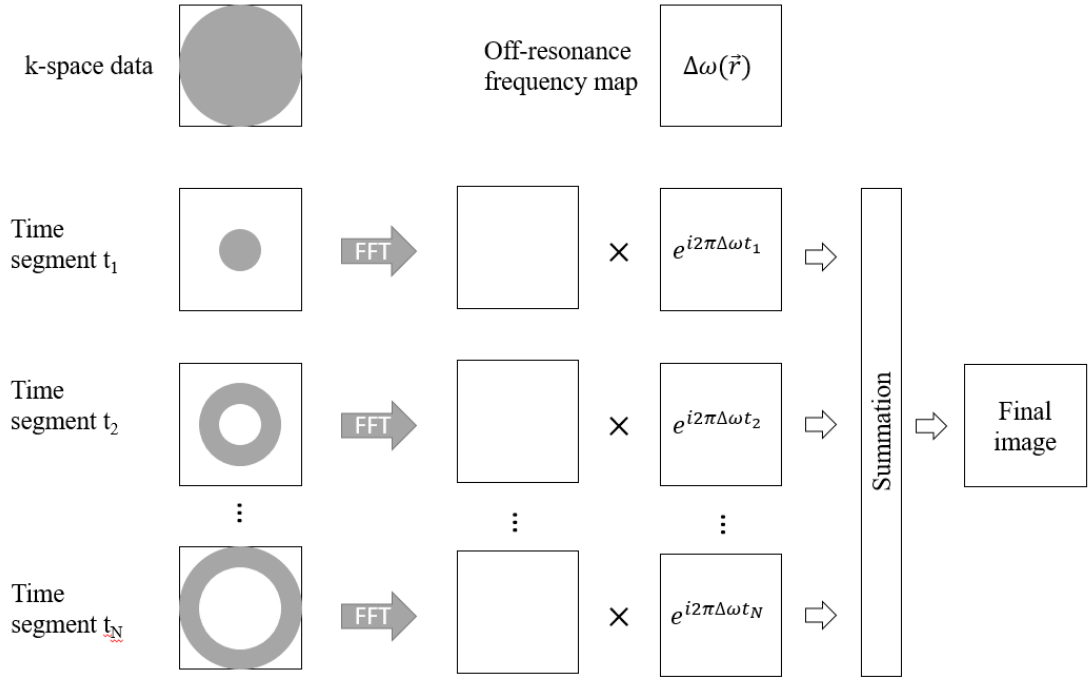

Figure 6.9 Time segmented off-resonance correction (redrawn from [166])

Both segmentation-based off-resonance corrections require an off-resonance (B_0) frequency map, and their performance heavily depends on the accuracy of the B_0 map. The off-resonance frequency map can be obtained from a variable echo time (TE) method, but accurate off-resonance mapping can be difficult, especially in high field strength systems where phase accumulates at a higher rate. The variable echo time method exploits the phase difference to estimate off-resonance. In the region of low or no MR signal, the phase can be arbitrary and the estimated off-resonance frequencies are less accurate. In addition, the extent of blurring due to the low signal region is limited because of its low magnitude. Therefore, the off-resonance correction is usually only applied to regions exceeding a magnitude threshold. Figure 6.10 shows a spiral trajectory image and the corresponding off-resonance frequency map acquired with a 3 T GE Signa PET/MR system. The off-resonance map was segmented into frequency bins (Figure 6.10 C). After conjugate phase correction for each frequency segment, the final corrected image was integrated by combining pixels according to their off-resonance frequency (Figure 6.10 D). To exclude the influence of low intensity regions, the correction was only applied to regions with a signal magnitude greater than 1% of the maximum signal magnitude. Although the correction method suppressed the blurring in certain regions, the frequency segmented method introduced image artefacts due to the inaccurate frequency

indexing, which was derived from the off-resonance frequency map. Therefore, a pixel-level accurate off-resonance frequency map is a prerequisite for effective deblurring.

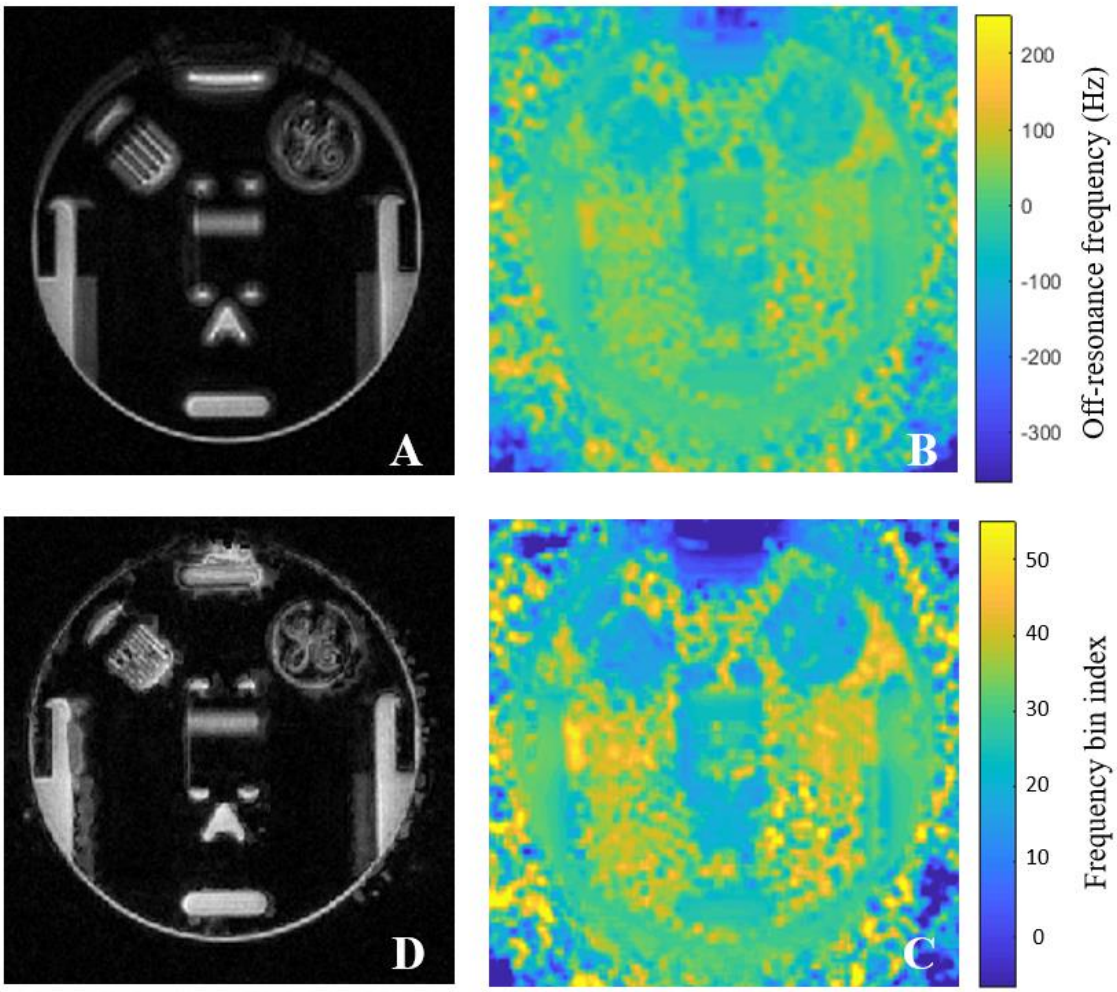

Figure 6.10 Spiral image (A) and an off-resonance frequency map (B) were acquired. The off-resonance map was segmented by frequency (C) and frequency segmented off-resonance correction was applied to the image (D) (acquired using a 3 T GE Signa PET/MR)

The auto-focusing off-resonance correction was proposed to remove the dependence on the off-resonance frequency map. Instead of phase modulation according to the frequency map, the auto-focusing method estimates the local off-resonance frequency by optimizing a focusing criteria function $fc(\omega)$:

$$fc(\omega) = \iint \left| Imag\{I(x,y;\omega)e^{-i\phi_l(x,y;\omega)}\}\right|^{\alpha} dxdy \qquad 6.22$$

where $I(x, y; \omega)$ is the image corrected with off-resonance frequency ω (using the same conjugate phase correction as in the frequency segmented method), $\phi_l(x, y; \omega)$ is the phase of the low spatial frequency component of $I(x, y; \omega)$ which is calculated by setting the high frequency component of k-space to zero followed by inverse FFT, α is a scaling parameter of value 0.5 to 1, and $Imag()$ is an operator to calculate the imaginary part of a complex number[170]. The focusing criteria are evaluated for each pixel at a range of off-resonance frequencies, and the pixel value in the corrected image is updated if a smaller $fc(\omega)$ is achieved at a particular frequency ω. For example, $fc(\omega)$ was calculated in three regions of interest (ROIs) at different off-resonance frequencies (Figure 6.11 A), and the minimum $fc(\omega)$ appeared at off-resonance frequencies of -36, 8, and -36 Hz. A separate off-resonance frequency map (Figure 6.11 B) was generated through the variable TE method, and the mean off-resonance frequencies were calculated in each ROI. The focusing criteria estimated off-resonance frequencies were close to the frequency measured with the variable TE method, indicating the auto-focusing method as a substitute method for off-resonance estimation and correction.

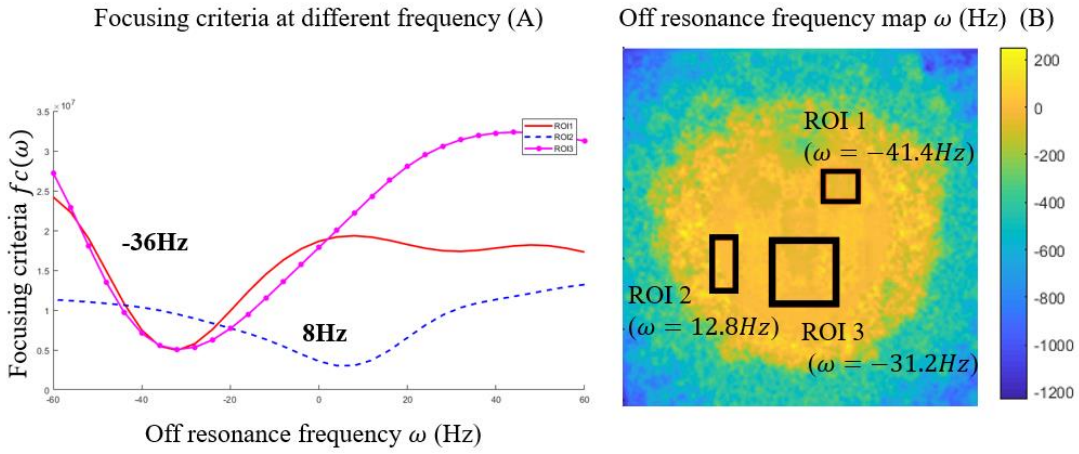

Figure 6.11 Focusing criteria at different frequencies (A) and off-resonance frequency map (B) (acquired using a 3 T GE Signa PET/MR)

The auto-focusing method is a pixel-level algorithm, and the sensitivity of the focusing criteria can cause local inhomogeneity of estimated off-resonance frequencies. Figure 6.12 B shows an image after the auto-focusing correction, in which staircase artefacts appear near the edge of the GE mark. In the estimated off-resonance frequency map (Figure 6.12 D), staircase artefacts

appear at the edges with high contrast, and the frequency is noisy over the image. A median filter was applied to the off-resonance frequency map to eliminate the staircase artefact and smooth the estimated off-resonance frequency map (Figure 6.12 E). The corresponding image was shown in Figure 6.12 C. Although the staircase artefacts were suppressed in the image, frequency map smoothing is a trade-off between deblurring performance and image artefacts, especially at locations with small structures and high contrast.

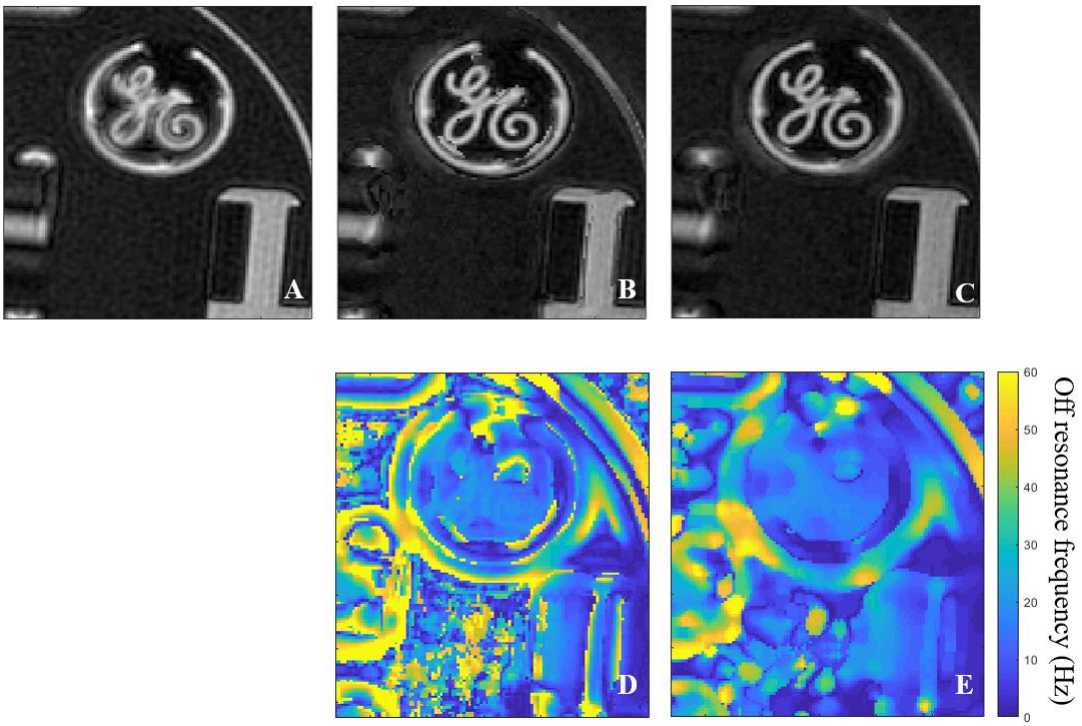

Figure 6.12 Spiral images with no off-resonance correction (A), with auto-focusing off-resonance correction (B) and with additional medial filtering of off-resonance frequency map (C). D and E are estimated off-resonance frequency maps of images B and C. (acquired using a 3 T GE Signa PET/MR)

In summary, the stack-of-spirals sequence offers high sampling efficiency but is vulnerable to off-resonance blurring artefacts. The off-resonance correction requires a more accurate B_0 mapping or focusing criteria. The current performance of off-resonance measurement or estimation in the 3 T PET/MR system impairs the application of the stack-of-spiral sequence in cardiac imaging.

6.4 Stack-of-stars Sequence

Like the stack-of-spirals sequence, the stack-of-stars sequence is a non-Cartesian trajectory in the x and y direction with an additional phase encoding in the z-direction. Instead of a spiral trajectory, the stack-of-stars sequences traverse the x/y k-space with a radial trajectory, also called the projection trajectory (Figure 6.13).

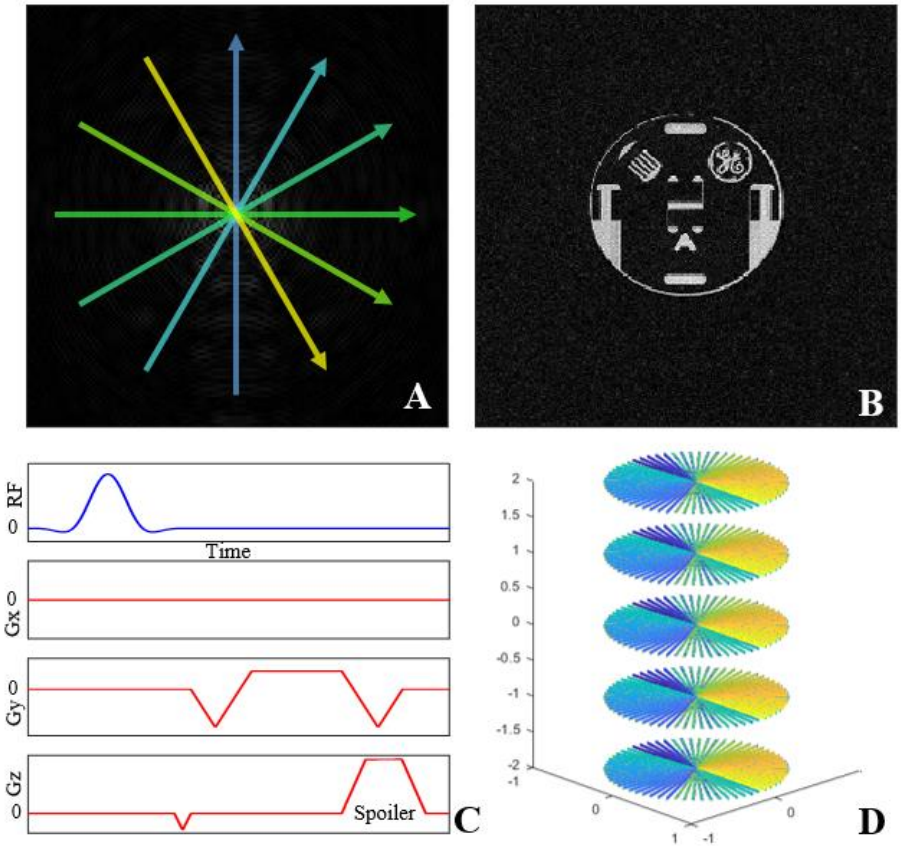

Figure 6.13 Radial trajectories, k-space (A), image (B), gradient waveform (C) and 3D trajectories of a 3D stack-of-stars sequence. (acquired using a 1.5 T GE 450w)

The design of the radial gradient waveform is more straightforward than that of the spiral trajectory. When the spoke angle is parallel to the y-direction, the radial trajectory is effectively a rectilinear Cartesian trajectory, requiring no Gx gradient. A gradient echo stack-of-stars sequence with pre-phase and re-phase gradient in the readout direction was modified from the product spiral sequence, and the gradient waveform is shown in Figure 6.13 C. The phase

encoding gradient in the slice direction (Gz) enables a stack of trajectories in the slice direction (Figure 6.13 D). The spoiler gradients (Figure 6.13 C) in the proposed stack-of-stars sequence disrupt the T_2 coherence in the transverse plane. The main source of signal in the sequence is the refocused free induction decay (FID) signal and is influenced by the T_1, $T_2^*$and proton density. Assuming a longitudinal steady-state and perfect transverse spoiling, the signal intensity of the proposed spoiled gradient echo sequence can be expressed as:

$$S = k[H]\frac{\sin\alpha\,(1 - e^{-TR/T1})}{(1 - (\cos\alpha)\,e^{-\frac{TR}{T1}})}e^{-TE/T2^*} \qquad 6.23$$

where S is the signal intensity, k is the scaling coefficient, $[H]$ is the proton density, α is the flip angle. The signal intensity is differentiable and reaches a maximum when the flip angle equals the Ernst angle, which is calculated as:

$$\alpha_E = \arccos\,(e^{-\frac{TR}{T1}}) \qquad 6.24$$

where α_E is the Ernsts angle.

An additional rotation matrix can distribute the gradient moments between the Gx and Gy directions, allowing the rotation of trajectories and a circular/cylindrical k-space coverage. The rotation of the radial trajectories replaces the traditional phase encoding gradients. As a non-Cartesian trajectory, the radial trajectories are subject to B_0 inhomogeneity and gradient non-linearity, which results in blurring artefacts. However, the angle of each radial trajectory is constant for each spoke, and the trajectory shift due to the off-resonance effect will be parallel to the spoke angle. In a spiral trajectory, the trajectory shift spreads in multiple directions as the trajectory rotates. Compared to the spiral trajectory, the radial trajectory surfers less off-resonance blurring.

The Fourier central slice theorem indicates that the MR signal for a radial spoke at angle θ is the 1D Fourier transformation of the projection of the imaging object onto an axis at angle θ. The imaging mechanism of a radial sequence is like that of X-ray computed tomography (CT), in which linear X-ray attenuation is projected and recorded at each gantry angle. The inverse Fourier transformation of the radial spoke data reveals a projection view of the imaging object.

Figure 6.14 A illustrates the MR signal after 1D IFFT along the spoke dimension, and the image demonstrates the rotational projection view like the sinogram in a CT acquisition. The reconstruction of radial sequence images is similar to that of CT reconstruction. The filtered back-projection method applies filtering in the frequency domain before the 1D IFFT for each spoke. A back projection and summation algorithm then reconstruct the images (Figure 6.14 C). Like other non-Cartesian sequences, the image of the radial sequence can be reconstructed with the gridding method. The signals from each spoke were gridded to Cartesian k-space (Figure 6.14 B), followed by a 2D IFFT for image reconstruction (Figure 6.14 D). Both reconstruction methods can provide good images with appropriate filtering and parameter selection. The gridding method and the more advanced iterative reconstruction methods can exploit additional information such as coil sensitivity, under-sampling patterns and image sparsity and are more often used than the filtered back-projection methods in practice.

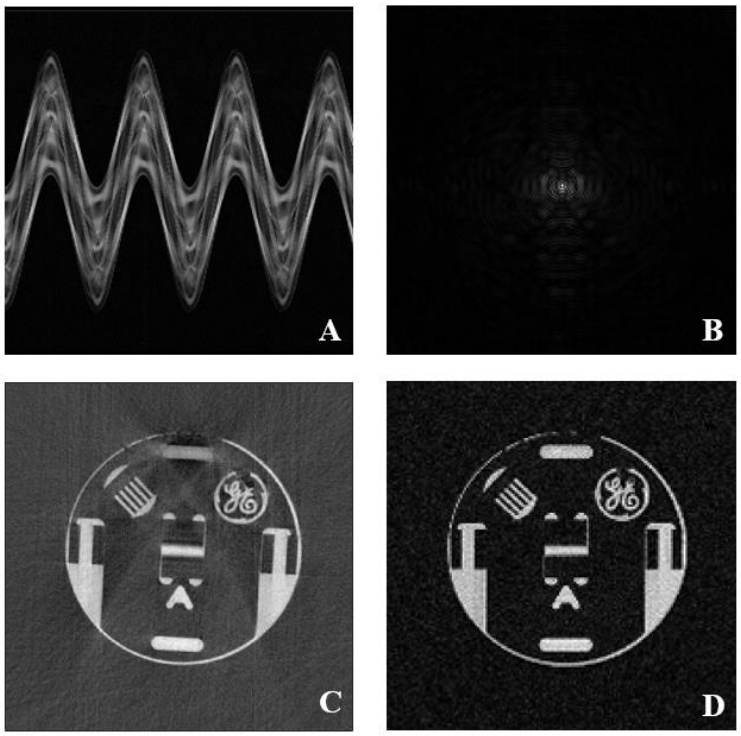

Figure 6.14 A sinogram was created by inverse Fourier transforming the signal of each spoke (A). The same data were gridded to a k-space (B). The phantom images were reconstructed with the filtered back-projection (C) method and 2D IFFT (D). (acquired using a 1.5 T GE 450w)

Another advantage of radial sequences is the inherent incoherence of the aliasing artefacts. For

Cartesian sequences with rectilinear trajectories, data under-sampling results in wrap-around/aliasing artefacts and impairs the image interpretation. For radial sequences, angular under-sampling creates incoherent streaky artefacts but preserves the shape of the imaging object. The incoherence property makes radial sequences suitable for use with imaging acceleration techniques such as compressed sensing (CS). CS exploits the sparsity of MR images and the incoherence of the under-sampling artefacts and uses an iterative optimization method to reconstruct images from the under-sampled MR signal[171]. The performance of CS relies on the incoherence of the sampling pattern. Rotation of the radial trajectories introduces incoherence to the radial acquisition and improves the reconstruction accuracy with iterative optimization algorithms. In addition, each radial spoke covers an even amount of low and high spatial frequencies, which is desirable to the under-sampling reconstruction process[172].

Besides incoherence, the rotational scheme of a radial acquisition adds an additional property in k-space coverage. Conventionally, the number of spokes is predefined, and the adjacent radial spokes are rotated with the same angle to cover the direction from 0 to π evenly. The trajectories cover a circular k-space area (Figure 6.15 A). When acquiring radial data with a particular rotation angle between adjacent spokes, one can achieve relatively uniform k-space coverage with an arbitrary number of radial spokes. This particular angle is termed the golden angle (111.25^{o}), and the k-space coverage is closest to uniform when the number of spokes belongs to the Fibonacci series (e.g., 13 spokes in Figure 6.15 C). Compared to the evenly rotated image in Figure 6.15 B, the golden angle radial image (Figure 6.15 D) contains more streaky artefacts due to the less uniform k-space coverage. However, the quasi-random golden angle scheme introduces more incoherence to the sampling pattern and allows the reconstruction with an arbitrary number of spokes from the recorded signal. The relatively uniform coverage is beneficial when the number of spokes is not available (e.g., in real-time imaging) and when spoke level gating and reordering are necessary to provide temporal and motion resolved images.

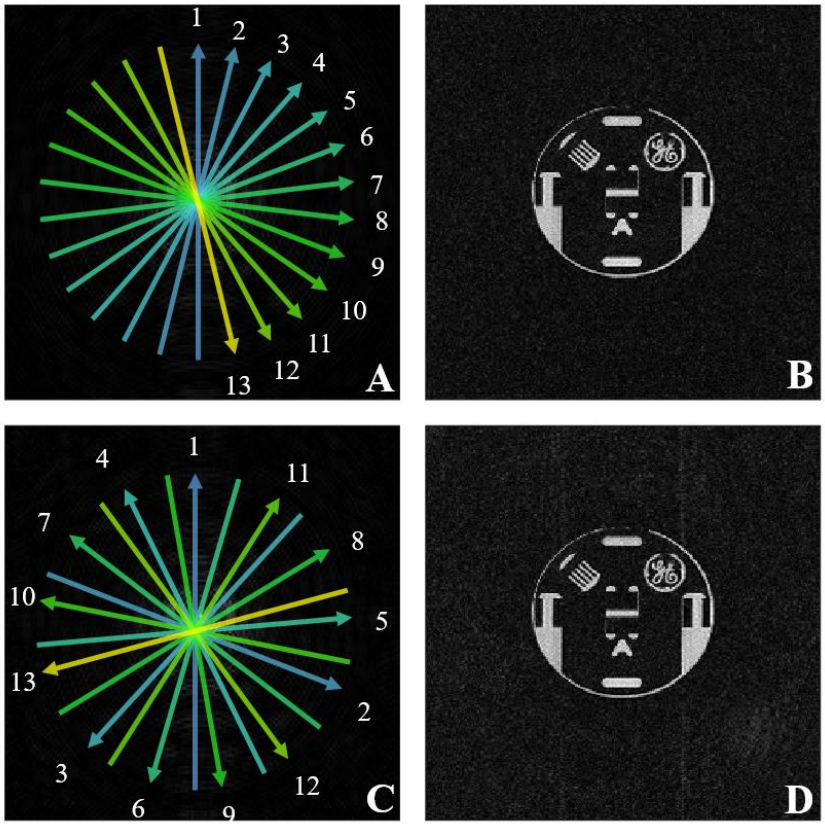

Figure 6.15 Evenly rotated (A) and golden angle rotated (C) radial trajectories, and their images (B, D) (acquired using a 1.5 T GE 450w)

While increasing incoherence in the sampling pattern, the radial sequence also requires accurate gradient performance to control the rotated trajectory. Delays in gradient arrival time could cause a shift of the k-space trajectories and degrade the image quality. For a sequence with a rectilinear trajectory, the gradient delay can be corrected by measuring the delay along the readout direction. For a radial sequence, the readout directions are rotating and different for each spoke. The gradient delays may be different due to the combination of gradients in the x and y-direction. The gradient delay correction for a radial sequence requires a pair of antiparallel calibration spokes at different spoke angles with directions 0 to π (Figure 6.16 A). The amount of gradient delay is estimated by comparing the relative shift between the two antiparallel spokes. In the absence of gradient delay, the forward spoke data should be the same as the temporal reverse of the backward spoke data. Any gradient delay will cause a temporal shift between the forward and backwards spoke, and the delay is half of the temporal difference. To estimate gradient delay, the following function is calculated:

$$g(x) = FT\left(\left|S_f\right|\right) * conj\left(FT(|S_b|)\right) \quad 6.25$$

where S_f is the forward spoke (Figure 5.13 B), S_b is the backward spoke (Figure 6.16 C), FT is the Fourier transformation[173]. Fourier transformation of $g(x)$ gives the cross correlation of the forward and backward spokes, and the peak location indicates the relative shift between the two peaks (Figure 6.16 D). However, the gradient delay is usually small compared to the sampling time, and the cross-correlation method does not provide enough temporal resolution. The slope of $g(x)$'s phase is used to estimate a precise delay. Since the phase of $g(x)$ is defined only in regions with non-zero signal intensity, the slope is estimated with a linear regression within the support of the object Figure 6.16 E). The amount of k-space shift due to gradient delay is calculated as:

$$k_{shift} = -slope \cdot \frac{Baseresolution}{2\pi} \quad 6.26$$

The estimation is repeated for different directions and replicated for angles π to 2π. Figure 6.16 F illustrates a gradient delay map (in the unit of k-space step) in different directions.

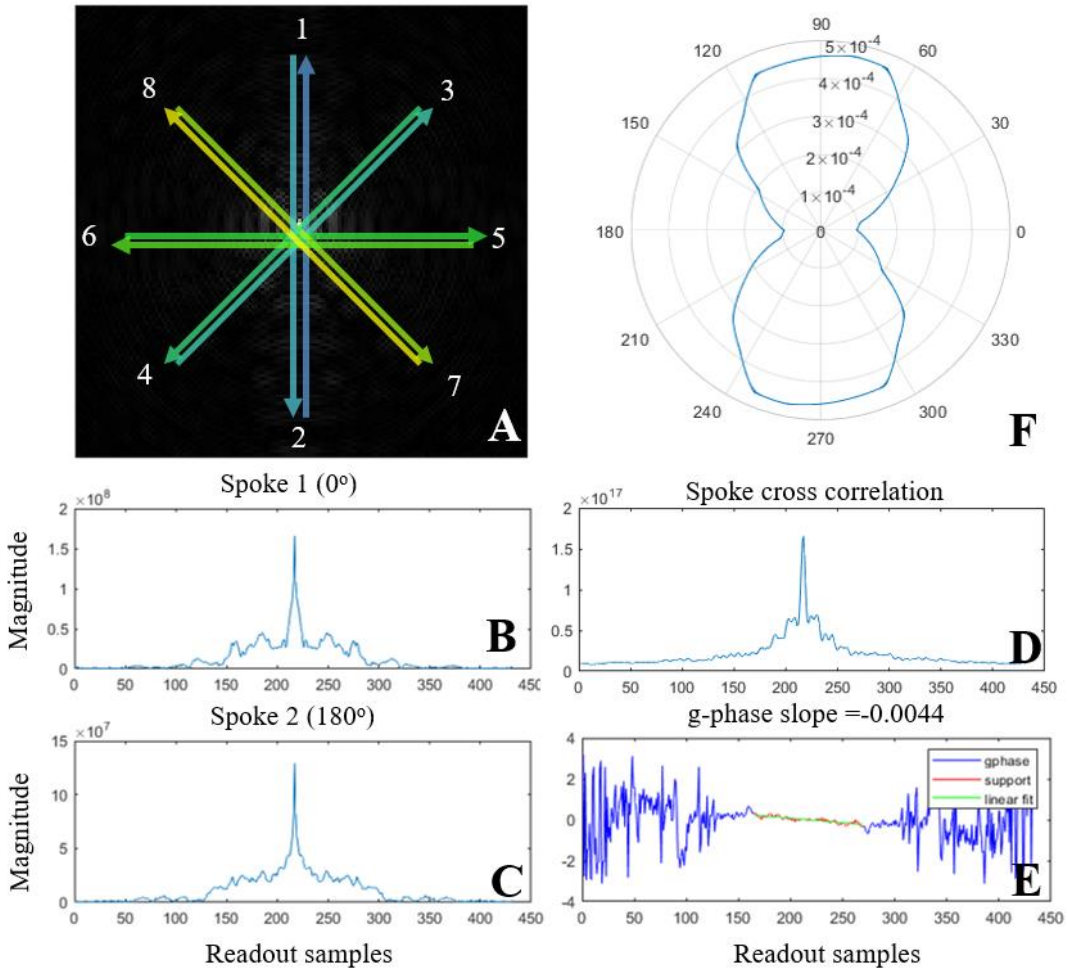

Figure 6.16 Gradient delay estimation uses a pair of antiparallel spokes for each orientation (A). The forward spoke (B) and the temporal reversed backwards spoke (C), and their cross correlation (D) is calculated. The gradient delay is estimated by the slope of the $g(x)$'s phase (E), and a gradient delay map in unit of k-space step (F) is generated by repeating the estimation for all directions. For multi-coil images, the gradient delay is summed and weighted by the L2 norm of signals in each channel to avoid weak signals from a particular coil. (acquired using a 1.5 T GE 450w)

The gradient delay causes a time delay in the k-space acquisition and is equivalent to frequency modulation in the image domain. The gradient delay correction can be performed by frequency modulation in the image domain or a shift in the k-space domain. The estimated gradient delay from the previous step is in the unit of k-space steps, and the corrected k-space trajectory is generated by shifting the spoke trajectory opposite to the delay direction (Figure 6.17 A, C). After k-space gridding, the gradient delay corrected image (Figure 6.17 D) shows

slightly better intensity homogeneity than the uncorrected image (Figure 6.17 B).

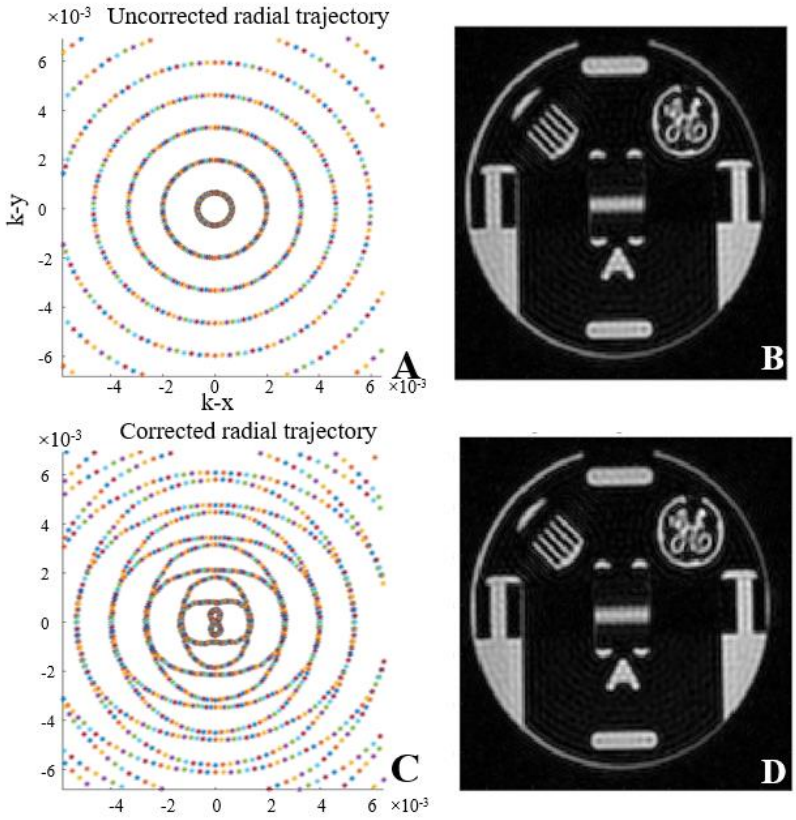

Figure 6.17 The ideal radial trajectory (A) is shifted according to the estimated gradient delay in each direction (C). The images reconstructed with the two trajectories are shown in B and D. Acquired using a 1.5 T GE 450w

The radial stack-of-stars SPGR sequence was tested on a healthy volunteer for the imaging heart, liver, and brain (Figure 6.18 A-C). The images were acquired with golden angle spoke rotation, free breathing, and no gating in a 1.5 T GE 450w scanner (FOV 40 cm (heart and liver); 32 cm (brain), flip angle 20^{o}, 512 sample points, 544 radial spokes, TE 5.1 ms, TR 11 ms, NEX=1, voxel 0.8×0.8×2 mm^3 (heart); 0.8×0.8×4 mm^3 (liver); 0.5×0.5×2 mm^3 (brain), acquisition time 10:21 min (heart, ECG triggered, 30 slices); 1:30 min (liver, non-triggered, 15 slices); 3:00 min (brain, non-triggered, 30 slices), RBW ±125kHz). The heart and liver images were acquired using a 30-channel anterior thoracic array coil and a posterior array coil; a 24-channel brain array coil was used for the brain image. The images were reconstructed with a gridding method and gradient delay correction. Heart and liver images

were acquired with a free-breathing product stack-of-stars sequence[1] in the volunteer (Figure 6.18 D, E), using a non-golden angle rotation, in a 1.5 T GE 450w scanner using a 30 channel flexible anterior (AIR^{TM}) and a built-in posterior spine array coil (FOV 40cm, slice thickness 1.5 mm, flip angle 12^{o}, 320 sample points, 342 radial spokes, TE 2.1 ms, TR 4.5 ms, NEX=1, voxel 1.2×1.2×1.5 mm^3, RBW ±125kHz).

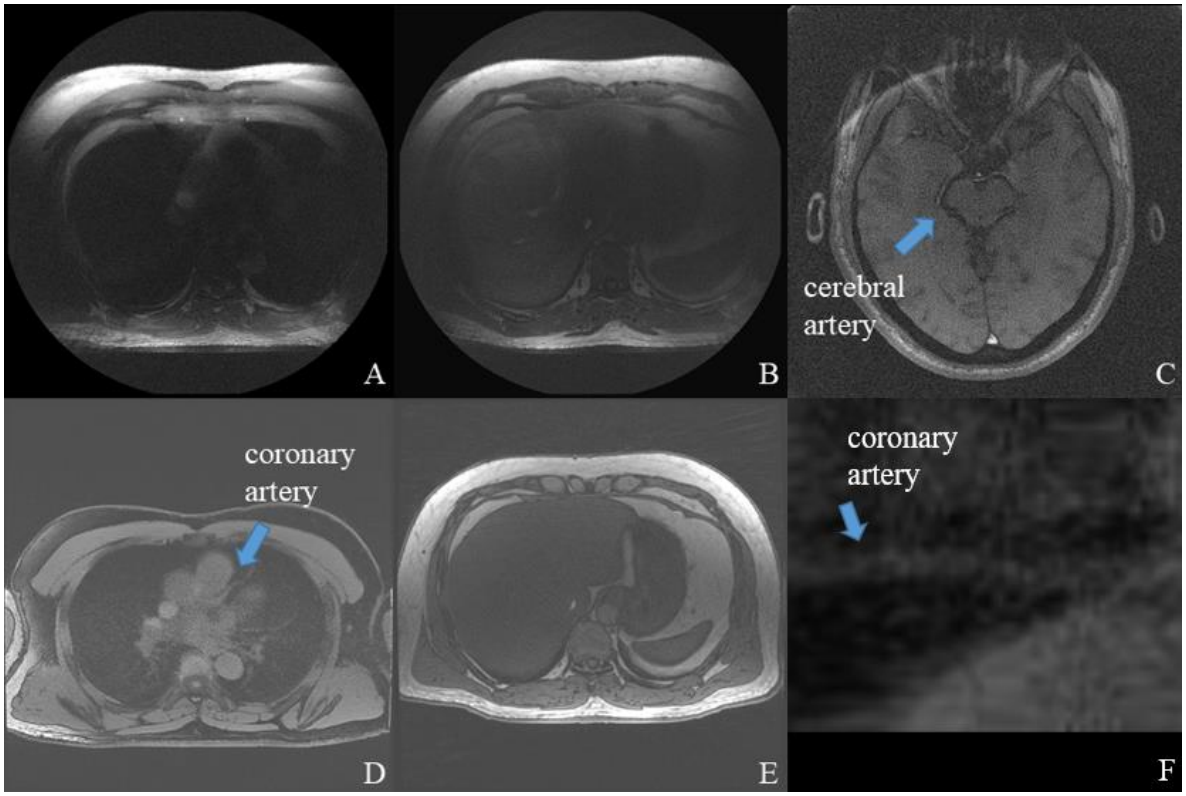

Figure 6.18 Stack-of-stars images of a healthy volunteer in the heart (A), liver (B) and brain (C, arrow indicates middle cerebral artery). Product stack-of-stars images of the volunteer are shown in the heart (D, arrow indicates left anterior descending artery) and liver (E). (F) shows a curved plane view along the coronary artery in (D) (Images acquired with 1.5 T GE 450w)

The stack-of-stars images (Figure 6.18 A, B) in the heart and liver show a strong signal

[1] Note that all sequences developed in this thesis were developed on either the GE Healthcare DV26.0 or MP 26.0 software release which did not implement a 3D Stack-of-Stars sequence. At the end of this thesis work two of the 1.5T MR-only systems were upgraded to DV 29.1 which featured GE's commercial implementation of 3D Stack-of-Stars. The PET/MR system running MP 26.0, does not, at the time of writing, feature a 3D Stack-of-Stars implementation

attenuation near the centre of the images, making the liver and heart difficult to visualize. The signal intensity and image quality near the anterior or the posterior regions are relatively better than the centre. The attenuation could relate to the dimensions of the thoracic phase array coil, which was overlaid on a former that supported the coil over the volunteer's chest. The gap between the former and the volunteer's chest could reduce the coil sensitivity in the heart. The increasing of TR may improve the SNR in the chest at the cost of a prolonged scan time. In addition, limitations such as B_1 receiving non-uniformity could cause biased and non-uniform intensity across the image. Bias correction methods described in Ch 5.2 were applied to reduce the bias in signal intensity across the FOV. However, the correction methods amplified the noise in the centre of FOV due to the low SNR and decreased the overall image quality in regions of interest.

In the stack-of-stars brain image (Figure 6.18 C), the coils were designed for the head, and the elements were closer to the brain, hence there is less signal attenuation in the image. The image quality of the brain image is also better than the heart and liver images, despite some anterior attenuation near the nose due to the object exceeding the prescribed FOV. The anatomical structures in the brain, such as the middle cerebral arteries, are visualized in the image. In addition, the high intensity from the fat region indicates a fat saturation pulse is necessary to improve the appearance of the heart or liver image.

The stack-of-stars sequence had a longer TE (5.1 ms) and TR (11 ms) compared to the product sequence (TE 2.1 ms, TR 4.5 ms), which prolonged the scan time and caused intensity decay in collected MR signals. An alternative RF pulse with a shorter duration, such as a minimum phase RF pulse, and improvements on the gradient design could shorten the minimum TE and TR and increase signal intensity. In addition, the flip angle of the proposed stack-of-stars sequence (20^o) was higher than the product sequence (12^o). Given the tissues of interest (arterial wall, plaque, blood) have typical T_1 relaxation times between 500-2000 ms and the signals are spoiled gradient echoes, the Ernst angle that maximizes the signal intensity is between 6^o-11^o (according to Eqn 6.24). The high flip angle would decrease the signal intensity in Figure 6.18 A, B and C, and a smaller flip angle should be used to improve the signal intensity and shorten the RF duration. Due to the lack of scanning time near the end of this research, imaging parameters of the proposed stack-of-stars sequence were not optimized with the volunteer's scan. Tuning of the imaging parameters such as TE, TR, bandwidth, and fat saturation may further improve imaging quality.

The product stack-of-stars images with the flexible anterior array coils demonstrate more uniform intensity in the heart and liver region because the flexible coils conformed to the volunteer's chest and offered better sensitivity. Despite blurring due to cardiac and respiratory motion, the coronary artery and liver vessels are seen in the image. With a golden angle spoke rotation and retrospective binning in the reconstruction, the image quality of the stack-of-stars sequence could be further improved, and the stack-of-stars sequences could be potentially used for cardiac imaging in the PET/MR system.

The radial trajectory repeatedly traverses the centre of k-space. Although it decreases the sampling efficiency, the oversampled k-space centre is more resistant to motion artefacts. The over-sampled k-space centre is also beneficial for parallel imaging reconstruction when low-resolution images were reconstructed from the under-sampled data sets[172]. With golden angle acquisition, the retrospective binning and iterative reconstruction methods can provide motion resolved image reconstruction. Moreover, each radial spoke contains motion information and can function like a navigator. Without further sequence modification and prolonged scan time, the radial data provides motion estimation that can be used for retrospective data sorting[160]. Two common methods for extracting motion information for radial spokes are the 0D and 1D methods. The 0D method exploits the magnitude of the peak spoke signals, which oscillates under periodic motions such as respiratory and cardiac motions. The peak spoke signals located at each spoke's centre were extracted and sorted by their acquisition time. A principal component analysis (PCA) compresses information across the different coil channels, and a bandpass filter was applied to the first principal component to remove frequencies exceeding physiological ranges. Figure 6.19 A illustrates the peak spoke signals from the volunteer liver scan (liver image shown in Figure 6.18). The oscillatory waveform resulted from the cardiac and respiratory motion of the volunteer (heart rate 90 beats per second (1.5 Hz), respiratory motion 16 per second (0.27 Hz)). The respiration and cardiac motion frequencies were determined by their peak magnitude within the physiological ranges (0-0.5 Hz for respiration, 0.5-2Hz for cardiac motion). A respiratory frequency of 0.29 Hz and cardiac motion of 1.44 Hz were detected in Figure 6.19 B. The motion frequency was then used for motion signal generation and data sorting to reduce motion artefacts.

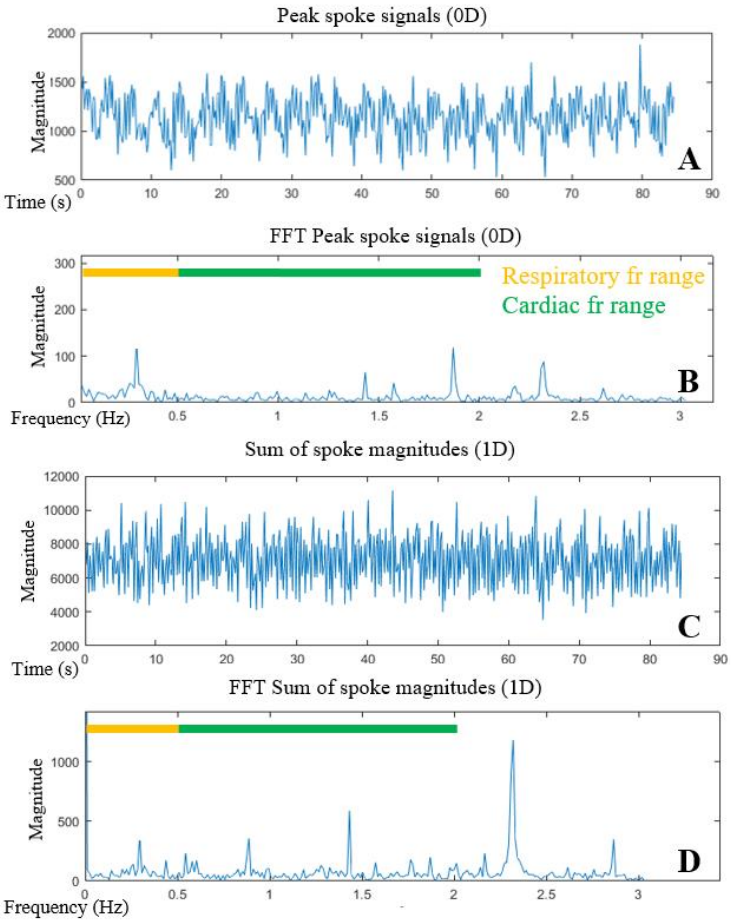

Figure 6.19 Self-gating signals were extracted from the peak spoke signals (A, B) and from the sum of spoke magnitudes (C, D)

The peak spoke signal is a rough summary of the motion states in each spoke. Higher-order features could better represent the motion states and facilitates more accurate motion estimation. For 1D self-gating analysis, the spoke signals were transformed with an IFFT to obtain the image domain information. The 1D features such as summation and centre of mass were applied to the transformed spoke data. Because motion influences both the magnitude and phase of the acquired data, the self-gating features can be extracted from the magnitude, phase, real and imaginary parts of the data. Figure 6.19 C illustrates the sum of spoke magnitudes in the time series. PCA coil compression and filtering were applied before feature extraction. The frequency spectrum indicates a peak respiratory frequency of 0.27 Hz and a peak cardiac frequency of 1.46 Hz (Figure 6.19 D). Compared to the 0D frequency spectrum, the 1D sum of magnitude method improves the estimation accuracy for motion frequency. The magnitude of the cardiac frequency is more distinguishable in the 1D spectrum, making the peak detection

more robust under noise due to additional motion.

With the extracted cardiac and respiratory motion signal, the radial data can be retrospectively sorted according to different cardiac and respiratory motion states. For each cardiac and respiratory motion state, the k-space was covered by a series of radial spokes with golden angles. The total scan time and retrospective sorting limited the number of spokes for each motion state. An iterative reconstruction scheme with compress sensing techniques could exploit the sparsity along the motion dimension and the incoherence in golden angle radial spokes. The XD-GRASP algorithm demonstrated cardiac and respiratory motion resolved reconstruction of the 2D cine cardiac images[174]. With the 3D free breathing stack-of-star sequence described above, the XD-GRASP algorithm may reconstruct the cardiac and respiratory resolved 3D cardiac images. The XD-GRASP reconstruction was applied to the 3D cardiac image acquired with the PET/MR scanner (Figure 6.18 A). However, the lack of signal in the chest created difficulties in coil sensitivity estimation and impaired the iterative reconstruction.

In summary, the application of the proposed stack-of-stars sequence for cardiac imaging in the PET/MR system still requires improvement in imaging parameter selection, coil sensitivity, shortening of TE and TR, and bias correction. The self-navigating property of the radial spokes can also offer motional frequency estimation, which facilitates the sorting of data in image reconstruction. Cardiac and liver images obtained with the recently available product sequence indicates the stack-of-stars sequence is an efficient sequence with high image quality. With appropriate preparation pulses (MSDE/DANTE blood suppression, fat saturation, T2 preparation), stack-of-stars trajectory and compress sensing techniques, the proposed MR sequence is promising for a continuously acquired free breathing MR imaging in the PET/MR system, revealing the motion, morphology and inflammation of coronary atherosclerosis.

Chapter 7Conclusion

7.1 Conclusion

Coronary atherosclerosis is a systematic and chronic inflammatory disease that can generate one or more plaques distributed along the coronary tree. Adverse clinical events such as acute coronary syndromes are primarily associated with plaque rupture when the stress exceeds the material strength of the plaque. Both biomechanics and inflammation play crucial roles in the development, progression and rupture of coronary plaques[1,2,74]. The advancement of coronary imaging techniques facilitates the development of new biomechanical and inflammatory biomarkers, where traditional image-based features (such as X-ray angiography-defined luminal stenosis) are insufficient to assess plaque vulnerability accurately and thereby predict future adverse events.

The accuracy of biomechanical feature estimation depends on the reliability of the model. Compared to 2D FEA models, 3D FEA models include the modelling of axial stress and coronary bending. These more realistic 3D models increased the magnitude of peri-luminal PSS and occasionally changed the location of peak peri-luminal PSS that was predicted by 2D FEA. However, the model construction and solution for 3D FEA can be time-consuming, especially when the fully coupled FSI strategy is adopted. Comparison between different modelling strategies showed that 3D structure only FEA can significantly reduce the solution time while providing PSS estimation with good agreement with the fully coupled FSI model. Non--oscillatory fluid features (such as pressure and TAWSS) showed little to a modest difference between CFD and fully coupled FSI models.

Further investigation of the influence of bending indicated that patient-specific bending in 3D FEA models significantly increased the estimated peri-luminal PSS. The estimated PSS is more sensitive to bending with a high magnitude. An averaged bending profile could alleviate the PSS underestimation when patient-specific bending was not available. The cyclic coronary bending introduced a strong oscillatory factor to the model and increased the magnitude of

oscillatory fluid features (such as OSI, and RRT). Coronary central line analysis with two-phase CCTA indicates a good correlation between coronary curvature and coronary bending. The coronary systolic or diastolic curvature may then be used to estimate coronary bending for clinical or biomechanical analysis. The assessment of 3D PSS's predictive power in the plaque vulnerability assessment requires a survival analysis with a larger patient cohort.

In vivo imaging of the coronary vasculature is a challenging area of current research. PET/MR offers a number of advantages for the simultaneous acquisition of morphological data using MR together with functional data using PET. The coronary PET imaging with ^{68}Ga-DOTATATE has shown excellent sensitivity to macrophage and inflammation, and high power in discriminating high-risk vs low-risk coronary lesions[66]. This thesis investigated two aspects of PET/MR for coronary imaging: the accurate MR attenuation correction in thoracic PET/MR scans and the development of a robust free-breathing image acquisition method. For free-breathing MR image acquisition, two methods were attempted: 3D stack-of-spirals and 3D stack-of-stars.

The hybrid bias correction of thoracic ZTE images combined the advantages of the surface fitting and histogram-based methods, and provided normalised ZTE images for both the soft-tissue and lung regions. The hybrid bias correction method facilitated quantitative analysis of the thoracic ZTE images, such as segmentation and attenuation map generation. The bias-corrected ZTE images were converted to the pseudo-CT and the subsequent MR attenuation map generation. When used with the Dixon MR attenuation map, the pseudo-CT based lung attenuation improves the accuracy of PET reconstruction in the lung.

The stack-of-spirals sequence suffered from substantial off-resonance artefact in the PET/MR system that requires a more accurate B_0 field mapping or auto-focusing criteria. The B_0 field mapping in the 3 T PET/MR system was more challenging than in the 1.5 T system, because the higher static magnetic field strength accelerated the off-resonance phase accumulation. The auto-focusing method was less sensitive to the field strength, but the estimated B_0 field was noisy and was more time-consuming in 3D images. The stack-of-stars sequence was more resistant to off-resonance artefacts because of its trajectory directions. However, significant signal decay was detected in the centre of the chest and the abdomen. Various factors contributed to the signal decay, including the imaging parameter selection/optimization (flip angle, TE/TR, bandwidth, fat saturation), the field inhomogeneity (B_0 field for off-resonance

effect and intensity bias), and the sensitivity of the anterior thoracic array coil.

In summary, this dissertation performed 3D reconstruction and biomechanical simulation on coronary atherosclerosis, showing the 3D structure only FEA was a time efficient and accurate modelling strategy. Simulation with patient specific bending highlight the significance of bending in the calculation of maximum periluminal PSS and the oscillatory fluid parameters. To further improve the image quality of PET/MR and reveal the association of coronary inflammation, ZTE based bias correction and pseudo-CT generation were proposed. MR attenuation correction with ZTE-pseudoCT showed improvement in PET reconstruction accuracy compared to the Dixon attenuation correction by manufacture. In addition, a free breathing non-Cartesian MR sequence was attempted to improve the MR image quality and acquisition efficiency. Although the image quality was not ideal due to various limitations, the attempted stack-of-radial sequence showed promising characteristics and may improve the image quality and efficiency with future improvements.

.

7.2 Limitations

All 3D biomechanical models in this thesis were constructed as single tubes, and the sub-branches were excluded due to the geometrical complexity of the structure mesh at coronary bifurcations. Because of flow distribution between different sub-branches, the absence of sub-branches in our model could influence the calculation of fluid features such as pressure and TAWSS, especially at the bifurcation site. The movement and bending of the sub-branches could influence the PSS estimation. Another limitation in the biomechanical models was the residual axial stress. The VH-IVUS and DSA imaging and the subsequence 3D geometry reconstruction were performed in a pressurised and stretched state. The model needs to return to a residual stress-free state for 3D FEA. Although the VH-IVUS mesh was depressurised with a circumferential shrinkage, the axial residual stress was not corrected because the axial shrinkage of the coronary vessel was unknown. The lack of axial residual stress correction can lead to the underestimation of PSS[175]. In addition, the resolution of IVUS is 200 μm and exceeds the thickness of a thin fibrous cap (<65 μm in thickness)[51]. Therefore, the geometry of thin fibrous cap was not modelled, and an unrealistic lipid exposure existed in our models. The

absence of the fibrous cap can change the peri-luminal stress calculation and cause abnormal stress in the exposed lipid elements. In this study, a 99.5% criterion was applied to minimise the potential distortion

The 2D structure mesh and 3D vascular reconstruction were based on a series of assumptions mentioned in Chapter 2.2. The violation of these assumptions could cause inaccuracy in the coronary mesh. Moreover, the bending displacements of coronary vessels were simplified as the displacement of a few surfaces on the vessel's outer wall. In reality, coronary vessels attach to the epicardial surface and are surrounded by a layer of loose connective tissue[176]. The simplification of bending application may cause stress concentrated at the loading surfaces, creating uneven stress distribution along the vessel.

In the hybrid bias correction of thoracic ZTE images, the bias field was synthesised from the surface fitting and the histogram-based methods for the soft tissue and lung region. The two independent bias correction methods may create relative intensity differences, and the soft tissue and lung tissue in the hybrid bias corrected image may not be consistent. Regional intensity differences must be considered for quantitative analysis of the entire ZTE image. The accuracy of lung segmentation and pseudo-CT conversion were influenced by the co-registration accuracy between different images. Cardiac and respiratory motions not only cause image artefacts but also create difficulties in accurate image co-registration. The lung segmentation was less accurate near the edge, and occasionally included rib bone in the lung mask. The misclassification between bone and lung could significantly influence the subsequent pseudo-CT generation. A linear model was used to convert ZTE into pseudo-CT. However, the histogram plot of ZTE and CT intensity implies a more complicated relationship between the intensities. Because the lung contains tissues with different attenuating behaviour (e.g. artery, air), a piecewise linear model or high order model could potentially improve the pseudo-CT mapping accuracy. In addition, the lung remodelling between ZTE and CT acquisition further limits the accuracy of pseudo-CT conversion.

The synthesis of Dixon/CT and Dixon/pCT attenuation correction maps creates attenuation differences at the edges of lung segmentation, which could influence the PET reconstruction near the edges. The PET reconstruction with CT based attenuation correction may serve as a better reference in evaluating the accuracy of Dixon/pCT attenuation correction. In the PET reconstruction, the bone, as a strong attenuator, was not included in the soft tissue region and

can cause an overestimation of regional SUV.

In the off-resonance correction of the stack-of-spirals sequences, both the time-segmented phase conjugate correction and the auto-focusing correction were performed at pixel level after smoothing the estimated B_0 field. The pixel level corrections brought the inaccuracy of off-resonance frequencies into the corrected images. A surface model (e.g. B-spline surface) fitted to the noisy off-resonance map could potentially suppress the noise and offers better deblurring performance.

In the stack-of-stars sequence development, signal attenuation in the central FOV was the major artefact. Parameters in the image acquisition were not optimized. The minimum TE and TR were limited by the RF pulse and gradient design. The prolonged TE increased the susceptibility to the off-resonance effect. The flip angle used in the volunteer's scan was greater than the ideal Ernst angle for blood and vascular tissue, causing unnecessary signal decay. The long TE and the large flip angle increased the spoke time and reduced the time resolution of the proposed sequence.

The available thoracic coil arrays in the PET/MR system were curved on a former to support the coil over the volunteer's chest. The distance between the coil and the patient's chest resulted in a reduction of SNR in the heart. A coil compatibility issue limited the usage of flexible anterior array coil, which could alleviate the signal attenuation in the heart and liver. The low intensity in the heart impaired the coil sensitivity estimation and the subsequent iterative reconstruction.

Fat saturation pulse and bias field correction may further improve the image appearance and facilitate quantitative analysis. Gradient delay estimation of the proposed stack-of-stars sequence was performed with 16 pairs of anti-parallel spokes in different directions. The gradient delay for each spoke was linearly interpolated between the 16 directions. Error in the gradient delay interpolation might distort the k-space trajectory and image artefacts.

7.3 Future directions

The cohort size of studies in this thesis is relatively small, and the survival analysis and statistical vulnerability assessment of the biomarkers were not feasible. Given the good

agreement and short solution time of the 3D structure only FEA model, PSS estimation with a larger cohort can assess the predictive power of 3D PSS in predicting major adverse cardiac events. To compensate for the lack of a thin fibrous cap, the integration with OCT images could add geometric information of the thin fibrous cap and improves the accuracy of the 3D coronary model. Although the experimental measurement of coronary residual stress is difficult, a shrinkage along the tangent direction of the central line may partially compensate for the error due to residual stress and pressurisation.

The ZTE to pseudo-CT conversion in this thesis used a segmentation-based approach and pixel value mapping. Other approaches such as deep learning using a CNN could exploit the texture and locational features in the image and could potentially produce more accurate pseudo-CT images. However, the training of a CNN would require a larger sample size with co-registered ZTE and CT images. The current ZTE segmentation showed good results for lung segmentation and is also promising for bone segmentation. Further processing of the lung and bone segmentation with the morphological operation or additional segmentation steps could improve the accuracy of bone segmentation, and will add the important bone segmentation to the MR attenuation correction process.

Optimization of the imaging parameters (flip angle, TE, TR and fat saturation) and compatibility with a flexible anterior array coil could improve the SNR, shorten the scan time and improve the time resolution. Additional calibration and bias correction methods, such as the PURE method, may help to normalise the intensity within the body. The current stack-of-stars sequence uses a SINC RF pulse, and the substitution of an RF pulse with a shorter duration, such as a minimum phase RF pulse with a small flip angle, could further reduce the minimum TE and TR. Preparation pulses such as DANTE may suppress the signal from the blood pool, providing better contrast for the characterization of the coronary vessel wall. With better image contrast in the chest, retrospective binning and iterative reconstruction algorithms such as the XD-GRASP may provide cardiac and respiratory motion resolved 3D images.

The cellular behaviour can be modulated by the mechanical environment through the mechanotransduction pathway. As an important mechanical factor, the bending of coronary vessels may be associated with inflammation in the coronary vessels. With a suitable motion resolved MR angiography sequence, PET/MR may provide coronary bending and inflammation in one scan. The association between bending and other metabolic features could

be explored with different PET radioactive tracers, revealing more functional biomarkers for the coronary atherosclerosis vulnerability assessment.

Reference

1. Hansson, G. K., Libby, P. & Tabas, I. Inflammation and plaque vulnerability. *Journal of Internal Medicine* **278**, 483–493 (2015).

2. Falk, E. Pathogenesis of atherosclerosis. *Journal of the American College of Cardiology* vol. 47 C7–C12 Preprint at https://doi.org/10.1016/j.jacc.2005.09.068 (2006).

3. Cardiovascular diseases (CVDs). https://www.who.int/en/news-room/fact-sheets/detail/cardiovascular-diseases-(cvds).

4. GBD 2013 Mortality and Causes of Death Collaborators. Global, regional, and national age-sex specific all-cause and cause-specific mortality for 240 causes of death, 1990-2013: a systematic analysis for the Global Burden of Disease Study 2013. *Lancet* **385**, 117–71 (2015).

5. BHF. Cardiovascular disease statistics - BHF UK Factsheet. *British Heart Foundation* (2018) doi:10.1017/CBO9781107415324.004.

6. Liu, J. L. Y., Maniadakis, N., Gray, A. & Rayner, M. The economic burden of coronary heart disease in the UK. *Heart* **88**, 597–603 (2002).

7. Mathers, C. D. & Loncar, D. Projections of global mortality and burden of disease from 2002 to 2030. *PLoS Medicine* **3**, e442 (2006).

8. Libby, P., Ridker, P. M. & Hansson, G. K. Progress and challenges in translating the biology of atherosclerosis. *Nature* vol. 473 317–325 Preprint at https://doi.org/10.1038/nature10146 (2011).

9. Bentzon, J. F., Otsuka, F., Virmani, R. & Falk, E. Mechanisms of plaque formation and rupture. *Circulation Research* **114**, 1852–1866 (2014).

10. Barquera, S. *et al.* Global overview of the epidemiology of atherosclerotic

cardiovascular disease. *Archives of Medical Research* **46**, 328–338 (2015).

11. Nievelstein, P. F., Fogelman, A. M., Mottino, G. & Frank, J. S. Lipid accumulation in rabbit aortic intima 2 hours after bolus infusion of low density lipoprotein. A deep-etch and immunolocalization study of ultrarapidly frozen tissue. *Arterioscler Thromb* **11**, 1795–805 (1991).

12. Berliner, J. A. *et al.* Atherosclerosis: basic mechanisms. Oxidation, inflammation, and genetics. *Circulation* **91**, 2488–96 (1995).

13. Wentzel, J. J. *et al.* Endothelial shear stress in the evolution of coronary atherosclerotic plaque and vascular remodelling: current understanding and remaining questions. *Cardiovascular Research* **96**, 234–243 (2012).

14. Zmysłowski, A. & Szterk, A. Current knowledge on the mechanism of atherosclerosis and pro-atherosclerotic properties of oxysterols. *Lipids Health Dis* **16**, 188 (2017).

15. Galkina, E. & Ley, K. Immune and inflammatory mechanisms of atherosclerosis (*). *Annu Rev Immunol* **27**, 165–97 (2009).

16. Yu, X.-H., Fu, Y.-C., Zhang, D.-W., Yin, K. & Tang, C.-K. Foam cells in atherosclerosis. *Clinica Chimica Acta* **424**, 245–252 (2013).

17. Sluimer, J. C. *et al.* Thin-walled microvessels in human coronary atherosclerotic plaques show incomplete endothelial junctions relevance of compromised structural integrity for intraplaque microvascular leakage. *J Am Coll Cardiol* **53**, 1517–27 (2009).

18. Heistad, D. D. Unstable coronary-artery plaques. *New England Journal of Medicine* **349**, 2285–2287 (2003).

19. Falk, E., Nakano, M., Bentzon, J. F., Finn, A. V. & Virmani, R. Update on acute coronary syndromes: the pathologists' view. *European Heart Journal* **34**, 719–728 (2013).

20. Burke, A. P. *et al.* Healed plaque ruptures and sudden coronary death: Evidence that subclinical rupture has a role in plaque progression. *Circulation* **103**, 934–940 (2001).

21. DeWood, M. A. *et al.* Thrombosis in acute myocardial infarction and sudden death: angiographic aspects. *Cardiovasc Clin* **18**, 195–211 (1987).

22. Virmani, R., Kolodgie, F. D., Burke, A. P., Farb, A. & Schwartz, S. M. Lessons from sudden coronary death: a comprehensive morphological classification scheme for atherosclerotic lesions. *Arterioscler Thromb Vasc Biol* **20**, 1262–75 (2000).

23. Farb, A. *et al.* Coronary plaque erosion without rupture into a lipid core. A frequent cause of coronary thrombosis in sudden coronary death. *Circulation* **93**, 1354–63 (1996).

24. Virmani, R., Burke, A. P., Farb, A. & Kolodgie, F. D. Pathology of the vulnerable plaque. *J Am Coll Cardiol* **47**, C13–C18 (2006).

25. Mann, J. & Davies, M. J. Mechanisms of progression in native coronary artery disease: role of healed plaque disruption. *Heart* **82**, 265–8 (1999).

26. Stary, H. C. *et al.* A definition of advanced types of atherosclerotic lesions and a histological classification of atherosclerosis. A report from the Committee on Vascular Lesions of the Council on Arteriosclerosis, American Heart Association. *Arterioscler Thromb Vasc Biol* **15**, 1512–31 (1995).

27. Stary, H. C. *et al.* A definition of initial, fatty streak, and intermediate lesions of atherosclerosis. A report from the Committee on Vascular Lesions of the Council on Arteriosclerosis, American Heart Association. *Circulation* **89**, 2462–78 (1994).

28. Lindsey, J. B., House, J. A., Kennedy, K. F. & Marso, S. P. Diabetes duration is associated with increased thin-cap fibroatheroma detected by intravascular ultrasound with virtual histology. *Circ Cardiovasc Interv* **2**, 543–8 (2009).

29. Moreno, P. R. The high-risk thin-cap fibroatheroma: a new kid on the block. *Circ Cardiovasc Interv* **2**, 500–2 (2009).

30. Teng, Z. *et al.* Coronary plaque structural stress is associated with plaque composition and subtype and higher in acute coronary syndrome: The BEACON i (Biomechanical Evaluation of Atheromatous Coronary Arteries) study. *Circulation: Cardiovascular Imaging* **7**, (2014).

31. Stone, G. W. *et al.* A prospective natural-history study of coronary atherosclerosis. *Belgium (B.B. N Engl J Med* **364**, 226–35 (2011).

32. Calvert, P. A. *et al.* Association between IVUS findings and adverse outcomes in patients with coronary artery disease: The VIVA (VH-IVUS in Vulnerable Atherosclerosis) study. *JACC: Cardiovascular Imaging* **4**, 894–901 (2011).

33. Greenland, P. *et al.* 2010 ACCF/AHA Guideline for assessment of cardiovascular risk in asymptomatic adults. *Journal of the American College of Cardiology* vol. 56 e50–e103 Preprint at https://doi.org/10.1016/j.jacc.2010.09.001 (2010).

34. Nasir, K. *et al.* Electron beam CT versus helical CT scans for assessing coronary calcification: current utility and future directions. *American Heart Journal* **146**, 969–977 (2003).

35. Budoff, M. J. *et al.* Assessment of coronary artery disease by cardiac computed tomography: a scientific statement from the American Heart Association Committee on Cardiovascular Imaging and Intervention, Council on Cardiovascular Radiology and Intervention. *Circulation* vol. 114 1761–1791 Preprint at https://doi.org/10.1161/CIRCULATIONAHA.106.178458 (2006).

36. Owen, D. R. J., Lindsay, A. C., Choudhury, R. P. & Fayad, Z. A. Imaging of atherosclerosis. *Annu Rev Med* **62**, 25–40 (2011).

37. Greenland, P. *et al.* ACCF/AHA 2007 Clinical expert consensus document on coronary artery calcium scoring by computed tomography in global cardiovascular risk assessment and in evaluation of patients with chest pain. A report of the American College of Cardiology Foundation. *Journal of the American College of Cardiology* vol. 49 378–402 Preprint at https://doi.org/10.1016/j.jacc.2006.10.001 (2007).

38. Hoffmann, U., Ferencik, M., Cury, R. C. & Pena, A. J. Coronary CT Angiography. *Journal of Nuclear Medicine* **47**, (2006).

39. Hutcheson, C., Maldonado, N., Aikawa, E. & Hutcheson, J. D. Small entities with large impact: microcalcifications and atherosclerotic plaque vulnerability. *Current Opinion in Lipidology* **25**, 327–332 (2014).

40. Conte, E. *et al.* FFRCT and CT perfusion: A review on the evaluation of functional impact of coronary artery stenosis by cardiac CT. *International Journal of Cardiology* **300**, 289–296 (2020).

41. Choudhury, R. P., Fuster, V., Badimon, J. J., Fisher, E. A. & Fayad, Z. A. MRI and characterization of atherosclerotic plaque: emerging applications and molecular imaging. *Arterioscler Thromb Vasc Biol* **22**, 1065–74 (2002).

42. Popma, J. J. Braunwald's Heart Disease: a textbook of cardiovascular medicine. 392–428 (2007).

43. Yuan, C., Mitsumori, L. M., Beach, K. W. & Maravilla, K. R. Carotid Atherosclerotic Plaque: Noninvasive MR Characterization and Identification of Vulnerable Lesions. *COPD: Journal of Chronic Obstructive Pulmonary Disease* **5**, 105–116 (2008).

44. Noguchi, T. *et al.* High-intensity signals in coronary plaques on noncontrast T1-weighted magnetic resonance imaging as a novel determinant of coronary events. *J Am Coll Cardiol* **63**, 989–999 (2014).

45. Sakuma, H. *et al.* Detection of coronary artery stenosis with whole-heart coronary magnetic resonance angiography. *J Am Coll Cardiol* **48**, 1946–1950 (2006).

46. Lysel, M. S. Van. *Abrams' Angiography : Interventional Radiology*. (Little, Brown and Company, 1997).

47. Brody, W. R. Digital subtraction angiography. *IEEE Transactions on Nuclear Science* **29**, 1176–1180 (1982).

48. Meaney, T. F. *et al.* Digital subtraction angiography of the human cardiovascular system. (1980).

49. Lansky, A. J. *et al.* Quantitative angiographic methods for appropriate end-point analysis, edge-effect evaluation, and prediction of recurrent restenosis after coronary brachytherapy with gamma irradiation. *J Am Coll Cardiol* **39**, 274–280 (2002).

50. Little, W. C. *et al.* Can coronary angiography predict the site of a subsequent myocardial infarction in patients with mild-to-moderate coronary artery disease? *Circulation* **78**, 1157–1166 (1988).

51. Mintz, G. S. *et al.* American College of Cardiology clinical expert consensus document on standards for acquisition, measurement and reporting of intravascular ultrasound

studies (ivus): a report of the american college of cardiology task force on clinical expert consensus do. *J Am Coll Cardiol* **37**, 1478–1492 (2001).

52. Ma, T. *et al.* Multi-frequency intravascular ultrasound (IVUS) imaging. *IEEE Transactions on Ultrasonics, Ferroelectrics, and Frequency Control* **62**, 97–107 (2015).

53. Nasu, K. *et al.* Accuracy of in vivo coronary plaque morphology assessment. *J Am Coll Cardiol* **47**, 2405–2412 (2006).

54. Nair, A. *et al.* Coronary plaque classification with intravascular ultrasound radiofrequency data analysis. *Circulation* **106**, 2200–2206 (2002).

55. Rodriguez-Granillo, G. A. *et al.* In vivo intravascular ultrasound-derived thin-cap fibroatheroma detection using ultrasound radiofrequency data analysis. *J Am Coll Cardiol* **46**, 2038–2042 (2005).

56. Nasu, K. *et al.* Accuracy of in vivo coronary plaque morphology assessment: a validation study of in vivo virtual histology compared with in vitro histopathology. *J Am Coll Cardiol* **47**, 2405–2412 (2006).

57. Prati, F. *et al.* Correlation between high frequency intravascular ultrasound and histomorphology in human coronary arteries. *Heart* **85**, 567–70 (2001).

58. Brown, A. J. *et al.* Direct comparison of virtual-histology intravascular ultrasound and optical coherence tomography imaging for identification of thin-cap fibroatheroma. *Circulation: Cardiovascular Imaging* **8**, (2015).

59. Podoleanu, A. G. Optical coherence tomography. doi:10.1259/bjr/55735832.

60. Liu, L. *et al.* Imaging the subcellular structure of human coronary atherosclerosis using micro–optical coherence tomography. *Nature Medicine* **17**, 1010–1014 (2011).

61. Yabushita, H. *et al.* Characterization of human atherosclerosis by optical coherence tomography. *Circulation* **106**, 1640–1645 (2002).

62. Jang, I.-K. *et al.* Visualization of coronary atherosclerotic plaques in patients using optical coherence tomography: comparison with intravascular ultrasound. *J Am Coll Cardiol* **39**, 604–609 (2002).

63. Tearney, G. J. *et al.* Quantification of macrophage content in atherosclerotic plaques by optical coherence tomography. *Circulation* **107**, 113–119 (2003).

64. Niccoli, G. *et al.* Plaque rupture and intact fibrous cap assessed by optical coherence tomography portend different outcomes in patients with acute coronary syndrome. *European Heart Journal* **36**, 1377–1384 (2015).

65. Alie, N., Eldib, M., Fayad, Z. A. & Mani, V. Inflammation, atherosclerosis, and coronary artery disease: PET/CT for the evaluation of atherosclerosis and inflammation. *Clin Med Insights Cardiol* **8**, 13–21 (2014).

66. Tarkin, J. M. *et al.* Detection of atherosclerotic inflammation by 68Ga-DOTATATE PET compared to [18F]FDG PET imaging. *J Am Coll Cardiol* **69**, 1774–1791 (2017).

67. Silveira, L. *et al.* Correlation between near-infrared Raman spectroscopy and the histopathological analysis of atherosclerosis in human coronary arteries. *Lasers in Surgery and Medicine* **30**, 290–297 (2002).

68. Bourantas, C. V. *et al.* Hybrid intravascular imaging: Recent advances, technical considerations, and current applications in the study of plaque pathophysiology. *European Heart Journal* **38**, 400–412b (2017).

69. Guo, X. *et al.* An FSI modeling approach to combine IVUS and OCT for more accurate patient-specific coronary cap thickness and stress/strain calculations. *Journal of Biomechanical Engineering* **140**, (2017).

70. Samady, H. *et al.* Coronary artery wall shear stress is associated with progression and transformation of atherosclerotic plaque and arterial remodeling in patients with coronary artery disease. *Circulation* **124**, 779–788 (2011).

71. Jadvar, H. & Colletti, P. M. Competitive Advantage of PET/MRI. *Eur J Radiol* **83**, 84 (2014).

72. Rischpler, C., Nekolla, S. G., Dregely, I. & Schwaiger, M. Hybrid PET/MR Imaging of the Heart: Potential, Initial Experiences, and Future Prospects. *Journal of Nuclear Medicine* **54**, 402–415 (2013).

73. Richardson, P. D., Davies, M. J. & Born, G. V. R. Influence of plaque configuration and stress distribution on fissuring of coronary atherosclerotic plaques. *The Lancet* **334**, 941–944 (1989).

74. Brown, A. J. *et al.* Role of biomechanical forces in the natural history of coronary atherosclerosis. *Nature Reviews Cardiology* **13**, 210–220 (2016).

75. Brown, A. J. *et al.* Plaque structural stress estimations improve prediction of future major adverse cardiovascular events after intracoronary imaging. *Circulation: Cardiovascular Imaging* **9**, (2016).

76. Costopoulos, C. *et al.* Plaque rupture in coronary atherosclerosis is associated with increased plaque structural stress. (2017) doi:10.1016/j.jcmg.2017.04.017.

77. U, S. *et al.* Association between biomechanical structural stresses of atherosclerotic carotid plaques and subsequent ischaemic cerebrovascular events--a longitudinal in vivo magnetic resonance imaging-based finite element study. *Eur J Vasc Endovasc Surg* **40**, 485–491 (2010).

78. Tang, D. *et al.* Sites of Rupture in Human Atherosclerotic Carotid Plaques Are Associated With High Structural Stresses. *Stroke* **40**, 3258–3263 (2009).

79. Bezerra, H. G. *et al.* Atheromas that cause fatal thrombosis are usually large and frequently accompanied by vessel enlargement. *Cardiovascular Pathology* **10**, 189–196 (2001).

80. Motoyama, S. *et al.* Computed tomographic angiography characteristics of atherosclerotic plaques subsequently resulting in acute coronary syndrome. *J Am Coll Cardiol* **54**, 49–57 (2009).

81. Yamagishi, M. *et al.* Morphology of vulnerable coronary plaque: insights from follow-up of patients examined by intravascular ultrasound before an acute coronary syndrome. *J Am Coll Cardiol* **35**, 106–111 (2000).

82. Bourantas, C. V. *et al.* Clinical and angiographic characteristics of patients likely to have vulnerable plaques: Analysis from the PROSPECT study. *JACC: Cardiovascular Imaging* **6**, 1263–1272 (2013).

83. Nakahara, T. *et al.* Coronary artery calcification: From mechanism to molecular imaging. *JACC: Cardiovascular Imaging* **10**, 582–593 (2017).

84. Agatston, A. S. *et al.* Quantification of coronary artery calcium using ultrafast computed tomography. *J Am Coll Cardiol* **15**, 827–832 (1990).

85. Elias-Smale, S. E. *et al.* Coronary calcium score improves classification of coronary heart disease risk in the elderly: The Rotterdam study. *J Am Coll Cardiol* **56**, 1407–1414 (2010).

86. Polonsky, T. S. *et al.* Coronary artery calcium score and risk classification for coronary heart disease prediction. *JAMA* **303**, 1610 (2010).

87. Tian, J. *et al.* Distinct morphological features of ruptured culprit plaque for acute coronary events compared to those with silent rupture and thin-cap fibroatheroma: A combined optical coherence tomography and intravascular ultrasound study. *J Am Coll Cardiol* **63**, 2209–2216 (2014).

88. De Bruyne, B. *et al.* Fractional flow reserve–guided PCI versus medical therapy in stable coronary disease. *New England Journal of Medicine* **367**, 991–1001 (2012).

89. Pijls, N. H. J. *et al.* Measurement of fractional flow reserve to assess the functional severity of coronary-artery stenoses. *New England Journal of Medicine* **334**, 1703–1708 (1996).

90. Tonino, P. A. L. *et al.* Fractional flow reserve versus angiography for guiding percutaneous coronary intervention. *n engl j med* **3603**, (2009).

91. Nørgaard, B. L. *et al.* Diagnostic performance of noninvasive fractional flow reserve derived from coronary computed tomography angiography in suspected coronary artery disease. *J Am Coll Cardiol* **63**, 1145–1155 (2014).

92. Koo, B.-K. *et al.* Diagnosis of ischemia-causing coronary stenoses by noninvasive fractional flow reserve computed from coronary computed tomographic angiograms. *J Am Coll Cardiol* **58**, 1989–1997 (2011).

93. Kwak, B. R. *et al.* Biomechanical factors in atherosclerosis: mechanisms and clinical

implications. *European Heart Journal* **35**, 3013–3020 (2014).

94. Stone, P. H. *et al.* Prediction of progression of coronary artery disease and clinical outcomes using vascular profiling of endothelial shear stress and arterial plaque characteristics: the PREDICTION Study. *Circulation* **126**, 172–81 (2012).

95. Gao, H. & Long, Q. Effects of varied lipid core volume and fibrous cap thickness on stress distribution in carotid arterial plaques. *Journal of Biomechanics* **41**, 3053–3059 (2008).

96. Wang, L. *et al.* Fluid-structure interaction models based on patient-specific IVUS at baseline and follow-up for prediction of coronary plaque progression by morphological and biomechanical factors: A preliminary study. *Journal of Biomechanics* **68**, 43–50 (2018).

97. Soulis, J. V, Farmakis, T. M., Giannoglou, G. D. & Louridas, G. E. Wall shear stress in normal left coronary artery tree. *Journal of Biomechanics* **39**, 742–749 (2006).

98. Teng, Z. *et al.* Material properties of components in human carotid atherosclerotic plaques: A uniaxial extension study. *Acta Biomaterialia* **10**, 5055–5063 (2014).

99. Loree, H. M., Kamm, R. D., Stringfellow, R. G. & Lee, R. T. Effects of fibrous cap thickness on peak circumferential stress in model atherosclerotic vessels. *Circ Res* **71**, 850–8 (1992).

100. Cheng, G. C., Loree, H. M., Kamm, R. D., Fishbein, M. C. & Lee, R. T. Distribution of circumferential stress in ruptured and stable atherosclerotic lesions: A structural analysis with histopathological correlation.

101. Imoto, K. *et al.* Longitudinal structural determinants of atherosclerotic plaque vulnerability. *J Am Coll Cardiol* **46**, 1507–1515 (2005).

102. Teng, Z. & Gillard, J. H. Biomechanical structural stresses of atherosclerotic plaques. *Article in Expert Review of Cardiovascular Therapy* (2010) doi:10.1586/ERC.10.130.

103. Kang, S.-J. *et al.* Plaque structural stress assessed by virtual histology-intravascular ultrasound predicts dynamic changes in phenotype and composition of untreated coronary artery lesions. *Atherosclerosis* **254**, 85–92 (2016).

104. Hoffman, A. H. *et al.* Stiffness properties of adventitia, media, and full thickness human atherosclerotic carotid arteries in the axial and circumferential directions. *Journal of Biomechanical Engineering* **139**, 124501 (2017).

105. Ohayon, J., Finet, G., Treyve, F., Rioufol, G. & Dubreuil, O. A three-dimensional finite element analysis of stress distribution in a coronary atherosclerotic plaque: In-vivo prediction of plaque rupture location. *Research Signpost* **37661**,.

106. Jerman, T., Pernus, F., Likar, B. & Spiclin, Z. Blob enhancement and visualization for improved intracranial aneurysm detection. *IEEE Transactions on Visualization and Computer Graphics* **22**, 1705–1717 (2016).

107. Jerman, T., Pernus, F., Likar, B. & Spiclin, Z. Enhancement of vascular structures in 3D and 2D angiographic images. *IEEE Transactions on Medical Imaging* **35**, 2107–2118 (2016).

108. Lee, T. C., Kashyap, R. L. & Chu, C. N. Building skeleton models via 3-D medial surface axis thinning algorithms. *CVGIP: Graphical Models and Image Processing* **56**, 462–478 (1994).

109. Prause, G. P. M., Dejong, S. C., Mckay, C. R. & Sonka, M. Towards a geometrically correct 3-D reconstruction of tortuous coronary arteries based on biplane angiography and intravascular ultrasound. *International Journal of Cardiac Imaging* **13**, 451–462 (1997).

110. Huang, Y. *et al.* Non-uniform shrinkage for obtaining computational start shape for in-vivo MRI-based plaque vulnerability assessment. *Journal of Biomechanics* **44**, 2316–2319 (2011).

111. Huang, Y. *et al.* The influence of computational strategy on prediction of mechanical stress in carotid atherosclerotic plaques: Comparison of 2D structure-only, 3D structure-only, one-way and fully coupled fluid-structure interaction analyses. *Journal of Biomechanics* **47**, 1465–1471 (2014).

112. Wang, Q. *et al.* Multi-patient study for coronary vulnerable plaque model comparisons: 2D/3D and fluid–structure interaction simulations. *Biomechanics and Modeling in*

Mechanobiology 2021 20:4 **20**, 1383–1397 (2021).

113. Konta, T. & Bett, J. H. N. Patterns of Coronary Artery Movement and the Development of Coronary Atherosclerosis. *Circulation Journal* **67**, 846–850 (2003).

114. Yang, C. *et al.* Cyclic Bending Contributes to High Stress in a Human Coronary Atherosclerotic Plaque and Rupture Risk: In Vitro Experimental Modeling and Ex Vivo MRI-Based Computational Modeling Approach. *Mol Cell Biomech* **5**, 259 (2008).

115. Yang, C. *et al.* In Vivo IVUS-Based 3-D Fluid-Structure Interaction Models With Cyclic Bending and Anisotropic Vessel Properties for Human Atherosclerotic Coronary Plaque Mechanical Analysis. *IEEE Transactions on Biomedical Engineering* **56**, 2420–2428 (2009).

116. Dumont, K., Stijnen, J. M. A., Vierendeels, J., Vosse, F. N. van de & Verdonck, P. R. Validation of a Fluid–Structure Interaction Model of a Heart Valve using the Dynamic Mesh Method in Fluent. *http://dx.doi.org/10.1080/10255840410001715222* **7**, 139–146 (2006).

117. Tang, D., Yang, C., Kobayashi, S., Zheng, J. & Vito, R. P. Effect of Stenosis Asymmetry on Blood Flow and Artery Compression: A Three-Dimensional Fluid-Structure Interaction Model. (2003) doi:10.1114/1.1615577.

118. Teng, Z. *et al.* 3D Critical Plaque Wall Stress Is a Better Predictor of Carotid Plaque Rupture Sites Than Flow Shear Stress: An In Vivo MRI-Based 3D FSI Study. *J Biomech Eng* **132**, 031007 (2010).

119. Huang, X. *et al.* Higher critical plaque wall stress in patients who died of coronary artery disease compared with those who died of other causes: A 3D FSI study based on ex vivo MRI of coronary plaques. *Journal of Biomechanics* **47**, 432–437 (2014).

120. Guo, X. *et al.* Quantify patient-specific coronary material property and its impact on stress/strain calculations using in vivo IVUS data and 3D FSI models: a pilot study. *Biomechanics and Modeling in Mechanobiology 2016 16:1* **16**, 333–344 (2016).

121. Pinho, N. *et al.* Correlation between geometric parameters of the left coronary artery and hemodynamic descriptors of atherosclerosis: FSI and statistical study. *Medical &*

Biological Engineering & Computing 2018 57:3 **57**, 715–729 (2018).

122. Tang, D. *et al.* 3D MRI-Based Multicomponent FSI Models for Atherosclerotic Plaques. *Annals of Biomedical Engineering* **32**, 947–960 (2004).

123. Pratumwal, Y., Limtrakarn, W. & Premvaranon, P. The analysis of blood flow past carotid bifurcation by using the one-way Fluid Solid Interaction technique (FSI). *Journal of Research and Applications in Mechanical Engineering* **2**, 57–64 (2014).

124. Tao, X., Gao, P., Jing, L., Lin, Y. & Sui, B. Subject-Specific Fully-Coupled and One-Way Fluid-Structure Interaction Models for Modeling of Carotid Atherosclerotic Plaques in Humans. *Medical Science Monitor : International Medical Journal of Experimental and Clinical Research* **21**, 3279 (2015).

125. Z, T. *et al.* In vivo MRI-based 3D mechanical stress-strain profiles of carotid plaques with juxtaluminal plaque haemorrhage: an exploratory study for the mechanism of subsequent cerebrovascular events. *Eur J Vasc Endovasc Surg* **42**, 427–433 (2011).

126. DE, K., SF, R., M, A. & GA, H. A methodology to analyze changes in lipid core and calcification onto fibrous cap vulnerability: the human atherosclerotic carotid bifurcation as an illustratory example. *J Biomech Eng* **131**, (2009).

127. Wang, Q. *et al.* Multi-patient study for coronary vulnerable plaque model comparisons: 2D/3D and fluid–structure interaction simulations. *Biomechanics and Modeling in Mechanobiology 2021* 1–15 (2021) doi:10.1007/S10237-021-01450-8.

128. Liu, H. *et al.* IVUS-based computational modeling and planar biaxial artery material properties for human coronary plaque vulnerability assessment. *Mol Cell Biomech* **9**, 77–93 (2012).

129. Tang, D. *et al.* 3D MRI-Based Multicomponent FSI Models for Atherosclerotic Plaques. *Annals of Biomedical Engineering* **32**, 947–960 (2004).

130. Huang, Y. *et al.* The influence of computational strategy on prediction of mechanical stress in carotid atherosclerotic plaques: Comparison of 2D structure-only, 3D structure-only, one-way and fully coupled fluid-structure interaction analyses. *Journal of*

Biomechanics **47**, 1465–1471 (2014).

131. Malvè, M., García, A., Ohayon, J. & Martínez, M. A. Unsteady blood flow and mass transfer of a human left coronary artery bifurcation: FSI vs. CFD. *International Communications in Heat and Mass Transfer* **39**, 745–751 (2012).

132. Chen, W. & Jeudy, J. Assessment of Myocarditis: Cardiac MR, PET/CT, or PET/MR? *Current Cardiology Reports 2019 21:8* **21**, 1–10 (2019).

133. JH, R. *et al.* Imaging atherosclerotic plaque inflammation with [18F]-fluorodeoxyglucose positron emission tomography. *Circulation* **105**, 2708–2711 (2002).

134. Li, X. *et al.* 68Ga-DOTATATE PET/CT for the detection of inflammation of large arteries: correlation with18F-FDG, calcium burden and risk factors. *EJNMMI Res* **2**, 52 (2012).

135. Torrado-Carvajal, A. Importance of attenuation correction in PET/MR image quantification: Methods and applications. *Revista Española de Medicina Nuclear e Imagen Molecular (English Edition)* **39**, 163–168 (2020).

136. Keereman, V., Mollet, P., Berker, Y., Schulz, V. & Vandenberghe, S. Challenges and current methods for attenuation correction in PET/MR. *Magnetic Resonance Materials in Physics, Biology and Medicine* vol. 26 81–98 Preprint at https://doi.org/10.1007/s10334-012-0334-7 (2013).

137. Hofmann, M. *et al.* MRI-Based Attenuation Correction for PET/MRI: A Novel Approach Combining Pattern Recognition and Atlas Registration. *J Nucl Med* **49**, 1875–1883 (2008).

138. Martinez-Möller, A. *et al.* Tissue Classification as a Potential Approach for Attenuation Correction in Whole-Body PET/MRI: Evaluation with PET/CT Data. *J Nucl Med* **50**, 520–526 (2009).

139. Eiber, M. *et al.* Value of a Dixon-based MR/PET attenuation correction sequence for the localization and evaluation of PET-positive lesions. *European Journal of Nuclear Medicine and Molecular Imaging 2011 38:9* **38**, 1691–1701 (2011).

140. Madio, D. P. & Lowe, I. J. Ultra-fast imaging using low flip angles and fids. *Magnetic*

Resonance in Medicine **34**, 525–529 (1995).

141. Ljungberg, E. *et al.* Silent zero TE MR neuroimaging: Current state-of-the-art and future directions. *Progress in Nuclear Magnetic Resonance Spectroscopy* **123**, 73–93 (2021).

142. Wu, Y. *et al.* Water- and fat-suppressed proton projection MRI (WASPI) of rat femur bone. *Magnetic Resonance in Medicine* **57**, 554–567 (2007).

143. Wiesinger, F. *et al.* Zero TE MR bone imaging in the head. *Magnetic Resonance in Medicine* **75**, 107–114 (2016).

144. Hofmann, M. *et al.* MRI-Based Attenuation Correction for Whole-Body PET/MRI: Quantitative Evaluation of Segmentation- and Atlas-Based Methods. *Journal of Nuclear Medicine* **52**, 1392–1399 (2011).

145. Lau, J. M. C. *et al.* Evaluation of attenuation correction in cardiac PET using PET/MR. *Journal of Nuclear Cardiology 2015 24:3* **24**, 839–846 (2015).

146. Leynes, A. P. *et al.* Zero-Echo-Time and Dixon Deep Pseudo-CT (ZeDD CT): Direct Generation of Pseudo-CT Images for Pelvic PET/MRI Attenuation Correction Using Deep Convolutional Neural Networks with Multiparametric MRI. *J Nucl Med* **59**, 852–858 (2018).

147. Song, S., Zheng, Y. & He, Y. A review of Methods for Bias Correction in Medical Images. *Biomedical Engineering Review* **3**, 1–10 (2017).

148. Tustison, N. J. *et al.* N4ITK: Improved N3 bias correction. *IEEE Transactions on Medical Imaging* **29**, 1310–1320 (2010).

149. Hou, Z. A review on MR image intensity inhomogeneity correction. *International Journal of Biomedical Imaging* **2006**, 1–11 (2006).

150. Leynes, A. P. *et al.* Hybrid ZTE/Dixon MR-based attenuation correction for quantitative uptake estimation of pelvic lesions in PET/MRI. *Medical Physics* **44**, 902–913 (2017).

151. Bloch, F., Hansen, W. W. & Packard, M. Nuclear Induction. *Physical Review* **69**, 127 (1946).

152. Purcell, E. M., Torrey, H. C. & Pound, R. V. Resonance Absorption by Nuclear Magnetic Moments in a Solid. *Physical Review* **69**, 37 (1946).

153. Buonincontri, G., Kaggie, J. D. & Graves, M. J. *Fast Quantitative Magnetic Resonance Imaging*. *Morgan & Claypool Publishers* vol. 15 (Morgan and Claypool Publishers, 2020).

154. LAUTERBUR, P. C. Image Formation by Induced Local Interactions: Examples Employing Nuclear Magnetic Resonance. *Nature 1973 242:5394* **242**, 190–191 (1973).

155. WA, E., JM, H., G, J. & T, R. Spin warp NMR imaging and applications to human whole-body imaging. *Phys Med Biol* **25**, 751–756 (1980).

156. Dweck, M. R., Puntmann, V. O., Vesey, A. T., Fayad, Z. A. & Nagel, E. MR Imaging of Coronary Arteries and Plaques. *JACC: Cardiovascular Imaging* **9**, 306–316 (2016).

157. Spuentrup, E. *et al.* Free-breathing 3D Steady-State Free Precession Coronary MR Angiography with Radial k-Space Sampling: Comparison with Cartesian k-Space Sampling and Cartesian Gradient-Echo Coronary MR Angiography—Pilot Study1. *https://doi.org/10.1148/radiol.2312030451* **231**, 581–586 (2004).

158. Börnert, P. *et al.* Direct comparison of 3D spiral vs. Cartesian gradient-echo coronary magnetic resonance angiography. *Magnetic Resonance in Medicine* **46**, 789–794 (2001).

159. Wang, Y. & Ehman, R. L. Retrospective Adaptive Motion Correction forNavigator-Gated 3D Coronary MR Angiography. *Imaging* **11**, 208–214 (2000).

160. Paul, J. *et al.* High-resolution respiratory self-gated golden angle cardiac MRI: Comparison of self-gating methods in combination with k-t SPARSE SENSE. *Magnetic Resonance in Medicine* **73**, 292–298 (2015).

161. Chiribiri, A., Botnar, R. M. & Nagel, E. Magnetic Resonance Coronary Angiography: Where Are We Today? *Current Cardiology Reports* **15**, (2013).

162. Ibrahim, T. *et al.* Serial contrast-enhanced cardiac magnetic resonance imaging demonstrates regression of hyperenhancement within the coronary artery wall in patients after acute myocardial infarction. *JACC Cardiovasc Imaging* **2**, 580–588 (2009).

163. Edelman, R. R., Chien, D. & Kim, D. Fast selective black blood MR imaging. *https://doi.org/10.1148/radiology.181.3.1947077* **181**, 655–660 (1991).

164. Xie, Y. *et al.* Improved black-blood imaging using DANTE-SPACE for simultaneous carotid and intracranial vessel wall evaluation. *Magn Reson Med* **75**, 2286 (2016).

165. Wang, J. *et al.* Improved suppression of plaque-mimicking artifacts in black-blood carotid atherosclerosis imaging using a multislice motion-sensitized driven-equilibrium (MSDE) turbo spin-echo (TSE) sequence. *Magnetic Resonance in Medicine* **58**, 973–981 (2007).

166. Bernstein, Matt A and King, Kevin F and Zhou, X. J. *Handbook of MRI pulse sequences*. (Elsevier, 2004).

167. Pauly, J. M. *Reconstruction of Non-Cartesian Data*. vol. 7 (2007).

168. Fessler, J. A. & Sutton, B. P. Nonuniform fast Fourier transforms using min-max interpolation. *IEEE Transactions on Signal Processing* **51**, 560–574 (2003).

169. Chen, W. & Meyer, C. H. Semiautomatic off-resonance correction in spiral imaging. *Magnetic Resonance in Medicine* **59**, 1212–1219 (2008).

170. Noll, D. C., Pauly, J. M., Meyer, C. H., Nishimura, D. G. & Macovskj, A. *Deblurring for Non-2D Fourier Transform Magnetic Resonance Imaging*. *MAGNETIC RESONANCE IN MEDICINE* vol. 25 (1992).

171. Ye, J. C. Compressed sensing MRI: a review from signal processing perspective. *BMC Biomedical Engineering 2019 1:1* **1**, 1–17 (2019).

172. Block, K. T., Uecker, M. & Frahm, J. Undersampled radial MRI with multiple coils. Iterative image reconstruction using a total variation constraint. *Magnetic Resonance in Medicine* **57**, 1086–1098 (2007).

173. Block, K. T. & Uecker, M. *Simple Method for Adaptive Gradient-Delay Compensation in Radial MRI*.

174. Haji-Valizadeh, H. *et al.* Accelerated, free-breathing, noncontrast, electrocardiograph-

triggered, thoracic MR angiography with stack-of-stars k-space sampling and GRASP reconstruction *. *Magn Reson Med* **81**, 524–532 (2019).

175. Wang, L. *et al.* Effects of residual stress, axial stretch, and circumferential shrinkage on coronary plaque stress and strain calculations: A modeling study using IVUS-based near-idealized geometries. *J Biomech Eng* **139**, 0145011 (2017).

176. Maleszewski, J., Lai, C. K. & Veinot, J. P. Anatomic Considerations and Examination of Cardiovascular Specimens (Excluding Devices). *Cardiovascular Pathology: Fourth Edition* 1–56 (2015) doi:10.1016/B978-0-12-420219-1.00001-X.